Touchdown Dynamics and the Probability of Terrain Related Failure of Planetary Landing Systems

– A Contribution to the Landing Safety Assessment Process –

Vom Fachbereich Produktionstechnik

der

UNIVERSITÄT BREMEN

zur Erlangung des Grades
Doktor-Ingenieur
genehmigte

Dissertation

von

Dipl.-Ing. Lars Witte

Gutachter: Prof. Dr. rer. nat. H. Dittus
Fachbereich Produktionstechnik
Universität Bremen

Prof. Dr. phil. nat. J. Oberst
Fachgebiet Planetengeodäsie
Technische Universität Berlin

Tag der mündlichen Prüfung: 20. November 2015

» The objectives of the LM[1] landing planning strategy are to anticipate the lunar environmental problems and to plan the landing approach so that the combined spacecraft systems, including the crew, will most effectively improve the probability of attaining a safe landing. «

(From *Cheatham 1966*)

[1] The Apollo Lunar Module

Abstract: The landing safety assessment is an integral element of the planning of a planetary landing mission. In addition to the position dispersion around the nominal landing site it has to consider the topographic characteristics of that place, which might endanger the landing system. The presented thesis contributes to this assessment process with the modelling and deduction of the functional limits of a landing system and its terrain-related failure probabilities. A mathematical method, adopted from reliability engineering methods, has been developed in order to determine these terrain-related failure probabilities from touchdown dynamics data. A legged landing platform is used as a study object. Its touchdown dynamics is represented by a high-fidelity numerical multibody simulation which is validated by experimental data from a dedicated test campaign. The numerical simulation then provides the input data for the analysis process. However, the analysis of the terrain-related failure probabilities remains incomplete without knowledge about the geotechnical properties of the landing site such as the terrain slope and roughness. This information is obtained from a landing site characterization. For that purpose, this thesis adds a further analysis step which extracts this information from high resolution digital terrain models under consideration of the specific baselength determined by the landing platform's footprint. A robotic lunar landing mission is used as case study to integrate the different analysis steps into an exemplary landing safety assessment. On the basis of this example a realistic application procedure is proposed and its usability is demonstrated.

Übersicht: Die Sicherheitsbewertung des Landevorgangs ist ein integraler Bestandteil der Planung von planetaren Landemissionen. Diese berücksichtigt neben den möglichen örtlichen Abweichungen vom nominellen Landeplatz auch dessen topographische Gegebenheiten, die eine sichere Landung gefährden könnten. Die vorliegende Arbeit leistet durch die Modellierung und Ableitung der funktionalen Grenzen eines Landesystems und seiner geländebedingten Ausfallwahrscheinlichkeit einen Beitrag zu diesem Bewertungsprozess. Um aus den Daten einer Landedynamikanalyse die Ausfallwahrscheinlichkeiten abschätzen zu können, werden mathematischen Methoden erarbeitet, die sich aus der technischen Zuverlässigkeitsanalyse ableiten lassen. Als Anwendungsobjekt dient eine Plattform mit Landebeinen, deren Aufsetzdynamik durch ein hochdetailliertes Mehrkörpersimulationsmodell numerisch abgebildet wird. Die Validität des Modells konnte anhand experimenteller Daten aus einer Landetestkampagne überprüft werden. Mithilfe dieses numerischen Modells werden dann die Eingangsdaten für den Analyseprozess erzeugt. Eine solche Analyse der geländebedingten Ausfallwahrscheinlichkeiten bleibt jedoch unvollständig ohne die Bereitstellung geeigneter geotechnischer Informationen, wie die Geländeneigung und Rauigkeit. Diese Informationen werden durch eine Landestellencharakterisierung gewonnen. Hierzu wird im Rahmen dieser Arbeit ein weiterer Analyseschritt eingefügt, der diese Informationen unter Berücksichtigung der sich aus dem Fußkreisdurchmesser der Plattform ergebenden Basislänge aus hochauflösenden digitalen Geländedaten extrahiert. Anhand einer robotischen Mondlandemission werden die verschiedenen Analysezweige in einer beispielhaften Landesicherheitsanalyse integriert und durchgerechnet. Anhand dieses Beispiels wird eine realistische Einsatzmöglichkeit vorgeschlagen und die Anwendbarkeit des Verfahrens demonstriert.

Preface

Die vorliegende Arbeit entstand während meiner Tätigkeit als wissenschaftlicher Mitarbeiter am Institut für Raumfahrtsysteme des Deutschen Zentrums für Luft- und Raumfahrt (DLR) in Bremen. Das Institut wurde 2007 gegründet und die ersten Jahre waren geprägt durch die Aufbauarbeit, mit welcher zunächst die Forschungsthemen und Projekte und die dafür notwendigen Labore und Arbeitsmittel geschaffen wurden, um ein wissenschaftliches Arbeiten zu ermöglichen. Die neu entstandene Arbeitsgruppe „Landetechnologie“ der Abteilung Explorationssysteme hat dabei den fachlichen Rahmen gebildet, in welchem diese Dissertation entstanden ist.

Daher gebührt an dieser Stelle zunächst auch der Dank meinem früheren Institutsleiter beziehungsweise jetzigem DLR-Raumfahrtvorstand und Doktorvater Herr Prof. Dr. H. Dittus sowie meinem früheren Abteilungsleiter Herr Dr. T. van Zoest, die mir während der vergangenen Jahre die Freiräume zur Entwicklung und Fertigstellung meines Dissertationsprojektes gewährt haben. Weiterhin gilt mein Dank auch Herrn Prof. Dr. J. Oberst für die Begutachtung der Arbeit sowie Herrn Prof. Dr. A. Rittweger für die Übernahme des Prüfungsvorsitzes.

Ein weiterer wesentlicher Faktor zum Gelingen der Arbeit war das freundschaftliche Arbeitsklima in der Arbeitsgruppe Landetechnologie und im Verbundprojekt Landetechnologie in Kooperation mit Airbus Defence & Space, Bremen. Namentlich genannt seien an dieser Stelle Herr Silvio Schröder (DLR) and Herr Robert Buchwald (Airbus DS) mit denen gemeinsam die experimentellen Untersuchungen zur Landedynamik realisiert wurden. Durch die Diskussionen mit Silvio und Robert und vielen weiteren Kollegen hat diese Arbeit an Tiefe gewonnen.

Abschließend möchte ich besonders auch meiner Frau Tabea danken, die mich immer wieder ermuntert hat, die Arbeit an dieser Dissertation fortzusetzen. Indem sie mir stets den Rücken freigehalten hat, hat sie einen maßgeblichen Anteil am Gelingen dieser Arbeit.

Lars Witte

Contents

Nomenclature

Scalar Values

a	Acceleration
A	Area
C	Cohesion
d	Distance or Diameter
D_r	Relative Density (Soil Mechanics)
E	Energy, Elastic Modulus
F	Force
g	Gravity
h	Height
I	Light Intensity
I_{xx} / I_{yy} / I_{zz}	Inertia around x, y or z-axis
i	Counter Variable
k	Stiffness
m	Mass
N, n	Number or Counter
P	Probability
p / q / r	Roll / Pitch / Yaw Attitude Rate
R	Roughness
r	Radius or Resolution
S	Slope
s	Stroke or Displacement or Swath
t	Time
v	Velocity
w	Weight Factor

α	Confidence Level
ϑ	Terrain Property (Umbrella term for slope, roughness, or other terrain properties)
λ	Lagrange Multiplier or Scale Parameter of the Weibull Distribution,
μ	Coulomb's Friction Coefficient or Mean Value
ν	Poisson's Number
ρ	(Bulk-) Density or Correlation Coefficient
σ	Standard Deviation
τ	Shape Parameter of the Weibull Distribution
Φ	Internal Friction Angle (Soil Mechanics)
Φ / Θ / ψ	Roll / Pitch / Yaw Attitude Angle
χ	Azimuth

Subscripts

a	Outer (german: außen)
bc	Bearing Capacity
COM	Center of Mass
comp.	Compression
D	Drag
dd	Displacement Drag
Fail	Failure State
flat	a flat, terrain-feature-less surface
FP	Foot Print of of the Landing Gear
g	Gradient
gc	Ground Clearance
h	horizontal
i	Inner (german: innen) or Discrete Coordinate or Counter Variable
instable	State of Instability
lb	Lower Bound
lim	Limit
max	Maximum
ms	Mechnical Strength
n	Normal
obs.	observed (experimentally determined, including computer simulations)
p1	Primary Strut Number 1
Pad	Footpad
pred.	predicted
ps	Primary Strut
pss	Primary Strut Stroke
R	Roughness or Rock
S	Slope or Soil
s1	Secondary Strut Number 1
Safe	Safe State
ss	Secondary Strut
sss	Secondary Strut Stroke
stab	Stability Boundary
tens.	Tension
ub	Upper Bound
v	Vertical
x / y / z	Cartesian Coordinates

Mathematical Operators and Functions

$\lceil ( ) \rceil$	Ceiling Operator
E( )	Expectation
Exp( )	Exponential Distributed Random Number
max( )	Maximum Operator
min( )	Minimum Operator
N( )	Normal Distributed Random Number
Rayleigh( )	Rayleigh Distributed Random Number
Var( )	Variance
Weib( )	Weibull Distributed Random Number
Φ( )	Standardized Normal Distribution
$\hat{x}$	The Estimator of a Parameter (for example) x is indicated by the Circumflex "^"
x	General Vector (small letter, bold font)
X	General Matrix (capital letter, bold font)

Analysis Case Identifier

Analysis case identifiers are used to mark analysis data sets and describe the simulated conditions they represent in an abbreviated form. The consist of the following elements:

Lander model:	**LEM-4C** (Lander Engineering Model with four legs in the Cantilever configuration) or **RLL** (Robotic Lunar Lander),
Slope value:	Letter **S** followed by a number indicating the slope angle in degrees,
Roughness Feature:	Letter **F** for flat terrain (no roughness), **B** for a boulder followed by a number indicating its height, **C** for a crater followed by a number indicating its diameter,
Soil Property:	Letter **R** for a rigid (infinite soil bearing capacity) surface or letter **S** for a soft, finite bearing capacity surface,
Gravity:	Letter **L** for Lunar gravity.

Example: $\underbrace{\text{LEM-4C}}_{\text{Lander Model}} - \underbrace{\text{S15}}_{\substack{\text{Slope}\\\text{Value}}} - \underbrace{\text{B05}}_{\substack{\text{Roughness}\\\text{Feature}}} - \underbrace{\text{R}}_{\substack{\text{Soil}\\\text{Property}}} - \underbrace{\text{L}}_{\text{Gravity}}$

Abbreviations

CAD	Computer Aided Design
CDF	Cumulative Distribution Function (with prefix e: empirical CDF)
COM	Center of Mass
DLR	Deutsches Zentrum für Luft- und Raumfahrt (German Aerospace Center)
DN	Digital Number
DOE	Design of Experiments
DTM	Digital Terrain Model
ECSS	European Cooperation on Space Standarization
EDL	Entry, Descent and Landing
ESA	European Space Agency
FEM	Finite Element Model
FOV	Field of View
GIS	Geo Information System
GNC	Guidance, Navigation and Control
HDA	Hazard Detection and Avoidance
HIRISE	High Resolution Imaging Experiment
JPL	Jet Propulsion Laboratory
LAMA	Landing & Mobility Test Facility
LEM	Lander Engineering Model
LIDAR	Light Detection And Ranging
LM	Apollo Lunar Module
LOF	Limit of Function
LRO	Lunar Reconnaisance Orbiter
MBS	Multibody Simulation
MER	Mars Exploration Rover
MPF	Mars Pathfinder
MSL	Mars Science Laboratory
NAC	Near Angle Camera
NASA	National Aeronautics and Space Administration
PDF	Probability Density Function
RLL	Robotic Lunar Lander

1 Introduction

The landing of a spacecraft on the surface of a planetary body is one of the greatest challenges in space exploration endeavours. This results from the task to decelerate the vehicle in a relatively short period of time from its orbital entry velocity to a complete rest on the surface. Narrow targets for the vehicles position, velocity and attitude have to be met for a controlled landing within the vehicle's functional capabilities. As typically no ground control intervention is possible, a high degree of automation and autonomy is needed. The narrow band for the vehicle states and time criticality makes this mission phase hardly fault tolerant. The design of the system and its later operation are strongly affected by a planetary environment whose descriptors are still to some degree uncertain even if supporting information from orbiting spacecraft and previously successful landed missions is available. The environment, giving the context in which the spacecraft operates, is the entirety from gravity field, atmosphere, illumination conditions and surface properties.

Adler et al. 2012 summarize that "Entry, Descent and Landing (EDL) is defined to encompass the components, systems, qualification and operation to safely and usefully bring a vehicle from approach conditions to contact with the surface of a solar system body". The keywords "safely" and "usefully" should be noted in this statement. Hence the landing site selection is a pivotal element in the mission engineering process as it must satisfy these keywords which are a source of often conflicting priorities.

On one side the landing system is characterized by engineering constraints marking the spacecraft's capability to attain and accommodate a specific landing site. A mission design neglecting these constraints is prone to a landing failure and a loss of the mission. As a consequence scientific opportunities and professional reputation will be lost as well as public and political acceptance for costly exploration programs. All these consequences call for a safe landing. On the other hand the science case (or business case of emerging commercial programs) requires to land in an area suitable to meet the science objectives such as the vicinity to certain geological formations or terrain types. As they define the "usefulness" of a site their neglect compromises the scientific return and a degraded mission success can be regarded as a programmatic failure.

A considerable degree of uncertainty in the apriori knowledge about the environment, the absence of contingency operation options in the landing phase and fatal consequence in case of a failure demands for well analysed and justified decisions in the design and operations in landing missions.

A successful placing of the landing system adjacent to scientifically relevant objects without the reliance on luck is what *Cheatham 1966* regarded as "the science and art of mission planning". The Figure 1-1 illustrates this aspect. Both landings relied retrospectively on a good portion of luck not to strike one of the large boulders (Viking) or to encounter the steep sloped inner rim of a comparatively large crater (Luna).

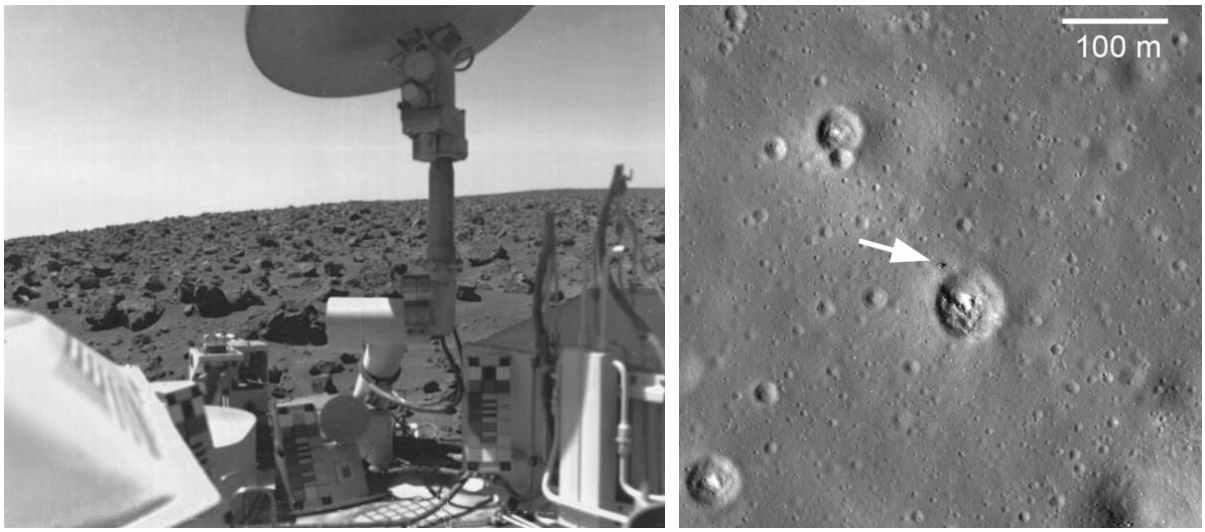

Figure 1-1 Luck or Mastery? Viking Lander 2 in a boulder-strewn field, seen by its onboard camera (left, image credit: NASA/JPL), Luna 24 landing position on the rim of a crater, seen by LRO (right, image credit: Arizona State University)

Given the above mentioned consequences of a landing failure it is understandable that all efforts are made by the involved engineering, science and programmatic communities to ensure a landing within the flight system's performance envelope while satisfying the mission's science objectives. In that regard the following section gives a brief overview on the historical development until the current state-of-the-art in landing site safety assessment.

1.1 Historical Context and State-of-the-Art

The Apollo lunar landings (1969 to 1972) and the Viking Mars landings (1976) can be regarded as by far most influencing historical missions within the Western political hemisphere. The system and mission design techniques developed for the "grandfather" missions are in many areas still unmatched today and provide a foundation for many recent missions.

Aside many engineering constraints on the landing site selection for the Apollo missions, a site's "landability" has been determined which is defined as the ability of the site to provide alternate touchdown spots for the Lunar Module in case the nominal spot turns out to be too hazardous during final approach. Landability is measured by *Cappellari 1972* as the ratio of the landable area with regard to the total area within a one kilometer radius around that nominal spot. This method thus required a distinction between "landable" and "unlandable" which were defined in a lunar surface specification to which the landing gear subsystem was designed to. Its design and the experimental and analytical establishment of the landing gear performance capabilities are described by *Rogers 1972*. In the early planning and design phase (~1965) the Lunar Module design relied on statistics in terms of size-frequency or magnitude surface descriptions for slope and roughness. The actual landing planning for later flights used remote sensing data gathered by the Lunar Orbiter missions and later orbital photography from the Apollo Command Module during preceding missions. The early flights for example aimed for sites with a safety oriented landability ratio of 0.8 whilst later missions with a grown experience and confidence deemed a ratio of 0.6 as safe. The complete analysis process including the various other factors in the landing site selection process is documented in *Cappellari 1972*.

For Mars Viking, a detailed landing performance capability assessment was performed as part of the lander design and development, described by *Muraca et al. 1975*. Several Monte-Carlo analyses were

carried out to determine 3σ-design values for accelerations, clearances, stability and leg forces. However, the level of fidelity on the landing system side was not matched by the necessary fidelity of the terrain model due to insufficient remote sensing resolutions. The landing site planning phase relied thereby on Mariner probe obtained orbital photography and Earth-based radar observations of the Martian surface. Surface hazards on lander-scale could only be inferred indirectly from the much coarser image resolutions. Viking orbiter photography led to a revision of the pre-planned sites as the improved image resolutions revealed unfavourable terrain formations on these particular sites. Despite that improvement the uncertainty on the actual boulder abundance remained as largest potential landing hazard according to *Masursky 1981*. Both Viking Lander 1 and 2 successfully landed during 1976. Post-landing surface images made by both landers indeed showed the presence of significant and unpredicted boulder coverage (see Figure 1-1) and *Masursky 1981* concludes "that the two landings on the surface of Mars involved some elements of luck…". Consequently a major recommendation for future missions was to significantly improve the resolution of remote sensing data products.

The US Mars exploration program was resumed in the 1990ies with the Mars Pathfinder mission (1997). The Mars Pathfinder mission still relied on Viking orbiter remote sensing data but at least profited from its improved interpretation based on Viking Lander ground truth data. The later Mars Exploration Rover (MER A and B, 2004) and the Phoenix (2008) mission then benefitted from the reconnaissance made by the Mars Global Surveyor (since 1997) and Mars Odyssey (since 2001) missions and later the Mars Reconnaissance Orbiter (since 2006) as outlined by *Golombek 2011*. The Phoenix mission marked also the return to legged landing principle more than 30 years after the Viking landings.

Both MER missions (*Golombek et al. 2003*, *Knocke et al. 2004*) and the Phoenix mission (*Spencer et al. 2009*, *Bonfiglio et al. 2011*) had foreseen each six trajectory correction manoeuvres to fine tune the targeted atmospheric entry interface and meet the (atmospheric) flight path requirements. At each manoeuvre date the error associated with the entry state was estimated. These navigation errors as well as aerodynamic uncertainties (implied from both the Martian atmosphere as well as vehicle properties) were considered in a Monte Carlo analysis of the EDL trajectory to calculate the landing site dispersion. Joint probability statements were determined based on a Gaussian bi-variate representation of the site dispersions and hazard classes from associated hazard maps and were compared to landing safety criteria. These "per pixel probabilities" are summed up as shown by equation 1.1 to the total probability for the targeted landing region. The terrain hazard classes are defined according to the degree a certain terrain is compatible with the flight system. The hazard classes H distinct between a safe (green) state, a "unsurvivable" (red) state and two further intermediate, marginal safe states.

$$P_{\text{Land in a hazard}} = \sum_i P_{\text{Land in Pixel i}} \cdot H_i \qquad 1.1$$

$$H_i = \begin{cases} 1, & \text{if hazard color of interest} \\ 0, & \text{otherwise} \end{cases}$$

The hazard maps contained the knowledge regarding potentially hazardous surface features in the intended landing region. The hazard magnitude from rock abundance has been classified and assigned as the colour of the pixel. The same principle has been applied to the potential hazards from slope.

The availability of such high resolution data in combination with geo-information (GIS) tools thus allowed for the first time a convolution of both the terrain property descriptors and flight system capabilities into a joint "in-spec probability" indicating the probability that the touchdown occurs within specified limits regarded as safe. These probabilistic assessments played subsequently a key role in deciding whether to perform planned trajectory correction manoeuvres or not.

Culminating in the most recent successful Mars Science Laboratory landing (2012), these missions have demonstrated not only a sophisticated set of analytical methods, but forms also a process which feeds back a probabilistic judgment criteria into a decision making process (here to execute a trajectory correction manoeuvre).

1.2 Research Idea and Objectives

Undoubtedly, the referenced manned lunar landing and robotic Mars landings[2] are very different mission types with unique environmental challenges. When it comes to the touchdown event the hazards stemming from terrain features such as slopes and roughness become comparable again and with it the associated aspects in landing site assessment. Common to all these missions is in that regard a discrete classification of the terrain into landable / unlandable or other respective hazard classes.

But equation 1.1 implicitly provides a starting point to a slightly different notation, which stems from the military domain and is known as "survivability" to the engineering communities.

Ball 2003 defines survivability as "the capability of a system to avoid or withstand hostile natural or manmade environments without suffering abortive impairment of its ability to accomplish its designated mission". A broader definition for survivability is given by *Richards 2009* with "the ability of a system to minimize the impact of a finite-duration disturbance on value delivery".

Survivability in its military notation is thereby defined according equation 1.2, and is in this probabilistic formulation equal to "not getting killed" with the kill probability being the union set of "susceptibility" and "vulnerability". Susceptibility is the probability of being hit, while vulnerability is the conditional probability of suffering a damage or impairment if being hit.

$$P_{Survival} = 1 - P_{Kill} = 1 - P_{Susceptibility} \cdot P_{Vulnerability} \qquad 1.2$$

Introducing this approach to planetary landings, susceptibility would mean the probability to encounter a potential hazardous terrain feature. It comprises all factors that expose the landing system to potential hazardous terrain features in the landing zone and is influenced by the landing site selection. Consequently it can be modelled as $P_{Land\ in\ pixel\ i}$ identical as in equation 1.1 as done with MER, Phoenix and MSL. The term vulnerability means in this case the probability to suffer a failure conditional to a touchdown on a certain terrain feature. This reflects the landing gear performance capabilities and is substantially influenced by design features such as lander size and geometry and energy absorbing elements. Adapted to the landing case and re-written accordingly, equation 1.2 appears as the following expression:

$$P_{Safe} = 1 - P_{Fail} = 1 - \sum_i P_{Land\ in\ Pixel\ i} \cdot P_{Fail\ |\ Land\ in\ Pixel\ i} \qquad 1.3$$

The difference to the state-of-art expressed in equation 1.1 that this thesis aims to formulate the landing success probability upon touchdown rather than then asking if the landing system stays within a specified discrete limit. The new and different term $P_{Fail\ |\ Land\ in\ Pixel\ i}$ is the conditional probability of terrain related failure which is inevitably linked to the kinematic and dynamic properties of the landing platform, hence the title of this thesis. The derivation of this term is the core of this work.

[2] Although this historical view only appreciates only US missions, the successes of other nations – especially the lunar program of the former Soviet Union and most recently China's successful robotic lunar landing – shall not remain unmentioned. The availability of public information with relevance for this thesis is too scarce to be referenced here.

The following aspects and specific questions arise and shall be addressed when pursuing this concept further:

- The underlying working hypothesis is that probabilistic methods are applicable to describe terrain-related failure phenomenon with identifiable parameters.
- How can these probabilities be derived from a touchdown system model in that case and what methods and tools are suitable to do so?
- How can the results be used to determine the operating regime in which the landing system is robust to perturbations and uncertainties?
- Finally, demonstrate the applicability and usefulness of the proposed approach in landing site safety assessment context.

Restating the objectives of this thesis, it shall contribute to the engineering of planetary landing missions by advancing analysis tools to incorporate the vehicle's ability to accommodate and withstand the planetary terrain into the systems and mission engineering process.

1.3 Structure of the Thesis

The analysis of the touchdown dynamics of a landing platform and derivation of its functional limits consists of several steps in a processing chain necessary to embed the landing platform model into a landing site analysis framework. The structure outlined below shall give an overview about which aspect in this chain is supported by a dedicated chapter.

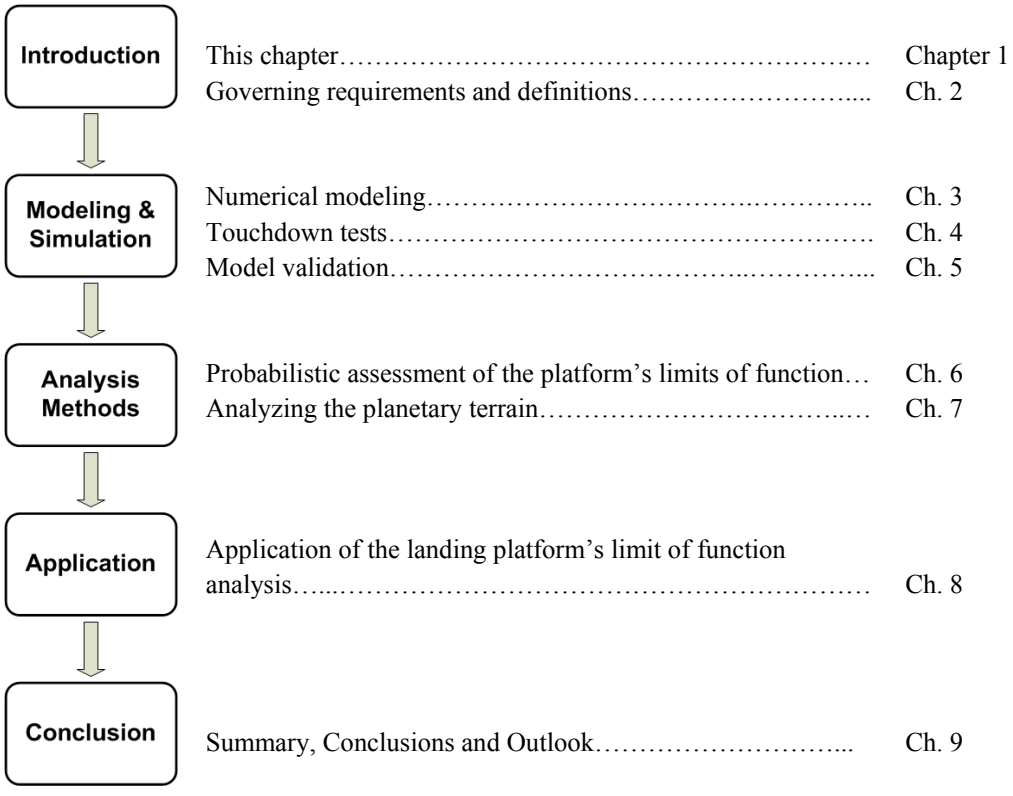

Figure 1-2 Structure of this thesis

In addition to this general introduction into this work, the **chapter 2** is dedicated to the specific introduction of touchdown systems, their typology and area of application as well as the functional and performance requirements typically imposed on these elements. The focus of this thesis is then put on

legged landing systems, whose governing functional and performance requirements on a landing platform design and operation are given. Such a system has to fulfill several functional requirements such as providing sufficient stability against tip-over, maintaining ground clearance to prevent undesired body contact to the planetary surface and load limitation to ensure the integrity of its structure and payload. These requirements are addressed through the platform's geometry, kinematic properties and energy absorbing elements. Their design principles and definitions are introduced and provide a base for the following modeling and simulation element, which consists thereby of three chapters.

Within **chapter 3** the development of a conceptual model of a legged landing platform which is implemented into a numerical multibody simulation tool is described. The landing platform is from a mechanical point of view a multibody system with kinematical closed loops. The energy absorbing elements as well as the footpad-to-soil contact mechanics are characterized by non-linear stress-strain relations. Due to the high non-linearity of the conceptual model the solution of the resultant equations of motion is not amenable to an analytic solution and calls for a numerical implementation whose implementation and parameterization is outlined.

A test campaign, described in **chapter 4**, using a physical lander engineering model of a landing platform, was conducted to provide experimental data for the validation of the numerical simulation. Such experimental validation shall ensure that predictions by the numerical simulation is plausible, credible and within acceptable error tolerances. Dedicated touchdown test cases were used to stimulate and measure the platform's functional performance. The lander engineering model, the used test facility and support elements are presented together with the underlying test plan of the campaign.

In order to validate the numerical model the experimental data is correlated in **chapter 5** with the data gained from its simulated counterpart. Quality and acceptance criteria are provided to assess the correlation results. The modeling-simulation-validation cycle is thereby an iterative process until satisfactory numerical model fidelity is achieved. The results of the final iteration loop is shown and discussed. A valid and credible simulation of the platform's kinematic and dynamic properties is a key aspect for the follow-on analysis of its functional limits.

A rigorous derivation of the analysis method is the subject of **chapter 6**. It provides the used mathematical preliminaries and develops step-by-step an analysis scheme to identify and represent the limits of function of the platform. As the touchdown conditions are typically not known exactly but can be expressed by an expected value and a dispersion parameter, the analysis outcome is itself of stochastic nature. Thus instead of having a deterministic limit of function it is assigned with a probability statement. Methods from the reliability engineering domain are adapted to link the results to terrain property descriptors.

As consequently the probability to exceed a functional limit is conditional to the geotechnical terrain properties it is reasonable to make an intermediate step through **chapter 7** and have a more detailed look onto digital terrain data being the source of the terrain context information. It thereby gives an overview on the required remote sensing data products and introduces the analytical means used to extract the terrain property descriptors such as slope and roughness figures from it. A sample digital terrain model is used hereby which acts in the following case study chapter as a reference landing site.

In **chapter 8** the analysis methods are combined and systematically applied to obtain probability of terrain-related failure expressions for the relevant platform landing failure modes. The interfaces to and contributions of adjoined landing system subsystems are elaborated, discussed and with regard to the case study reasonably assumed. This refers basically to the subsystems involved in the dispersion

of the landing points. The case study is thereby illustrative to the application of the methods derived in this thesis as they are put into a landing site safety assessment.

The thesis summarizes the achievements of this work as well as raised questions on future continuative or supplemental work in **chapter 9**.

2 Touchdown Systems – Typology, Requirements and Definitions

Prior to focusing explicitly on legged touchdown systems a step back is made to get an overview on touchdown systems in general. A first classification of concepts becomes obvious when past and current landing missions are evaluated with regard to their touchdown mass and velocity. Figure 2-1 shows such a classification based on data of 21 missions. Obviously the landing system variants form cluster in particular regimes of the mass-velocity-diagram. The particular mission is identified by a 3-letter code linking it to the underlying data and respective reference in Annex A1 – Touchdown System Reference Data.

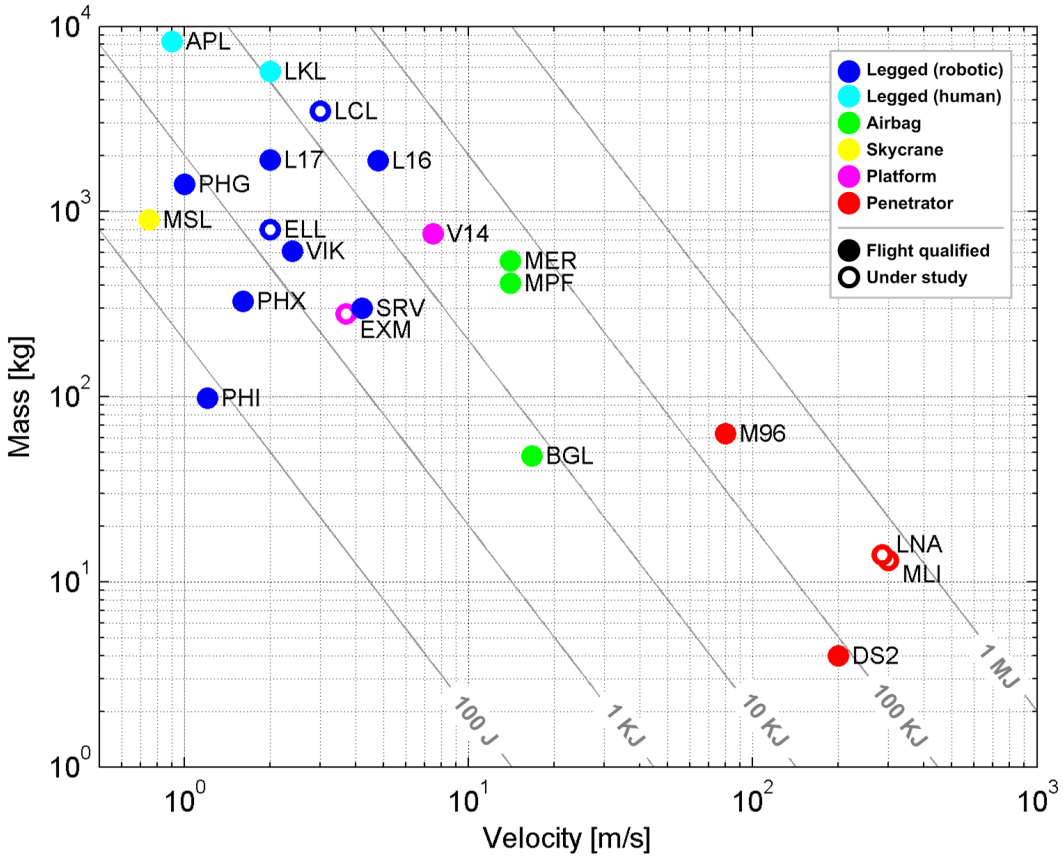

Figure 2-1 Touchdown velocity-mass-diagram for past and current missions, indicating the touchdown energy for certain types of landing systems. The three-letter codes identify the respective mission; refer also to Annex A1 for further details.

One class is given by penetrators which are designed to touchdown in a defined attitude, allowing it to penetrate into the surface. The payload compartment is enclosed in a hardened, bullet-like shell. The impact energy ranges between ~100kJ to 1MJ and is absorbed mainly by the planetary soil. These systems experience very high shock loads which limits its use for only small, comparatively low mass and highly ruggedized payloads.

Airbag landers are designed to touch down with velocities >10 m/s in an arbitrary attitude. The loads from the initial impact and bouncing are attenuated by the airbags. Having come to a rest the payload is released out of the airbag cluster or shell. Self-righting mechanisms like the paddle-like side walls of the Mars Pathfinder (MPF) and Mars Exploration Rover (MER) landing packages can correct an

unwanted orientation after landing. The touchdown energies of these landers are in the range of several 10kJ.

Platforms or pallet-like landing systems are designed to land in a defined attitude. They use a layer of crushable material as a means for energy absorption. The landed mass is in the order of several 100kg touching down with velocities of <10 m/s.

The Skycrane concept introduced with the Mars Science Laboratory (MSL) mission originates from the idea to land a planetary rover whose size and mass exceeds the useful regime of airbag technology. Hereby the concept utilizes the inherent capability of the rover's mobility system to accommodate the planetary terrain. This concept avoids thereby a dedicated landing platform with a rover egress system. The kinetic energy at touch down falls well below 1kJ.

Legged landers are likewise designed to touch down in a defined attitude on their landing legs. Energy dissipation and load attenuation is realized by absorber elements inside or attached to the stroking struts (ref. section 2.3 below). The touch down velocities are well below 10 m/s for which reason these landing systems are also sometimes dubbed "soft" landers. These relatively benign and controlled touchdown conditions while offering a large mass range make this concept appealing to a variety of landing missions ranging from small scientific probes to even heavy and human-rated assets. The importance of this concept is the key rationale for a further focus on legged landing systems within this work. Some of its functional and performance requirements have been implicitly mentioned in this short description and are re-formulated as requirements in the following section.

2.1 Performance and Functional Requirements

As indicated by the landing system topology above the requirements on landing systems are strongly dependent on the mission scenario and concept. In particular legged landing systems demand significant control authority and propulsive capabilities to match the narrow velocity and attitude targets to which the landing gear subsystem is or shall be designed to. The following table introduces touchdown conditions which can be regarded as typical for a legged platform. These touchdown conditions are requirements (*ESA 2008*) stem from an envisaged European legged lunar landing system identified as "ESA Lunar Lander", abbreviated as "ELL" in Figure 2-1. These values will act as reference for the case study in chapter 8. In this chapter a more detailed technical background of this mission is introduced as well.

Parameter	Value
vertical velocity v_v [m/s]	2.0 ± 1.0
horizontal velocity v_h [m/s]	0.0 ± 1.0
maximum platform pitch Θ and yaw Ψ attitude [°]	0.0 ± 5.0
maximum platform pitch q and yaw r attitude rate [°/s]	0.0 ± 1.0
maximum acceleration a_{max} [m/s²]	< 100
minimum ground clearance h_{gc} underneath the thrusters [m]	> 0.5

Table 2-1 Typical required touchdown conditions for a robotic landing system

Within this touchdown condition regime the landing platform shall provide the below stated functions (*Buchwald et al. 2008*):

1. The platform shall be dynamically stable. Thus the overturning or toppling of the platform shall be prevented. This requirement shall ensure that the platform comes to a rest on its landing legs within its intended orientation relative to the terrain surface.

2. The residual kinetic energy upon touchdown shall be dissipated in a controlled manner and thus limiting the resultant loads on the platform. The limit is defined by the payload and/or other subsystem being carried on the landing platform.

3. A minimum ground clearance shall be maintained after touchdown. This requirement shall ensure that parts of the spacecraft other than the touchdown system are not in contact with surface features, thus no unintended, additional load path are introduced (Remark: in some cases (Apollo) also the engine skirt was designed to crush upon an unintended but allowed surface contact of the descend stage engine).

2.2 The Definition of Landing Safety and Terrain-related Failures

The previous section introduced the legged landing vehicle class and some of its driving requirements. Prior to its further elaboration, the following section shall add to these specific requirements a set of high level objectives and requirements. These stem out of an already well defined set of definitions and provide the necessary mission and system engineering framework.

A safe landing marks the beginning of the surface operations phase of a landing mission. It is thus the necessary condition for the achievement of the mission objectives. Reference (*ECSS 2004*) defines "Safety" as "the system state where an acceptable level of risk with respect to fatality, injury or occupational illness, damage to launcher hardware or launch site facilities, damage to an element of an interfacing manned flight system, the main functions of a flight system itself, pollution of the environment, atmosphere or outer space, and damage to public or private property is not exceeded". The term "risk" is hereby defined as "the undesirable situation or circumstance that has both a likelihood of occurring and a potential negative consequence …". These definitions can be restated as "Safety is the absence of undesirable situations with negative outcomes". As the concept of risk involves a likelihood of occurrence, safety is likewise of a probabilistic nature.

Consequently *ECSS 2009* specifically requires that "operating ranges and performance limits for safe operation shall be established and specified".

An exceedance of the functional limits is regarded as a failure which is defined in *ECSS 2004* as "the termination of the ability of an item to perform a required function". The critical functions for the landing platform are to provide dynamic stability, energy absorption and ground clearance. Furthermore, failures are classified by *Birolini 1997* according their mode (the local effect or symptom), their cause and their effect (the consequences). The failures of the landing platform are coarsely described in Table 2-2.

Mode	Cause	Effect
The landing platform tips over.	The landing is dynamically unstable.	Loss of mission.
Excessive loads and/or shocks to the system and/or payload.	The energy absorption capability has been exceeded.	Potential of damage to system and/or payload resulting in partial or complete degradation of mission.
Ground contact with parts other than the footpads	The ground clearance has been insufficient to accommodate the terrain.	Potential of structural damage and/or impairment of the surface operations.

Table 2-2 Legged landing platform touchdown failure modes, causes and effects

The root causes of these failures can be both intrinsic (landing instability can be caused by excessive touch down velocities) or extrinsic and are here terrain-related (e.g. steep slopes). This work further assumes that the landing system is flight worthy and not impaired by defects or preceding failures of critical subsystems and also resulting in a landing failure prior to the planned touchdown event. A failure to land is thus not assessed as a matter of the system's technical reliability but to terrain-related failures as a consequence of an operational decision for a certain landing site.

To establish the operating ranges the functional limits of the required functions energy absorption, landing stability and ground clearance will be expressed as functions of relevant terrain properties. A safe landing in turn is then considered as landing in which the probability of exceeding the platforms functional limits is below an acceptable limit. It is thus both relying on the system technical capabilities and the operational decision for a certain landing site.

2.3 Design Concepts of Legged Platforms

The functions *dynamic stability, energy absorption* and *ground clearance* and their associated limits are themselves functions of the landing platform's leg kinematics, the number of legs, mass distribution and COM position h_{COM}, and geometrical properties such as the assembly height and landing gear footprint radius r_{FP} as well as the energy absorption characteristic. Figure 2-2 sketches some of these key design factors.

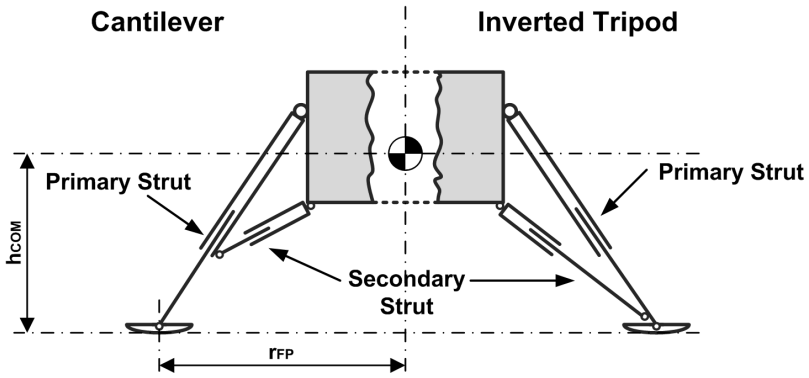

Figure 2-2 Leg kinematics and geometric properties: The Cantilever principle (left) attaches the secondary strut to the upper tube of the primary strut, the Inverted Tripod principle (right) attaches the secondary strut to the moving lower tube of the primary strut

The leg kinematics, known as “Cantilever” and “Inverted Tripod”, are distinguished by the position of the joint between the primary strut and the secondary struts. The Cantilever type connects the secondary strut to the non-movable upper part of the primary strut (Figure 2-2, left) while the Inverted Tripod connects the secondary strut to the movable lower part of the primary strut (Figure 2-2, right). Representative of the Cantilever type is the Apollo Lunar Module (LM) landing gear described by *Rogers 1972*. The Viking Lander landing gear, described by *Holmberg et al. 1980*, represents the Inverted Tripod respectively. According to *Rogers 1972* the cantilever variant offers some slight advantages over the inverted tripod variant in terms of a lower mass and better ground clearance due to its shorter secondary struts. However this advantage is not too compelling to make it always the better variant. The ultimate design choice thus remains case dependent and to be determined during the system engineering process.

A reliable and efficient method to provide energy absorption and load protection to structures is the intentionally plastic deformation of designated elements. When loaded, the respective element deforms at first elastically and proportionally to the stroke. Upon exceedance of its yield point the element starts to deform plastically and irreversible. The associated force-stroke-curve however depends on the design and material choice of the energy absorbing element. Generally, the energy absorption capability is determined by integration of the absorber force F(s) over the stroke s, thus $E = \int F(s)\, ds$. A material to provide energy absorption functionality in the primary and secondary strut is a honeycomb structure made of metal or fibre foils. When loaded in normal direction to the honeycomb cells the onset of buckling of the cell walls leads to a collapsing of the cells and a plastic deformation of the cell walls (Figure 2-3 left). The limit forces F_{lim} at which the cells start to fail is determined by the cell diameter and the foil thickness and is a design characteristic of the particular honeycomb type.

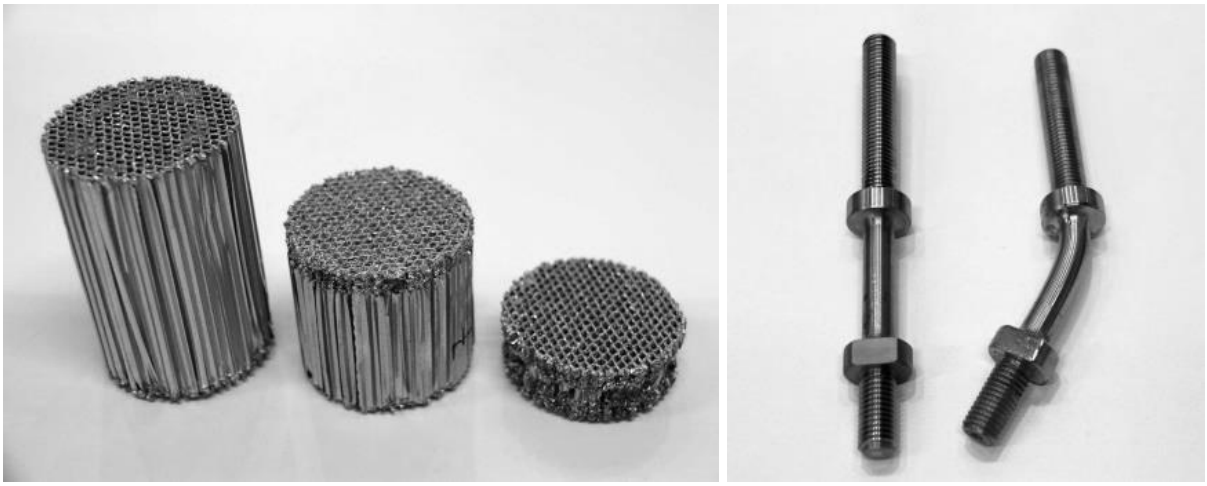

Figure 2-3 An aluminum honeycomb crash cartridge (left) with two different crush levels, and a steel bending rod (right) before and after deformation (both from the LEM, ref. chapter 4)

Figure 2-4 shows schematically how three such cartridges are integrated into the landing legs primary strut. The struts upper part is basically a tube containing the cartridge stages as well as some support elements. The struts lower part acts as a piston and can travel into the upper part. This type of leg assembly allows a defined unilateral loading onto the honeycomb cartridges.

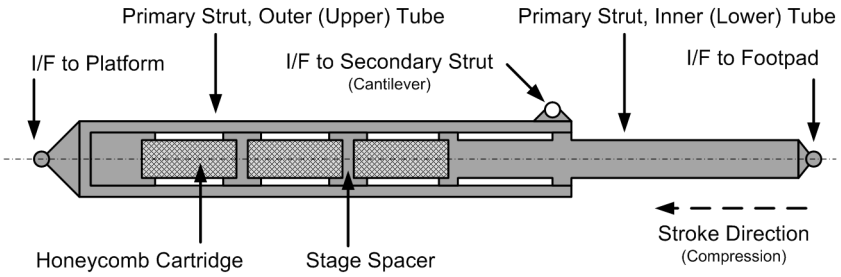

Figure 2-4 Cut-view of a primary strut assembly using three stages of honeycomb material. This design allows to use different and increasing crush strength for each cartridge

Aluminium honeycomb material can also be used in the secondary struts. A suitable design (Figure 2-5 a) realizes stroke capability in both the compression and tension direction although the cartridges experience compression loads only. An alternative concept for the secondary strut load limitation is a bending rod between the strut and the main body (Figure 2-5 b). A mainly lateral force leads to a deflection and ultimately to a plastic deformation of the rods when the yield point is exceeded. Such a bending rod is also shown in Figure 2-3 right.

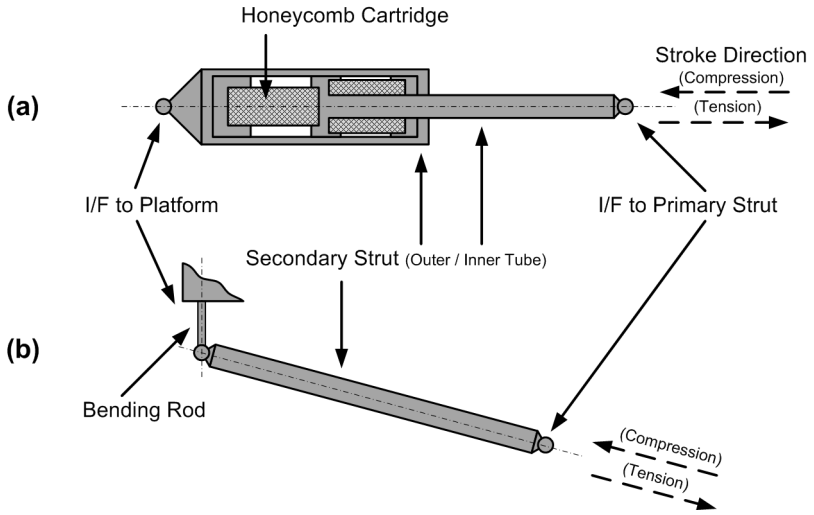

Figure 2-5 Secondary landing gear strut using honeycomb material in compression and tension direction (a, cut-view) and using a bending rod load limiter (b)

Exemptions from the use of plastically deforming material are the Rosetta lander Philae, which uses an electro-mechanical damping principle and the Surveyor lunar probe, having used an oleo-hydraulic absorber.

Another important factor is the accommodation of the landing legs during the launch, cruise and – if applicable – entry phase. Figure 2-6 shows the Apollo Lunar Module and Mars Viking lander leg assemblies in their stowed and deployed positions. The Apollo LM leg is stowed to fit the LM into the Spacecraft-LM-Adapter. A design constraint on the Viking leg mechanism is the shape of the aeroshell for its atmospheric entry phase. Although this function is not directly involved in the performance delivery at touchdown it is mentioned here for completeness as it can significantly affect the landing gear design and thus implicitly it's other functional performance.

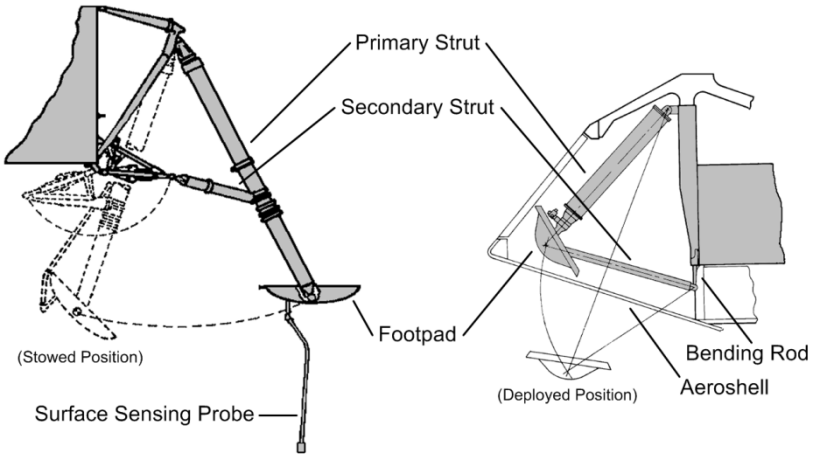

Figure 2-6 Apollo Lunar Module (left) and Viking Lander (right) leg assembly in stowed and deployed configuration (Apollo sketch re-drawn from *Rogers 1972*, Viking sketch from *Holmberg et al. 1980*, sketches are of different scale)

3 A Numerical Model of a Legged Landing Platform

A comprehensive analysis of the touchdown performance and terrain interaction demands a high-fidelity numerical simulation of the landing platform. There are (i) the large number of touchdown conditions, system states and environmental variables and (ii) the space environment, here especially the gravity, which are hard to cover with experimental tests. To obtain a suitable numerical model, the touchdown system is modeled as a numerical multibody system. It regards the principal properties and requirements of legged landing systems as introduced in the previous chapter. The multibody modeling theory stems predominantly from the domain of technical mechanics and mechatronic engineering. Its general set-up, model building, the associated nomenclature and way to mathematical representation is introduced subsequently before the specific case of the landing platform is introduced.

3.1 Multibody Models

Generally, multibody systems are any physical entities which consist of at least two bodies which are connected via a joint or other means allowing a relative motion between these bodies. The bodies can be rigid or flexible. The model elements *bodies*, *forces (torques)* and links (*joints/constraints)* are fundamental building blocks of any multibody system.

Bodies: define the geometry of the assembly and represent its mass and inertia properties. Each body adds six further degrees of freedom to the system. Weight is thus associated to bodies. External forces and torques are applied at discrete positions on the respective body.

Links: determine the degree of freedom between bodies. Links can be either joints or constraints. The latter type gains its importance as it is required to close a kinematic loop and is described as implicit algebraic equations dependent from the position of the body. Links are considered as massless, infinitely stiff model elements.

Forces and torques: are initiators of all motions of the multibody assembly. External forces stem from actuator and control forces (torques), or spring-damper elements and tribological interactions. Internal forces are forces of reaction acting in the links between the bodies.

An applied external force leads to a position and orientation change of that multibody system as a whole or between particular bodies.

For the set-up of the describing equations of motion formal methods exist. These “Principles of Mechanics” are Hamilton’s, Jourdain’s and d’Alembert’s principle which are described in *Schwertassek 1999*.

A key aspect in model building is the type of kinematic loops formed by the respective bodies. These are either open loop such as a kinematic tree or chain or closed loop. Open loops disaggregate if joints are cut open and the formulation of the differential equations for each body is simplified as the number of constraints for the assembled system is equal to the number of constraints in each joint. This is not the case for closed loop systems and additional compatibility conditions have to be regarded to close the kinematic loop. Algebraic equations describe these constraints and have to be solved in addition to the differential equations. *Schwerin 1999* gives this set of equations in their descriptor form which is also used in equation 3.1. Hereby the vector $\mathbf{x}$ contains the generalized coordinates, $\mathbf{g}$ describes the constraint conditions, λ is the Lagrange multiplier adding the constraint forces to the equation of motion and the matrix $\mathbf{G}$ is a Jacobian matrix containing the partial derivates $\partial\mathbf{g}/\partial\mathbf{x}$.

$$\mathbf{M} \cdot \ddot{\mathbf{x}} = \mathbf{f}(\mathbf{x}, \dot{\mathbf{x}}, \mathbf{t}) - \mathbf{G}(\mathbf{x})^{\mathbf{T}} \cdot \boldsymbol{\lambda} \qquad 3.1$$

$$\mathbf{g}(\mathbf{x}) = \mathbf{0}$$

Several working groups have set-up the equations of motion for a landing platform "by hand" (d'Alembert's method). Relevant work has been done by *Howlett 1967*, *Walton 1967* and *Zupp1971* in the forefront of the Apollo landing missions. The basic set of equations describing a touchdown system can be found there. The advantage of the strong formalization is exploited by modern Multibody Simulation software tools such (e.g.) SIMPACK (*SIMPACK 2013*) or MSC.Adams (*MSC 2013*) which provide a CAD-similar user interface allowing modeling the multibody elements of a mechatronic system directly. The elements and their links are interpreted and automatically transformed into set of equations making use of the aforementioned formal methods (Jourdain's principle, typically). The resultant equations of motion can be numerically solved in the time domain and provide a response of the modeled system to external inputs. In the following course of this work the focus is put on such computer-aided analysis of the landing platform. To provide at first however a software tool independent description the vehicle multibody topology, their case specific geometries as well as case specific forces laws are given.

3.2 Topology of Legged Landing System

The specific relations of the elements *bodies*, *joints/constraints* and *force elements* and their properties are forming together the landing platform multibody topology as depicted in Figure 3-1. In this figure the symbols for joints and constraints are annotated with the degrees of freedom given by the particular link element (for example *3r1t* means three rotational and one translatory degree of freedom). Both the symbols for joints/constraints and forces/torques are connected to each two bodies. They indicate the kinematic and dynamic relations between these bodies.

The leg assembly represents here a Cantilever-type configuration and is connected via its primary strut (upper part) and its secondary struts to the lander main body. Each secondary strut is connected via a constraint to the primary strut thus closing a kinematic loop and forming a statically determined structure. The force elements *F_PrimLoadLimiter_1*, *F_SecLoadLimiter_11* and *F_SecLoadLimiter_12* have a plastic-elastic force-stroke-behavior to represent the energy absorbing property when deforming plastically upon an applied force. The force element *F_Footpad_Surface_1* can assume either a hard (full elastic) or a soil (plastic) contact to represent various surface properties. Force elements *F_Friction_1* for Coulomb' friction in the telescoping primary strut and *F_Engine* to consider a main engine thrust profile complement the model set-up. For a better readability, Figure 3-1 omits the assembly for the leg assembly number 2, 3 and – if applicable – 4. They are of an identical topology as the shown leg assembly number 1 and are attached to the main body in a way that they are placed symmetrically around the landing systems vertical axis.

With this topology the kinematic and dynamic behavior of a landing platform is basically defined. The particular set values defining the respective model element's size, shape and dynamic properties in the numerical implementation are parametrized such that a generic and scalable model becomes available.

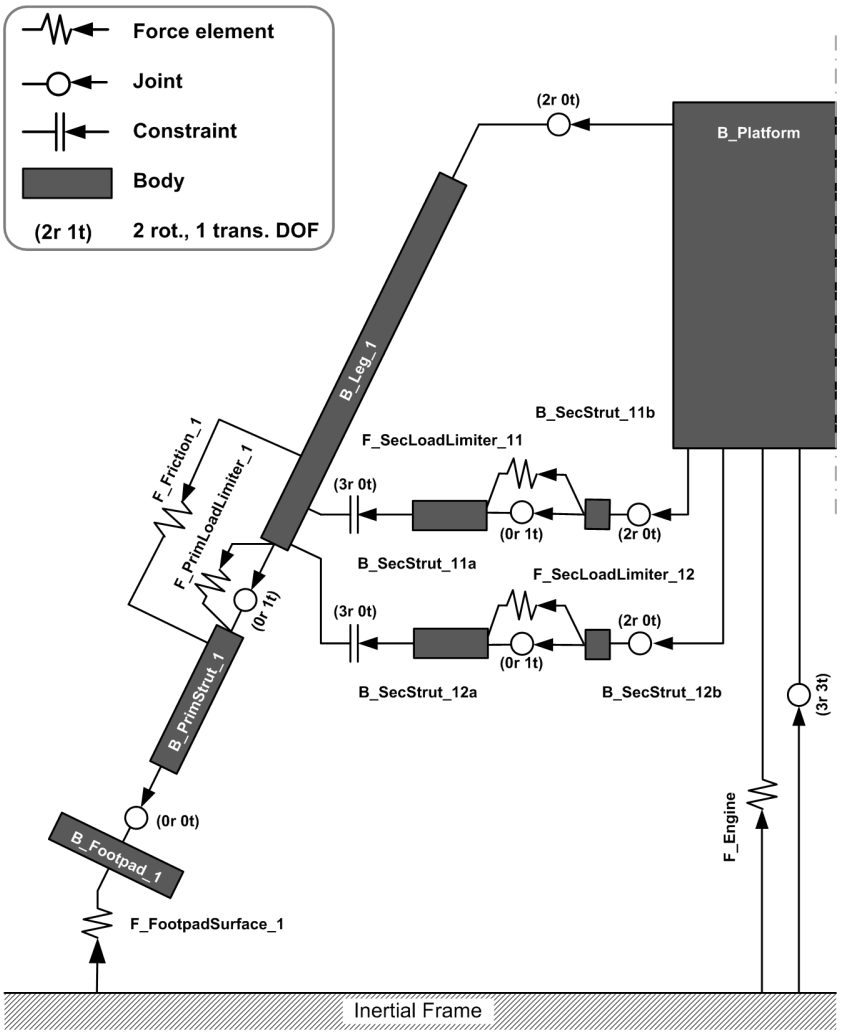

Figure 3-1 Legged landing platform multibody topology showing the kinematic relations between the different platform elements, their degrees of freedom as well as applied forces

3.3 Landing Platform Model Element Descriptions

This section provides a detailed description of the specific model elements, their characteristics and describing parameters for the legged landing platform model. The reference design is the Lander Engineering Model LEM (refer chapter 4.1) as it is also used as validation case. As far as applicable, model data is derived from or validated by reference test data.

3.3.1 Bodies

The legged landing system model implements all individual body elements as simple geometric shapes such as tubes or tubular primitives and cuboids. All simple body elements are defined by a few dimensioning parameters and the element mass (Table 3-1). Their volumes, average mass and the moment of inertia are derived from these input values. As force elements are modeled as massless elements, the mass of the honeycomb cartridges, guide bushings and support elements are associated to the body model elements of the strut parts. The masses of all minor construction elements such as nuts, bolts and brackets are allotted to the respective elements principal shape. The advantage is that the resulting landing platform's geometry model is completely parameterized and thus scalable as long as the underlying topology remains unchanged.

Base geometry (images reprinted from *Grote 2004*)	**Describing parameter**	**Affected body elements**
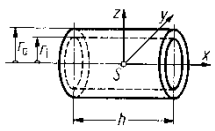	Outer radius r_a [m] Inner radius r_i [m] Height h [m] Mass m [kg]	B_Leg, B_PrimaryStrut, B_SecondaryStrut a/b B_Footpad, B_Platform, B_CenterMass
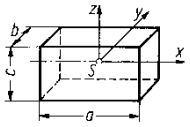	Length a [m] Width b [m] Height c [m] Mass m [kg]	B_Ballast, B_GripperFlange

Table 3-1 Base geometries for model body elements used to assemble the Lander Engineering Model (LEM) and a Robotic Lunar Lander. Annex A2 provides the respective values for these body elements.

The model represents here the LEM with a detailed body element description, mass breakdown and derived figures given in the annex A2 – Masses and Geometries of Landing System Models. The derived combined mass and moments of inertia are tabulated in Table 5-1 in comparison to the LEM's measured values. This multibody landing platform model is later used in chapter 8 as part of the case study in a larger, up-scaled variant representing a Robotic Lunar Lander in a four leg cantilever configuration.

3.3.2 Force Elements

Energy absorption and load protection in the primary and secondary struts is realized by means of dedicatedly plastically deforming elements as outlined in chapter 2.3. Its numerical representation implements the specific force stroke characteristics of these elements.

3.3.2.1 Primary Strut Force-Stroke-Behaviour

The modelled primary energy absorber considers three cartridges of aluminium honeycomb material. When loaded, the cartridges initially start to deform elastically proportional to the progressing stroke until the first force level F_{lim1} is reached. The honeycomb cells start to collapse and fold irreversible. When the maximum stroke of the first, weakest stage is reached and the stroke still progresses, the next cartridge engages. The particular characteristic of the honeycomb stages used in the LEM has been determined experimentally on component level by *Buchwald et al. 2012*. A data sample from this reference is plotted in Figure 3-2. Upon force onset the initial displacement is linearly increasing and determined by the elastic deformation of the honeycomb cartridge. When the limit force of in this case 3.7 kN is reached the plastic deformation starts and maintains the force level. The ripples seen around the limit force are due to each new buckling as the cartridge folds up. When the load is relieved the elastic portion of the deformation rebounds. The honeycomb energy absorber only accepts compressive loads.

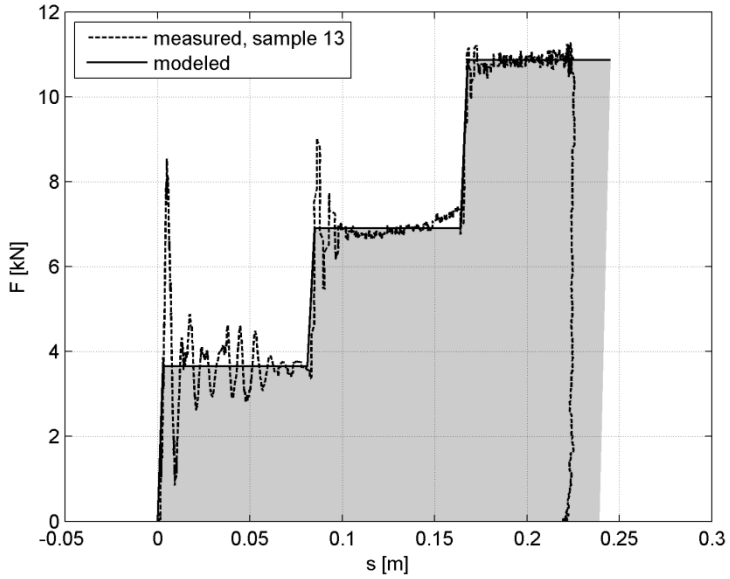

Figure 3-2 Measured and modeled force-stroke-curve of the three-staged primary strut of the LEM: the gray shaded area indicates the energy absorption capability of that strut.

The data is used here also to identify the parameter of the force-stroke relation of the elastic behaviour and respective crush strength model which is considered by the numerical touchdown simulation as modelled characteristic in the force element *F_PrimLoadLimiter_1*. The experimentally identified limit forces are tabulated in Table 3-2 and the resulting modelled curve is also shown in Figure 3-2. The stiffness of the combined stages has been identified as k_{ps} = 1.91 MN/m. The energy absorption capability is indicated as gray shaded area in this figure.

	Limit Force F_{lim} [kN]	**Max. Stroke s_{ps} [mm]**	**Max. Energy [J]**
Stage 1	3.7	77	285
Stage 2	6.9	77	530
Stage 3	10.9	77	840

Table 3-2 LEM honeycomb stage force stroke performance parameter identified from test data

3.3.2.2 Secondary Strut Force Stroke Behavior

In case of the LEM, the secondary struts are connected via bending rods of ~135 mm length as load limiting device to the main body. Likewise as the honeycomb elements, the characteristic force-stroke curve of the secondary energy absorbers used in the LEM has been determined experimentally on component level by *Buchwald et al. 2012*. Unlike the honeycomb energy absorber elements, the bending pin design can accept both compressive and tension loads. An experimental data sample from a tension-compression-test, showing a full tension-compression-cycle, is used here to identify the parameters of an analytic description of the characteristic curve (Table 3-3). The stiffness of the bending rods is k_{ss} = 350 N/m. The data sample is published in *Buchwald et al. 2012* and plotted here together with the modelled curve for the elastic, the compression and tension plastic force-stroke relation in Figure 3-3. The gray shaded area underneath the model curve indicates again the energy absorption capability as considered in the numerical simulation. Here the plastic tension area (positive forces/deformations) assumes a full elastic rebound which does not match the experimentally

determined behaviour. This actual behaviour is caused mainly by hardening effects in the material which are not considered in the model. As will be seen in chapter 4 this model simplification is however of insignificant influence.

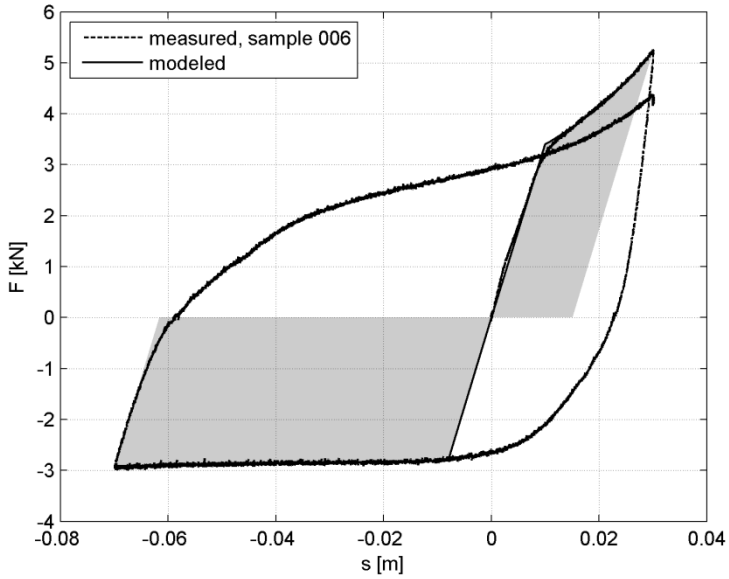

Figure 3-3 Measured and modeled force-stroke-hysteresis of LEM's secondary strut bending rods: the gray shaded area indicates the energy absorption capability in the compression and tension direction, respectively

	Force F(s) [kN]	Max. Stroke s_{ss} [mm]	Max. Energy [J]
Tension	$0.92 \cdot e^{42.0 \cdot s} + 2$	30	~85
Compression	$-2.8 \cdot e^{-0.61 \cdot s}$	70	~180

Table 3-3 LEM bending rod force stroke performance parameter identified from test data

3.3.2.3 Footpad-to-Soil Contact Force Law

In this multibody model approach, the footpad-to-soil contact force law is a key element in describing the dynamic interface between the landing system and the planetary body. The planetary surface contact mechanical properties can thereby coarsely classified according to the nature of the soil. A hard, rocky surface exhibits a stiff elastic contact between the surface and the footpad, while a granular, sandy or regolith-type surface can be characterized by an elastic-plastic behaviour. The hard surface contact is regarded as classical contact mechanical problem between two elastic bodies, which is therefore touched subsequently only briefly. Particular emphasis is however put on a granular soil model to account for the soil's contribution to both the touchdown energy absorption as well as its potentially detrimental effects on the lander's ground clearance.

Hard Surface Contact

The normal force F_n is numerically modelled as a mechanical spring whose equivalent stiffness k_R is calculated according the Hertzian contact mechanics by a cylinder with the radius r_{Pad} of the footpad

indenting a semi-infinite space (equation 3.2) of infinite elasticity. The elastic properties are determined by the footpad's elastic modulus E and its Poisson number ν.

$$\mathbf{F_n} = \underbrace{\mathbf{2 \cdot r_{Pad} \cdot E_{Pad} \,/\, (1 - \nu_{Pad}^2)}}_{:=\mathbf{k_R}\ [\mathbf{N/m}]} \cdot \mathbf{s_n} \qquad 3.2$$

The tangential force F_t at the pad-to-rock interface is determined by a Coulomb friction element (equation 3.3) with F_n being the normal force according to equation 3.2 and μ_R the friction coefficient at the contact plane between pad and soil.

$$\mathbf{F_t} = -\boldsymbol{\mu_R} \cdot \mathbf{sgn}(\mathbf{v_h}) \cdot \mathbf{F_n} \qquad 3.3$$

Granular Surface Contact

The main purpose of the force law implemented here is to correctly account for the soil's contributions to the overall energy absorption and its effects on the remaining ground clearance when the footpads penetrate the surface. This is illustrated by (Figure 3-4). The force-penetration behaviour is thus a point of major interest for a terrain interaction analysis. Relevant basic work on the impact of a disc-shaped footpad has been carried out during the Apollo era. The footpad soil interaction is thereby characterized by the initial impact and acceleration of the bulk material underneath the pad, velocity-dependent displacement drag and the equilibrium state when the pad has come to a rest (*Bendix 1968*).

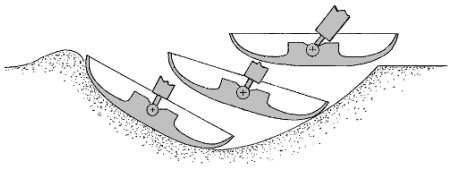

Figure 3-4 Illustration of a footpad penetrating into soil (redrawn from *Bendix 1968*)

For the purpose of a numerically efficient implementation into a multi body simulation of a landing platform a modified version of the original *Bendix 1968* model is reported by *Witte et al. 2010* which is subsequently restated. The footpad's force normal to the surface F_n is thereby the sum the soil's mechanical strength F_{ms} and the drag-like force F_{dd} is caused by the displacement of the granular media by the pad.

$$F_n = F_{ms} + F_{dd} \qquad 3.4$$

A block diagram of this part of the model is depicted in Figure 3-5 indicating F_{ms} and F_{dd} as functions of the pad's velocity v_n. The displacement drag is proportional to the square of the footpad velocity. It is determined by dimensionless coefficient C_D for which an analytic estimate is provided by *Bendix 1968*. Its underlying formula is provided in annex A3 – Soil Mechanical Data. The parameter ρ_s is the soil's bulk density, and A_{Pad} describes the footpad area projected onto the surface. Depending on its shape or curvature, A_{Pad} can be a function of the penetration depth s as well.

$$\mathbf{F_{dd}} = \underbrace{\mathbf{C_D \cdot \rho \cdot A_{Pad}}}_{:=\mathbf{b_{dd}}\ [\mathbf{Ns^2/m^2}]} \cdot \mathbf{v_{Pad}^2} \qquad 3.5$$

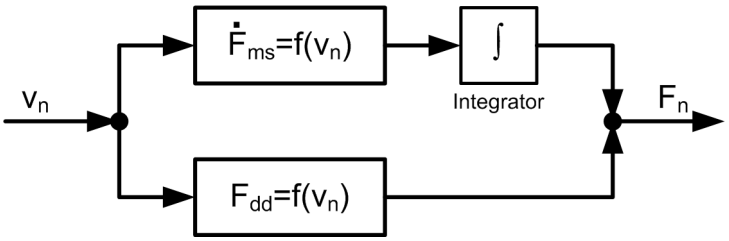

Figure 3-5 Block diagram of the footpad-soil contact force law: the contact force F_n is a function of the penetration velocity v_n and is composed of a drag-like force F_{dd} and the bearing capacity of the soil (F_{ms})

Regarding the soil's mechanical strength F_{ms}, the underlying assumption of this model is that the penetrating pad causes a punching shear failure of soil's stratum as the ultimate bearing capacity is immediately exceeded underneath the footpad. The force F_{ms} marks then an increase in mechanical strength of the soil along the pad's penetration path and can be considered as a strain-hardening effect. This part is identified as branch 1 in Figure 3-6. The loading branch (1) is described by equation 3.6. When pad velocity changes its sign, the force law shows a switching behavior and reverts to an elastic rebound (branch 2) which is determined by the confined soil's stiffness k_S ($k_S >> k_{ms}$). The term k_S is calculated by equation 3.2, however using an elastic modulus E_S and Poisson's number ν_S describing a granular soil under a confining pressure. The load is relieved until the force is offset and the pad separates (branch 3) from the surface. The surface height at this position is stored and remains as a non-reversible, plastic deformation. When reloaded again, the surface starts to deform plastically again, depending on the footpads position (1). However, if the maximum force F_n acting on the footpad (= F_{ms} at transition from (1) to (2)) is higher than the ultimate, static bearing capacity F_{bc} (equation 3.7) at depth s_n, than the switching law enters the branch (4). It thus reverts to a fully elastic behavior. This ultimate bearing capacity is determined by the soil mechanical foundation theory *Craig 2004*. The switch cases of this law are also given in Table 3-4, relating the branches of the force-stroke-curve to the time-derivatives of F_{ms} as used in the force law show by Figure 3-5. The gray shaded area in Figure 3-6 equals the energy absorbed the plastic deformation of the soil.

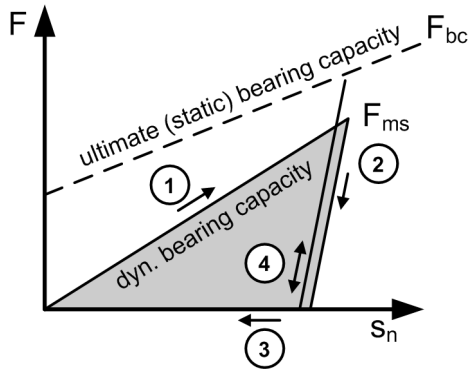

Figure 3-6 Soil's elastic-plastic force law (schematic): the bearing capacity increases with a deeper penetration s_n (branch 1). The elastic rebound (branch 2) gives the force law a saw-tooth-like shape. The gray shaded area thereby indicates the energy absorbed by the plastic deformation of the soil.

The dimensionless coefficient C_{ms} is as well an analytic estimate according to *Bendix 1968* dependant on certain soil mechanical descriptors. The coefficients C_{Nc}, $C_{N\gamma}$ and C_{Nq} describe bearing capacity factors based on the soil mechanical theory for shallow foundations and are found in *Craig 2004* and *Wilun 1972*. The calculation reference of these parameters is again given in in annex A3 – Soil Mechanical Data.

$$\mathbf{k_{ms} = C_{ms} \cdot \rho \cdot g \cdot A_{Pad}} \quad [\mathbf{N/m}] \qquad 3.6$$

$$F_{bc} = A_{Pad} \cdot \left(C_{Nc} + C_{N\gamma} + C_{Nq} \cdot s_n\right) \qquad 3.7$$

Branch	v_n	F_{ms}	$\dot{F}_{ms}$	Behavior Law
(1)	> 0	> 0	$k_{ms} \cdot v_n$	elastic-plastic, $F_{ms} \leq F_{bc}$
(2)	≤ 0	> 0	$k_s \cdot v_n$	elastic-plastic, $F_{ms} \leq F_{bc}$
(3)	≤ 0	≤ 0	0	elastic-plastic, $F_{ms} \leq F_{bc}$
(4)	> 0	≤ 0	$k_{ms} \cdot v_n$	full-elastic, $F_{ms} > F_{bc}$

Table 3-4 Force-penetration curve switch cases: these cases define the change of the force law's behavior and determine its shape as shown in Figure 3-6

Parallel to the surface a conventional Coulomb friction term considers the friction at pad-to-soil interface (similar to equation 3.3). Although parallel to the surface a drag-like force acts as well, it is comparatively small and can be neglected in this case. The model is implemented into the multibody simulation and uses its solvers to integrate the dynamic state F_{ms} and descriptive states of the switch law.

Footpad-to-soil model validation

An additional test campaign by *Schröder et al. 2011* on component level revisiting the footpad soil mechanics was executed in order to provide data for validation of this model. These tests used a test footpad loaded by an additional mass. This set-up was dropped into a bed with soil simulant material. As the set-up incorporates no own means for energy absorption, the complete energy is dissipated into the soil. The set-up for this particular test case has a footpad diameter of 300 mm, a mass of 200 kg and an impact velocity of 3.0 m/s onto fine quartz sand (type Wf34). The data shown in Figure 3-7 – both measured and simulated – represents the contact force $F_n = F_{ms} + F_{dd}$ normal to the pad and the penetration depth s_n normal to the soil surface. Its soil mechanical descriptors are summarized in annex A3 – Soil Mechanical Data. The footpad-to-soil simulation model achieves generally a very good correlation with the test data and particularly matches the peak force, pulse width and penetration depth. The force law switch from elastic-plastic to full elastic behavior can be seen in the normal force F_n curve at time t ~ 0.1 s.

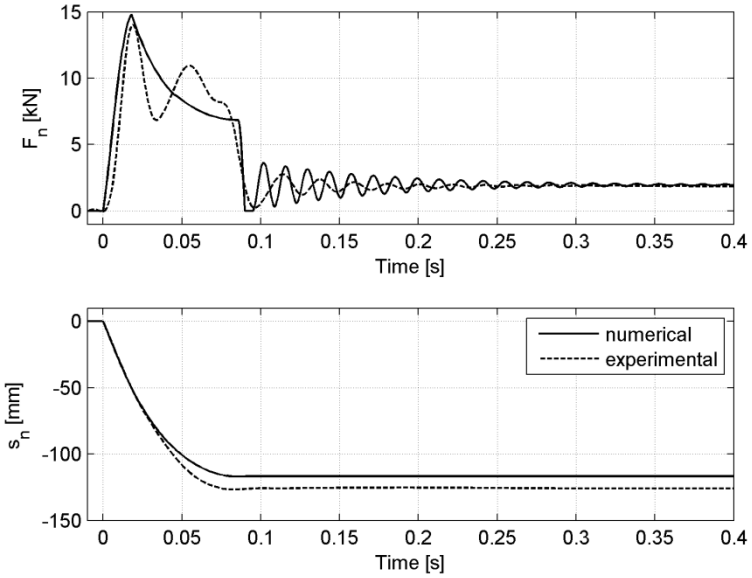

Figure 3-7 Experimental data from a dedicated footpad drop test validate the numerical results from the footpad-to-soil contact force law: the force F_n (top) peak and pulse width as well as the penetration depth (bottom) are well correlated

Figure 3-8 shows again the simulated footpad normal force F_n and in addition its two components, the force from mechanical strength F_{ms} and the force from displacement drag F_{dd}. The decomposition into these two forces clearly indicates that the peak of the normal force is dominated by the velocity-dependent force F_{dd} while the bearing capacity builds up along the pad's penetration path until it takes over the complete load.

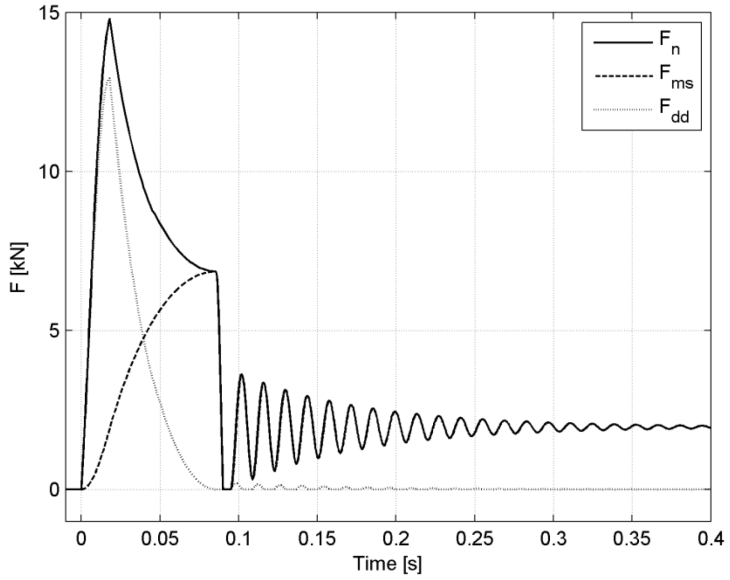

Figure 3-8 Simulated footpad forces – normal force F_n and its components force due to mechanical strength F_{ms} and displacement drag F_{dd}

3.3.2.4 Force of Friction in the Telescoping Strut

A further force element models Coulomb's friction in the guide bushing of the telescoping primary strut elements (equation 3.8). The force $F_{SS,n}$ normal to the stroke axis is exerted by the secondary strut forces F_{SS}. The considered friction factor is $\mu_{PS} = 0.35$.

$$\mathbf{F_{Friction}} = -\boldsymbol{\mu_p} \cdot \mathbf{sgn}(\dot{\mathbf{s}}_\mathbf{p}) \cdot \mathbf{F_{SS,n}} \qquad 3.8$$

3.3.2.5 Force from Main Engine Thrust

The main engine thrust effect is considered by a profile as defined by equation 3.9 and sketched in Figure 3-9. The time t_0 is defined as the time of first ground contact which is sensed by proximity or contact switches. Prior to touchdown the thrust offsets the vehicle's weight W. Main engine cut-off (MECO) occurs then with a delay time of $t_{DELAY} = t_{MECO} - t_0$. The thrust decay is modeled by *Zupp 1971* as exponential function with a decay time constant T_D. This force law is not considered for the validation cases (chapter 5) as the experimental reference cases (chapter4) are non-propelled drop tests.

$$\mathbf{F_{\_Engine}}(\mathbf{t}) = \begin{cases} \mathbf{F_{THRUST}}, & \mathbf{t} \le \mathbf{t_{MECO}} \\ \mathbf{F_{THRUST}} \cdot \mathbf{e}^{-(\mathbf{t}-\mathbf{t_{MECO}})/\mathbf{T_D}}, & \mathbf{t} > \mathbf{t_{MECO}} \end{cases} \qquad 3.9$$

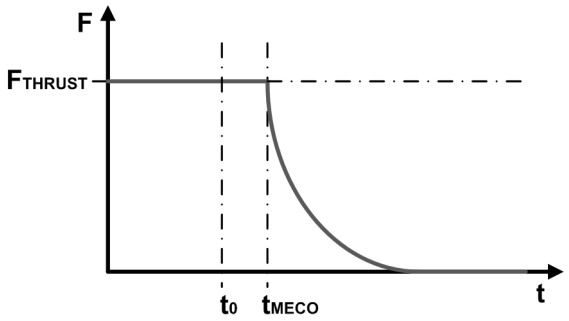

Figure 3-9 Schematic engine thrust profile: upon main engine cut-off signal (MECO) the thrust force decays with a given decay rate T_D

3.4 Dynamic and Kinematic Measurements

Up to this point all model elements needed to simulate a legged landing platform are introduced. With the declared purpose of this numerical model to explore the limits of the functions of the touchdown system, some definitions and metrics are required to evaluate their degree of utilization. This section shall therefore introduce suitable formulations to measure this utilization. These metrics are then implemented in the multibody simulation and its results are part of the output data file for a further post-processing.

3.4.1 Measurement of Stability

The degree of remaining stability margin until tip-over is represented as the shortest distance d_{STAB} between the vehicle's COM and a so called "stability plane". This plane is spanned by the gravity vector and a vector defined between the positions of each two adjacent footpads as depicted in Figure 3-10.

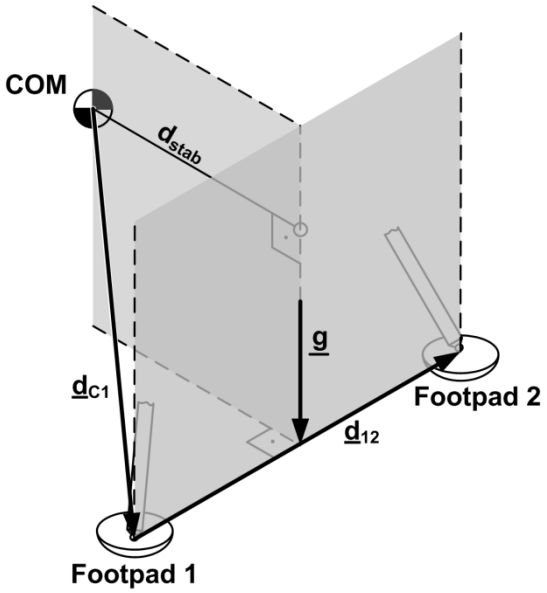

Figure 3-10 Definition of the stability boundary: stability is measured as distance between the platform's COM and a plane defined by the gravity vector and two adjacent footpads

The stability distance d_{STAB} is yielded then (eq. 3.10) by projecting the vector $\underline{d}_{C1}$ connecting the COM and the footpad's center onto the vector normal to the stability plane as formulated by the following equation representing the footpad 1 to footpad 2 side. Thus the number of stability planes equals to the number i of landing legs. The stability of the vehicle is determined by the minimum of the all i stability distances. This metric was originally suggested by *Zupp 1971*.

$$d_{stab,1}(t) = \underline{d}_{C1} \bullet \left(\underline{g} \times \underline{d}_{12}\right) / \left|\underline{g} \times \underline{d}_{12}\right| \qquad 3.10$$

The landing platform is statically stable as long as its COM is contained within the circumference of its footpads as the platforms weight causes a moment around the instantaneous center of rotation to turn it back. The platform however becomes instable when the COM is outside this circumference as the resulting moment further increase the tilt angle. The platform is dynamically stable when the rotational kinetic energy is insufficient to lift the COM through the stability plane. The limit of this function is consequently $d_{stab,LOF} = 0$ as $d_{stab} < 0$ means an instable platform while $d_{STAB} > 0$ indicates the remaining stability reserve. An example data plot is shown in Figure 6-8.

3.4.2 Measurement of Ground Clearance

The remaining ground clearance is defined as the minimum distance d_{gc} between the landing platform's belly and the planetary terrain surface underneath. Sensitive system components such as the engine nozzles, instruments or sensors are thereby considered in the numerical model by a reference envelope as shown in the following figure. The associated limit of this function is $d_{gc,LOF} = 0$. The geometry of terrain features such as crater or boulder is stored as digital terrain model (DTM), made available to the numerical simulation and evaluated at run-time. Chapter 7 elaborates further on the terrain undulations, their modeling and consideration in a numerical simulation. An example data plot regarding a minimum ground clearance measurement is shown as well in Figure 6-8.

$$d_{gc} = z_{Lander} - z_{Terrain} \qquad 3.11$$

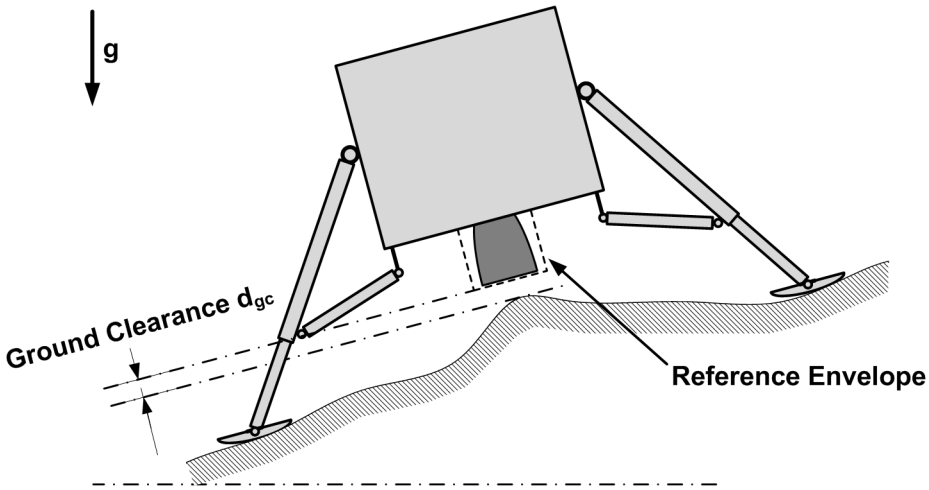

Figure 3-11 Definition of ground clearance: ground clearance is measured between the platform's lowest structural component and the terrain's highest protuberance within the footpad circumference

3.4.3 Measurement of Energy Absorption

The energy absorption capability is defined by the force-stroke relation of the particular load limiting element. These relations have been introduced in this chapter in the sections 3.3.2.1 and 3.3.2.2 as they are also an integral part to consider in the model set-up. This energy absorption capability is expended when the maximum demonstrated or certified stroke values $s_{PS,max}$, $s_{SS,max.compression}$ or $s_{SS,max.tension}$ are reached. Consequently in case of the LEM-4C, taken as reference model in this chapter, the stroke limits in Table 3-2 and Table 3-3 apply. The actual strokes of all four primary struts and eight secondary struts are then checked against these defined limits. Exemplary leg stroke data plots are shown in the validation chapter in

3.5 Implementation and the Use of SIMPACK

For the purpose of model implementation this work uses the commercially available multi body simulation software SIMPACK (Version 9.1.1, 64 Bit). This software is used for modeling, analysis and design of general mechanical and mechatronic systems out of a wide range of engineering domains (*SIMPACK 2013*). It makes use of the mechanical principles mentioned afore, allowing a formalized generation of the equations of motion. The following brief overview highlights the software elements used in this work. A detailed description can be found in *SIMPACK 2012*.

The software suite consists basically of a pre-processor, the Solver and a post-processor. The pre-processor is the primary means to set up the model. A CAD-like graphical user interface (GUI) supports the assembly of the model topology and its visualization. Standard model elements are selected from dedicated element libraries. The elements are capable of parametrization and the application specific parameter settings can be read-in from data arrays or functions which are used to import the force-stroke curves of the landing platforms energy absorbing elements (section 3.3.2.1 and 3.3.2.2) and the terrain model (chapter 7). New user specific model elements can be incorporated as User Routines, linking customer developed code to the SIMPACK program environment. Referring to this the footpad-soil force law (*Witte et al. 2010*, refer to section 3.3.2.3) has been transferred by *Liebernickel 2012* into a SIMPACK executable user routine.

The solver part offers several numerical integration methods to handle the sets of ordinary or algebra-differential equations generated automatically from the model topology by the pre-processor. This

work uses solvers capable of root detection to handle the various model state transitions such as elastic to plastic force law changes and no-contact to contact situations.

The post-processor supports the simulation result analysis with a data plot capability and video animations of the systems motion. The results can also be exported to other software environments for a further processing.

A scripting environment allows the programming of batch jobs or automatization of repetitive tasks either in the model building, its solving or port-processing. Referring to this, the set-up of a script acting as a parameter variation shell to support the automatized analysis of the lander model response to varying input parameter was done by *Liebernickel 2012*. This includes also the interfaces from the Parameter Variation shell to the simulation model and to the results extraction. The analysis described in chapter 6 makes use of this functionality.

Figure 3-12 shows an image taken from the SIMPACK model setup window depicting the implemented LEM model. The implemented model yields an executable simulation of the landing platform touching down onto a planetary terrain. This model is validated in chapter 5 by experimental data and subsequently used for the further work.

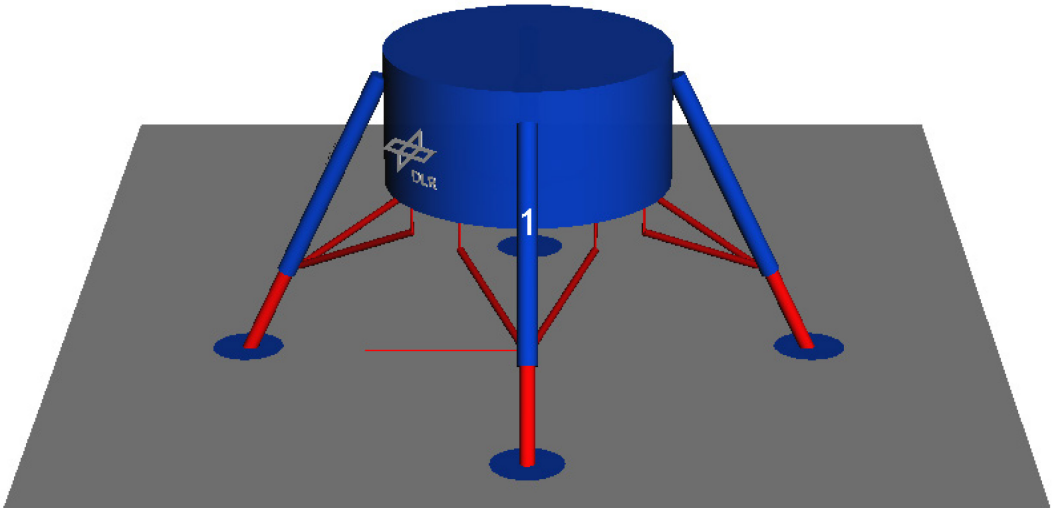

Figure 3-12 Image of the SIMPACK multibody LEM model

4 Experimental Touchdown Investigations

Although the concept and involved technologies for a soft landing with legged landing systems is not new in essence, Europe's technology readiness level in this area is regarded still insufficient. Dedicated development tests are necessary to close this knowledge gap and mitigate the risks of design failures (*Buchwald et al. 2008*). A test campaign to gather such data was conducted in the joint project "Landing Technology" between the DLR Institute of Space Systems and Airbus Defense & Space, Bremen. In particular the joint project had the objective to investigate experimentally the touchdown dynamics of planetary landing systems. Primary objective is the characterization of legged landing systems in different configurations as reference objects as they represent a class of systems widely used in space exploration endeavors and the validation of numerical models of such vehicles. The validation and verification of the touchdown simulator described in chapter 5 of this thesis makes use of experimental data on the landing platform's touchdown behavior. The following sections therefore describe the test object and experimental set-up which was used to gain the experimental data.

4.1 The Lander Engineering Model (LEM)

The Lander Engineering Model, abbreviated the LEM, is a bread board of touchdown system consisting of a central landing platform which provides attachment points for 3 or 4 leg assemblies. The leg assembly itself is configurable into two variants, which are the Cantilever and the Inverted Tripod, introduced in chapter 2.3).

This modularity of the test article allows to set-up four different configurations which are depicted in Figure 4-1. The leg assembly is complemented by the footpads and the energy absorbing elements made of honeycomb cartridges in the primary strut and bending rods between the secondary struts and the platform. The LEM is designed by Airbus Defense & Space as a contribution to the joint project. The full bread board definition is described in *Buchwald et al. 2011*.

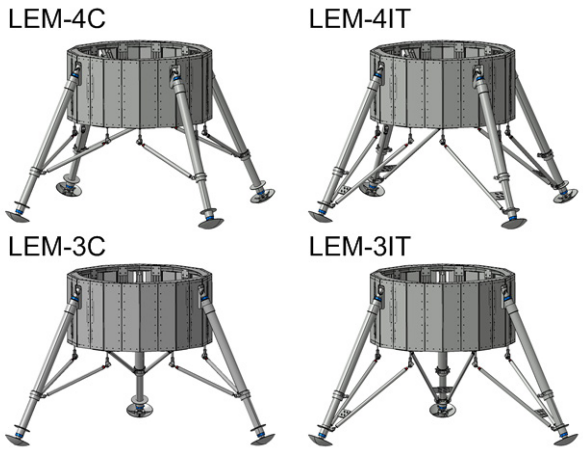

Figure 4-1 LEM variants: 3 and 4 legs, inverted tripod (IT) and cantilever (C), LEM images: Airbus DS

The physical make-up of the experimental platform is of aluminum frames as main load bearing elements and a sheet metal skin to provide sufficient stiffness. It provides furthermore attachment points for the sensor and test equipment (refer also to section 4.4 of this chapter) and ballast and trim masses to adjust and fine tune the overall mass-property. Clamping jaws on a central metal tube provide the mechanical interface to the robotic arm of the test facility (section 4.2 of this chapter).

In the further scope of thesis a case study example based on a four legged landing system is used to demonstrate the application of the analysis methods derived in this thesis. For that reason the test data stemming from the LEM-4C variant is exploited in the subsequent chapters. The following further descriptions of the test article and set-up focus consequently only on this LEM variant. The principal dimensions and the reference coordinate system are defined in Figure 4-2. The body properties are given in Table 4-1. The body reference coordinate system has its origin in the center of the platform's lower baseplate. The x-axis points into the notional main engine thrust direction and the y-axis points into the leg 1 direction. Angles and angular rates are defined as in the Luftfahrtnorm *LN 9300*.

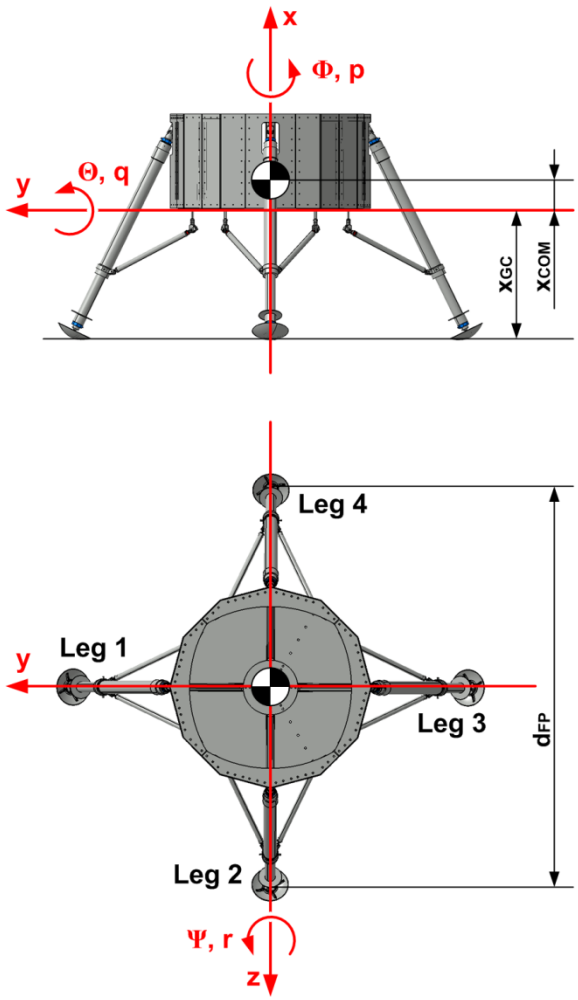

Figure 4-2 LEM body-fixed coordinate system and principal dimensions definition

Property	Value
Mass m [kg]	310.7
Moment of Inertia I_{xx} [kg·m²] (*)	$141.4^{+17.3}_{-00.0}$
Center of Mass x_{COM} [mm]	115^{+4}_{-8}
Ground Clearance x_{gc} [mm]	806
Landing Gear Footprint d_{FP} [mm]	2400

(*) Values for I_{yy}, I_{zz} have not been measured

Table 4-1 LEM-4C geometry and mass properties

4.2 The Landing & Mobility Test Facility

The test campaign made use of DLR's Landing & Mobility Test Facility (LAMA) hosted by the Institute of Space Systems in Bremen. The facilities general purpose is to support the design, development and verification of planetary mobility concepts on an experimental base.

Landing system touchdown tests can be done with operating modes, which are (i) the scaled model drop test and (ii) the weight-offloaded mode. The test object handling – meaning the set-up of touchdown velocities and test object position and attitude as prescribed by the test plan – is realized by a commercial off-the-shelf 6-axis robotic arm on a rail track with a nominal lift capability of 500kg.

The facility is complemented by a soil bin with a size of 10m x 4m of which a section of 4m x 4m is tiltable up to 30° to simulate terrain slope. The soil bin can be prepared to either provide a hard, a soft (granular soil) or mixed surface. An overview of the facilities architecture is given by Figure 4-3. A more detailed description of the facility is given by *Witte et al. 2009*. The test facility coordinate system provides the Earth-fixed reference frame with its z-axis being parallel to the gravity vector and pointing upwards. The x-axis is oriented along-track to the robot system and the y-axis is cross-track oriented.

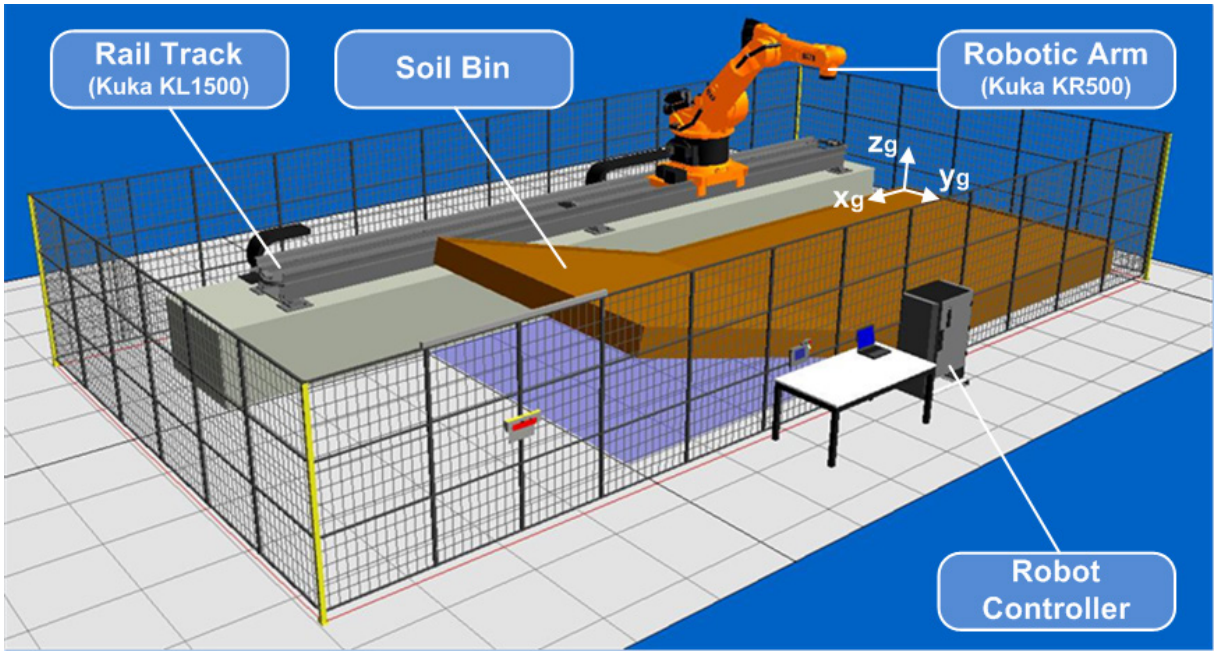

Figure 4-3 Overview of the Landing & Mobility Test Facility LAMA

The particular LEM tests made use of the drop test mode. In this mode a pneumatic gripper in the robots hand flange gets hold at the clamping jaws at the test object. The robot lifts the test object and positions it at the predetermined drop point. The required horizontal velocity is set-up by the robot system while the vertical velocity is realized basically through a free fall from the predetermined drop height (*Witte 2011*). Figure 4-4 illustrates this sequence.

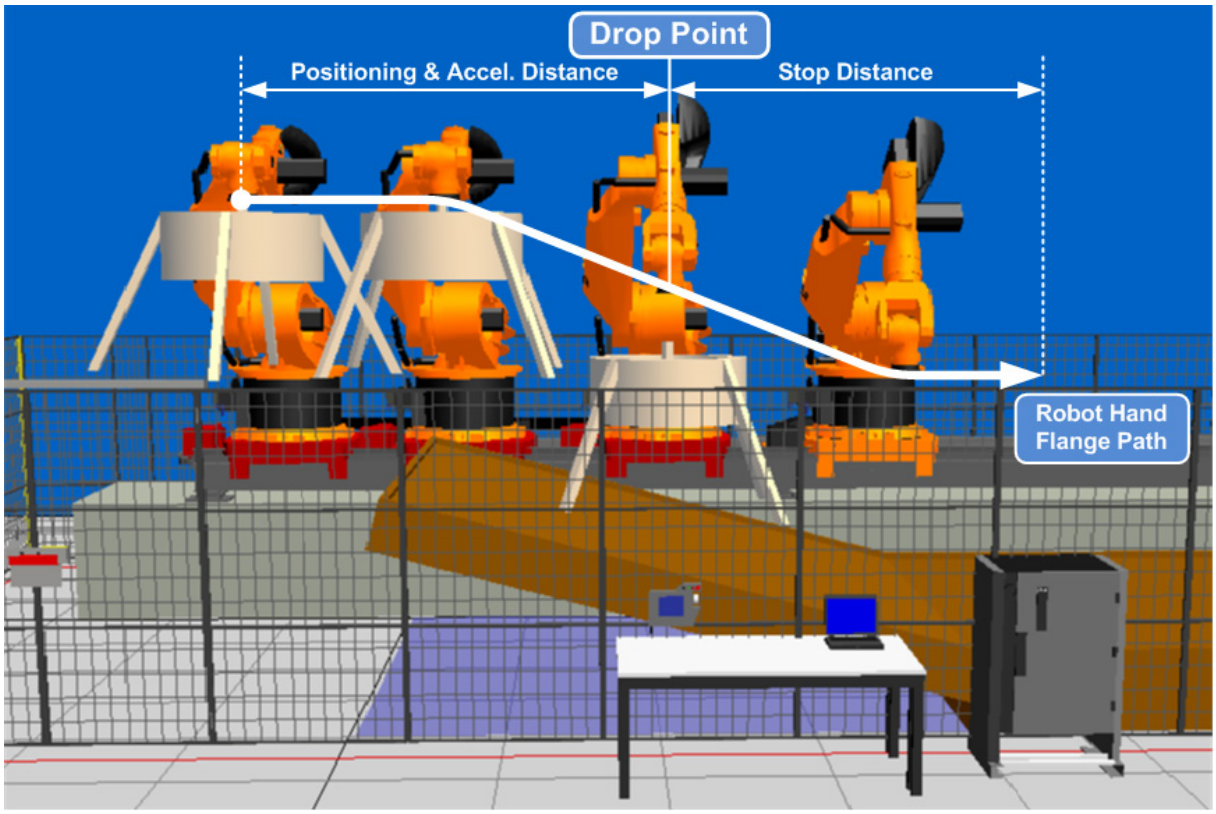

Figure 4-4 Principal operations sequence in the drop test mode

4.3 Test Plan

The test plan describes load cases which address the test objectives by stimulating the different functions of the touchdown system. Especially during the Apollo era a large effort has been put into the experimental investigation of the Lunar Module touchdown dynamics. Some of the knowledge gained in this program has been used as apriori information and is reflected in the test plan for this campaign. In particular:

- The test plan features two symmetric landing gear orientations. The "1-2-1" landing mode has one leading and one trailing leg identified as most critical for leg loads. The "2-2" landing mode has each two leading and trailing legs, identified as most critical with regard to dynamic stability (*Blanchard 1968*).
- The leading legs in a touchdown scenarios are blocked by an obstacle as such constrained configuration proofed to be critical for landing stability and primary and secondary strut compression loads (*Rogers 1972*),
- The secondary strut tension loads become critical when unconstrained and on a low surface friction (*Rogers 1972*).

Four load cases have been adopted by *Buchwald et al. 2011* for the LEM test campaign and are described in detail below. Table 4-2 summarizes the key experiment parameter.

Test 1 – stability boundary (stable): The touchdown occurs on a15° sloped surface with v_z = -3.0m/s and v_x = -1.0m/s. The legs 1 and 2 are oriented towards the downhill direction. The legs 3 and 4 are trailing ("2-2" orientation). Figure 4-5(c) illustrates this situation. This scenario minimizes the stability

distance (refer also to chapter 3.4.1) between the two leading legs and the platform COM. With blocked legs 1 and 2 a destabilizing moment is provoked.

Test 2 – stability boundary (unstable): This set-up basically repeats the test 1 set-up however with the difference that the surface slope is here 20° to provoke an unstable condition. Thus the steeper angle lets the platform topple over. Both test 3 and set-ups are selected to have two measurements which constrain the stability boundary.

Test 3 – stroke and energy absorption (primary and secondary strut compression load): The touchdown occurs on a sloped surface with leg 1 leading into the downhill direction. Velocities are in the vertical axis v_z = -3.0m/s and horizontally v_x = -1.0m/s. Figure 4-5(a) depicts the situation of the first contact with the trailing edge 3. Upon touchdown the platform gains an angular momentum. The subsequent touchdown of leg 1 into the obstacle yields a maximum load case for the primary strut as the resulting direction of contact force is nearly along its axis. The touchdown sequence of the legs is the 1-2-1 orientation.

Test 4 – stroke and energy absorption (secondary struts tension load): The touchdown occurs on an unsloped surface with v_z =.-3.0m/s and v_x = -1.0m/s. Figure 4-5(b) depicts the situation with all 4 legs touching down simultaneously. Due to the leg assembly kinematics, the legs are forced to slide outwards. To support this tendency, the surface consists of an oiled steel plate which minimizes the contact friction between at the pad/surface interface as the friction counteracts the outward motion. This touchdown scenario results in maximum tension load case for the secondary struts load limiters.

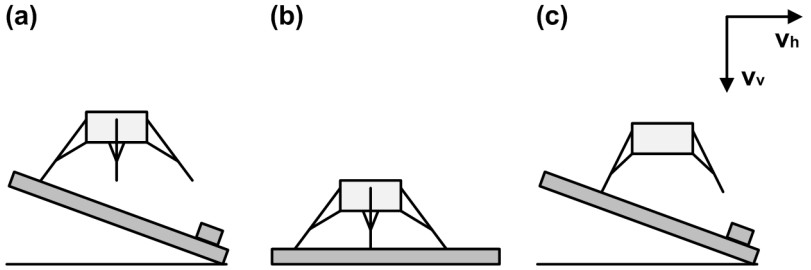

Figure 4-5 Schematic illustration of the test load cases, (a) maximum loads on the primary strut and secondary strut's compression direction, (b) maximum load on the secondary struts tension direction, (c) determination of the stability limit; refer to Table 4-2 for specific details

No.	Objective	Velocity $v_{xg}/v_{yg}/v_{zg}$ [m/s]	Attitude Φ/Θ/Ψ [°]	Orientation	Slope [°]	Surface Cond.	Remark
1	Stability (marginal stable)	-1.0 / 0.0 / -3.0	-45.0/0.0/0.0	2-2	15	obstacle	Figure 4-5 (c)
2	Stability (marginal unstable)	-1.0 / 0.0 / -3.0	-45.0/0.0/0.0	2-2	20	obstacle	Figure 4-5 (c)
3	Max. primary and secondary strut compression load	-1.0 / 0.0 / -3.0	0.0/0.0/0.0	1-2-1	20	obstacle	Figure 4-5 (a)
4	Max. secondary strut tension load	-1.0 / 0.0 / -3.0	0.0/0.0/0.0	1-2-1	0	Steel/oil	Figure 4-5 (b)

Table 4-2 LEM-4C drop test cases: this table provides the specific touchdown conditions set by the test facility for the different load cases

4.4 Instrumentation, Data Acquisition and Integration

The LEM is equipped with sensors for the acquisition of relevant data on forces, strokes and the vehicle dynamics. The associated measurement points are depicted in Figure 4-6 and explained subsequently.

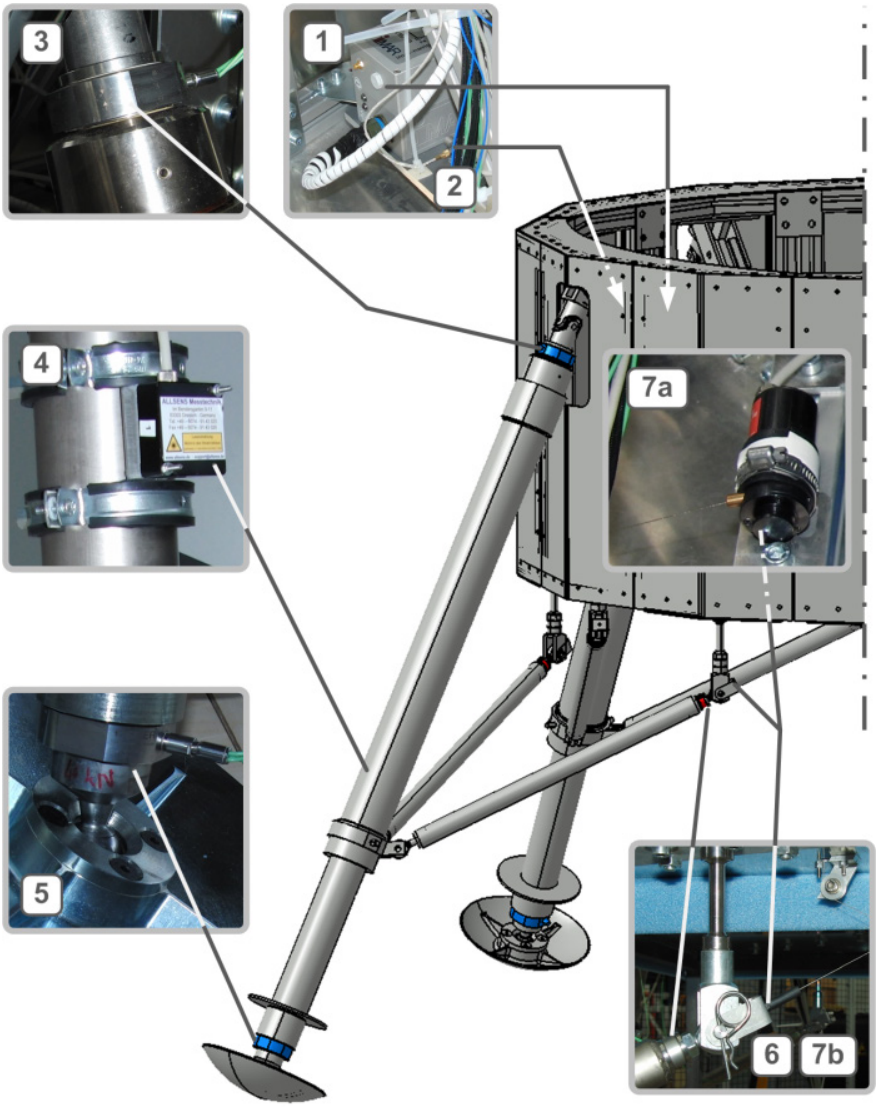

Figure 4-6 Measurement points of the LEM data acquisition architecture: different types of sensors measure forces, displacements and accelerations as well as the platform's angular rates and attitude. The numbers refer to detailed information in the main text about the respective sensor

(1) A 3-axis Inertial Reference Unit (IMU, type iMAR iVRU-BB-M, sampling rate 100Hz) is mounted inside the platform body and measures its accelerations, angular rates and attitude in the body reference frame.

(2) A 3-axis accelerometer (type Kistler 8792A25, sampling rate 1kHz) is located adjacent to the IMU and measures additionally the platform's high frequent accelerations. It complements the IMU in that regard.

(3) A 3-component force sensor (type Kistler 9067C, sampling rate 2kHz) is integrated into the load path of each primary-strut-to-body interface. The sensor z-axis is aligned to the strut's center line.

(4) A laser displacement sensor (type Allsens AM200-500, sampling rate 2kHz) is mounted to each primary strut parallel to its center line. This sensors measures the primary strut's stroke.

(5) A 3-component force sensor (type Kistler 9067C, sampling rate 2kHz) is integrated into the load path of each footpad-to-primary-strut interface to measure the contact forces passed into the landing platform. The sensor z-axis is aligned to the strut's center line.

(6) A single axis force sensor (type Kistler 9021A) is integrated into the load path of each secondary strut.

(7) A wire draw sensor (type MicroEpsilon WDS-250-MPM, sampling rate 2kHz) measures the stroke of each secondary load limiter. The sensors are installed inside the platform body (position 7a) whilst connected to the bending rod (position 7b).

The data acquisition unit is located outside the test cell and connected via an umbilical to the LEM test object. Additionally the motion states and force/torque data of the test facilities robot system is recorded. Video cameras for the test observation complement the data acquisition architecture.

Figure 4-7 illustrates the experimental set-up prior to a drop test. The acquired data is used and discussed in chapter 5.

Figure 4-7 A LEM-4C test set-up prior to a drop test: the photo shows the LEM held by the facility's robotic arm. the concrete obstacle on the tilted ramp is visible in the foreground

5 Validation of the Numerical Model

The assessment of the landing platform's functional performance and especially the derivation of failure probabilities rely largely on the existence of a credible numerical model of the landing platform to conduct the required touchdown simulations. This is mainly due to a technical and a programmatic reason: (i) the relevant space environment cannot be fully simulated physically in an Earth-based test laboratory and (ii) the necessary resources to conduct a large (statistical relevant) numbers of system level tests are limited. The analysis results based on the virtual testing using the numerical model depends then consequently on the accuracy of the simulated system dynamics. Its credibility is thereby defined in *NASA 2008* as "the degree of elicit believe or trust in the modeling and simulation results".

The necessity to rely on such computed results is not uncommon in disciplines such as aerospace, automotive and nuclear engineering and accordingly requirements and methods to achieve confidence in the outcome of modelling and simulation activities are generally governed by the terms *verification* and *validation*. Their particular role in a modelling and simulation project is illustrated in Figure 5-1. The building of a model starts with the analysis of the "real word" object under study. The formulation of mathematical equations describing this object is yielding a conceptual model (*Oberkampf et al. 2004*). Continuative, the computerized model is then a representation of the conceptual model as an executable computer code. Its execution in turn yields a simulation of the real word object.

Model *verification* covers thereby all activities to ensure that the code and the numerical solution of the mathematical equations adequately represent the conceptual model. According to *Oberkampf et al. 2004* it "provides evidence that the conceptual model is solved correctly […] by the computer code".

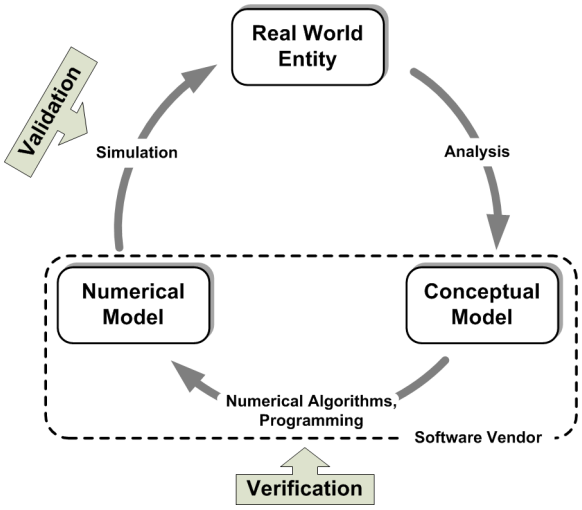

Figure 5-1 The definition of verification and validation and its role in modelling and simulation

Verification activities embrace aspects stemming from software engineering and software quality assurance, including formal code reviews and checking. Specifically, verification requires the testing of numerical algorithms versus any exact solution of the reference case. The reference case can be provided by a simple equivalent mechanical system amenable to a closed analytic solution or – if such equivalent system is not sufficient – otherwise obtained highly trustworthy benchmark data. A basic approach to this method is shown by *Schiehlen 2012* where the longitudinal oscillations of a metal bar are numerically analyzed using FEM and MBS methods and are verified by the exact analytical solution. Verification is applicable especially to the performance in terms of stability, convergence, and precision of numerical integrators implemented to solve certain classes of differential equations.

In case commercial software products are used for modelling and simulation the verification domain is largely in the responsibility of the respective software vendor. This is the case for this thesis as the landing platform analysis yields its topology (chapter 3.2) and describing parameter which are entered via a graphical user interface into the multibody software tool. Related quality assurance activities for the SIMPACK simulation tool are outlined in *Schwientek 2004*. Nevertheless the reliance on a tool – if grown mature over years and with heritage in its engineering domain – provides already some confidence in the correctness of the computational model. The verification aspect is not pursued further in this study and it remains open to discussion how to integrate verification "evidence" for commercial software tools into a model credibility analysis as prescribed by (e.g.) *NASA 2008*.

Model *validation* activities shall ensure that the simulated outcome is an accurate representation of the real world. To cover however such wide range of engineering domains, validation requirements and approaches are often formulated generic. In the following section both general and specific requirements and definitions are reviewed and an own set of criteria adapted. This set of criteria is then applied to the touchdown simulation model as set up in chapter 3.

5.1 Validation Concept

Validation aims at the identification and quantification of errors from both the conceptual and computational model, which implicitly requires that the model is also solved correctly. This latter part of validation affirms however that a suitable integration method is chosen to solve the model equations rather than replacing its formal verification. For the validation purpose, the simulated system behavior is compared to experimentally obtained results. It thus shall reduce the inherent uncertainty on the representativity of the model structure and on the model parameter (the "epistemic uncertainty").

Looking specifically into the spaceflight profession, some guidance is found in the ECSS framework regarding structural finite element methods (*ECSS 2008a*, *ECSS 2008b*). A "test-analysis correlation" shall be executed to (1) validate the mathematical model, (2) validate the test data, (3) select reliable test data for mathematical model update and (4) to detect erroneous areas in the mathematical model. Remarkably this requirement accepts that not all deviations between test and analysis (simulation) are attributable to deficiencies in the numerical model. *Oberkampf et al. 2004* also points out that such correlation shall not imply that the experimental data is more accurate than the simulated data as it only assumes that "*the experimental measurements are the most faithful representation of reality for the purpose of validation*" The correlation techniques and quality criteria in these references however consider specific structural dynamic measurements which are not applicable to the kinematic and dynamic nature of the landing platform multibody dynamics analysis. With that primer on validation the validation approach to assess the multibody model of the landing platform is subsequently elaborated further.

The work flow of activity executed for the validation of the numerical simulation model is depicted in Figure 5-2. The numerical model set up is described in detail in chapter 3 "A Numerical Model of a Legged Landing Platform" and is based on the analysis of the landing platform design. The parallel activity of the physical model building, which is in this case the Lander Engineering Model LEM, and the experimental test campaign conducted to obtain benchmark data in a laboratory environment is described in chapter 4.3. The numerical simulation is then used to replicate the test cases already applied to the LEM in the computer domain. Both the measured and the simulated data sets are correlated subsequently. The associated activity includes the application of qualitative and quantitative criteria to judge if the numerical simulation represents the landing platforms functional limits within an acceptable tolerance compared to the benchmark data set. If a criterion is not met, the numerical model fidelity is refined and the simulation of the test cases and the correlation is redone. This

iteration loop leads to a stepwise improvement of the numerical model which is released for further use after acceptance.

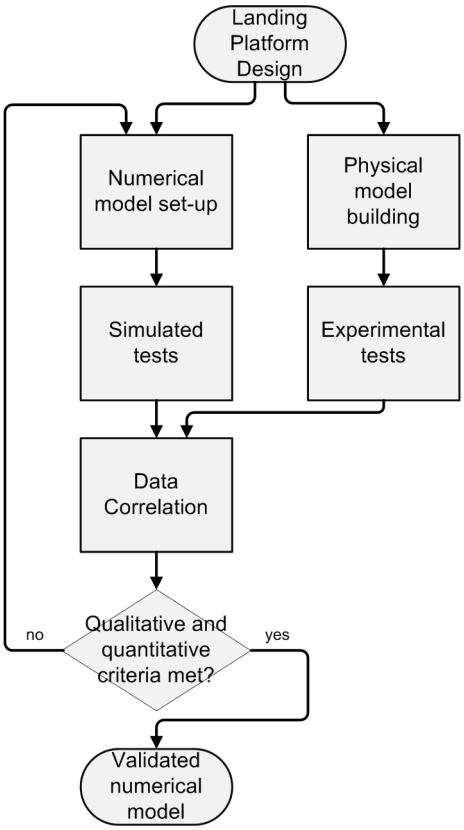

Figure 5-2 Simulation model validation process: the process foresees an iterative refinement of the numerical touchdown simulation until qualitative and quantitative criteria are met and the model is declared as validated

5.1.1 Quantitative Validation Measures

It is assumed for a moment that the numerical simulation produces ideal and error free results $s(t_i)$ at time steps t_i. Likewise the measured test data $m(t_i)$ obtained from an experimental campaign is assumed as error-free. Then the equality $s_i = s(t_i) = m(t_i) = m_i$ and $t_i = t_0+i\cdot\Delta t$ must be true. In the absence of errors the data pairs $\{s_i, m_i\}$ consequently are points on a linear curve with unity slope.

Data Correlation: The empirical correlation coefficient (equation 5.1) is applicable to such linearly related data pairs as a measure of goodness of fit. It is normally (*Ross 2006*) used to express how well a linear regression model represents a data set. Although no regression is applied in this case it is used as dimensionless indicator how well the data pairs related to a linear curve. A correlation coefficient of $\rho = 0$ means here that the simulation data is entirely unrelated to the measured data. A coefficient of $\rho = 1$ indicates a fully deterministic relation. The correlation coefficient ρ defines the first quantitative criteria for the representivity of the numerical touchdown dynamics simulation.

$$\rho = \sum_{i=1}^{n}(s_i - \bar{s}) \cdot (m_i - \bar{m}) \,/\, (\sum_{i=1}^{n}(s_i - \bar{s})^2 \cdot \sum_{i=1}^{n}(m_i - \bar{m})^2)^{1/2} \qquad 5.1$$

Absolute Errors: A second criterion used is the weighed absolute error which is observed between the experimental and simulated test data:

$$e_{wa} = \sum_{i=1}^{n}|s_i - m_i| \cdot |m_i| \,/\, \sum_{i=1}^{n}|m_i| \qquad 5.2$$

As the simulation is used to predict the functional limits of the landing platform, any deviation in the range of the demonstrated (= measured) performance limits is of higher criticality than in the low performance regime. It assesses the error between the simulated and measured states while using under laboratory condition measured experimental data as a benchmark. The criterion weighs accordingly larger values (= higher performance demand) stronger.

Model Consistency: The quantitative validation means are complemented by a model consistency check, which compares basic geometric and mass properties between the physical model and its numerical representation.

5.1.2 Qualitative Validation Means

Kramer 1998 refers to this validation approach as model-object comparison and summarizes additional qualitative measures of which the following set is regarded.

- The controllability and observability principle shall be fulfilled. This means that states which exhibit no change upon an excitation by a test signal are either incorrectly modeled or superfluous.
- The principle of causality must be fulfilled, meaning that a physical effect must not be ahead in phase of its root cause.
- Time response and steady states. The time response and the end- or steady states of both the model and object shall be of a similar nature (stable, unstable or periodic behavior or steady states).
- Kinematic principles shall be fulfilled. This means that certain states cannot change independently of each other (e.g. a position must be the integration of an associated velocity).

A deviation or violation of these heuristic criteria is an indicator for an incomplete, erroneous numerical model or that numerical artifacts are generated during the model time integration. Any such indication shall trigger a revision of the numerical model implementation as prescribed by the validation process shown in Figure 5-2.

5.2 Application of the Validation Concept

The previous chapter 4 has introduced the Lander Engineering Model (LEM) and a series of tests dedicated to characterize the LEM's performance. This physical model of a landing platform and the experimental data from the tests are used in this section to validate the numerical model by using the criteria introduced above. Following the model consistency check the experimental data is correlated with the simulated version of the respective test case. Therefore the sections 5.2.2 to 5.2.5 refer to touchdown conditions identified as test cases 1 to 4 in chapter 4.3. Each of these sections shows selected data which is most indicative to its particular test case. The associated results from the application of the quantitative validation means in terms of the equations 5.1 and 5.2 are tabulated at the end of each section. Image sequences obtained from high speed camera test observation complement and illustrate key events in the touchdown sequence. The validation results for all associated data channels are tabulated in the annex A4 – Ancillary Validation Data for completeness of this chapter.

5.2.1 Model Consistency Check

Prior to actually executing the simulations a consistency check on the geometry and mass properties of the numerical model with respect the physical model was made. This comparison is given by Table

5-1 below. The table indicates small (< 5%) deviations of the numerical lander model from its physical counterpart. These deviations are caused by the chosen modeling approach for the individual component bodies which models them as simplified primitives. The deviations in the presented order are deemed acceptable for the following touchdown analysis.

Property	Value for the LEM-4C PHYSICAL model	Value for the LEM-4C NUMERICAL model	Model deviations, abs. / rel.
Mass m [kg]	310.7	310.9	+0.2kg / +0.06%
Moments of Inertia [kg·m²]			
I_{xx}	141.4 (+17.3 / -0.0)	146.1	+4.7kg·m² / +3.3%
I_{yy}	Not available	110.5	
I_{zz}	Not available	110.5	
Center of Mass x_{COM} [mm]	115 (+4 / -8)	118	+3mm / +2.6%
Ground Clearance x_{gc} [mm]	806	778	-28mm / -3.4%
Landing Gear Footprint d_{LG} [mm]	2400	2388	-12mm / -0.5%

Table 5-1 LEM geometry and mass properties consistency check: the comparison of modeled and measured platform properties indicates a high conformity

5.2.2 Stability Load Cases – Stable Touchdown

The touchdown occurs with a vertical velocity of 3.0m/s and a horizontal velocity of 1.0m/s into the downhill direction. The platform orientation conforms to a 2-2 landing mode with legs 3 and 4 being the trailing and legs 1 and 2 the leading legs. The surface slope is 15°. This touchdown condition is also identified as “Test 1” in the experimental campaign. The associated image sequence is shown by Figure 5-3. The time series data is given by the Figure 5-4 and Figure 5-5 and the associated qualitative validation means provided by Table 5-2.

Time 0.00s: The initial surface contact by the footpads 3 and 4 introduce a negative rotation rate of $q \sim r \sim -125$ °/s as the platform has a roll angle of 45° with regard to the geodetic reference frame. This phase concurs with the engagement of these legs load limiting elements. The force-stroke-history is exemplary shown for the trailing leg 4 and the leading leg 1. The maximum force experienced in this instant is $F_{p4} \sim -6.2$kN and a stroke of $s_{p4} \sim -40$mm.

Time 0.11s: The touchdown of the footpads 1 and 2 into the obstacle causes a reduction of the rotation rates p and q with much of the kinetic energy absorbed by the engaging struts. The stroke $s_{p1} \sim -95$mm indicates that the first honeycomb cartridge stage has been expended fully and the stage partly. The maximum force level at the leg-to-platform interface is $F_{p1} \sim -6.3$kN. The footpads 3 and 4 have lifted off in this phase as the platform continues to tilt into the downhill direction.

Time 0.38s: The platform has reached its maximum tilt angle of $\Psi \sim \Theta \sim -15°$ (the effective tilt angle into the downhill direction is 21.2°) and starts to rotate back at a positive rate of q and r.

Time 0.68s: At this instant in the time series the platform has attained its final and stable rest position with its landing feet on the surface. The residual energy is decaying subsequently.

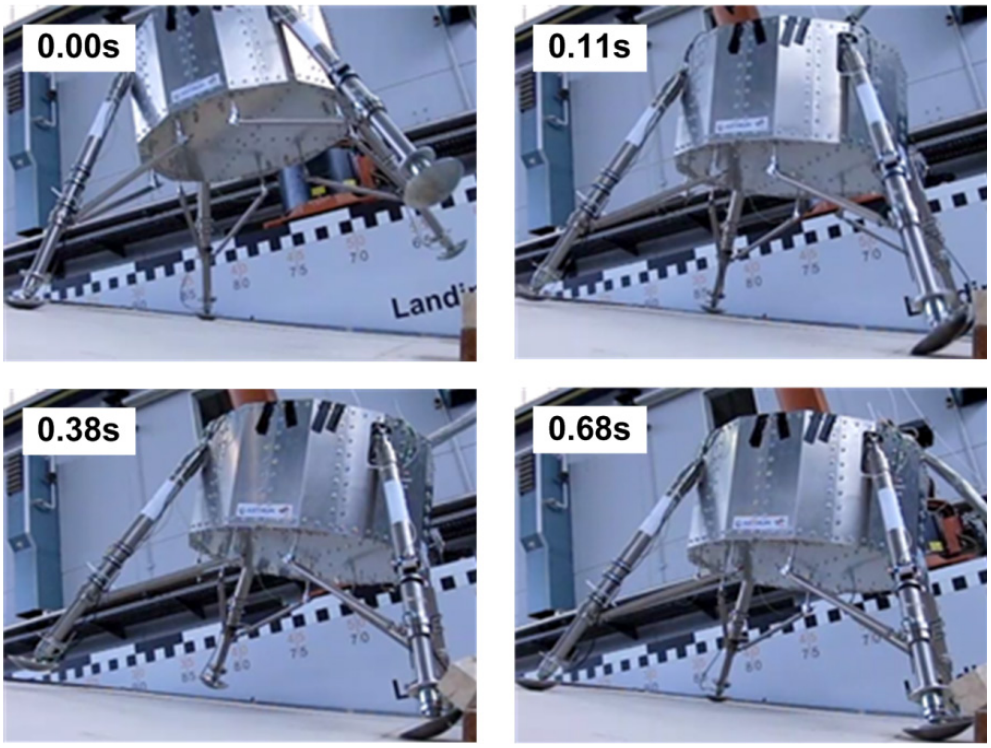

Figure 5-3 Test case 1 touchdown sequence and stable landing: The initial surface contact at time = 0.00s by the trailing footpads 3 and 4; touchdown of the leading footpads 1 and 2 into the obstacle at t = 0.11s; at t = 0.38s the footpads 3 and 4 have lifted off as the platform continues to tilt into the downhill direction; the platform has come to final rest on its feet at t = 0.68s

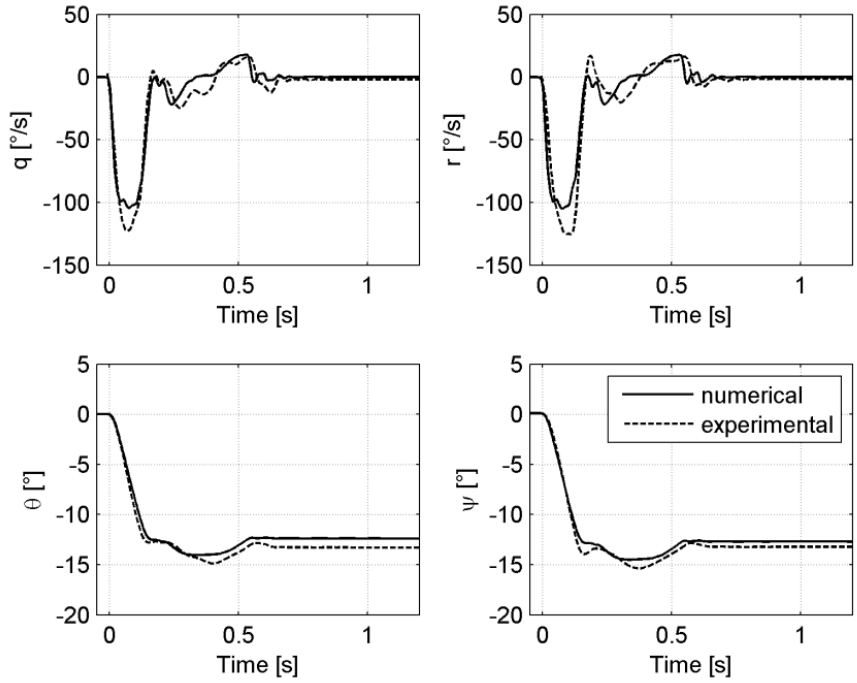

Figure 5-4 Test case 1 – attitude and angular rates: a high correlation is achieved between the measured and simulated angular rates q and r and the resulting platform attitude angles Θ and Ψ

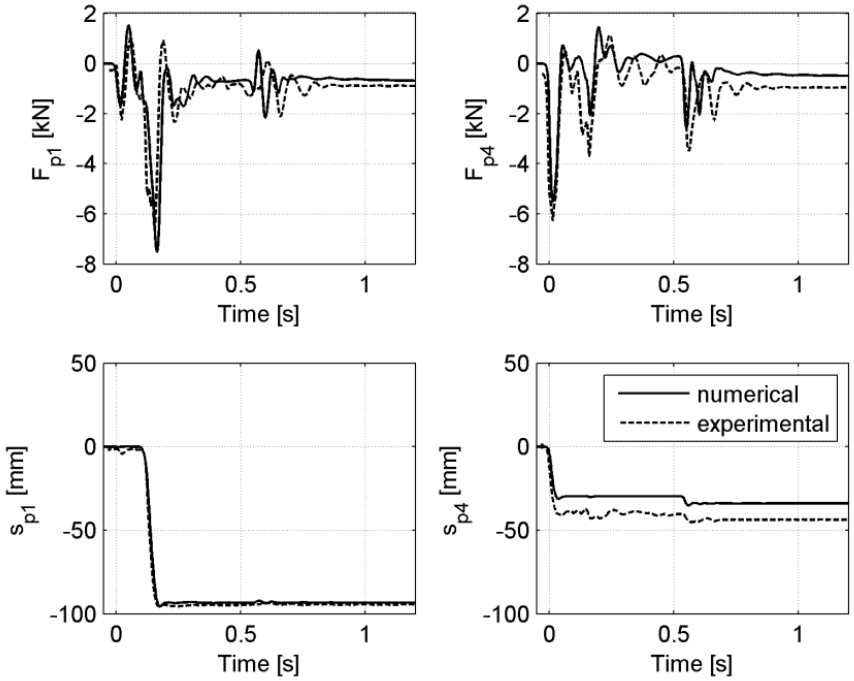

Figure 5-5 Test case 1 – primary strut force and stroke data: a high correlation is achieved between the measured and simulated forces and strokes of the leading legs and trailing leg 4. The stroke of leg 4 is however under-predicted by the simulation

	Correlation coefficient [-]	Weighed absolute error	
r	0.961	16.80	°/s
q	0.979	10.57	°/s
Ψ	0.997	0.52	°
Θ	0.993	0.72	°
$\mathbf{F_{p1}}$	0.715	0.73	kN
$\mathbf{F_{p4}}$	0.794	0.94	kN
$\mathbf{s_{p1}}$	0.999	1.44	mm
$\mathbf{s_{p4}}$	0.970	10.03	mm

Table 5-2 Test case 1 validation figures

5.2.3 Stability Load Cases – Instable Touchdown

Similar to the previous test case, the touchdown occurs with a vertical velocity of 3.0 m/s and a horizontal velocity of 1.0 m/s and with a platform orientation conforming to a 2-2 landing mode. However, the surface slope is increased to 20°. This touchdown condition is also identified as "Test 2" in the experimental campaign. It is similar to the test case 3 except the landing mode (2-2 instead of 1-2-1). The associated image sequence is shown by Figure 5-6. The time series data is given by the Figure 5-7 and Figure 5-8 and the associated qualitative validation means provided by Table 5-3.

Time 0.00s: The initial contact of the footpads 3 and 4 initiates the platform tilting into the downhill direction at rotation rates $q \sim r \sim 120°/s$. This starting condition differs basically not from its counterpart test 1. The maximum force experienced in this case is $F_{p4} \sim -6.0kN$ and the measured stroke is $s_{p4} \sim -35mm$.

Time 0.14s: Due to the steeper slope the impact of the footpads 1 and 2 into the obstacle occurs however slightly later than as in test 1. At this instant in time the footpads 3 and 4 have lifted off already again from the surface. The leg 1 touchdown is characterized by a force of $F_{p1} \sim -6.7kN$ and a stroke of $s_{p1} \sim -107mm$. A subsequently intermittent positive attitude rate reverts again into a negative rate yielding a steady increase in the platform attitude Ψ and Θ.

Time 0.66s: This rate $q \sim r \sim -20°/s$ is maintained during the subsequent period until the platform crosses its stability boundary (refer to chapter 3.4.1 for a detailed definition).

Time 1.11s: In the experimental test setup the platform is restrained by a cable (visible in the event images) to prevent any damage to the test platform and facility. The numerical simulation is automatically terminated when the stability distance parameter indicates an unstable situation.

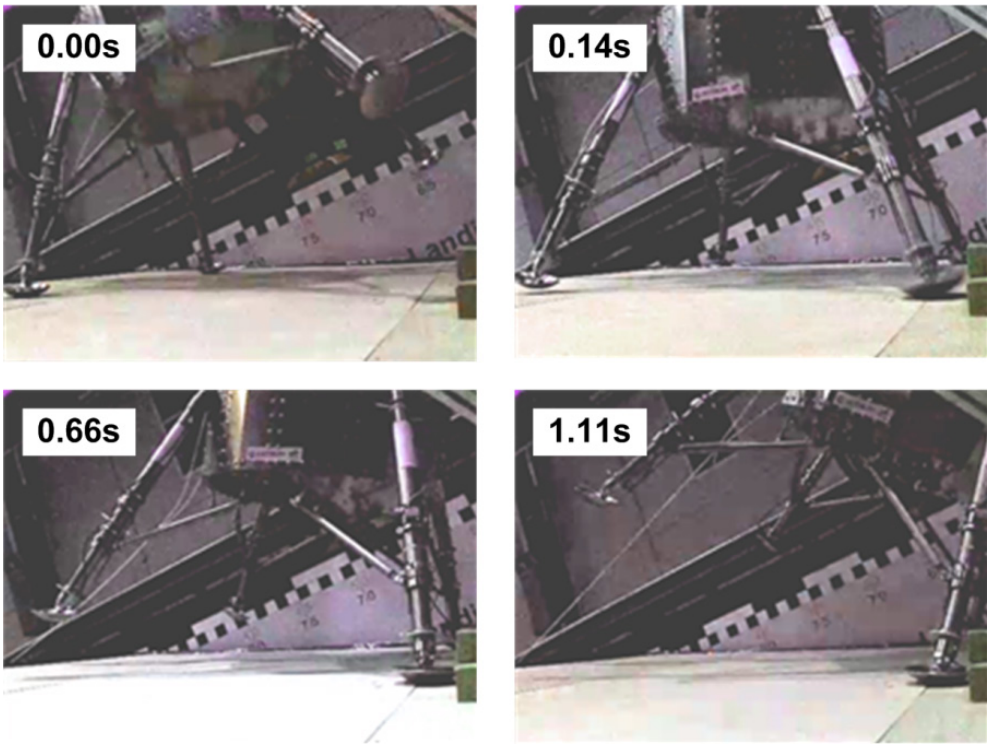

Figure 5-6 Test case 2 touchdown sequence and instable landing: Initial contact of the trailing footpads 3 and 4 at t = 0.0s; impact of the footpads 1 and 2 into the obstacle at t = 0.14s; the platform maintains a significant rotation rate and crosses its stability boundary at t = 0.66s; the platform is instable at t = 1.11s and is just held by a restraint cable

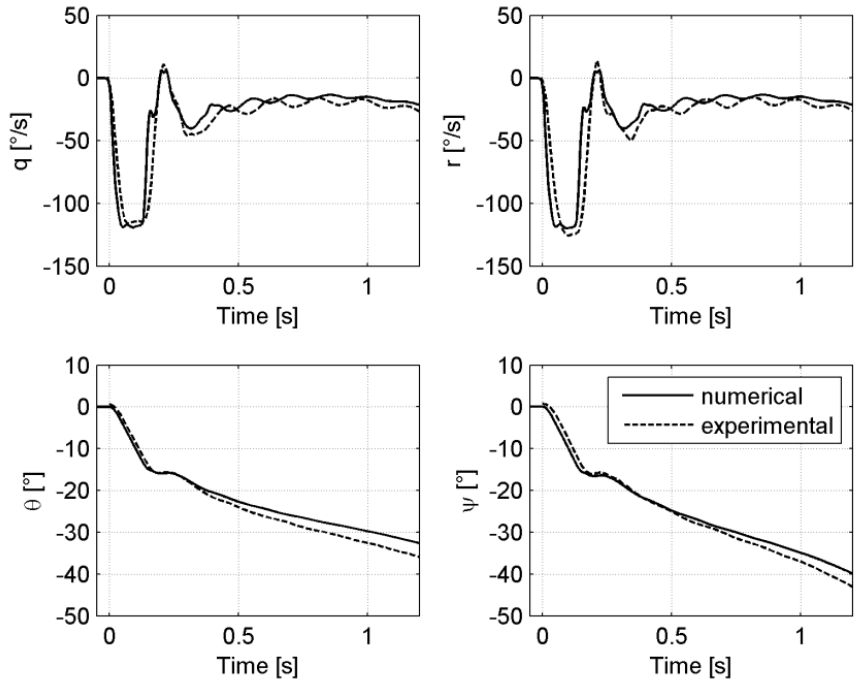

Figure 5-7 Test case 2 – attitude and angular rates: a high correlation is achieved between the measured and simulated angular rates q and r and the resulting platform attitude angles Θ andΨ; the curve diverge increasingly when the platform becomes instable

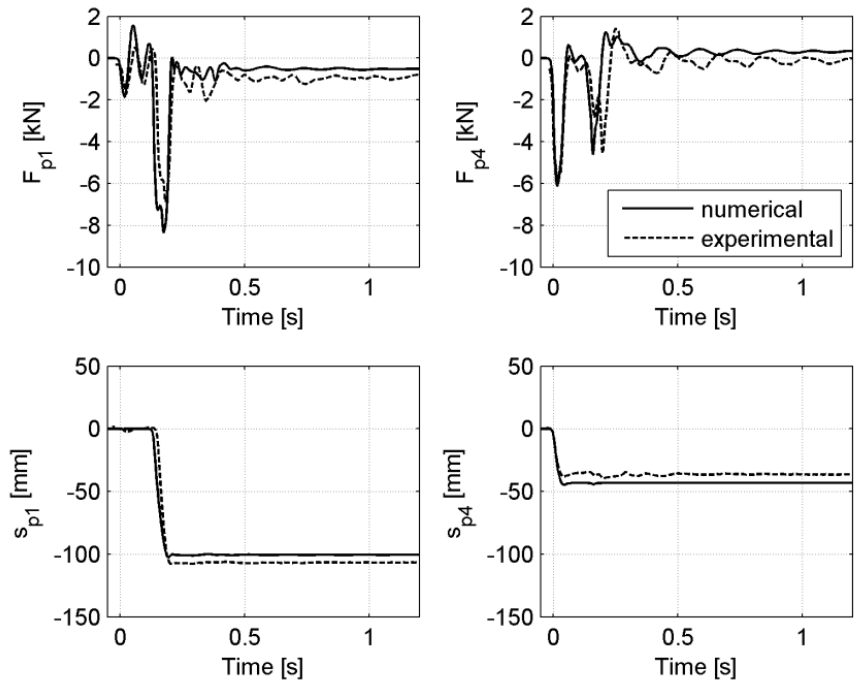

Figure 5-8 Test case 2 – primary strut force and stroke data: a high correlation is achieved between the measured and simulated forces and strokes of the leading legs and trailing leg 4

	Correlation coefficient [-]	Weighed absolute error	
r	0.893	12.44	°/s
q	0.925	10.27	°/s
Ψ	0.999	1.50	°
Θ	0.998	2.04	°
$\mathbf{F_{p1}}$	0.824	0.81	kN
$\mathbf{F_{p4}}$	0.854	1.13	kN
$\mathbf{s_{p1}}$	0.987	6.34	mm
$\mathbf{s_{p4}}$	0.974	6.65	mm

Table 5-3 Test case 2 validation figures

5.2.4 Primary and Secondary Strut Compression Loads

The touchdown occurs with a vertical velocity of 3.0 m/s and a horizontal velocity of 1.0 m/s into the downhill direction. The orientation of the platform conforms to a 1-2-1 landing mode with leg 1 being the leading and leg 3 the trailing leg. The surface slope is 20°. This touchdown condition is also identified as "Test 3" in the experimental campaign. The associated image sequence is shown by Figure 5-9. The time series data is given by the Figure 5-10 and Figure 5-11 and the associated qualitative validation means provided by Table 5-4.

Time 0.00s: Footpad 3 touches the surface and a negative rotation rate of r ~ -160°/s around the z-axis is caused by the contact force.

Time 0.15s: The footpads 2 and 4 have contact to the surface. The impact is hardly distinguishable from the subsequent footpad 1 impact.

Time 0.16s: Footpad 1 touches down into the obstacle. Due to the superposition of the horizontal velocity and the angular rate r the primary strut 1 experiences its maximum energy input. An interface force of F_{p1} ~ -7.8kN corresponds to this initial contact. The stroke s_{p1} ~ 140 mm indicates that the first honeycomb cartridge stage has been expended fully and the second stage partly. Simultaneously the secondary load limiters engage and are forced inward into their compression direction. The force-stroke-history of the secondary strut 11 indicates a maximum force of F_{s11} ~ 2.9kN and a stroke of s_{s11} ~ 80 mm. Complementary the force-stroke-history for the secondary strut 12 is F_{s12} ~ 2.7kN and s_{s12} ~ 44 mm respectively. The negative rotation rate is cancelled during leg 1 engagement, becomes intermittently positive and resumes a negative value of r ~ -25°/s. Footpad 3 lifts-off again during this phase.

Time 0.51s: The platform has reached a maximum yaw angle of Ψ ~ -26° and starts rotating back (positive rate r). Footpad 3 touches down again at t = 0.74s and the platform settles subsequently in its final rest position.

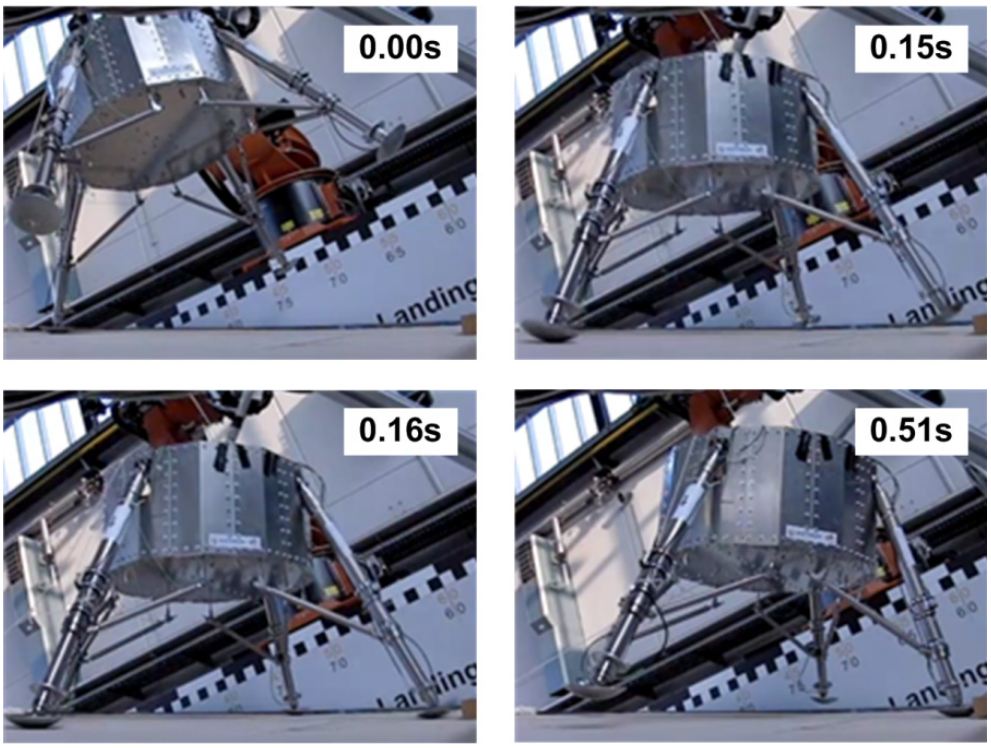

Figure 5-9 Test case 3 touchdown sequence with maximum load on a primary strut and secondary strut (compression): The trailing footpad 3 touches the surface and initiates a rotation at t = 0.0s; the footpads 2 and 4 have contact to the surface at t = 0.16s; footpad 1 touches down into the obstacle at t = 0.16s; the platform has reached its maximum yaw angle of Ψ and starts rotating back at t = 0.51s

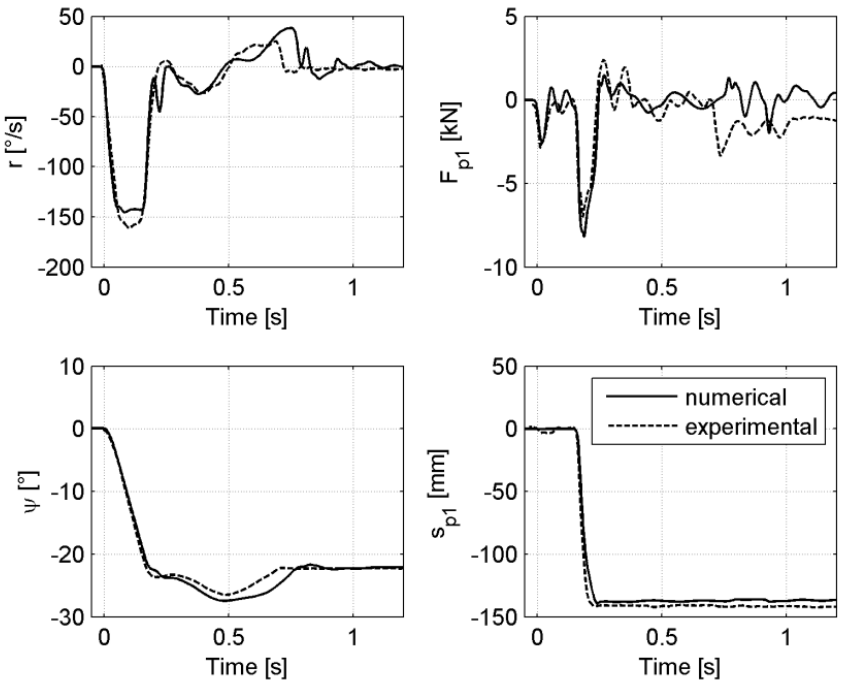

Figure 5-10 Test case 3 – Attitude and angular rate, primary strut force and stroke data: a high correlation is achieved between the measured and simulated angular rate r and the resulting platform attitude angle Ψ; a likewise high correlation is achieved for the leading leg 1 force and stroke data

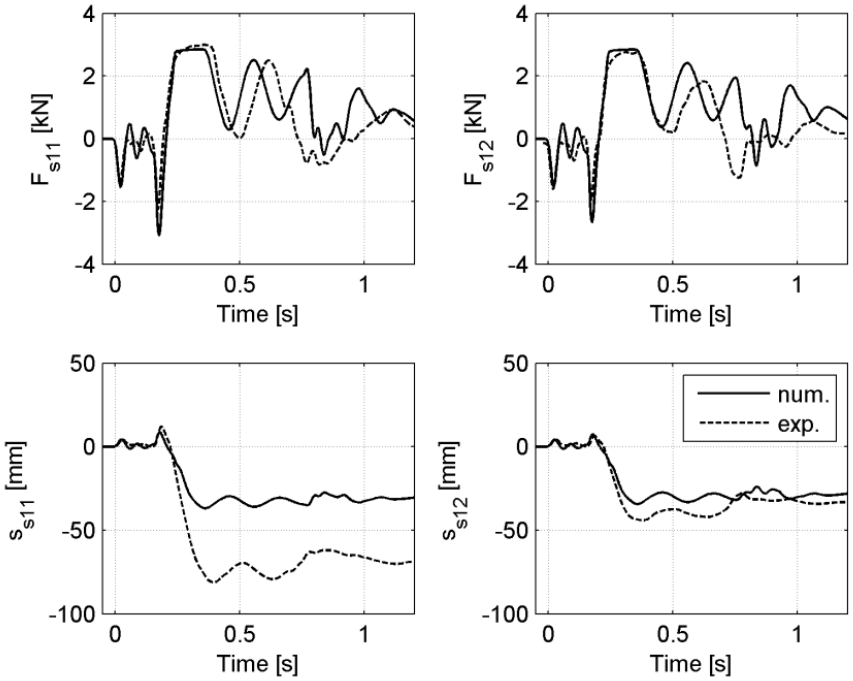

Figure 5-11 Test case 3 – secondary strut force and stroke data: the correlation for the leading leg 1 secondary struts is still fair to good, however the stroke data of secondary strut stroke s_{s12} (bottom left) shows a significant mismatch between measured and simulated data likely attributable to a deficiency in the test set-up (refer to main text for further explanations)

	Correlation coefficient [-]	Weighed absolute error	
r	0.967	10.71	°/s
Ψ	0.989	0.83	°
F_{p1}	0.810	1.43	kN
s_{p1}	0.997	4.88	mm
F_{s11}	0.676	0.54	kN
F_{s12}	0.805	0.52	kN
s_{s11}	0.983	37.61	mm
s_{s12}	0.970	7.07	mm

Table 5-4 Test case 3 validation figures

The numerical simulation exhibits generally a good accordance with the experimental results and as also stated by the quantitative validation figures in Table 5-4. However a striking difference is seen for the secondary strut 11 actually observed displacement which is nearly double the numerical prediction. This actual deformation is also confirmed by post-test inspection (Figure 5-12). The anticipated performance for a symmetrical in-plane test is a nearly equal deformation on both sides. The most probable cause is here a deficiency in the test set-up leading to non-symmetric touchdown.

The simulated force-stroke behavior for both secondary struts 11 and 12 is basically identical as expected for a symmetric touchdown condition and concurs well with the experimental data of the

secondary strut 12. It is thus assumed that the stroke of secondary strut 11 is an outlier to a not further identifiable deficiency in the test set-up. This condition calls for a repeated test, which however was not possible in the test campaign.

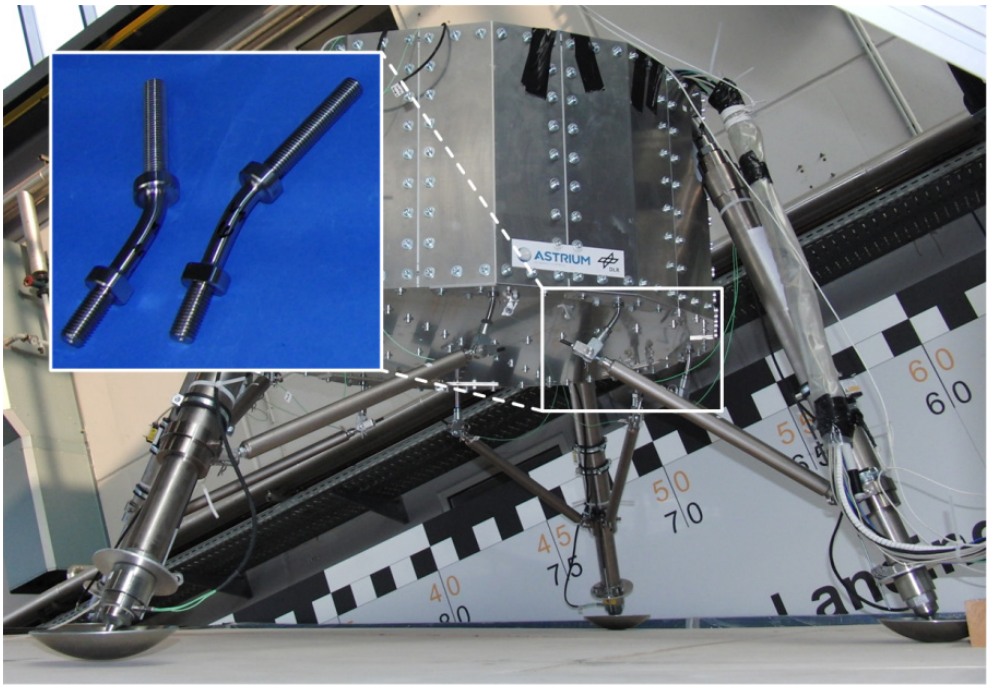

Figure 5-12 Test case 3 post-test condition and inspection of leg 1 secondary strut energy absorbers

5.2.5 Secondary Strut Tension Loads

The touchdown occurs with a vertical velocity of 3.0 m/s and a horizontal velocity of 1.0 m/s and with a platform orientation conforming to a 1-2-1 landing mode. However, the surface slope is 0° and the friction is lowered by a cover of an oiled steel plate. This touchdown condition is also identified as "Test 4" in the experimental campaign. As the existing high speed video footage is not sufficient to resolve the key touchdown events here, only the post-test condition is shown in Figure 5-13. The time series data is given by the Figure 5-14 and Figure 5-15 and the associated qualitative validation means provided by Table 5-5.

Time 0.00s: All footpads have contact to the surface simultaneously. Upon this initial contact the legs are forced outward leading to a maximum tension load of the secondary load limiters. Again the force-stroke-history of the secondary strut 11 and 12 are shown exemplary. The secondary strut is displaced by $s_{s11} \sim 14$ mm corresponding to a force $F_{s11} \sim -2.6$kN and respectively the secondary strut 12 stroke is characterized by $s_{s12} = 10$mm and $F_{s12} = -2.3$kN. Approximately half of this initial stroke is attributable to an elastic deformation as the final value settles at $s_{s11} \sim 7.5$ mm and $s_{s12} \sim 5$mm. At the same time the primary strut stroke indicates a force of $F_{p1} \sim -6.9$kN and a displacement of $s_{p1} \sim -84$mm.

Time 0.14s: Due to the elastic energy stored after the initial touchdown and the low surface friction the platform bounces off the surface and has gained its maximum rebound height at this instant in the time series. This is visible in Figure 5-14 (top right) as the primary strut 1 interface forces of leg 1 to the platform become zero again.

Time 0.20s: The second touchdown occurs at this instant in time and causes a second pronounces load peak at the leg-to-platform interfaces. The residual kinetic energy is however insufficient to cause further plastic deformations in the energy absorbing elements.

Time 0.47s: The platform settles after some more slight rebounds.

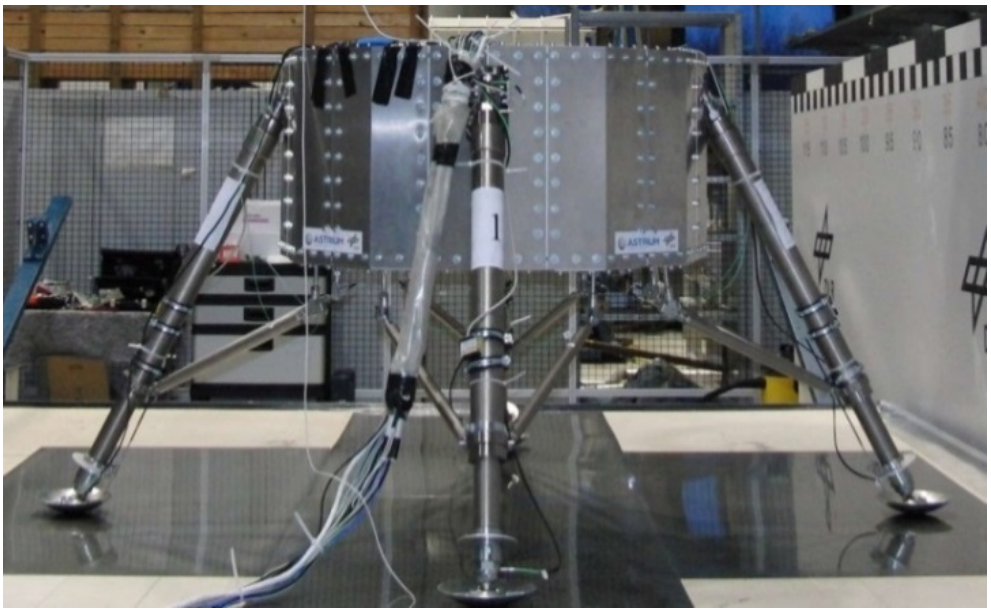

Figure 5-13 Test case 4 (maximum load on secondary struts tension direction) post-test condition: the image shows the platform in its final rest position after the drop on an oiled steel plate.

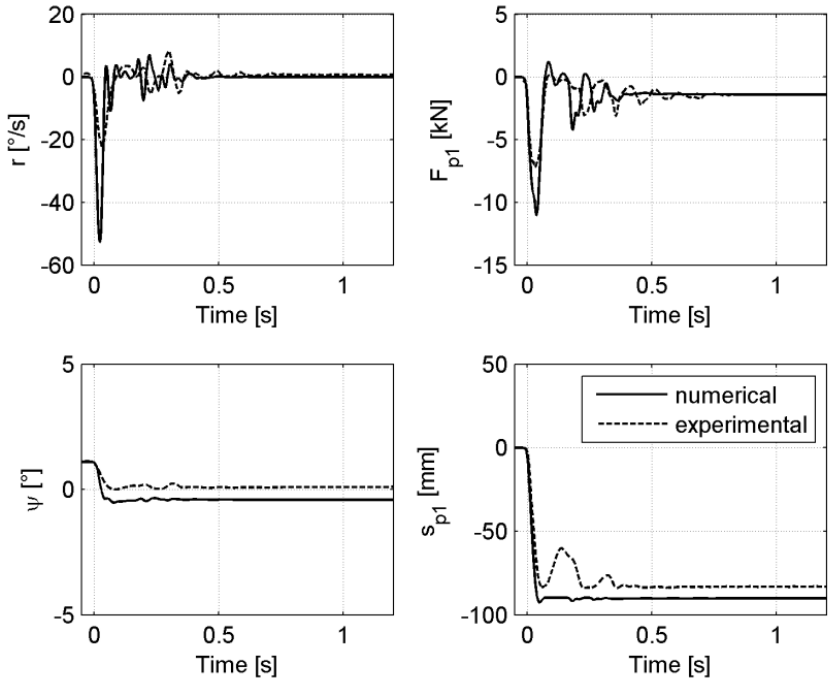

Figure 5-14 Test case 4 – Attitude and angular rate, primary strut force and stroke data: a high correlation is achieved between the measured and simulated angular rate r and the resulting platform attitude angle Ψ; a likewise high correlation is achieved for the leading leg 1 force and stroke data

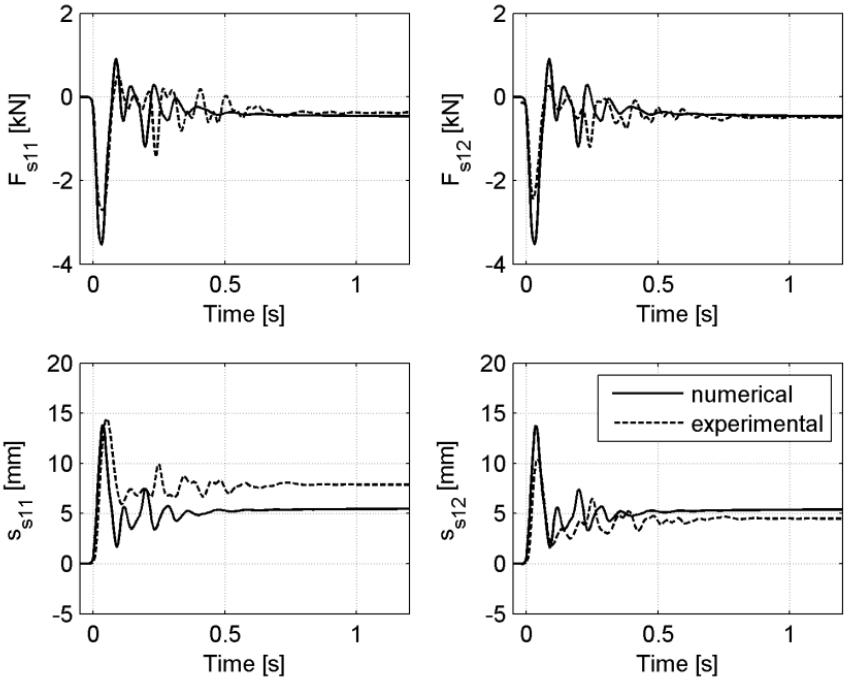

Figure 5-15 Test case 4 – secondary strut force and stroke data: the correlation for the leading leg 1 secondary struts is fair to good, again a mismatch is shown between the measured and simulated stroke of secondary strut 11.

	Correlation coefficient [-]	Weighed absolute error	
r	0.808	9.40	°/s
Ψ	0.950	1.44	°
$\mathbf{F_{p1}}$	0.832	0.78	kN
$\mathbf{s_{p1}}$	0.885	8.80	mm
$\mathbf{F_{s11}}$	0.842	0.30	kN
$\mathbf{F_{s12}}$	0.847	0.28	kN
$\mathbf{s_{s11}}$	0.579	2.68	mm
$\mathbf{s_{s12}}$	0.793	1.08	mm

Table 5-5 Test case 4 validation figures

5.2.6 Validation Summary and Discussion

The previous sections 5.2.2 to 5.2.5 provided selected time series data – measured and simulated – and its associated correlation and error figures, which are most meaningful for their particular load cases. The following validation summary and discussion is based on these quantitative validation means obtained from the complete data set per test case, tabulated in annex A4 – Ancillary Validation Data.

The data thereby suggests that the degree of correlation and the error magnitudes at the different measurement points are fairly independent of the particular test case. The correlation and error numbers are then averaged across the test cases by deriving both their mean and median to make a test case independent assessment of the model's credibility. The median figures are used which provides

more robustness to outliers in the test data as apparent at least in some clear cases (refer test case 3, section 5.2.4). The following table summarizes the observed correlation coefficients and absolute errors. It also provides a relative error which is computed from the absolute errors with regard to the LEM's respective limit of function value given in the last column.

			Correlation Coeff. ρ	Error, absolute	Error, relative	LEM LOF
Platform	**Attitude Rate q, r**		0.94	10.6 °/s	-	-
	Attitude Θ, Ψ		0.99	1.1 °	2.1 %	52.5 ° (1)
Primary Strut	**Force F_P**		0.83	0.83 kN	-	-
	Stroke s_P		0.99	7.7 mm	5.0 %	154 mm (2)
Secondary Strut	**Force F_s**	**compr.**	0.61	0.54 kN	-	-
		tension	0.82	0.54 kN	-	-
	Stroke s_S	**compr.**	0.93	6.2 mm	8.8 %	70 mm
		tension	0.55	4.2 mm	14.0 %	30 mm

(1) Stability distance $d_{stab} = 0$ is equivalent to $52.5° = \arctan(r_{FP}/h_{COM})$

(2) Two honeycomb cartridges considered

Table 5-6 Validation results – correlation coefficients and absolute errors are combined values for all test cases, relative errors are absolute errors with respect to the LEM limits of functions values; the validation results associated to the individual test cases are provided in Annex A4

Platform attitude and angular rates: An excellent correlation ($\rho > 0.9$) between measurement and simulation is achieved for angular rates and body angles. The errors between the angular rates are in the order of 11°/s while the errors between the platform attitudes are in the order of 1.2°. They are thereby independent to overall rates and attitudes induced by the test condition.

Primary struts: A very good correlation ($\rho > 0.8$) is achieved for the primary strut interface forces with a general error of less than 1kN and some outliers of less than 1.5kN. Excellent correlation ($\rho > 0.9$) is again achieved however for the primary strut strokes. The absolute errors are in the order of up to 8mm.

Secondary struts: Fairly good correlation ($\rho > 0.7 – 0.9$) is achieved for the secondary strut forces. The errors are in the range of 0.3kN in the tension direction and 0.5kN in the compression direction. With regard to the secondary strut strokes a correlation factor of $\rho > 0.9$ is achieved in the compression direction while a comparatively poor coefficient of $\rho > 0.5$ characterizes the tension direction. The associated errors are in the range of 4.2mm in the tension direction and 6.2mm in the compression direction respectively. The poorer correlation particularly for the secondary struts is explainable as this particular element of the landing leg assembly is strongly determined by the stress-strain hysteresis of the bending rods being amenable to the laws of structural dynamics. This area turns out to be most sensitive to the simplification of the elastic-plastic behavior made in chapter 3.3.2.2. Nevertheless, the low pass filtering effect of the integration of the (various) body accelerations into the platform's overall velocity and position states makes it less susceptible to unaccounted higher order structural dynamic modes as indicated by the excellent platform attitude and attitude rate figures.

Having the determination of the platforms limits of function (LOF) in mind, two aspects can be preliminarily concluded. At first the performance measurements for such LOF analysis should be based on positions, displacements and attitude data due to its least susceptibility for unaccounted structural modes. Secondly, as the particular absolute errors reveal a fairly test case independent order of magnitude, a relative determination error can be estimated with regard to the limit of function values. Finally it can be stated that the LEM numerical model exhibits a high degree of correlation to the physical LEM. The observed errors are acceptable to make plausible and dependable predictions on its touchdown dynamics and failure rates in the following analysis chapters. A broader background on the quantification of a model's validity is provided by *Müller 2003*. Further improvements to this touchdown dynamics model shall take a higher fidelity of the secondary strut's force-stroke characteristic into account.

6 Deriving the Probability of Terrain-related Failure

In this chapter a mathematical framework is developed and introduced step-by-step which analyses the landing platform's touchdown dynamics and evaluates the degree to which its functions *provide stability*, *maintain ground clearance* and *absorb energy* are utilized. This analysis is done in the context of the platform's expected initial touchdown conditions as well as terrain properties. At first, the chapter starts with theoretical considerations on the mathematical framework and gets more application-oriented while integrating the elements of the touchdown dynamics simulation from the previous chapters.

6.1 Mathematical Preliminaries

The term *function* is here generally used in its technical sense as a characteristic behavior of a technical artifact and here specifically related to the touchdown system as defined in chapter 2.3. A function can be realized by either hardware or software and can be characterized by measurable properties. This definition from *Haueis et al. 2007* is applicable to complete systems as well as to sub-assemblies or single components. In the mathematical sense a function is a relation between an input and an output value set. Mathematical functions are used in the following to represent technical functions. They are annotated as *analytical* or *numerical functions*, respectively.

The range of intended, specified and verified fulfillment of a function, in its technical sense, is limited by the "Limit of Function" (LOF) value (*Haueis et al. 2007*), whereas an upper bound and/or lower bound LOF can be defined. While an operation close to the LOF is still within the verified range it might concur with an increasing sensitivity to varying input values. Thus the robustness of function delivery when approaching the LOF might decrease. A function value exceeding its LOF is defined as failure or unsafe state according to the requirements and definitions provided in chapter 2.2. The values of the respective LOF of a function shall be defined in the system specification.

The according mathematical expression for the limit state is $g(\mathbf{x_{LOF}}) = c_{LOF}$, where $\mathbf{x_{LOF}} = \{ x_1, x_2, \ldots, x_n \}$ are input variables and c_{LOF} represents the specified and verified limit of the required performance. The function g is continuous and relates the input $\mathbf{x}$ to an output $\mathbf{y}$. Dependent on c_{LOF} being defined as upper or lower bound the exceedance or undercut of this value means a state of failure. Equation 6.1 is an example for a lower bound limit, consequently $g(\mathbf{x}) > c_{LOF}$ means a safe state and $g(\mathbf{x}) < c_{LOF}$ represents a state of failure, operational malfunction or unintended performance. The sign of relation changes accordingly in case of an upper bound limit. This fundamental approach is also exploited in First-Order Reliability Methods (FORM, e.g.*Cizelj et al. 1994*) however adapted in this thesis in a different way. In simple cases the performance function can be an analytic dependency while more generally it can be a numerically determined relation.

$$g(x) - c_{LOF} \begin{cases} \leq 0, & \text{failure} \\ > 0, & \text{safe state} \end{cases} \qquad 6.1$$

For real world problems the input and initial variables and boundary conditions are typically not known with certainty as they are affected by dispersions and deviations ("aleatoric uncertainty" *Stamatelatos et al. 2002*). To reflect the aleatoric uncertainty in the knowledge of the exact value of a certain input value x they are considered as random numbers X rather than deterministic values. It describes the distribution of the actual values around the desired or commanded values. In case of the touchdown system the initial values and its distribution are determined by the control and guidance dispersions of the landing system. Section 6.2.1 of this chapter will resume this aspect.

X is described by its probability density function (PDF) f_X and the associated cumulative density function (CDF) F_X.

Thus Y = g(X) holds true, as the random number X is transformed into another random number Y, which is then similarly described by its PDF f_Y and CDF F_Y respectively.

Rather than having a deterministic statement that a particular input x leads to a failure case or not, a probability statement such as $P_{fail} = F_Y(y \leq c_{LOF})$ is obtained.

Example: For the derivation of the assessment method initially a simple, single and real-valued analytic function Y = g(X) is considered. For sake of a simple and illustrative example, it is further assumed that the system input is described by a Rayleigh-distributed random variable $X \sim \text{Rayleigh}(\sigma_x)$ whose PDF and CDF are given by the equations 6.2 and 6.3. Figure 6-1 shows in its lower right window the associated PDF and CDF for this example. The example's parameter $\sigma_x = 2.4$, a = -0.05 and c = 1.8 are arbitrarily chosen.

$$f_x(x) = \frac{1}{\sigma_x^2} \cdot x \cdot e^{-\frac{1}{2}x^2/\sigma_x^2} \quad , \qquad x \in \mathbb{R}_{\geq 0} \qquad 6.2$$

$$F_x(x) = 1 - e^{-\frac{1}{2}x^2/\sigma_x^2} \qquad x \in \mathbb{R}_{\geq 0} \qquad 6.3$$

The behavior of the notional system is assumed to be mathematically described by a quadratic function (eq. 6.4, shown in the upper right window in Figure 6-1).

$$y = g(x) = a \cdot x^2 + c \qquad 6.4$$

$$f_Y(y) = f_X(x)/\left(\frac{dy}{dx}\right) \qquad 6.5$$

with $dy/dx \neq 0$ and $x = g^{-1}(y)$

The application of the transformation rule (eq. 6.5, *Schwarzlander 2011*) to this purposefully chosen input parameter X yields an exponentially distributed output $Y \sim \text{Exp}(\sigma_y)$ with $\sigma_y = 2a\sigma_x^2$. Its PDF and CDF are given by the equations 6.6 and 6.7 (Figure 6-1, upper left).

$$f_Y(y) = -\frac{1}{2a\sigma_x^2} \cdot e^{-\frac{1}{2a\sigma_x^2}(y-c)} \qquad 6.6$$

$$F_Y(y) = e^{-\frac{1}{2a\sigma_x^2}(y-c)} \qquad 6.7$$

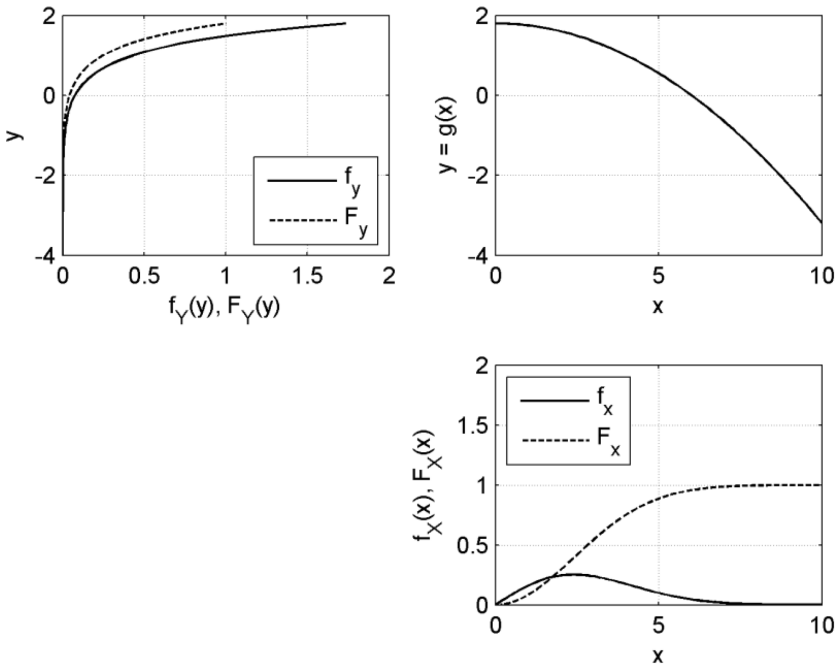

Figure 6-1 Example for the transformation of a random number: a Rayleigh-distributed random number (bottom right: PDF f_X and CDF F_X) is transformed by a quadratic function (top right: $y = a \cdot x^2 + c$) into an exponential-distributed random number (top left: PDF f_Y and CDF F_Y)

This initial case in which a Rayleigh-distributed random number has been transformed into an exponentially distributed number by a quadratic function is however special in that regards as such analytic transformations are only found for rare cases or are restricted to certain classes of functions. In a next step it is less restrictively assumed that the (yet same example) relation Y = g(X) is not known analytically anymore but the "system behavior" can be probed or "tested" by dedicated deterministic inputs x yielding y. This is shown in Figure 6-2, upper right.

The domain of definition $x \in [0, 10]$ of the input value set is systematically sampled by equally distributed, but not necessarily equi-distant inputs x_i, i = 1...n. The probability associated to each of these samples is considered by a weight factor w_i which is equal to the probability density of the underlying PDF at x_i (equation 6.8). With regard to the example the sample positions and their weights are shown in Figure 6-2, bottom right.

$$w_i(x_i) = f_X(x_i) \qquad 6.8$$

Figure 6-2 upper left shows the same sample weights mapped by the function g onto the co-domain y. It is noted that in this case the sample spacing is not equi-distant anymore but becomes infinitesimal small when converging against the upper limit of the co-domain. This technique is closely related to the concept of a histogram filter and its derivative the particle filter which is described in more detail in *Thrun et al. 2006*. The usage of weight factors to reflect a sample's likelihood rather than drawing it directly from its underlying distribution is a quite common technique also known as importance sampling and belongs to the family of variance reduction methods to improve the efficiency of Monte-Carlo simulations (*Kroese et al. 2011*).

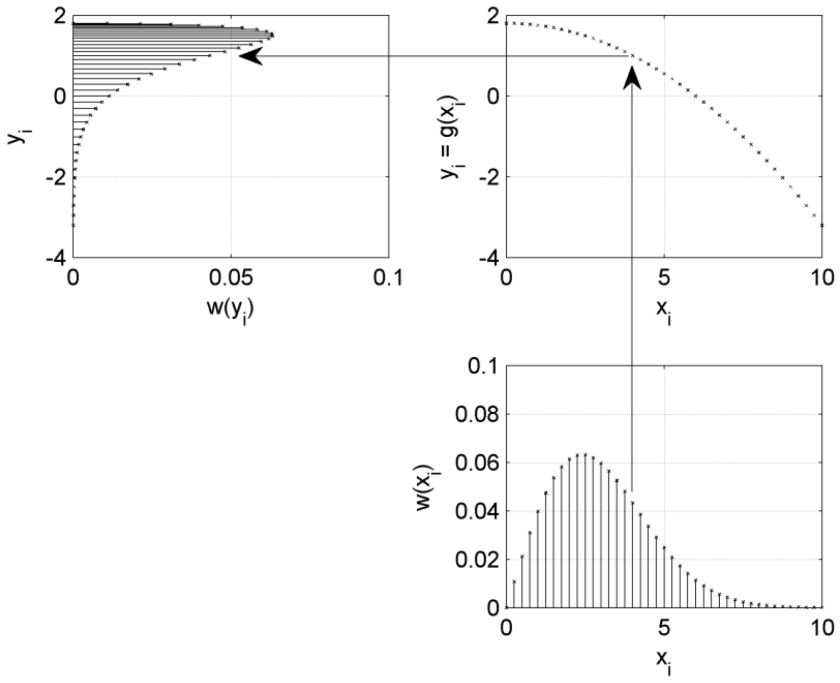

Figure 6-2 Example of the transformation of a random number through a histogram filter: the input distribution (bottom right) is assumed to be represented by histogram; the relation y = g(x) is assumed deterministic but not necessarily represented by an analytic function; the initial input bins (x_i) of the histogram are mapped uniquely onto y_i. For reference purpose however, this example is a discrete variant of the analytic example shown in Figure 6-1 above.

The empirical CDF for Y = g(X) is calculated according to equation 6.9 as the cumulative sum of the normalized sample weights.

$$\hat{F}_Y(y) = \frac{\sum_{i=1}^{N} w_{i\,\{i:y_i \le y\}}}{\sum_{i=1}^{N} w_i} \qquad 6.9$$

An approximate 1-α/2 confidence bound for this cumulative distribution is obtained from equation 6.10 (*Kroese et al. 2011*) with $t_{1-\alpha/2}$ being the respective quantile of Student's t-distribution (table from *Bronstein et al. 1997*).

$$F_Y(y) \le \hat{F}_Y(y) + t_{1-\alpha/2} \cdot \sqrt{\hat{F}_y(y) \cdot \left(1 - \hat{F}_y(y)\right)/N} \qquad 6.10$$

Figure 6-3 shows the curves for the analytical solution to this example as well as both the empirical and its 95%-confidence curves determined with these equations.

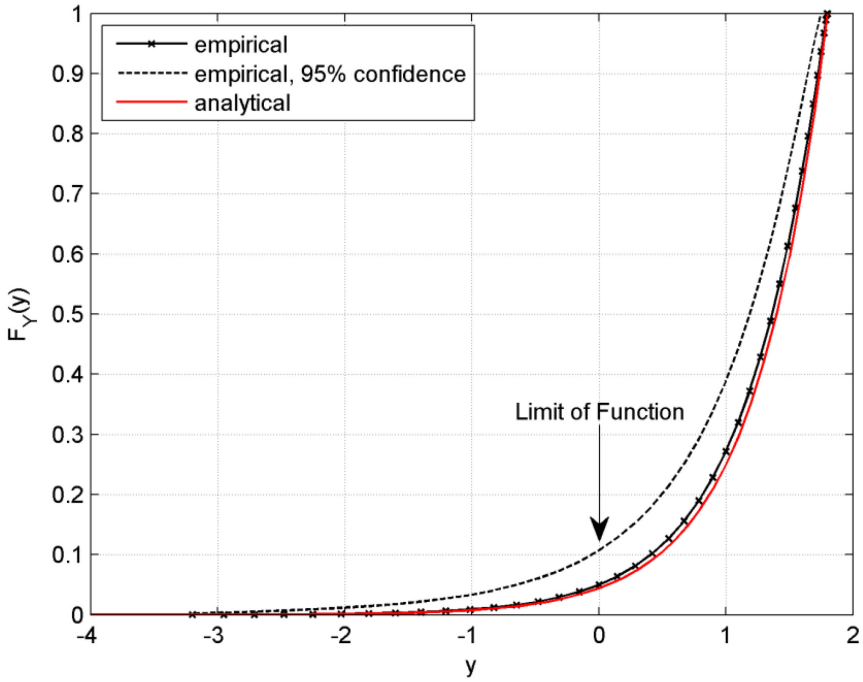

Figure 6-3 This figure compares of analytical and empirical CDF of the example (compare Figures 6-1 and 6-2) and indicates that the discrete variant converges against its analytic reference. In addition, a 95% confidence boundary is provided for the discrete, "empirical" variant of the example. If the limit of a technical function is reached at y = 0, then the associated probability can be read from this graph.

If it assumed that the limit of this (technical) function is $c_{LOF} = 0$ than the probability that the system fails (is out of its functional limits) at a given input distribution of X is identified $P_{Fail} = P(y \leq y_{LOF}) = F_Y(y_{LOF}) = 0.044$.

The "true" value of this analytic example according equation 6.7 is $P_{Fail} = 0.0439$. Considering a confidence bound ($\alpha = 10$) the probability to fail is with 95% confidence not higher than $P_{Fail,95} = 0.107$.

The method outlined in this section and the equations 6.8, 6.9 and 6.10 provide a non-parametric, hence very general form to estimate a cumulative distribution function as no assumptions are made about certain describing parameter. The subsequent section is dedicated particularly to the integration of the numerical touchdown simulation and the sampling of the specified range of initial touchdown conditions.

6.2 Embedding the Numerical Touchdown Simulation

In the prevailing case of this thesis the relation between the input values – the initial touchdown conditions – and the output values – the performance measurements – is not an analytic expression anymore but the numerical solution of a considerably large set of differential-algebraic equations as introduced in chapter 3.2. Nevertheless, such multibody simulation is a deterministic simulation which means that a single execution of the model at a specific initial condition is uniquely and repeatable associated to the output result. Thus when a vehicle function is described by a mathematical relation – either analytic or numerically – than the degree of functional utilization is unambiguously associated to its set of initial values. Consequently, the previously introduced mathematical function $y = g(x)$ is now synonymous for the algorithmic relation between the landing platform response y to a touchdown condition x.

This feature can be exploited to evaluate the numerical touchdown system model at distinct points of the input value space to gather information on its response space. The same method of probing the system behavior as done in the example of the previous section becomes feasible under this premise.

When planning the sampling pattern however, some economic considerations become mandatory in cases where computations are very expensive in terms of processing time. Given that, the input space must be covered with a minimum of sample points. This is the domain of "Design of Experiments" (DOE) techniques which is not only applicable to the mentioned computer based analysis but any kind of experiments. Accordingly, a large number of space filling designs have been proposed and are discussed by *Montgomery 2009*. The positioning of the sample points can be arranged in a determined order or randomly placed but all have in common that they place the sample points evenly or uniformly across the input space. The Figure 6-4 shows some examples of such pattern for a 2-dimensional variable space – given by f_1 and f_2 – and 20 samples: in (a) the *sphere packing* method is used, which maximizes the distance between pairs of design points. In (b) the result of the *Latin Hypercube* algorithm is shown, which spreads the sample points uniformly along the space diagonal and then permutes the samples along the column. In (c) the sampling pattern is generated using the *maximum entropy* method which minimizes the amount of information within the distribution of the set of sample points. The last method applied in (d) is the *uniform distribution* through a random number generator. The examples are generated using the DOE toolbox of the statistics software JMP (*JMP 2014*).

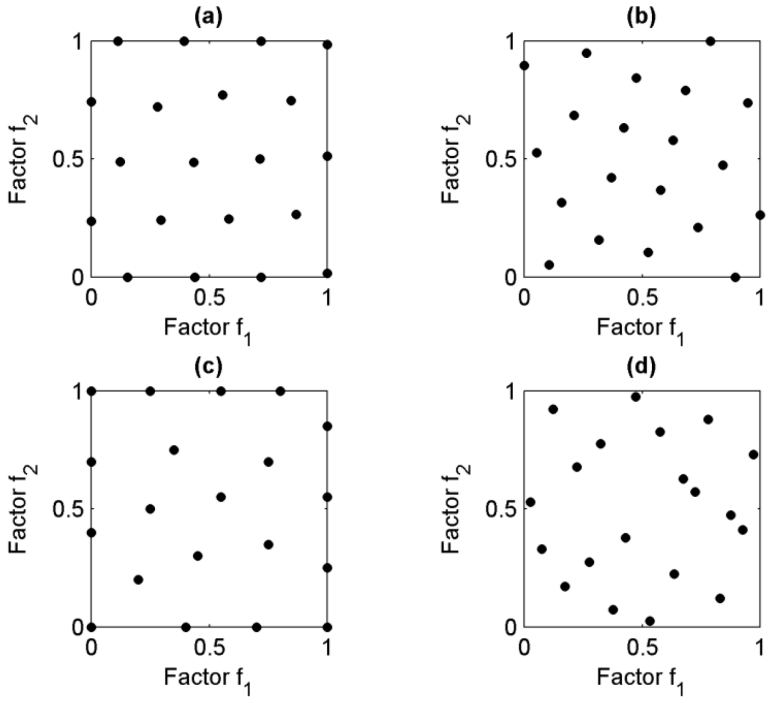

Figure 6-4 Examples of space filling designs: (a) sphere packing, (b) Latin Hypercube, (c) maximum entropy, and (d) uniform distribution

Arranged sample pattern can to a certain degree ensure an optimum ratio of information content to analysis effort but require additional planning effort to "construct" such a pattern. Stochastic sampling makes use of a (pseudo-) random number generator to place the samples. The latter method is implementation-wise easy when a computer build-in random number generator is used, however the disadvantage is that the such generated random numbers tend to form occasionally point clusters. This

disadvantage is overcome by oversampling the input region but yet penalizing the ratio of information content versus effort.

Coming back to the particular case of this work, the numerical simulation of one touchdown event over simulated 5 seconds takes approximately 20 to 40 seconds of CPU-time[3] dependent on the individual touchdown condition. Taking a practical view, it can be stated that the model execution is fast compared to some structural FEM or CFD simulations which may take hours or days on comparable computer hardware. This eases the necessity to implement optimized space-filling designs and justifies the implementation of a random sampling using the uniform distribution. As a lower limit of samples to be taken here it is required that at least two samples per input variable shall be combined. Thus the number n of samples for k input variables shall be:

$$n \gg 2^k \qquad 6.11$$

The further practical realization of this sampling environment nests the deterministic, validated touchdown simulation into a sampling shell (Figure 6-5). The following steps are executed by this computer routine:

1. The pre-processing, taking place in that shell, is initialized itself with the required initial condition ranges. At the beginning of each loop (counter i) independent and identically distributed random numbers are drawn from a uniform distribution U.
2. The simulator is initialized with these values and started. Supplemental information and illustration on this step is provided below in section 6.2.1.
3. A result file with time series data of the platform's motion states and the dedicated performance measurements is stored at the end of the time integration of each simulation run. A numerical routine as part of the sampling shell extracts the performance measurements which determine the degree of utilization of the associated function. This degree of functional utilization is measured as an extreme value or stationary end value. Supplemental information and illustration on this step is provided below in section 6.2.2.

The entire sampling loop is repeated until the required number (eq. 6.11) of result values is generated which can be further analyzed with statistical methods.

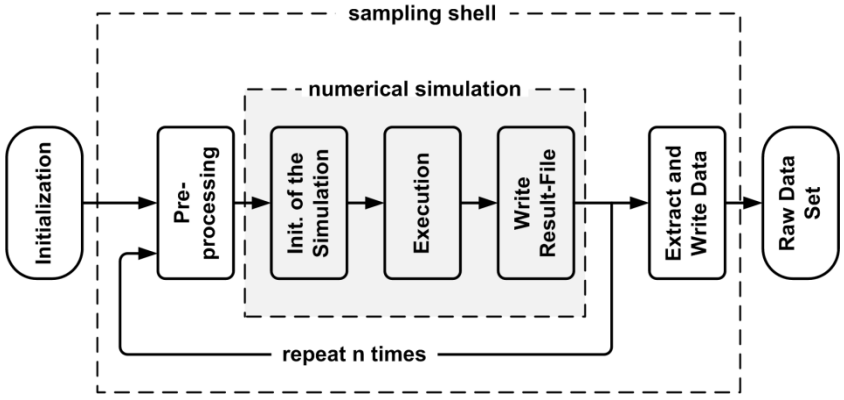

Figure 6-5 Sampling shell and activity flow: the numerical touchdown simulation is nested in computer script which repeatedly runs this simulation with varied input parameter. The performance measurements are taken from the simulated landing system response and are stored for further processing

[3] Hardware: CPU 2.8GHz, 8GB RAM, 64bit OS, SIMPACK Software: RADAU5 solver (*SIMPACK 2012*)

6.2.1 Initial Conditions

The initial touchdown conditions **x** are determined by the platform's velocity and angular orientation at its first ground contact. At a later point in this thesis, when the responses to distinctive surface features such as craters and boulders are investigated also initial position dispersions are added. The allowances for these motion states at touchdown are expressed as engineering requirements imposed on the landing platform design. Applicable parameter ranges have been introduced in chapter 2.1 with regard to recent European landing system studies. These are now taken as a reference case to illustrate the stochastical analysis of the landing platform. The method introduced in section 6.1 does not yet require the assumption of a particular probability density function for the parameter but only uniform sampling across the parameter range.

The pre-processing, taking place in the sampling shell, is initialized with these initial condition ranges. At the beginning of each loop the random numbers are drawn from the uniform distribution $U(a_{lb}, a_{ub})$ with a_{lb} and a_{ub} (lower / upper bound) defining the range for each parameter (Table 6-1).

Initial Condition		**Pre-processing** $\mathbf{a_{lb}, a_{ub}}$	**Post-processing**	
Velocity, vertical	v_v [m/s]	1.0, 3.0	Gaussian	μ=2.0; 3σ = 1.0
Velocity, horizontal	v_h [m/s]	0.0, 1.5	Rayleigh	3σ=1.0
Azimuth	χ [°]	-180, 180	Uniform	a_{lb}=-180; a_{ub}=180
Roll Attitude	Φ [°]	-180, 180	Uniform	a_{lb}=-180; a_{ub}=180
Pitch Attitude	Θ [°]	-5, 5	Gaussian	μ=0.0; 3σ = 5.0
Yaw Attitude	Ψ [°]	-5, 5	Gaussian	μ=0.0; 3σ = 5.0

Table 6-1 Distribution parameter for initial conditions – pre- and post-processing (refer chapter 2.1 or *ESA 2008*). The pre-processing assumes all parameter uniformly distributed. Their non-uniformity, if applicable, is re-introduced in the post-processing.

It shall be noted that instead of initializing both Cartesian lateral velocity components v_{hy} and v_{hz} they are expressed here as length v_h and direction χ (ground track azimuth) of the velocity vector. From a mathematical point of view there is no reason to favor polar coordinates however this expression is somewhat more intuitive to understand a certain touchdown behavior (e.g. whether a touchdown is characterized as downhill or cross-slope landing).

The ambient environmental conditions are kept fix during a sampling series and act as independent parameter when comparing different series. These ambient conditions considered here are the terrain slope and its roughness, and the soil's bearing capacity.

To provide again an illustrative example, the LEM-4C is put into an assumed lunar gravity environment. The terrain is considered as flat, rigid plane with a slope of 5°. This scenario is identified as *LEM-4C-Slope05-Flat-Rigid-Lunar*, or abbreviated *LEM-4C-S05-F-R-L*.

The initial conditions generated with this setting out of n = 300 simulation runs are displayed in Figure 6-6 as a histogram. The height of the bars indicates the numbers of samples n per bin. In this figure, each parameter range is subdivided into 30 bins, yielding ~10 sample per bin as dictated by the uniform distribution.

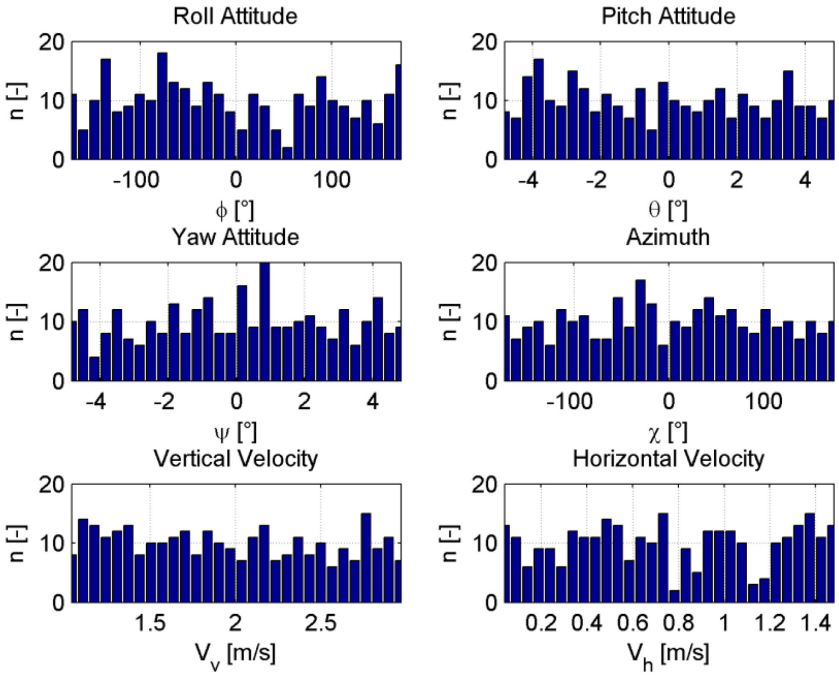

Figure 6-6 Histogram of initial values of the LEM-4C-S05-F-R-L example

Additionally, the distribution of the sampling points across the touchdown velocity regime is depicted in Figure 6-7 which indicates some light clustering.

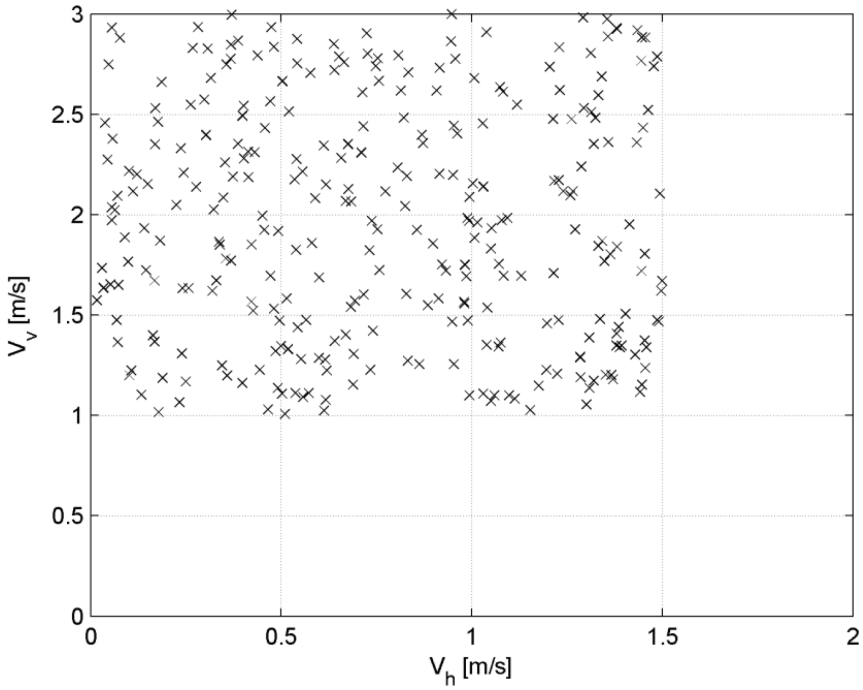

Figure 6-7 Sampling pattern of the touchdown velocity domain

6.2.2 Measurement of the Touchdown Performance

The definitions and metrics with regard to stability, ground clearance and energy absorption utilization have been introduced in chapter 3.4. They are continuous measurements taken during the simulation execution. At this stage of the investigation the complete temporal behavior of the platform is not of primary interest anymore but only the extremes in the performance measurements since they are used in the post-processing step to determine the envelope for the respective degree of stability, ground clearance and energy absorption. Minimum and maximum operators are therefore applied to the respective sets of data files containing the measurements regarding each platform function.

Measurements of Stability: Stability is measured as defined by equation 3.9. As an example, Figure 6-8 (top) presents time series data from the test cases 1 (stable touchdown) and 2 (instable touchdown) which have been already used as validation cases in chapter 5.2. The stable case is intermittently rotating into the downhill direction and falls back onto its landing feet. The minimum stability distance of the unstable case crosses zero as its center of mass passes through the stability plane. The numerical simulation is terminated once this condition is detected. The minimum degree of stability is measured through the following equation for all four (LEM-4C) stability walls. This equation essentially applies a minimum-operator to equation 3.9.

$$d_{stab} = \min\{d_{stab,i}(t)\} \quad i = 1 \dots 4 \qquad 6.12$$

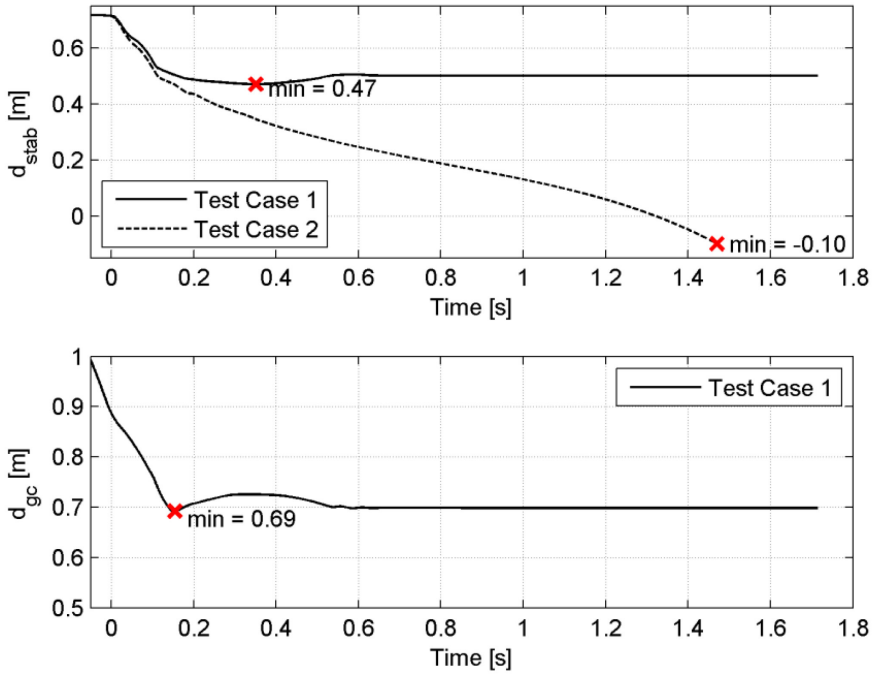

Figure 6-8 Minimum stability and ground clearance time series data from the simulation of the validation test cases 1 and 2: Only the respective minimum values are stored as performance measurement for stability and ground clearance for the further statistical post-processing.

Measurement of Ground Clearance: Ground clearance is measured through equation 3.10. Similar to the stability metric, the minimum ground clearance value reached in the period between initial touchdown and final rest is measured (equation 6.13) and stored. Figure 6-8 (bottom) for example illustrates this using again time series data from the validation test case 1.

$$d_{gc} = \min\big(d_{gc}(t)\big) \qquad 6.13$$

Measurement of Energy Absorption: The degree of utilization of this function is measured via the observed displacements s (refer to chapter 3.4.3) for each of the LEM-4C's four primary struts and eight secondary struts according the following equations.

$$s_{ps} = \max\{s_{ps,i}(t)\} \; i = 1 \dots 4 \qquad 6.14$$

$$s_{ss,tension} = \min\{s_{ss,i}(t)\} \; i = 1 \dots 8 \qquad 6.15$$

$$s_{ss,compression} = \max\{s_{ss,i}(t)\} \; i = 1 \dots 8 \qquad 6.16$$

Associated time series data is shown in chapter 5.2 where especially the Figure 5-10, Figure 5-11 and Figure 5-15 are illustrative to this aspect. The respective limit of function is dependent on the specific design of landing platform. Reasonable values are obtained during the leg assembly's component level testing and can be described as maximum allowed or certified displacements. Relevant test data for the LEM-4C test article is as well shown in chapter 3.3.2.

All the resulting performance measurements are exported in the time domain and filtered to extract the respective performance. The extracted numbers are for their part displayed as a histogram in Figure 6-9. Although no particular distribution for the initial conditions are set, the output distributions, yet still equally weighted, show already a remarkably difference to the initial uniformity. The data set obtained thereby contains all information on the platform's functional performance for a given terrain setting but without pre-assumptions on the distribution of its initial touchdown conditions. This will be considered and introduced during the further data processing.

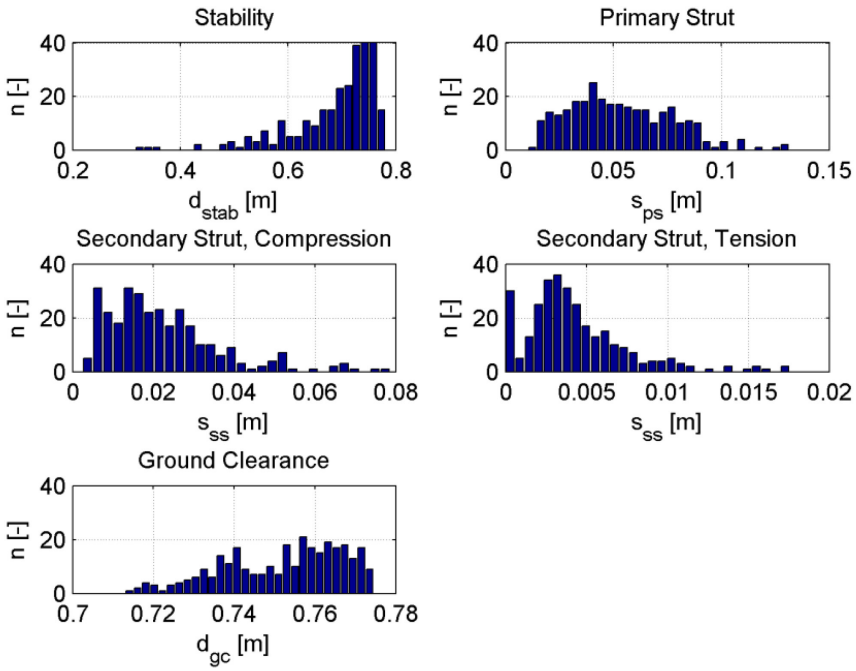

Figure 6-9 The histograms show the distribution of the performance measurements from raw data set of the LEM-4C-S05-F-R-L example.

6.3 Data Analysis and Parametric Modeling

With the data sampling completed, the post-processing begins. This is subdivided into basically two steps of which the first factors in the actual probability distribution of the initial touchdown conditions and derives the resulting cumulative distribution of the performance measurements. The second step determines if the probabilities to exceed a (technical) functional limit can be described also by an analytic function to a terrain property.

6.3.1 Step 1: Initial Post-processing

At this point the mathematical prerequisites introduced in section 6.1 are resumed to process the raw data set obtained from the model evaluation into meaningful information. Equation 6.9 thereby defines the empirical, non-parametric CDF as a means to determine the probability of a limit of function exceedance. It however, requires the consideration of the actual dispersion of the initial conditions via the weight factors. These dispersions stem from the guidance and control variability driven by the GNC and propulsion noise and their integration marks an important interface to these subsystems of the landing vehicle. The individual weight-factors follow the premise made by equation 6.8 and probability density functions provided by Table 6-1 are multiplied into a single weight factor as show below.

$$w_i = w_{V_v,i} \cdot w_{V_h,i} \cdot w_{\chi,i} \cdot w_{\Phi,i} \cdot w_{\Theta,i} \cdot w_{\Psi,i} \qquad 6.17$$

It is noteworthy that the transformation of a bi-variate Gaussian distribution for the lateral (Cartesian) velocity components $V_{h,y}$ and $V_{h,z}$ into polar coordinates yields a Rayleigh-distribution for the velocity vector length V_h and a uniform distribution for the azimuth χ. This is a well-known example for transformation of a bi-variate distribution and is fully described by *Schwarzlander 2011*.

This combined weight factor w_i is equivalent to the density of the multivariate PDF formed by the individual and independent distributions of the initial condition parameters, evaluated at the point i. While the main reason to run each sampling series with uniformly distributed inputs is to enable an importance sampling across its parameter range, a welcomed side-effect is however the shifting of the GNC interface from the pre-processing to this post-processing stage. This means that changes in the GNC dispersion pattern can be considered and incorporated into the platform's response without re-running the numerical touchdown simulation as long as such changes remain inside the already probed initial value range. For example the platform attitude (Table 6-1) is permitted in a range of ±5° while later development stages could indicate that ±2° is achievable with a certain improved GNC design. In such a case the post-processing would be repeated just with an adjusted weight factor accordingly.

The empirical distribution functions for the originally unweighted raw data and the resultant weighted set appear as shown in Figure 6-10. These curves are obtained from the application of the equations 6.8 and 6.9 to the primary strut stroke data from the LEM-4C-S05-F-R-L example. Comparing both empirical cumulative distribution functions (eCDF) it can be seen that the weighted curve, considering the actual initial dispersions, has shifted to the left side. This effect is expected because the actual touchdown velocities, Gaussian-distributed, have a higher probability density in the lower velocity domain. The kinetic energy of all sample touchdowns is less than the initial uniform distribution suggests. Hence the probability for higher primary strut strokes decreases. Secondly, the appearance of the weighted curve can be characterized as "stepped" compared to the smooth appearance of the unweighted curve. The weighted curve is yielded by cumulating weight factors with considerable difference in magnitude rather than the equally large factors of the unweighted curve. The respective probability values for the LOF of interest can be obtained by inter- or extrapolation.

Figure 6-10 also shows a third curve being a parametric PDF fitted into the empirical, weighted distribution function. This becomes desirable in some cases to infer from an empirical set of observations to the continuous range of the independent variable. In these cases it is necessary to revert to parametric models by identifying and fitting a suitable distribution function to the empirical data set. The path to a suitable parametric estimate is described subsequently.

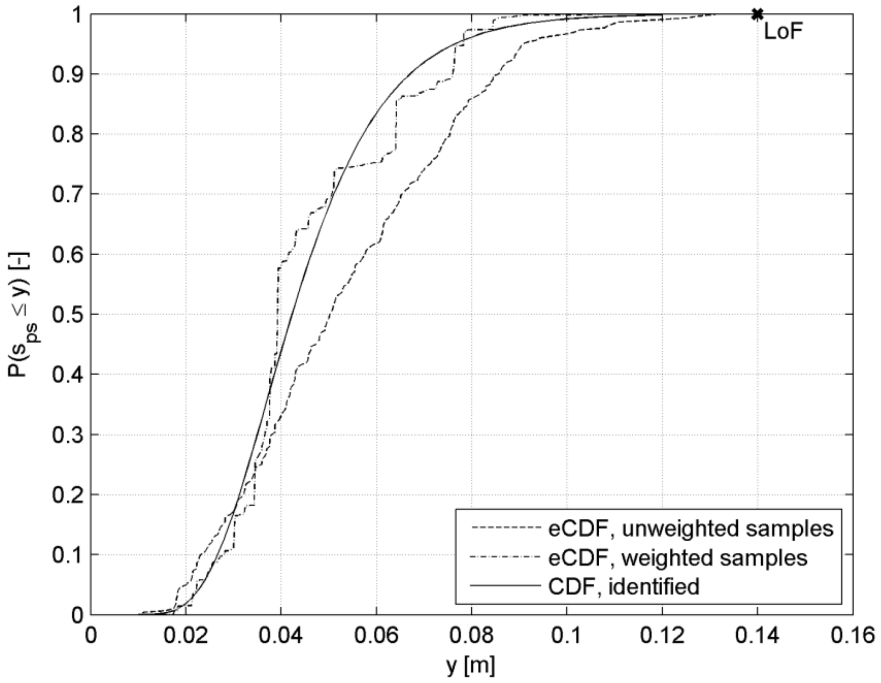

Figure 6-10 Empirical CDF for primary strut stroke data based on 300 samples: the curve of the unweighted sample just consider the uniform initial distribution of the touchdown conditions, the weighted samples take into consideration the actual touchdown conditions of the landing platform under study. Based on this CDF, an parametric CDF are identified as LogNormal-distributed

The first step to obtain a parametric model is to identify a suitable class of PDF. A graphical method to evaluate the suitability of a candidate distribution function is the quantile-quantile-plot (abbreviated: QQ-plot). When $P = F_Y(y_P)$ holds true then the associated abscissa y_P is the quantile of its distribution F_Y. The QQ-plot thereby compares the observed quantile $Q_{observed} = y_i$ to the predicted quantile $Q_{predicted} = F_C^{-1}(P_i)$ for an observed (empirically obtained) probability $P_i = F_Y(y_i)$. The mathematical function F_C^{-1} is thereby the inverse of the proposed candidate distribution function. If F_C provides a plausible candidate to represent the empirical data then $Q_{observed}$ and $Q_{predicted}$ are linearly related to each other Crowder 1991. Such relation can be quite easily confirmed by visual inspection of the curves or quantitatively by performing a goodness-of-fit check. If a linear relation is stated, the slope and intercept obtained from a linear regression provide then an estimation of the distribution function's location and scale parameter.

An overview on distribution functions – discrete and continuous – frequently used to describe the reliability of technical systems is found in *Birolini 1997*. Since the performance measurements are taken on continuous landing platform motion states the list of candidate distribution functions for a parametric modeling can be limited to continuous distributions accordingly. The candidate functions used in the further course of this work are the Normal- and Log-Normal distribution as well as the Weibull- and Exponential distribution whose general properties, formulation and characteristic is

given subsequently. These functions are complemented by their QQ-plot coordinates as well as their linear relation for the parameter estimation purpose.

Normal distribution: this distribution is probably the most widely known function to model random errors around a central value. Its density is characterized by a symmetric, bell-shaped curve defined by the expectation μ and standard deviation σ. The letter Φ denotes here the standard normal distribution.

CDF: $F_{Norm}(y) = \int_{-\infty}^{y} \frac{1}{\sqrt{2\pi}\sigma} \exp\left(-\frac{(\vartheta-\mu)^2}{2\sigma^2}\right) d\vartheta$ y, $\mu \in \mathbb{R}$; $\sigma > 0$ 6.18

QQ-plot coordinates: $\langle y_i ; \quad \Phi^{-1}\left(\hat{F}_Y(y_i)\right)\rangle$

Regression: $\Phi^{-1}(F_Y) = \frac{1}{\hat{\sigma}} \cdot y - \frac{\hat{\mu}}{\hat{\sigma}}$

Logarithmic Normal distribution: this distribution is frequently used in engineering and scientific studies to model the lifetime of technical and natural systems according to *Limpert et al. 2001*. As "lifetime" is defined on $\mathbb{R}_{\geq 0}$, symmetric functions such as the normal distribution are unsuitable due to its unrestricted domain of definition. When a random number X is Log-Normal distributed than its natural logarithm log(X) is normal distributed. Consequently, its QQ-plot coordinates and parameter estimation are related again to the standard normal distribution Φ.

CDF: $F_{LogN}(y) = \int_{0}^{y} \frac{1}{\sqrt{2\pi}\sigma\vartheta} \cdot \exp\left(-\frac{(\ln\vartheta-\mu_L)^2}{2\sigma^2}\right) d\vartheta$ μ_L, y, $\sigma > 0$ 6.19

QQ-plot coordinates: $\langle \ln(y_i) ; \quad \Phi^{-1}\left(\hat{F}_Y(y_i)\right)\rangle$

Regression: $\Phi^{-1}(F_Y) = \frac{1}{\hat{\sigma}} \cdot \underbrace{\ln(y)}_{y^*} - \frac{\hat{\mu}}{\hat{\sigma}}$

Weibull distribution: this distribution has its applicability in the technical reliability to model failure behaviors with in- or decreasing failure rates such as an increasing rate due to wear or deterioration. Its location and scale parameter are λ and τ. It has in any case defined on $\mathbb{R}_{\geq 0}$, however can take very different shapes. Due to this feature The Weibull distribution is an important candidate to approximate yet unknown distributions and is also used to model rare events (*Beirlant et al. 2004*).

CDF: $F_{Weib}(y) = 1 - \exp(-\lambda y^{\tau})$ y, λ, $\tau > 0$ 6.20

QQ-plot coordinates: $\langle \ln(y_i) ; \ \ln\left(-\ln\left(1 - \hat{F}_Y(y_i)\right)\right)\rangle$

Regression: $\ln\left(-\ln(1 - F_Y)\right) = \hat{\tau} \cdot \underbrace{\ln(y)}_{y^*} + \ln(\hat{\lambda})$

Exponential distribution: This distribution describes failure phenomenon with a constant failure rate. It is however a special case of the Weibull distribution with $\tau = 1$ and thus equation 6.20 applies here.

Although many more distribution function with similar properties are known, the ability of the above introduced functions to take different symmetric and asymmetric shapes, their suitability to model also rare events, and their degree of familiarity in the engineering communities make them appealing as prime candidates for a parametric characterization of the observed touchdown failure frequencies (limit of function exceedance).

To illustrate its use, the QQ-plot for the primary strut stroke data based on the candidate distribution functions Normal, Log-Normal and Weibull according the equations 6.18, 6.19 and 6.20 is depicted in Figure 6-11 as example. A visual inspection of these plots suggests a quite good linearity for all candidate functions. However, especially some data points of the left tail of the Weibull plot deviate strongly from the linearity. This impression regarding the primary strut stroke is confirmed when the associated correlation coefficients, given in Table 6-2, are compared. According this table, the Weibull

distribution appears only as third choice to model the distribution of primary strut strokes. A further aspect to consider is the domain of definition of the candidate PDF. As a symmetric distribution, the Normal distribution is defined for $y \in \mathbb{R}$. The primary strut stroke s_{ps} is however loaded in its compression direction only, hence $s_{ps} \in \mathbb{R}_{\geq 0}$. Despite a high degree of correlation, the Normal distribution is in this case not a good choice either. The Log-Normal distribution offers in this case both the highest goodness-of-fit as well as a matching domain of definition. Based on this deduction, a Log-Normal distribution is fitted into the data set and the resulting CDF is shown in Figure 6-10, denoted as "identified CDF".

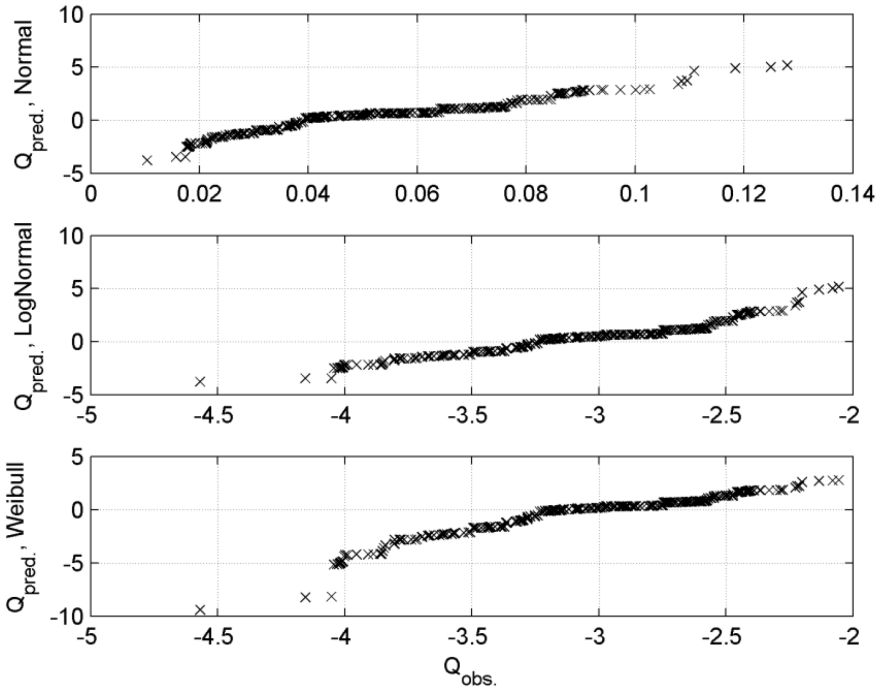

Figure 6-11 Quantile-Quantile or QQ-plots for the primary strut stroke data from the LEM-4C-S05-F-R-L example for the candidate probability distribution functions Normal-, LogNormal and Weibull-distribution

Distribution	Normal	LogNormal	Weibull
Correlation	0.968	0.971	0.949

Table 6-2 Goodness-of-fit of candidate distributions to primary strut stroke data

6.3.2 Step 2: Introducing Terrain-dependency

Summarizing up to this point, the previous sections of this chapter introduced the mathematical framework to determine cumulative distribution functions of the landing platform's functional performance based on the sampling results from the touchdown dynamics simulation. Terrain and environmental properties are kept frozen throughout a sampling series. The probability of exceedance of a functional limit or the failure probability P_{Fail} can be stated when evaluated at the respective LOF value. This relation is illustrated in Figure 6-12 (a). Now the terrain properties, here generically

denoted as ϑ, are introduced as variable. This adds a third dimension to the sketch as shown in Figure 6-12 (b) and reveals the relations between the failure probability P_{Fail}, the respective performance metric y and the possible influence of the terrain property. Figure 6-12 (c) reduces the view to the two-dimensional P_{Fail}- ϑ-plane. The probability of failure is then estimated at k distinct terrain property descriptors ϑ_i such that $\vartheta_1 < \vartheta_2 < \ldots < \vartheta_k$ is maintained. The initial touchdown conditions as defined by their particular distribution in Table 6-1 remain now unchanged between these repeated samplings. The aim is to determine its effect on the probability of functional exceedance and to determine if the data supports again a parametric model such that $P_{Fail} = f(\vartheta)$.

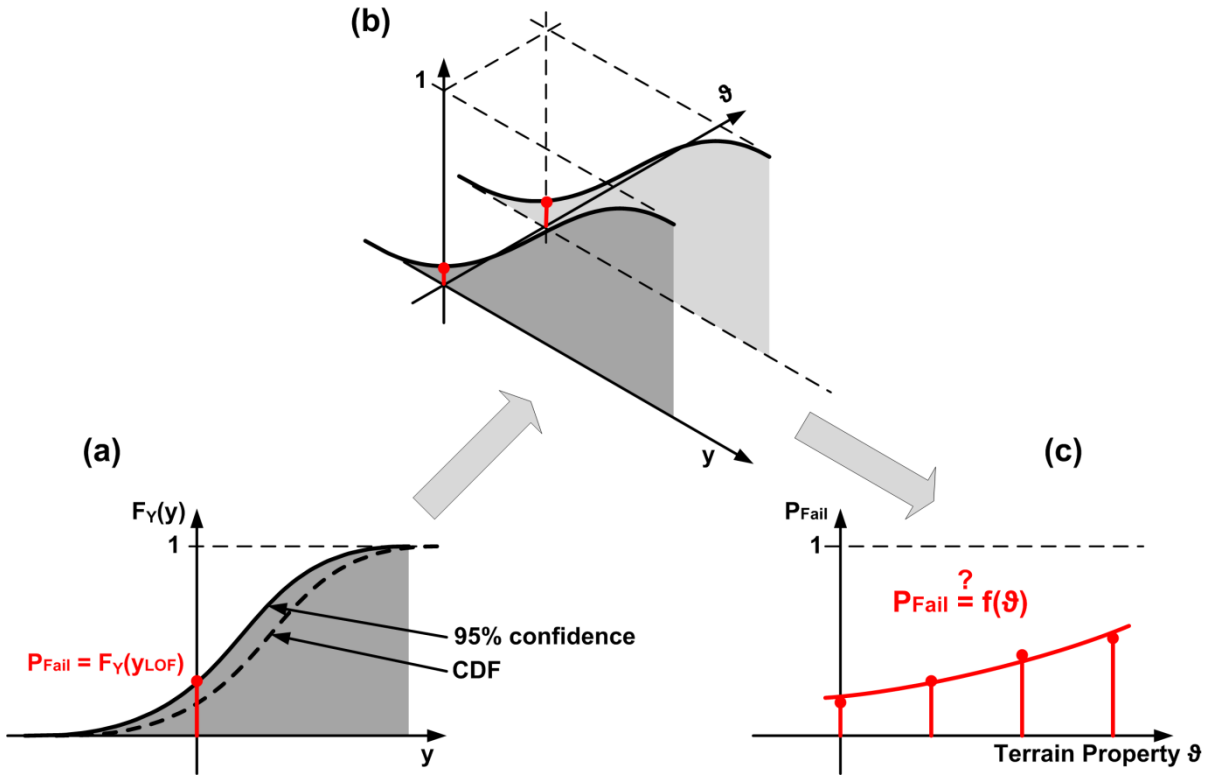

Figure 6-12 Terrain-dependency of failure probabilities: the probability of a failure is determined by the probability to exceed a respective LOF value (a) with 95% confidence for particular terrain property value ϑ; this analysis step is repeated for the same initial touchdown condition distributions but different terrain property values (b) and thus adding a further dimension to the analysis process; the final analysis step (c) reduces the view again to just the question whether a set failure probabilities follows an identifiable probability distribution or at least a trend. This aspect is investigated in the subsequent part of this chapter.

It is thereby at least reasonably to assume that with an increasing magnitude of a terrain property and hence severity of its influence the probability to fail likewise increases. To determine if this assumption is true and which parametric model is suitable in this case, the methods applied are the same as introduced in the previous section.

The following assessment of the LEM-4C's probability to be instable upon touchdown on sloped terrain continues the LEM-4C-S05-F-R-L example. Actually the sampling is repeated for terrain slope values s from 10° to 25° is 5° steps. The empirical CDF for the expected (nominal, eq 6.9) and 95%-confidence values according equation 6.10 are shown in Figure 6-13 for the 15° slope case. The probability of an instable touchdown is read-out at the $d_{stab,LOF} = 0$ limit of function and tabulated in Table 6-3. These curves are also an example for a CDF which is continuous but not continuous differentiable. Its left tail appears truncated as the numerical simulation is terminated upon instability

detection (refer also section 6.2.2 and Figure 6-8). The use of the non-parametric CDF is thus necessary here.

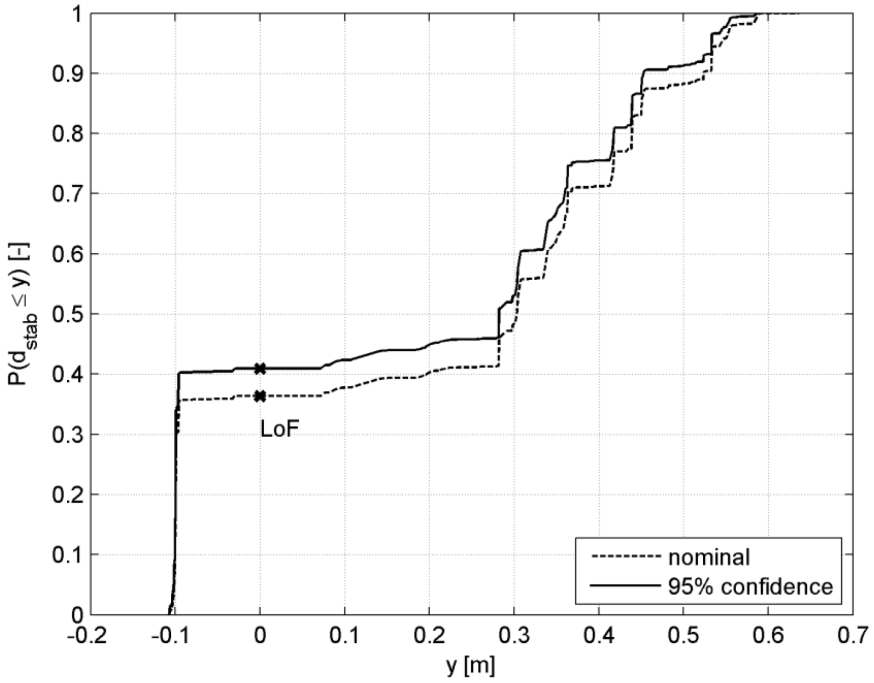

Figure 6-13 Cumulative distribution functions for touchdown stability data

Slope [°]	$P_{instable}$	$P_{instable}$ 95% conf.	Scenario identifier
5	0.0001	0.0008	LEM-4C-S05-F-R-L
10	0.0023	0.0068	LEM-4C-S10-F-R-L
15	0.3635	0.4090	LEM-4C-S15-F-R-L
20	0.7533	0.7941	LEM-4C-S20-F-R-L
25	0.9593	0.9780	LEM-4C-S25-F-R-L

Table 6-3 Probabilities with and without 95% confidence level for an instable touchdown with regard to terrain slope

The data set in Table 6-3 is evaluated if it supports a Weibull (eq. 6.20) or a Log-normal (eq. 6.19) distribution. The Normal distribution is disregarded in this particular case as terrain slope is defined on $\mathbb{R}_{\geq 0}$, hence a symmetric distribution is not reasonably here.

With regard to the Weibull candidate distribution the five data points are shown as QQ-plot in Figure 6-14 (top) and as probability over slope in the bottom part of same figure. Based on the QQ-plot the goodness-of-fit is checked with a correlation coefficient ρ given in Table 6-4. The parameter of Weibull distribution α and τ have been estimated and are provided in the same table. The Weibull curve obtained therefrom is also displayed in Figure 6-14 as CDF (bottom) and in QQ-plot style (top). It is important to note that these curves provide a least square fit to the data points whereas the 95%-

confidence level curve is a fit to the associated 95%-confidence data points and not a respective confidence level added to the nominal curve. The greatest effects on the curve fit have the data points within the left tail. Although small in absolute terms – the confidence interval for the 5° slope touchdown is $\Delta P = 7 \cdot 10^{-4}$ – it significantly shifts the estimated curve leading in this case to the meaningless result of a 95% confidence estimate intersecting and falling below the nominal curve. The probability to fail is largely underestimated in the range of 15° slope. The residual errors $\Delta P = F_{Weib}(s_i) - P_{fail}(s_i)$ are summarized in Table 6-6 and presented graphically in Figure 6-16.

Weibull	$\hat{\lambda}$	$\hat{\tau}$	**ρ**
nominal	3.49e-10	7.29	0.9822
95%	5.1e-08	5.68	0.9767

Table 6-4 Weibull distribution parameter estimates for the instable touchdown due to slope

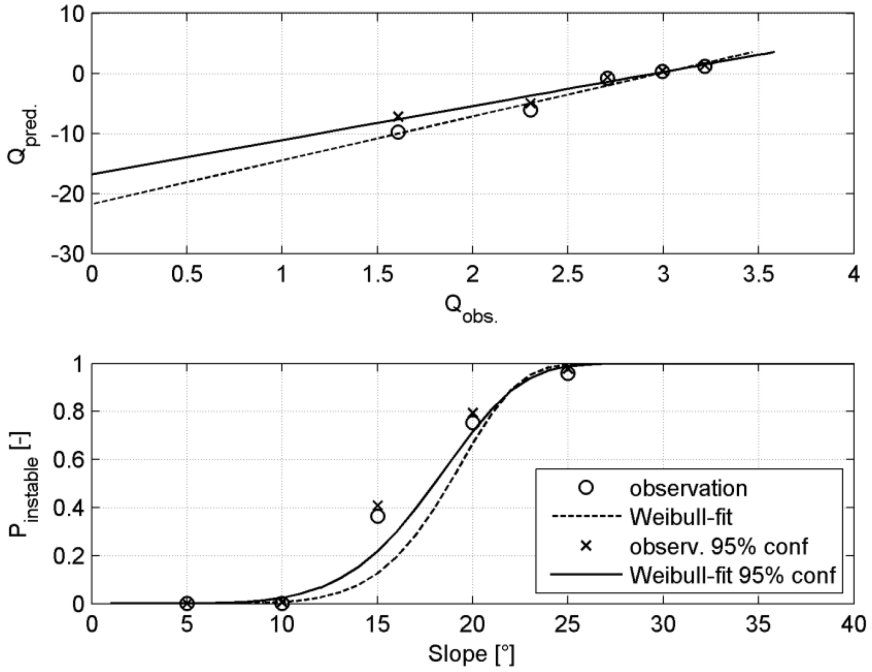

Figure 6-14 Weibull curve fit to touchdown stability data: the data fit is made for both data sets with and without 95%-confidence level using the QQ-plot coordinates (top). The visual impression of the resulting distribution curves already suggests that the Weibull-distribution is not an ideal choice in this case as it does not match the data points in the medium slope range

A similar display is given for the Log-Normal distribution by Figure 6-15 and Table 6-5. Its estimation errors are summarized as well in Table 6-6 and shown in Figure 6-16. This distribution matches the empirical determined (expected, nominal) probabilities with ~±0.03. The 95%-confidence curve has a tendency to slightly overestimate the failure probability except for high (25° slope) values. Concluding, this distribution obviously yields a better fit to the data points than the Weibull distribution. It is in this case a good choice to model the probability of an instable landing as a function of terrain slope.

LogNorm	$\hat{\mu}_L$	$\hat{\sigma}$	$\hat{\mu}$	ρ
nominal	2.82	0.27	16.83	0.9707
95%	2.75	0.30	15.66	0.9583

Table 6-5 Log-normal distribution parameter estimates for the instable touchdown due to slope

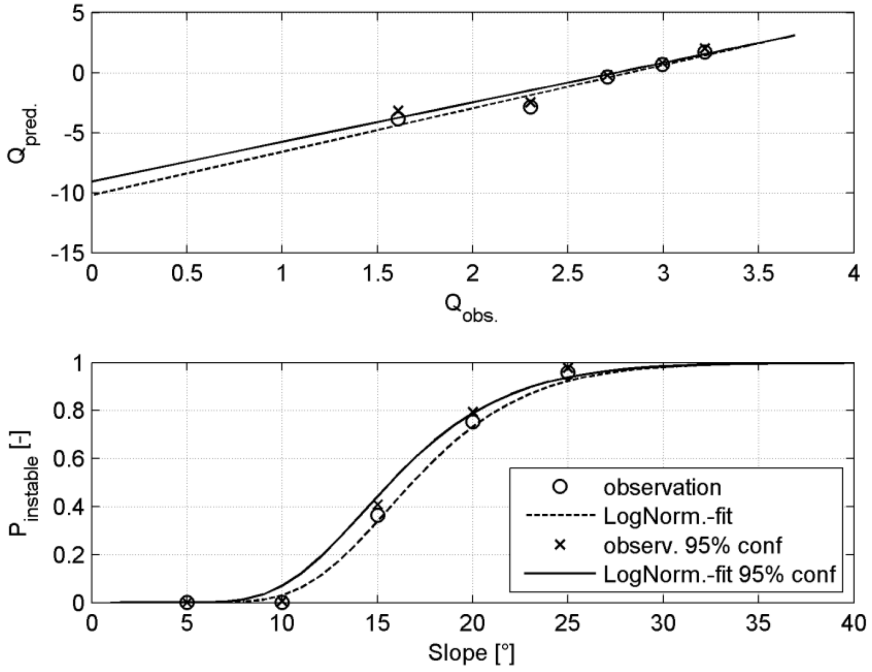

Figure 6-15 Log-normal curve fit to touchdown stability data: the data fit is made for both data sets with and without 95%-confidence level using the QQ-plot coordinates (top). The visual impression of the resulting distribution curves suggests a quite well fit of the data points

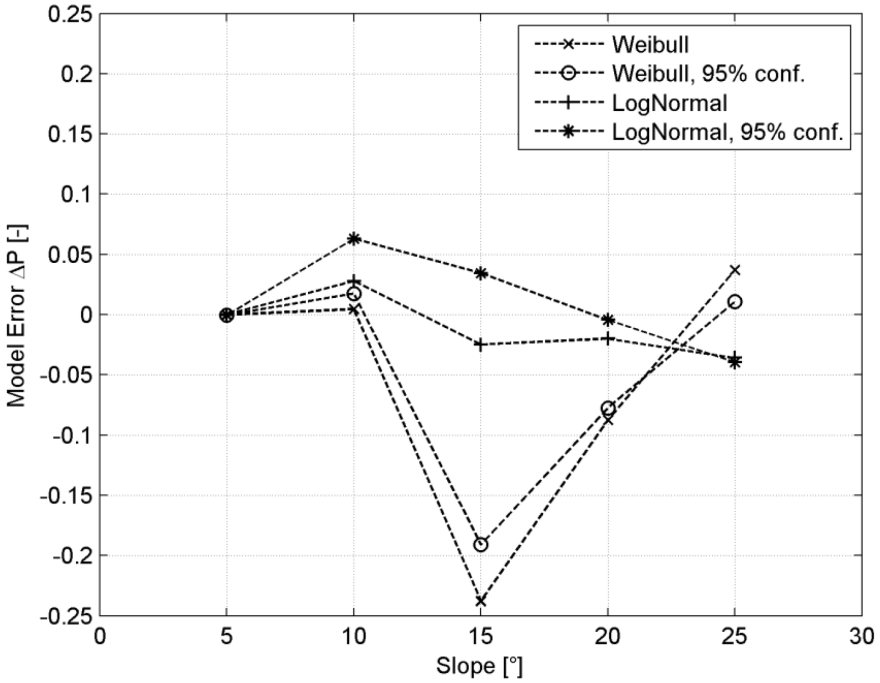

Figure 6-16 Curve fit estimation errors (refer also Table 6-6 below) for the Weibull and LogNormal-distribution: the graph confirms that the LogNormal distribution is the better choice to model the probability of an instable touchdown as a function of terrain slope

Slope [°]	Weibull		LogNormal	
	nominal	95% confidence	nominal	95% confidence
5	0.0000	-0.0003	0.0000	-0.0007
10	0.0047	0.0175	0.0278	0.0629
15	-0.2378	-0.1910	0.0247	0.0344
20	-0.0875	-0.0775	-0.0200	-0.0044
25	0.0370	0.0107	-0.0358	-0.0397

Table 6-6 Curve fit estimation errors for the Weibull and LogNormal model of an instable touchdown due to terrain slope

With the expressed goal of thesis to derive failure probabilities conditional to certain terrain property descriptors, the conclusion that the probability of an instable touchdown can be modeled as Log-normal distribution function with regard to slope is an important outcome. The mathematical and procedural methods to identify parametric models of the platform's behavior are thereby exemplary for the application to the other failure modes of such touchdown system. Its systematic application to the other touchdown failure modes is continued in the following section.

As it will be seen, not all LOF-exceedance probabilities relation to a terrain property descriptor can be described by a probability distribution such as done in case of the slope-dependent touchdown stability. To investigate if still a relation to slope or roughness exists, the data points are assessed

whether they follow an identifiable trend or if the underlying failure mode is independent from a terrain context. Therefore the following exponential magnitude-frequency-law is used:

$$\text{Trend:} \quad F_{\text{Trend}}(\vartheta) = a \cdot e^{b \cdot \vartheta} \qquad 6.21$$

$$\text{Regression:} \quad \ln\left(\hat{F}_{\text{Trend}}(\vartheta)\right) = \ln \hat{a} + \hat{b} \cdot \vartheta$$

The parameter identification for this function is treated identically as for the previously introduced probability distributions.

6.4 Application of the Analysis Scheme on the LEM-4C

This section sets forth the assessments on the LEM-4C's failure probability which have been started in the previous sections as exemplary cases. The analysis case LEM-4C-Sxx-F-R-L (Sxx = S05 … S25) used there is complemented now by further cases so that the following analysis plan is formed.

No.	Identifier	Slope [°]	Roughness [m]	Soil	Gravity [m/s²]
I	F-R-L	0/5/10/15/20/25	0 (flat plane)	rigid	1.62
II	F-S-L		0 (flat plane)	soft	
III	B05-R-L		0.5 (Boulder, 0.5m height)	rigid	
IV	C25-R-L		-0.4 to 0.1 (Crater, 25m diameter)	rigid	

Table 6-7 Analysis cases for LEM-4C: the cases are considered for a systematic investigation of the landing platform's reaction to varying terrain conditions. They basically consider varying slope, terrain roughness caused by boulder or crater and rigid or soft (granular) soil

The investigated case LEM-4C-Sxx-F-R-L acts here as reference. The analysis case LEM-4C-Sxx-F-S-L differs compared to the reference in the footpad-to-soil contact model which assumes now a soft, granular and regolith-type surface. The third case varies the terrain roughness by incorporating a boulder with a height h = 0.5m in the terrain surface mesh identically as described in chapter 7.3 and shown in Figure 7-9. The fourth case varies likewise the terrain roughness however by simulating a crater of diameter d = 2.5m as shown in Figure 7-9. All these four cases vary the terrain slope angle from 0° to 25° in 5° steps.

The analysis cases III and IV vary additionally the touchdown position at each sample in its sampling sequence to account for the very different contact conditions when hitting the terrain feature. Figure 6-17 shows a related position scatter plot belonging to LEM-4C-S00-B05-R-L. Each data point marks the touchdown position of the landing platform measured below the lander's center. The circular dispersion pattern is set up in a way that the zone of influence of that boulder is probed. A circle is superimposed to that plot outlining the boulder's circumference. Around one of the outer-most touchdown points another circle is drawn indicating the landing gear's footprint. The resulting contact conditions thus vary from "footpad on boulder" at initial or secondary contact or "lander body over boulder" to "no interference despite feature presence".

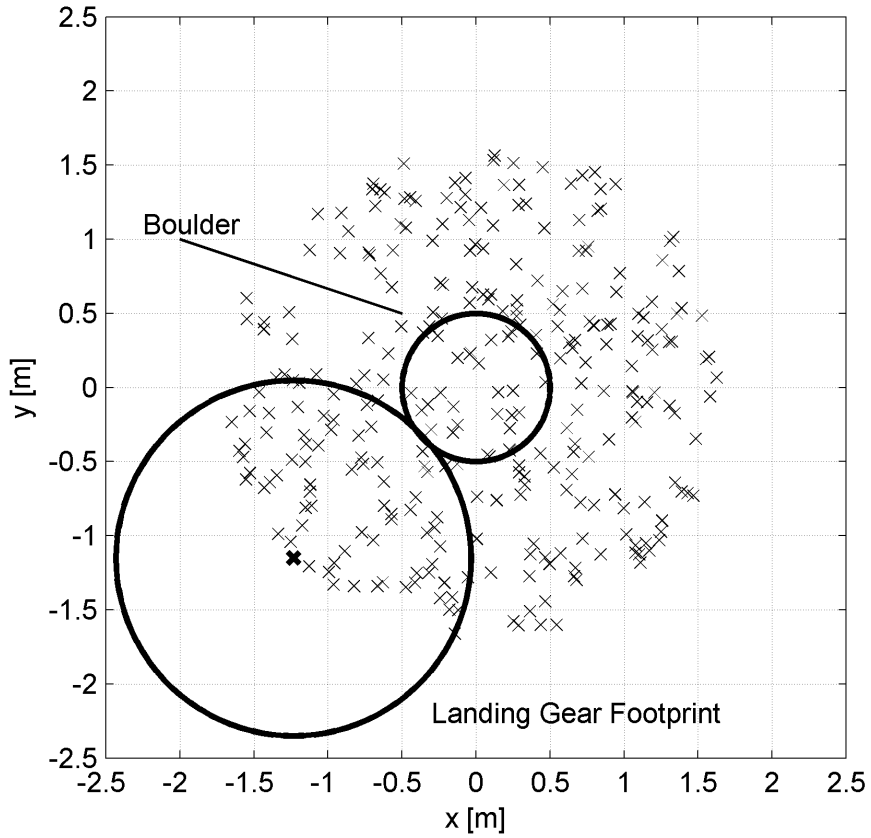

Figure 6-17 Touchdown positions with regard to terrain features (example LEM-4C-S00-B05-L): terrain features such as crater and boulder with a finite size and defined shape cause different contact conditions between them and the landing platform (e.g. a footpad touches down on a boulder or a touchdown occurs with a boulder "between the legs"). To consider these random conditions the touchdown positions are dispersed during a data sampling series. The radius of the position dispersion pattern is determined by the terrain feature size and the radius of the landing gear footprint. The size of this pattern is in this thesis defined as "sphere of influence" of that terrain feature (refer also to chapter 7.2 for further information and relevance of that definition).

6.4.1 Observations with regard to Landing Stability

The previous section has already shown on the basis of the LEM-4C-F-R-L case that the probability for an instable touchdown increases with a further increasing terrain slope. This section resumes this assessment with regard to landing stability by analysis the respective probability distributions also for the additional cases stated in Table 6-7. In Figure 6-15 the resulting log-normal distribution curves are shown together with the reference curve of the F-R-L case. The assumption of a soft, granular soil (case F-S-L) leads to a significant shift of the stability limit towards higher slope values. The cause of this shift is explained by the contribution of the soil to the overall dissipation of the touchdown energy. Regarding the influence of the terrain roughness from boulder or crater it can be stated that these features increase the variance of the distribution. In case of the boulder (case B05-R-L) this effect is however comparatively small and its associated curve remain quite similar as the reference case. The impact of the boulder on the stability boundary is thus small. This is contrary to the influence of the crater which causes a significantly larger variance. This further increases the probability of touchdown instability especially in the range of small slopes. As interim conclusion it can be stated that a

combination from terrain slope and crater-induced roughness means the most critical case with regard to touchdown stability.

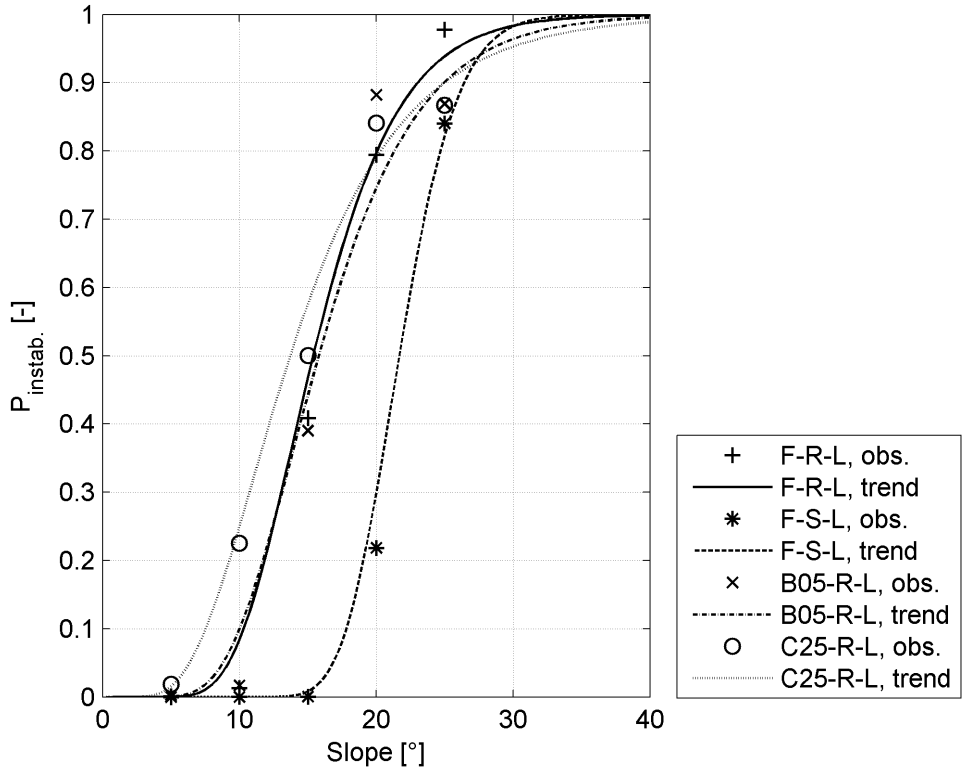

Figure 6-18 LogNormal curve fits to touchdown stability data from analysis cases I to IV for the LEM-4C. The data points ("observations") refer to the 95%-confidence values the sampling series results. All probabilities of an instable touchdown are shown as function of terrain slope and (not surprisingly!) these probabilities increase with steeper slopes. But they differ significantly when further terrain properties are varied: an instable touchdown is least likely on soft, granular soil (case F-S-L), it is most likely at shallower slopes and added crater caused roughness (case C25-R-L). The probabilities od instable touchdowns on rigid/flat (F-R-L) and added boulder roughness (B05-R-L) do not differ significantly from each other and are in a medium range.

6.4.2 Observations with regard to Ground Clearance

The correlation coefficient of the normal distribution based QQ-plot of the ground clearance data confirms this distribution function as suitable for the data sets involving a flat surface (cases F-R-L and F-S-L). Referring to this, Table 6-8 provides the correlation coefficient for the F-R-L case determined with the methods outlined in section 6.3.1. In addition to that the Figure 6-20 shows the associated empirical cumulative distribution functions.

Distribution	Normal	Log-Normal	Weibull
Correlation coefficient	0.986	0.942	0.984

Table 6-8 Goodness-of-fit of candidate distributions for ground clearance data

The probability to fall below the limit of function of $x_{gc,LOF} = 0$ is in this case $P(x \leq x_{gc,LOF}) = 10^{-20}$ which is a rather theoretical value. In order to assess the influence of the terrain slope the identified

mean and standard deviation values are plotted with respect to the slope values (Figure 6-19) instead of the LOF-probabilities. From this figure it can be taken that the expectation of ground clearance for a touchdown on soft, granular soil (F-S-L) is less than for the reference case on a hard surface which is caused by the yielding of the soil. Both cases have however in common the increase of the mean with higher slopes. The consequential loss of ground clearance is compared to the design value of $x_{gc} = 0.778$m, (Table 4-1) prior to energy absorber engagement.

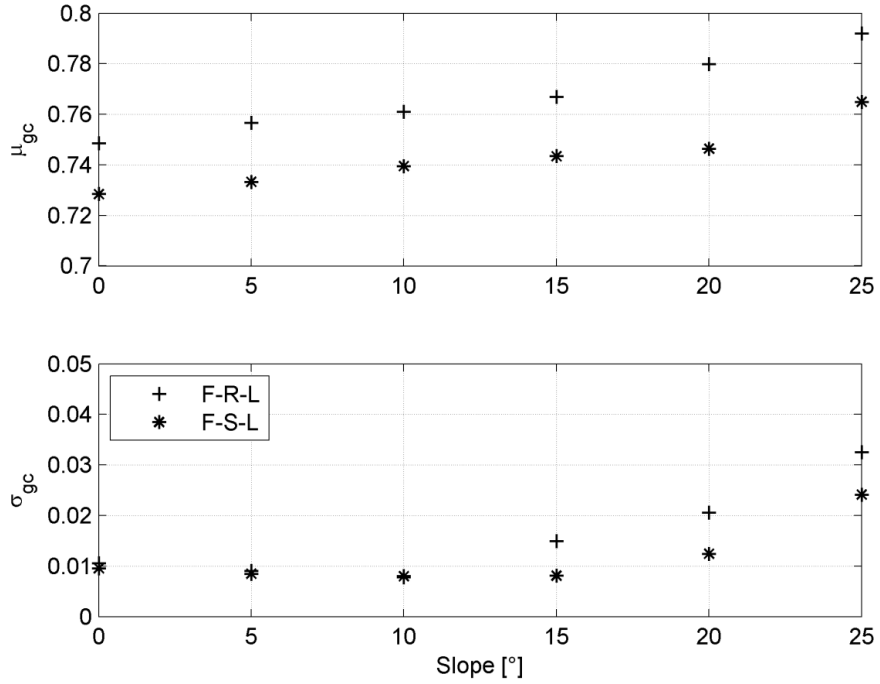

Figure 6-19 Slope dependence of the LEM-4C platform's ground clearance: the mean (top) and standard deviations (bottom) of the data sets are plotted over the slope value. The plot indicates that the ground clearance is least on zero degrees of slope. The ground clearance is further reduced by a touchdown on soft, granular soil (case F-S-L compared to F-R-L). The standard deviations do not differ in the relevant shallow slope range.

The lower ground clearance values at shallower slopes are explained by the higher relative frequency of touchdown configurations which bring all four legs simultaneously into surface contact (similar to test case 4, Table 4-2). This condition loads the secondary struts in their tension direction and the outward motion of the legs assembly lowers the lander body and effectively reduces the ground clearance. At steeper slope values the expected ground clearance exceeds the design value of $x_{gc} = 0.778$m. In parallel the standard deviation becomes slightly larger. Hereby touchdown cases take effect which are instable and never have ground contact with all four legs. Generally it can be stated however, that the standard deviation is relatively invariant to the surface slope. Up to this point it can be summarized that a soft, granular surface is the more critical case for a landing system's ground clearance.

The influence of terrain roughness generating terrain feature becomes evident through the analysis cases 3 and 4. Figure 6-20 shows therefore the empirical CDFs all four analysis cases for a slope of 0°. Especially the curve B05-R-L exhibits a shape which does not follow any parametric distribution function. The boulder-caused surface elevation deviation from the mean plane leads expectedly to reduction of the ground clearance while the crater-caused roughness both to an increase or reduction leads.

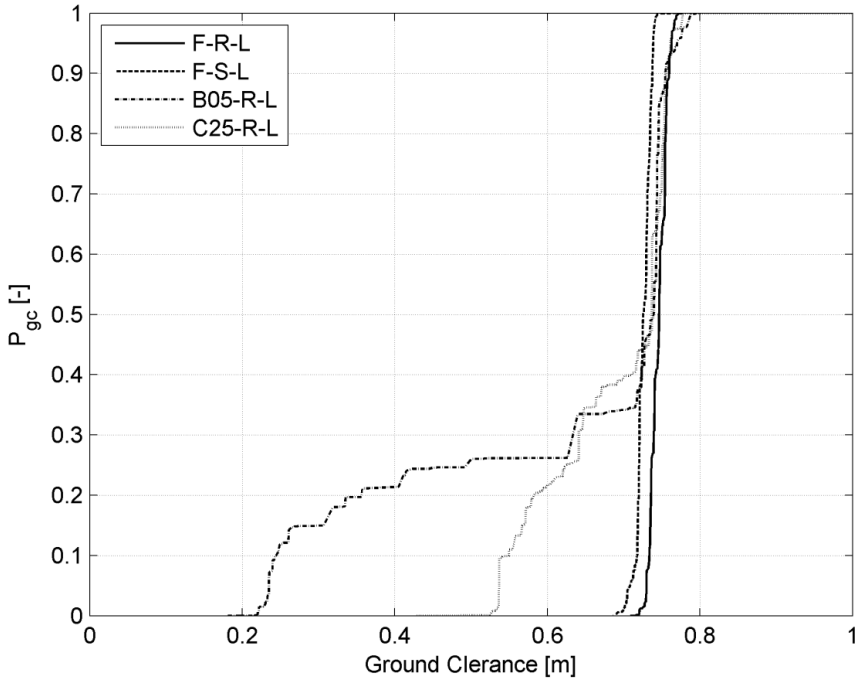

Figure 6-20 Empirical cumulative distribution functions for LEM-4C ground clearance data. The plot compares the effects the different terrain properties on a non-sloped surface: compared to the touchdowns on flat terrain (both F-S-L and F-R-L) a fraction of the touchdowns on the boulder and crater have a significantly reduced ground clearance (not surprisingly!). This reduction of clearance, however, matches the roughness value caused by this feature. The fractions of these further reduced values refer to the actual zones of influence of the terrain features. These findings are exploited in chapter 8 to calculate the actual probability for an unwanted contact between the platform's belly and the terrain

The CDF of the case B05-R-L matches quite well the curve of the reference case F-R-L however departs from this reference during ~33% of all touchdowns. The minimum remaining ground clearance is ~0.22m. This reduced clearance equals pretty exact the expected clearance with regard to the flat surface (F-R-L, $\mu = 0.748$m) minus the roughness value of the boulder ($h_{Boulder} = 0.5$m). The relative frequency is explained by the ratio of the area which is covered by the boulder's zone of influence and the area covered by the lander body. Figure 6-20 illustrates these relations. The interim conclusion is that the ground clearance value can be computed from the distribution with regard to a flat surface (the mean plane) minus the roughness value at that position whereas the touchdown on a soft, granular surface (see above) is the more constraining case.

6.4.3 Observations with regard to Landing Gear Strut Stroke

Primary Strut Stroke: Figure 6-21 plots the estimated probabilities to exceed the primary strut stroke limit as function of the terrain slope. The general impression is that the probabilities for all analysis cases are relatively independent to the terrain slope. The probabilities are thereby in a range of 10^{-3} and 10^{-2}. The variance of the data points is comparatively large in a range of one order of magnitude. The lowest probabilities are observed on a flat, rigid surface. Touchdowns on soft soil as well as crater or boulder tend to have higher probabilities. These are attributable to the added potential of blocking a sliding footpad. As the presence of small rocks or other small surface undulations cannot be excluded either by remote sensing data or by hazard detection and avoidance system during terminal landing, the dimensioning analysis case must consider roughness generating features.

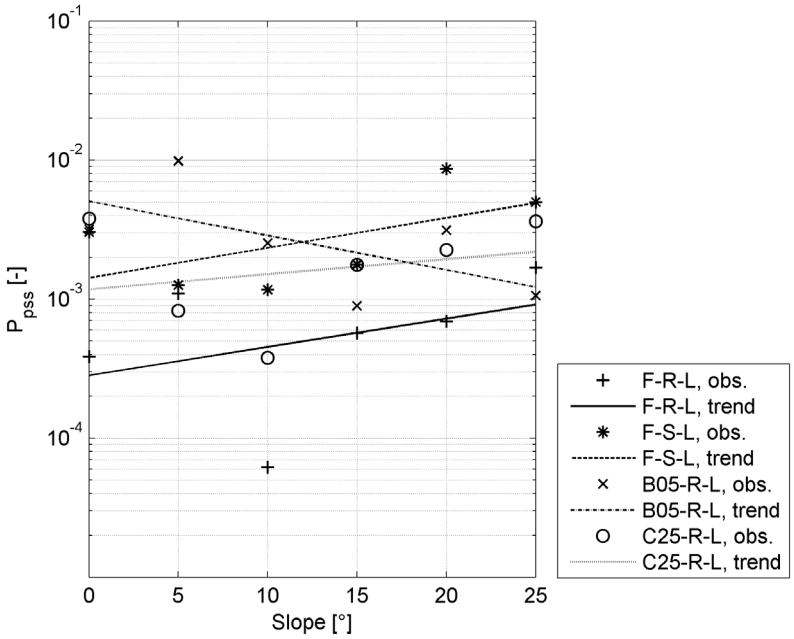

Figure 6-21 Probability to exceed the primary strut stroke limit of the LEM-4C. The data points ("observations") refer to the 95%-confidence values the sampling series results: The general impression is that the probabilities for all analysis cases are relatively independent to the terrain slope and no probability distribution is identifiable. The variance of the data points is comparatively large in a range of one order of magnitude. The lowest probabilities are observed on a flat, rigid surface (case F-R-L) and highest on boulder terrain (case B05-R-L).

Secondary Strut Stroke: Similar graphics (Figure 6-22, tension stroke and Figure 6-23, compression stroke) show the curves related to the secondary strut stroke. The probabilities to exceed the compression or tension stroke limits are likewise in an order of magnitude of 10^{-4} to 10^{-2}. The only exception is the touchdown case on soft soil which is both in tension and compression direction lower. It is however evident that a small dependency to the terrain slope exists for both stroke directions. With a steeper slope the probability to exceed the tension stroke direction decreases from ~10^{-2} to ~10^{-4}. In parallel it increases by the same order of magnitude for the compression stroke direction.

The observations are consistent with the experimental investigations (Chapter 5.2.4) whereas test case 4 confirmed that a touchdown on unsloped surface (accompanied by attitude angles of zero) is more critical for the tension stroke direction while touchdowns on a non-zero slope surface tend to yield in the compression stroke direction. For the same reason the least remaining ground clearance was observed on shallow slopes. Thus a higher probability to exceed the tension stroke limit and the reduced ground clearance on a flat surface are correlated to each other. The effect of a crater or boulder presence is as for the primary strut stroke a slight increase in the probability to exceed the stroke limit.

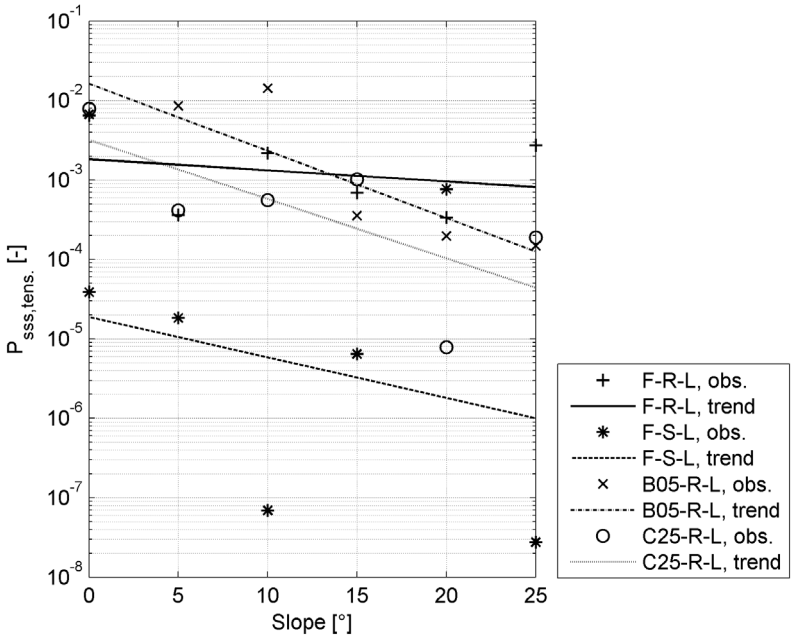

Figure 6-22 Probability to exceed the secondary strut tension stroke limit of the LEM-4C. The data points ("observations") refer to the 95%-confidence values the sampling series results: again the dependency on the terrain slope is comparatively small. No probability distribution but yet a clear trend is identifiable. The probabilities to exceed the tension stroke limit tend to decrease with higher slopes. They are highest for a touchdown on shallow, soft (granular) terrain.

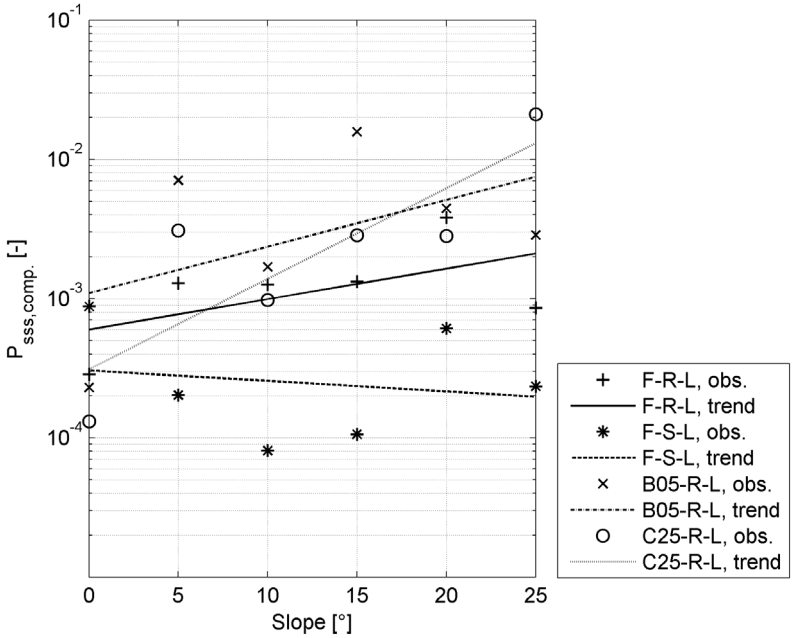

Figure 6-23 Probability to exceed the secondary strut compression stroke limit of the LEM-4C. The data points ("observations") refer to the 95%-confidence values the sampling series results: again the dependency on the terrain slope is comparatively small. No probability distribution but yet a clear trend is identifiable. The probabilities to exceed the compression stroke limit tend to increase with higher slopes (no clear statement can be made on the case F-S-L). On the relevant shallow sloped terrain, they are highest for touchdowns on boulder covered terrain.

7 Landing Site Characterization

In a touchdown event the shape and surface conditions of the landing site determine significantly the touchdown dynamics of the landing system. Consequently, the characterization of the landing site is of high importance. The development of the landing site assessment (see the brief overview in chapter 1.1) in more than 40 years of planetary exploration has already shown that high resolution image data is indispensable for the necessary characterization. Such a task is a domain of the planetary geodesy and one important means to do so is the representation of the terrain by a Digital Terrain Model (DTM). A DTM basically stores terrain elevation data in a raster or gridded data format. Processes and tools to generate and evaluate DTM's have already a solid foundation in Earth-based and extraterrestrial applications. In the following sections, its generation is only briefly outlined and the subsequent introduction of the algorithmic DTM evaluation is restricted only to terrain properties with relevance for the mechanical interaction which are the slope and roughness of the terrain.

7.1 Data Product Genesis

Remote sensing instruments used for this purpose are active or passive imaging sensors which measure the direction and intensity of the radiation reflected by the planetary surface (*Albertz 2007*). Passive, photographic type sensors rely on the sun light reflected from the planetary surface. The reflective properties of the terrain depend on its material composition, microscopic surface roughness and the angular relations between the sun, the terrain surface and the receiver. The differences in the reflectivity allow thus a discrimination of surface features. State-of-the-art imaging systems belong to the group of line scanners, which scan the surface underneath the orbit's trajectory with a sensor (CCD) where the pixels are arranged in a line. This scanner geometry is depicted in Figure 7-1. The Mars Reconnaissance Orbiter's High Resolution Imaging Experiment (HIRISE) belongs to this class of cameras. It is described in *McEwen et al. 2007*, and achieves surface resolutions of ~0.3m/pixel. Its role in down-selecting Martian landing sites has been already mentioned in the first chapter of this thesis.

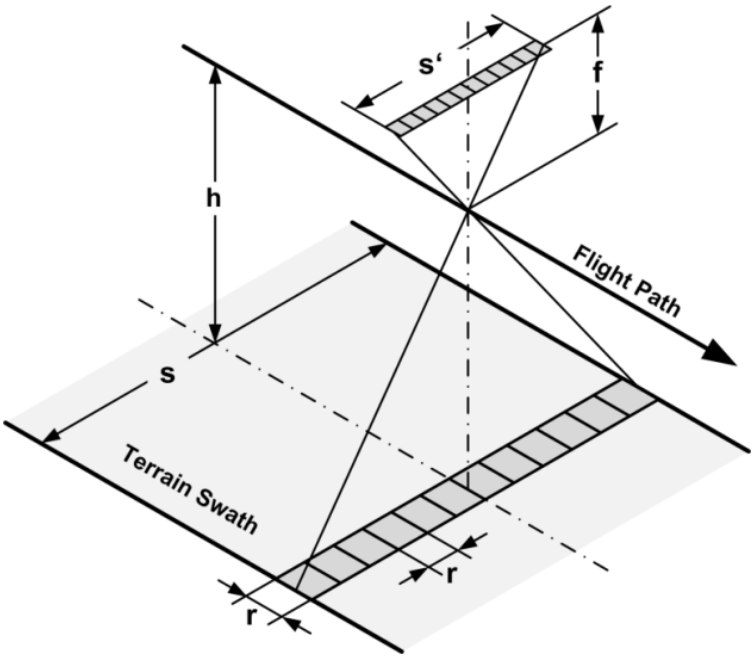

Figure 7-1 Schematic image acquisition by a line scanning camera, redrawn from *Albertz 2007*. The resolution r per pixel is thereby determined by the orbit altitude h and the focal length f.

The path from the measured raw data to a digital terrain model then requires several processing steps. First the raw data received from the space segment are brought into a decompressed format (a level 1 product). Then several corrections are applied to the data including radiometric and geometric calibrations. This level 2 considers already the spacecraft position and orientation allowing an assignment of image pixel to geodetic coordinates of the planetary body. The projection of a three-dimensional object onto a two-dimensional receiver plane inevitably leads to distortions including parallaxes effects of different terrain sections. Its correction requires apriori information on the true shape of that terrain section. Such terrain elevation data is typically provided by laser altimetry: active ranging systems emit a signal and measure the time of flight of the reflected signal, which allows determining the distance to the surface. Knowledge of the spacecraft's position enables a reconstruction the three-dimensional terrain profile. The correction of the terrain shape induced image distortions using such digital terrain model (DTM) lead to an ortho-rectified or level 3 data product. Laser altimetry derived DTM have typically a resolution of several meter or coarser and are consequently not sufficient to identify potential hazardous terrain features on a lander scale level. This situation can be improved using stereo-imaging techniques. Stereo image pairs can be either obtained from different orbits with overlapping camera swath or directly by dedicated stereo-cameras such as the HRSC camera described by *Scholten et al. 2005*. The subtle differences in the parallaxes of the same terrain section when imaged from different positions however provide a starting point to reconstruct the depth information. The production process towards a DTM generated from stereo image pairs starts with a pre-rectification of the individual images. This step makes again use of the laser altimeter data based DTM. Subsequently, the images are matched through the identification of conjugate points in both images. The same points on the surface, observed from different and known orbit positions, allow the reconstruction of the depth information in the image. The transformation of the three dimensional coordinates into planetary body fixed latitude, longitude, and height values and further suitable map projection complete the processing chain. The ortho-rectification step can be repeated to improve the ortho-image reconstruction using the yet obtained high resolution DTM. Data products involving such deeper processing are so called level 4 products (the full description of this process is found in *Scholten et al. 2005*). With image resolutions in the sub-meter range the required DTM resolution in the lander scale range can be obtained.

Such DTM and ortho-image generation, specifically with regard to the lunar case, is described in *Oberst et al. 2010*. The underlying lunar image data products were generated by the Lunar Reconnaissance Orbiter Camera (LROC) delivering images with a resolution of around 0.5m (*Robinson et al. 2010*).

As an example, the DTM for a landing site candidate – named the "Connecting Ridge" – for the ESA Lunar Lander is shown based on data from the Near Angle Camera (NAC). The data set, covering an area of 5 x 5 km² at a resolution of 2m/px, has been produced for ESA and is published by *Scholten et al. 2012*. The mission context for this site is provided later in chapter 8.1 as part of the case study. Figure 7-2 shows this DTM as a shaded relief (left) and the associated ortho-image (right). It is noteworthy that this ortho-image is a mosaic of several images. This Lunar South Pole region is characterized by pronounced shadowed zones due to the low sun elevation throughout the year (*De Rosa et al. 2012*) which makes it necessary to cover the landing site candidate with images taken during the seasonal variations of illumination. Some permanently shadowed zones however remain and prevent the derivation of its depth information. These areas appear as void (here black colored) spaces in the DTM shaded relief. This Connecting Ridge data set is used in the following as example data set to demonstrate the application of the slope and roughness determination algorithm.

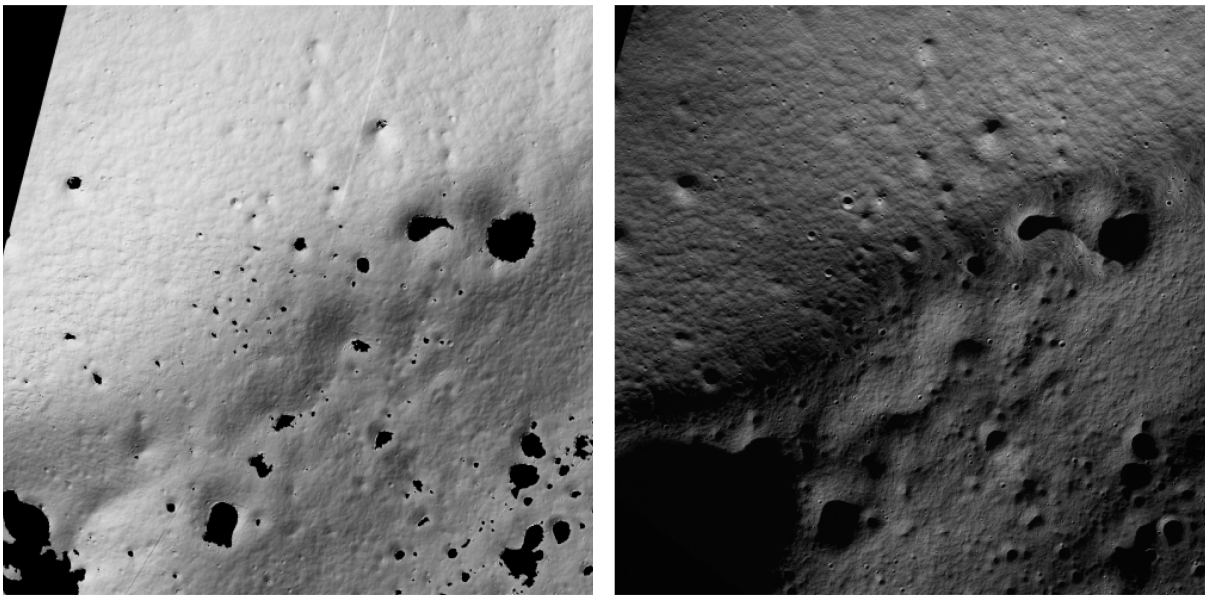

Figure 7-2 LRO Near Angle Camera based DTM (left) and image mosaic (right) of the Lunar South Pole landing site candidate "Connecting Ridge", taken from *Scholten et al. 2012*

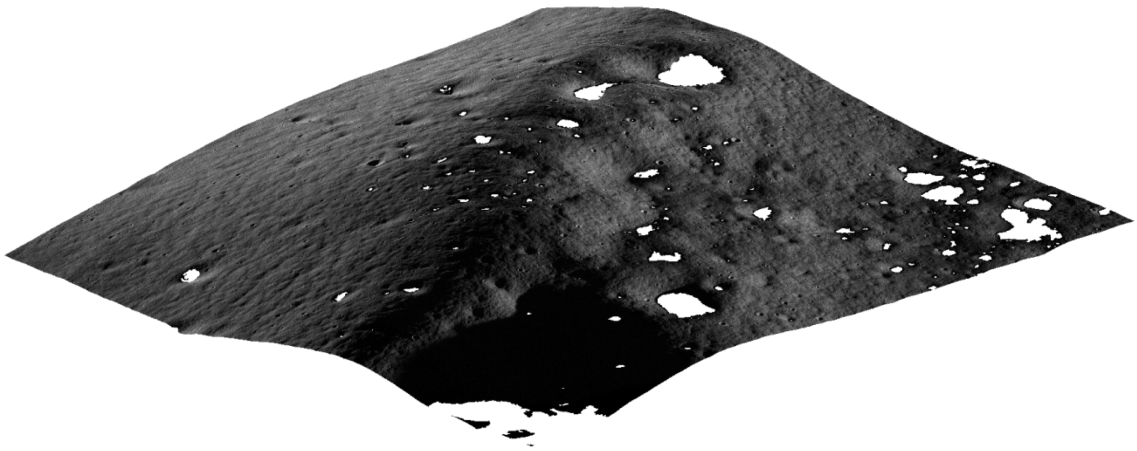

Figure 7-3 Combined view of "Connecting Ridge" – an overlay of the ortho-image on the digital terrain model

7.2 Terrain Slope and Roughness Determination

Terrain properties potentially hazardous to the landing platform are the terrain slope and its roughness. They significantly influence the mechanical contact at touchdown between the planetary surface and the landing system. Slope is hereby defined by *Johnson et al. 2002* as "the angle between the robust plane normal vector and the gravity vector" or by *De Rosa et al. 2012* as "the inclination relative to the local horizontal of the mean plane". The robust or mean plane is thereby the least error fit to the terrain surface underneath the landing system footprint. Roughness is defined as "the deviation from the mean plane and as such is a property of each point of the terrain below the lander …" (*De Rosa et al. 2012*) or the "difference between the robust plane and the elevation map" (*Johnson et al. 2002*). Roughness is thus the terrain undulation on a base length shorter than the landing gear footprint. Figure 7-4 illustrates the definitions.

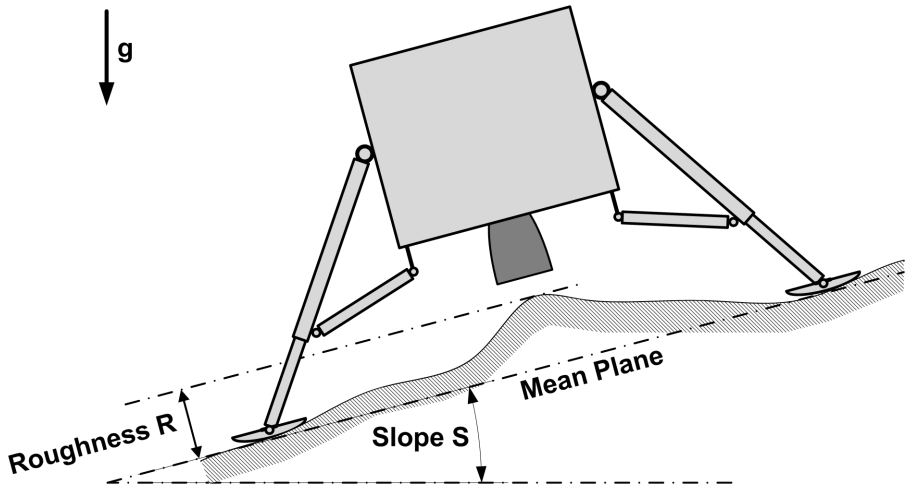

Figure 7-4 Definition of terrain slope and roughness: slope is the inclination of the mean plane compared to the local horizon; roughness is the deviation of the actual terrain to the mean plane

The process of the terrain characterization involves the following steps. First the area of interest is subdivided into smaller sections. Then for each grid element the slope and roughness values are determined by a moving window filter (Figure 7-5) and are stored in a respective terrain property matrix. The window covers n×n grid nodes with $n = \lceil d_{FP}/r_{DTM} \rceil$ being the next odd natural number determined by the landing gear footprint d_{FP}, the distance between two opposite footpads, and by the DTM resolution r_{DTM}.

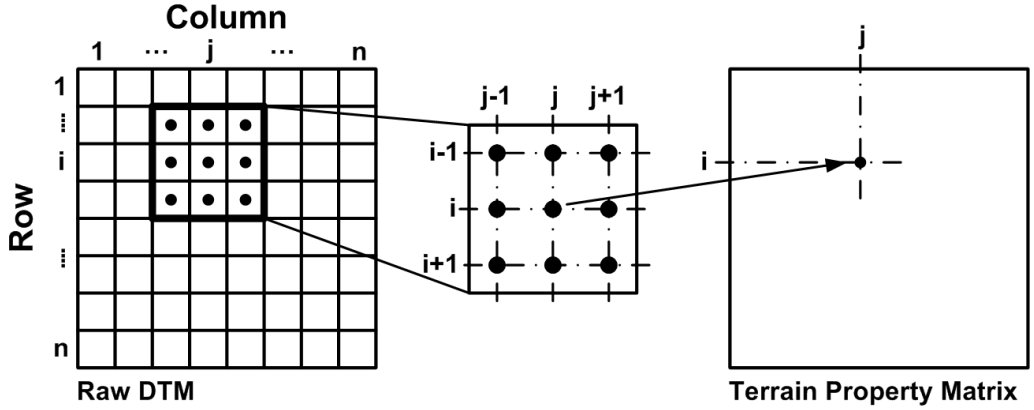

Figure 7-5 Moving window filter concept: a window of size n×n defined by the landing gear footprint is moved pixel-by-pixel across the DTM. The slope and roughness values for the terrain section covered by the window are derived and stored in respective matrices

As next step, the mean plane must be estimated in order to separate the two terrain properties from the DTM. This can be done by a bi-linear regression analysis of the neighboring grid points in the window. This assumes that the errors of the single data points are Gaussian. Least square methods minimize the residual errors when fitting a mathematical model to the sample data. As the square of the error significantly affects the parameter estimate, these estimation techniques are not robust to non-Gaussian outliers. Standard scientific and engineering statistics consider outliers typically as gross errors. In the analysis case of this work they can be also attributable to terrain features contributing to the terrain undulation according to the definition of terrain roughness. Therefore a more extensive treatment than just a regression approach is needed.

An algorithmic outlier classification implemented in the terrain data filter requires a computer implementable definition of an outlier which is checked for all data points versus a threshold. A very

robust method is known as RANSAC algorithm (Random Sample Consensus, *Caspary 2013*) which separates data points into a model conforming set and an outlier set. *Johnson et al. 2002* refers also to this method as a means to do real-time hazard detection from LIDAR scanning data during the terminal descent in a planetary landing. The original random-sample RANSAC concept thus assumes an unstructured point cloud as input stemming from such a scanning device. Its application on a DTM with an already defined grid allows thus a deterministic approach using predefined triangles. This is illustrated in Figure 7-6: out of this 3 × 3 node set N = 12 triplets are taken each defining a triangle. This thesis accordingly modifies the original random sample concept into a deterministic version and implements it into the filter concept.

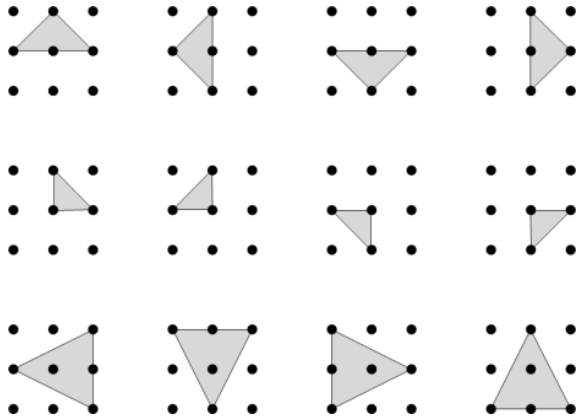

Figure 7-6 Data grid triplets for the robust plane search: 12 planes determined by pre-defined triplets are assessed whether they best fulfill a quality criterion and can be taken to further estimate a robust mean plane and to identify outliers within that moving window

The three corner points of each triangle span a plane whose parameters are determined. Then the distance between a plane and all further nodes in the set is determined. The median of the squared distances is taken as a quality criterion as suggested by *Johnson et al. 2002*. According to *Caspary 2013*, each of the triangles means a hypothesis that its data points represent the best of all planes according the quality criterion. Consequently, the plane yielding the least median of the squared distances is taken as a best references plane for the outlier detection. All points whose absolute deviation e_i from the reference plane is larger than the standard deviation σ_w of all n^2 nodes in the window are classified as outliers. The probability P to find a set free of outliers is estimated according equation 7.1 (its derivation is shown in *Caspary 2013*). The parameter ε represents the ratio of outliers to number of nodes in the data set. The worst case ratio is $\varepsilon = (n^2-1)/2n^2$. As an example, for $n^2 = 9$ data points and ε = 0.44 the likelihood to identify a sub-set free of outliers is still 89.5%.

$$P \approx 1 - (1 - (1 - \varepsilon)^3)^N \qquad 7.1$$

The set of inliers $\mathbf{x} = \{x_i \mid e_i < \sigma_w\}$, **y** and **z** accordingly, is used for a least square fit to identify the mean plane according the definition above. Each position x_i, y_i, z_i of a node of the inlier set shall satisfy a bi-linear equation of the form as given by equation 7.2.

$$z_i = \hat{g}_x \cdot x_i + \hat{g}_y \cdot y_i + \hat{b} \qquad 7.2$$

A bi-linear regression estimates the gradients g_x and g_y and the intercept b of this plane. Therefore linear equations for every node in the inlier set are brought into a matrix notation.

$$\underbrace{\begin{pmatrix} z_1 \\ \vdots \\ z_\eta \end{pmatrix}}_{\mathbf{z}} = \underbrace{\begin{pmatrix} x_1 & y_1 & 1 \\ \vdots & \vdots & 1 \\ x_\eta & y_\eta & 1 \end{pmatrix}}_{\mathbf{X}} \cdot \underbrace{\begin{pmatrix} \hat{g}_x \\ \hat{g}_y \\ \hat{b} \end{pmatrix}}_{\mathbf{k}} \qquad 7.3$$

The vector **k** is thereby the least-square estimator for the plane's gradients and intercept.

$$\mathbf{k} = (\mathbf{X}^{\mathrm{T}}\mathbf{X})^{-1}\mathbf{X}^{\mathrm{T}}\mathbf{z} \qquad 7.4$$

The estimator for the variance of g_x, g_y and b are derived from the diagonal of the covariance matrix (eq. 7.5). An estimator of the variance $\hat{\sigma}^2$ of the residual errors is given by equation 7.6. In that latter equation η is the number nodes in the inlier set and φ is the number of parameter describing the plane, thus φ = 3.

$$\mathrm{Var}(\mathbf{k}) = \hat{\sigma}^2 \cdot \mathrm{diag}(\mathbf{X}^{\mathrm{T}}\mathbf{X})^{-1} \qquad 7.5$$

$$\hat{\sigma}^2 = \left(\mathbf{z}^{\mathrm{T}}\mathbf{z} - \mathbf{k}^{\mathrm{T}}\mathbf{X}^{\mathrm{T}}\mathbf{z}\right)/(\eta - \varphi - 3) \qquad 7.6$$

In scalar notation the variance of the gradients (eq. 7.5) is $\sigma_g^2 = \sigma_{gx}^2 = \sigma_{gy}^2$ and is used subsequently to derive the variance of the terrain slope. The estimation of the terrain slope is yielded by a conversion of the gradient information through equation 7.7. The slope's variance is then described by equation 7.8 as a function of the gradient's variance and the slope. This approach has been described in full detail by *Zhou 2008*. Its description here is limited to a brief outline of the method.

$$\hat{S} = \arctan\sqrt{(\hat{g}_x^2 + \hat{g}_y^2)} \qquad 7.7$$

$$\hat{\sigma}_S^2 = \hat{\sigma}_g^2 \cdot \cos^4\hat{S} \qquad 7.8$$

As already defined earlier, terrain roughness is the difference of the measured elevation z_i of node i and the elevation of the mean plane $z_{0,i}$ at this node. The position p^* of the roughness value dominating the area underneath the landing platform is determined by the following equation.

$$p^* = \mathrm{argmax}_{p\epsilon\{m\}}\left(|z_p - \hat{z}_{0,p}|\right) \qquad 7.9$$

This determination requires a classification of data set points within and outside the landing system's footprint. The set {m} contains all nodes within the footprint of the landing gear such as shown in Figure 7-7 (left) as solid dots.

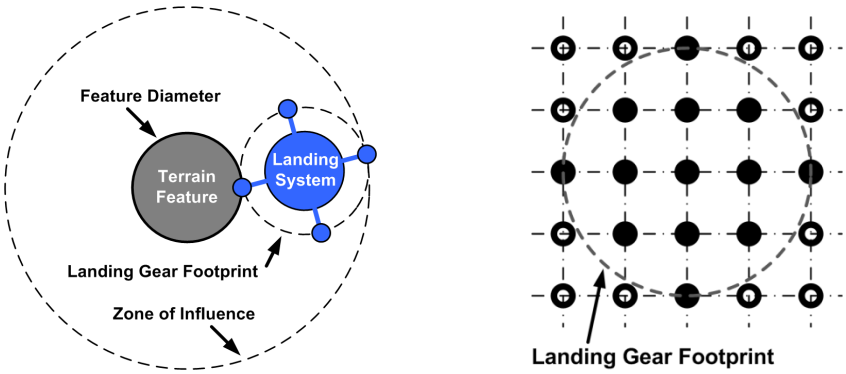

Figure 7-7 A terrain feature's zone of influence: this zone is defined in this thesis as the area in which an interaction between the roughness causing terrain feature (boulder, crater or else) can occur. Its radius is determined by the feature's radius and the landing gear footprint (left figure); to consider this during the DTM processing for roughness estimation only pixel of the moving window within this footprint radius are considered as potential rough points. The right figure indicates these points as solid dots within an exemplary 5×5 window.

The estimate of the dominating roughness value is then taken at the data point indexed as p^* (eq. 7.10). The convolution of the filter window with the undulation caused by a terrain feature has the effect that its dominating roughness value is assigned to all grid nodes in a zone with a radius of the feature's

radius plus the landing gear diameter (Figure 7-7 right). The zone is called here the "zone of influence" of that feature.

$$\hat{R}_{p^*} = z_{p^*} - \hat{z}_{0,p^*} \qquad 7.10$$

The expectation of the mean plane at point p^* on the plane is given by the following equation.

$$\hat{z}_{0,p^*} = \hat{g}_x \cdot x_{p^*} + \hat{g}_y \cdot y_{p^*} + \hat{b} \qquad 7.11$$

Complementary, the variance for that particular point is formulated by equation 7.12 with $\mathbf{x}_{p^*} = \{x_{p^*}, y_{p^*}, z_{p^*}\}$.

$$\sigma_{z0}^2 = \mathbf{x}_{p^*}^T \left(\mathbf{X}^T\mathbf{X}\right)^{-1} \mathbf{x}_{p^*} \cdot \sigma^2 \qquad 7.12$$

The variance of the roughness measurement is the added variance of the elevation of the mean plane at the point where the roughness value is taken and the variance of the measured elevations according to equation 7.6.

$$\hat{\sigma}_R^2 = \left(1 + \mathbf{x}_{p^*}^T \left(\mathbf{X}^T\mathbf{X}\right)^{-1} \mathbf{x}_{p^*}\right) \cdot \hat{\sigma}^2 \qquad 7.13$$

The estimates for the terrain slope (eq. 7.7), its variance (eq. 7.8) as well as the terrain roughness (eq. 7.10) and its variance (eq. 7.13) are the outputs of the presented algorithm when applied to a high resolution DTM.

7.3 Algorithm Verification

In this work the algorithms, briefly introduced in the previous section, have been implemented and coded using the scientific computing language MATLAB. The implementation has been verified by using two different cases: (i) a simple 2-dimensional (2D) example and (ii) a more realistic 3D example using parameterized models for crater and boulder.

2D verification case: Five arbitrarily chosen data points with spacing of 2m provide a reference or ground truth terrain model. Its true elevation is composed by a linear equation with some superimposed variance and an additional roughness value (a "boulder") at the position x = 2m. The associated parameters are given in Table 7-1 in the column "Ground Truth Reference Data". The resulting elevation data set is shown in Figure 7-8. Next, the mean plane was determined using the least square method without prior outlier detection. The result is shown as dashed line in Figure 7-8 and its estimated parameters are also given in Table 7-1. It is obvious that without outlier detection the slope of the mean plane is over-estimated (7° instead of 5°), the roughness value is under-estimated (0.42m instead of 0.56m) and the standard deviation is again over-estimated with 0.26m instead of 0.1m.

With enabled outlier detection however, the data point representing the "boulder" is classified as outlier and disregarded during the least square estimate of the mean plane. The estimates improve with regard to the slope value to 5.3° versus 5°, 0.6m versus 0.56m (roughness) and 0.12m instead of 0.1m regarding the standard deviation.

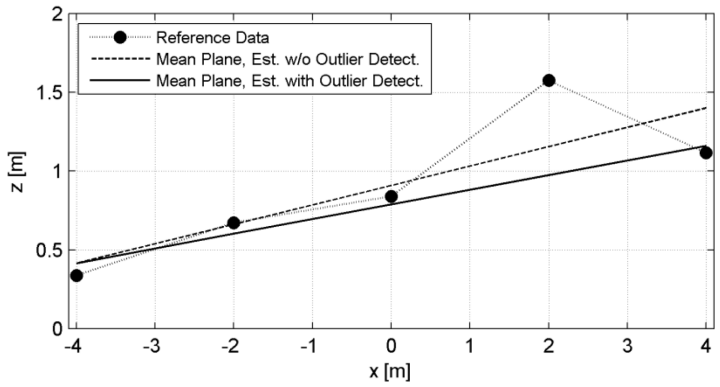

Figure 7-8 Algorithm verification – 2D example: 5 data points are taken as elevation data with a resolution of 2m/px („reference data" assuming a given terrain slope and a rough feature). Mean plane estimates with and without outlier detection are plotted in addition. The processing with outlier detection clearly identifies the rough feature and nearly matches the reference mean plane (refer also Table 7-1 below)

	Ground Truth Reference Data	Estimate w/o Outlier Detection	Estimate with Outlier Detection
Slope [°]	5.0	7.0	5.3
Roughness [m]	0.56	0.42	0.60
1σ-Error [m]	0.10	0.26	0.12

Table 7-1 Algorithm verification – 2D example – estimated versus true properties

3D verification case: While the terrain property "slope" is unambiguously defined as the inclination of the mean plane with respect to the gravity vector, the case for the terrain property "roughness" is less clear. Roughness, defined as deviation from the mean plane, can be caused by many different geological processes. Besides this measurable deviation roughness is also characterized by a certain shape associated with its geological nature. Therefore generic models for craters and boulders are introduced to investigate their impact on the terrain property estimation as they are most prominent sources of roughness.

Pike 1977 has shown that the size and shape of simple, bowl-shaped crater depend only from the kinetic energy of the impacting body, but – unlike complex crater – not from the gravity of its planetary target body. The forming of the crater bowl and rim follows a self-similar pattern. The rim height and the depth of the bowl can be mathematically described as a fraction of the crater diameter. It shall be noted here that Pike describes these relations in *Pike 1977* as power law, but in the case of small, simple crater the exponent of the diameter d is nearly one. These resultant simplified dimensions are given in Figure 7-9 (top). The total crater depth, for example, is ~20% of its diameter. The slope of the outer rim is approximately $s \sim \arctan(0.04 \cdot d / 0.4 \cdot r) = \arctan(0.2) \cong 11°$ independent of the crater diameter. Similarly, the slope of the inner rim is ~ 30°, which approximates the natural angle of repose.

The model approach for boulder is analogous and is based on the observation that boulder attain an orientation which has the lowest potential energy when being at rest on the surface. They consequently rest on the side with the shortest semi-axis. In addition they are frequently partially buried in the soil. Following the suggestion of *Bernard 2001* they are modeled here as half-spheres (Figure 7-9 bottom) with a height-to-diameter ration of h/d = 0.5.

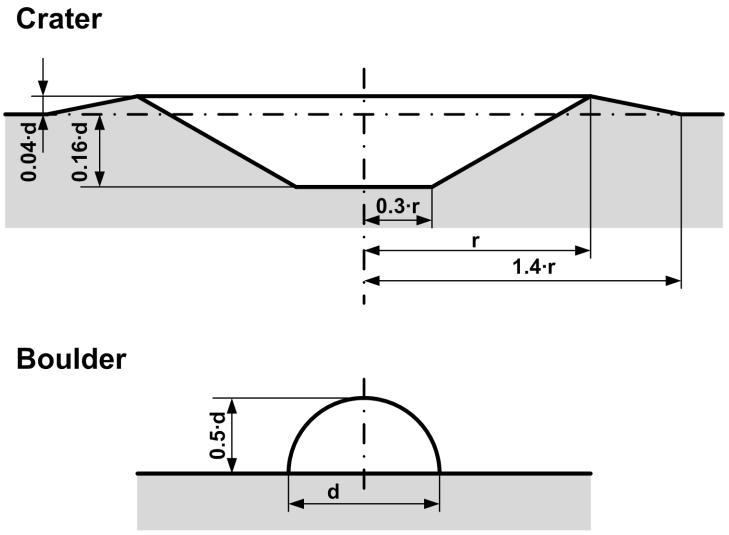

Figure 7-9 Generic terrain feature models: simplified and parameterized models for a crater (top) and boulder (bottom) are used to generate reference 3D terrain data for the algorithm verification

A crater model with a diameter of d = 2.5m is depicted in Figure 7-10 (right) as mesh grid with a resolution of 0.25m. This particular crater diameter is chosen as it approximately equals the landing gear footprint of the lander engineering model LEM-4C. Similarly, a boulder with a diameter of d = 1m is shown in Figure 7-10 (left). These generic DTM are used in the following part as ground truth reference to verify again the performance of the algorithm under particular consideration of crater and boulder caused roughness. These models are used in chapter 3.3 again as terrain surface representation in the multibody simulation model in order to directly investigate its influence on the touchdown dynamics. For that purpose they are read into the numerical multi body simulation as surface mesh.

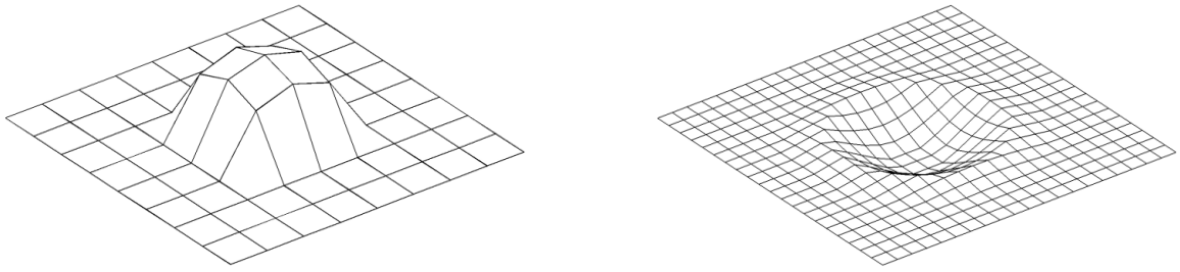

Figure 7-10 Algorithm verification – 3D examples for a boulder (left) and a crater (right)

The result of the application of the algorithm on the boulder model is shown in Figure 7-11. The area of influence of the boulder is assigned with a value of R = 0.5m according to the definition of roughness underneath the lander's landing gear footprint. The ambient terrain is not sloped and the algorithm correctly estimated it as zero. The roughness contribution of the boulder is thus separated from the slope contribution of the terrain as intended.

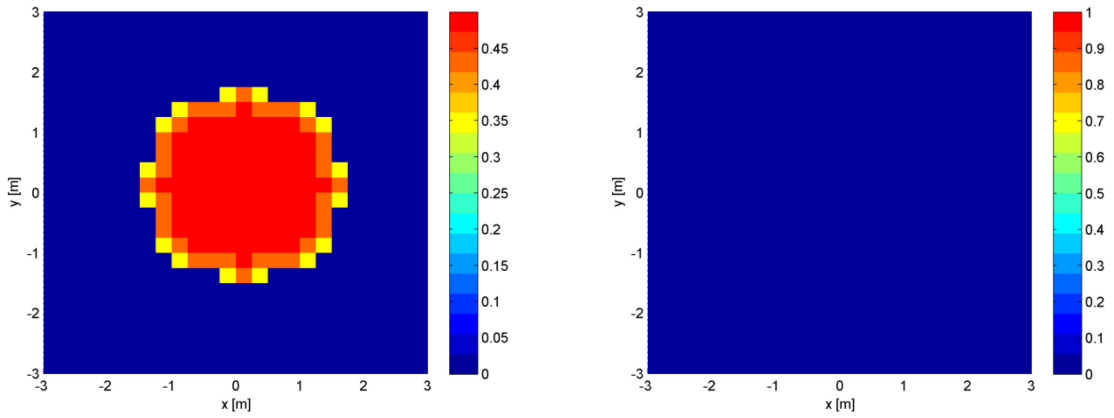

Figure 7-11 Estimation results from algorithm application on the boulder model, left: roughness [m], right: slope [°]

The application of the algorithm on the crater model is shown in Figure 7-12 in a similar way. The crater rim causes a positive roughness value, meaning it reduces the potential clearance between the terrain and the lander body at this respective position. The roughness value becomes negative insight the crater as the crater size matches the landing gear footprint which allows only for a partial but not full landing inside the bowl. For this reason the resulting slope values are smaller than the 30° of the inner rim.

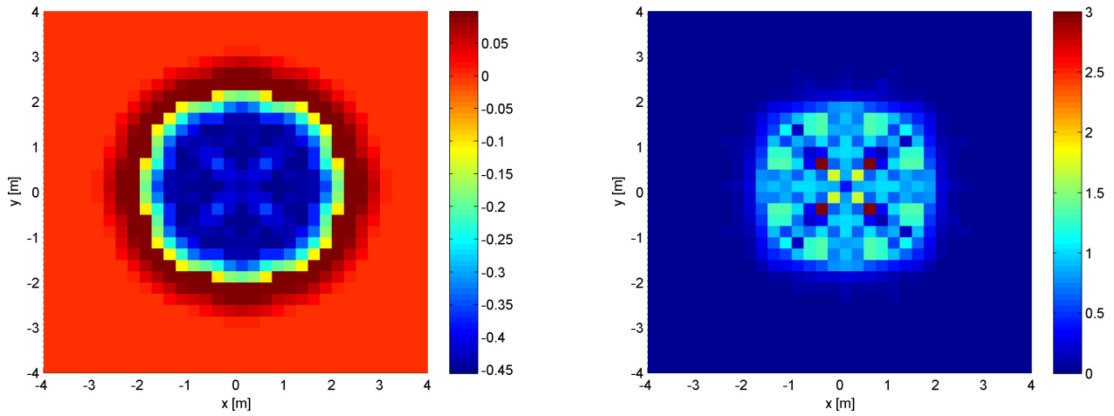

Figure 7-12 Estimation results from algorithm application on the crater model, left: roughness [m], right: slope [°]

7.4 Slope and Roughness Estimates for the Lunar South Pole site »Connecting Ridge«

The final section of this chapter provides the results of the algorithm application on the "Connecting Ridge" terrain model. The maps are given in the same polar stereographic projection as its source DTM. Figure 7-13 shows the expected mean slope according equation 7.7 for a landing gear footprint of 5.5m. This landing gear footprint refers to the medium sized robotic landing system introduced in chapter 8.1 as part of the case study. The roughness map is presented in a similar way in Figure 7-14 showing the expected values according equation 7.10. The visual inspection of this map indicates a few data artifacts appearing as straight lines of increased roughness values (e.g. in the upper right map quadrant). These artifacts coincide with the butt joint between adjacent source images and are caused by an insufficient image match. Likewise the edges of the data gaps are characterized by a similar

roughness value pattern which is here attributable to the transition into the permanently shadowed and thus no-data region.

Additional statistical information (Figure 7-15) reveals the frequency distribution of the slope and roughness magnitudes. These viewgraphs for example indicate that 90% of the Connecting Ridge area is characterized by slopes shallower than 20°. Similarly 90% of the roughness values are found between ~-0.3m and ~+0.2m. Figure 7-15 provides additionally magnitude-frequency distributions for the standard deviations associated to the expected slope and roughness values. 90% of the slope standard deviations are less than 0.28° whereas 90% of the roughness standard deviations are 0.07m.

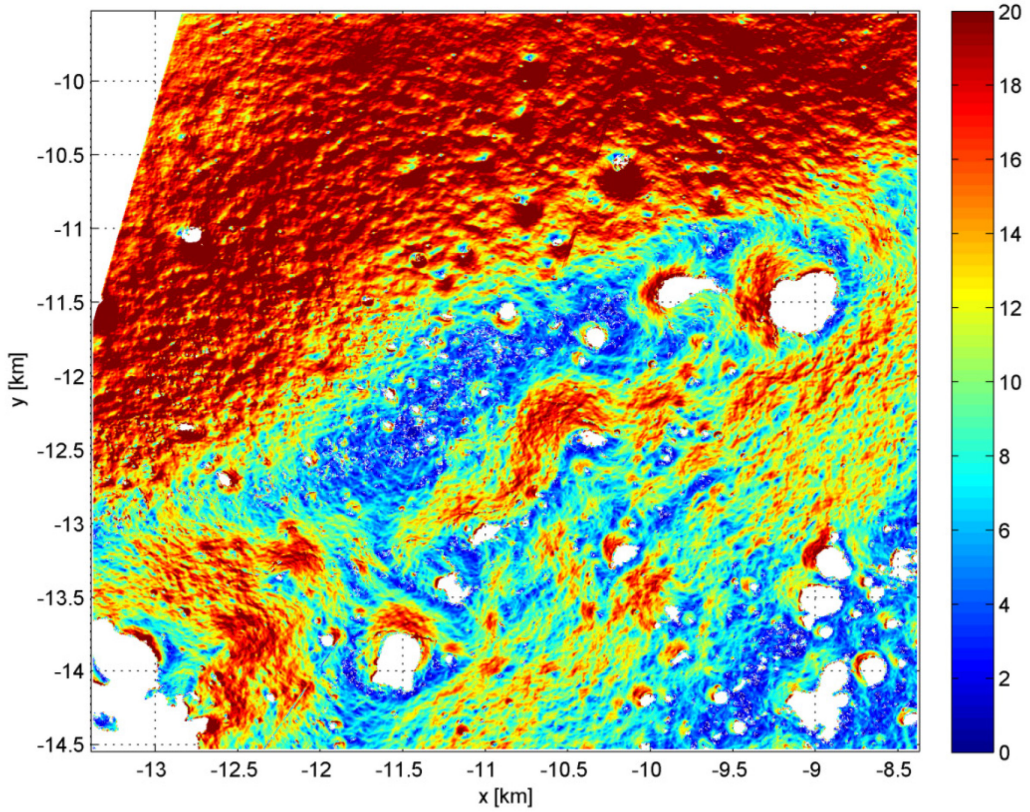

Figure 7-13 Slope map of the Connecting Ridge region, slope measured in [°]

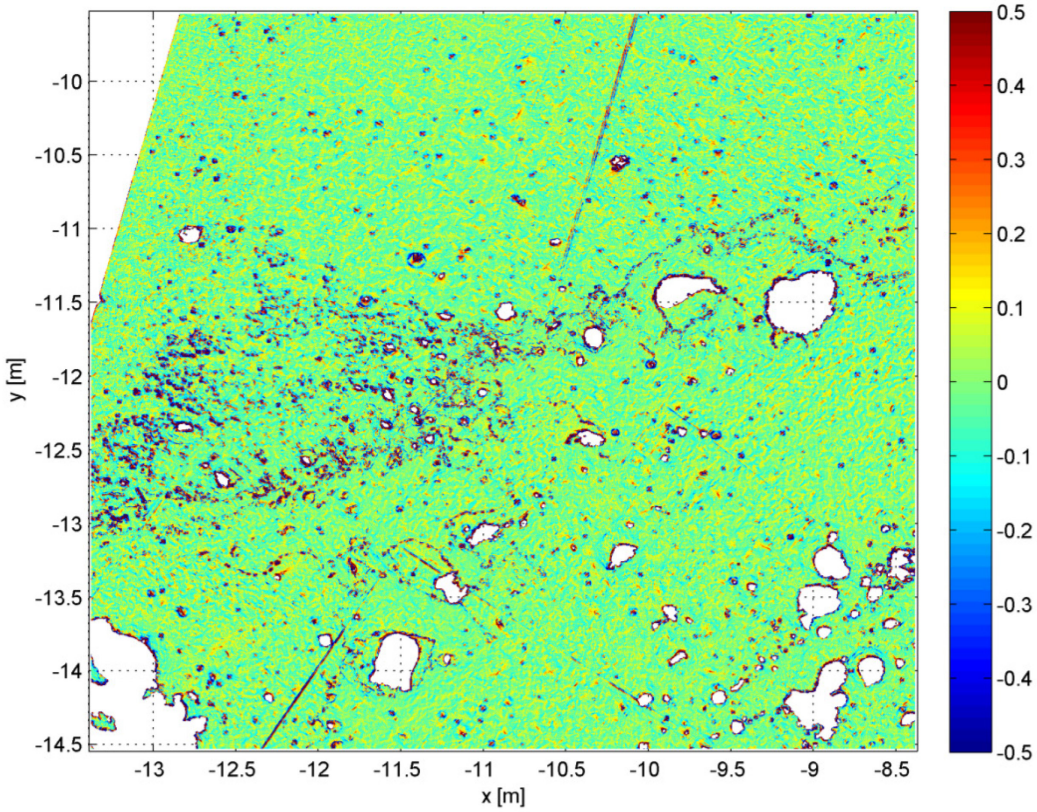

Figure 7-14 Roughness map of the Connecting Ridge region, roughness measured in [m]

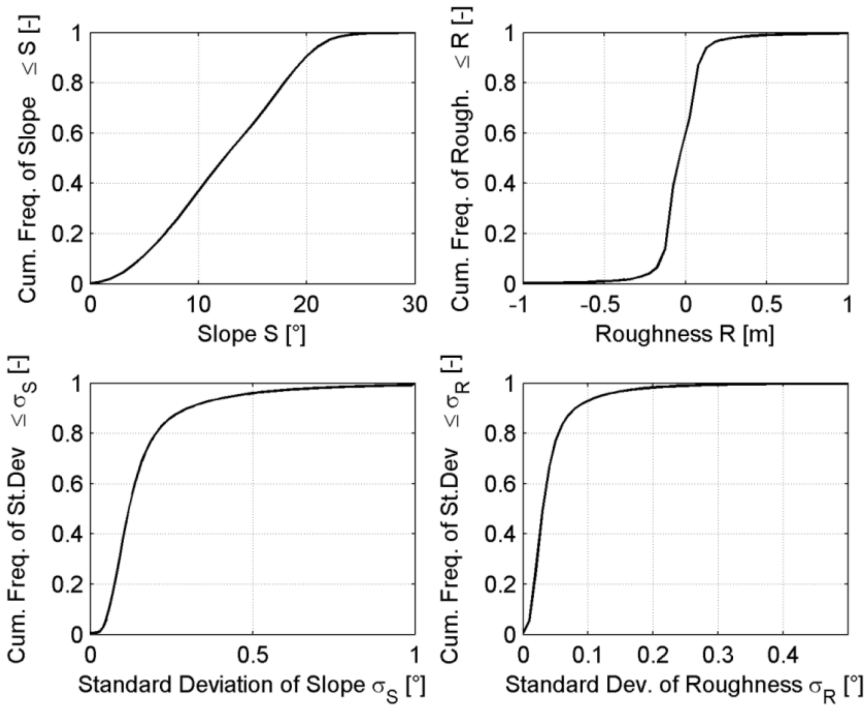

Figure 7-15 Magnitude-frequency distributions for slope and roughness estimates and associated standard deviations

8 Case Study – A Robotic Lunar Landing

In This chapter, as an example, the analysis scheme developed in the previous chapters shall be applied to a realistic mission scenario. A robotic lunar landing system is considered which is analyzed in close relation to the European Lunar Lander system and mission design. Although the mission was put on hold in 2012, the already published technical details provide a realistic context to demonstrate a successful application of the analysis methods developed in this thesis.

8.1 The European Lunar Lander and its Landing Sites

This mission was initially investigated under its programmatic title "MoonNEXT" by three industrial consortia in independent Phase A studies (2009 to 2010). It was continued from 2010 to 2012 on Phase B1 level as "European Lunar Lander" by the industrial contractor EADS Astrium Space Transportation, now Airbus Defense & Space. The programmatic aspects of this mission are described by *Pradier et al. 2010*. The key objective of the mission was not only to demonstrate soft and precision landing capability but also to land in the Lunar South Pole region at a specific site with extended illumination allowing a long duration surface operation (*Houdou et al. 2012*). Second order priorities to this objective were particular technology demonstrations such as real-time visual navigation techniques, autonomous hazard detection and avoidance, or the clustered pulsed engine concept. The Phase B1 study, summarized by *Diedrich et al. 2011*, yielded a preliminary spacecraft design, a list of landing site candidates and an estimate of the lander's payload capability. The configuration of this lander is shown with its principal dimensions in Figure 8-1 (left). It shows for comparison the LEM-4C in the same scale. The Lunar Lander features the same leg kinematics (Cantilever) as the LEM-4C, albeit having a 2.3-times larger footprint. The principal values of its geometry and mass properties are provided in Table 8-1. Table 8-2 complements its energy absorption capabilities of the leg's primary and secondary struts.

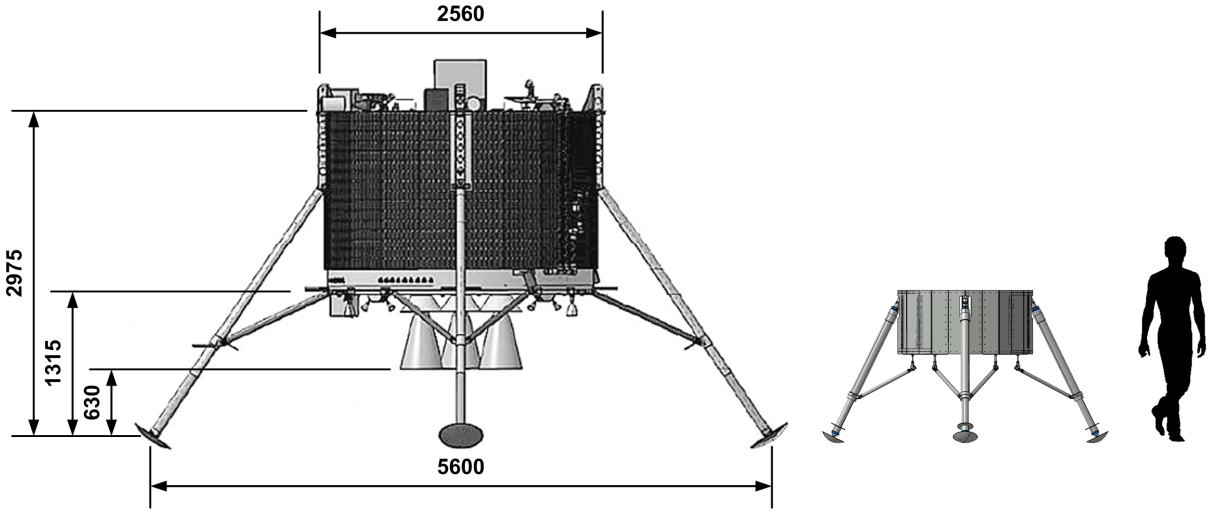

Figure 8-1 ESA Lunar Lander configuration (left, courtesy Airbus DS), LEM-4C (right) in the same scale, dimensions are in mm

Property	Value	Remark / Reference
Mass m [kg]	750	*Buchwald et al. 2011*
Moment of Inertia I_{xx}, I_{yy}, I_{zz} [kg·m²]	~700 / ~1000 / ~1000	*ESA 2008*
Landing Gear Footprint d_{FP} [mm]	5600	Figure 8-1
Height of COM h_{COM} [mm]	1820	$h_{COM} \sim 0.65 \cdot r_{FP}$ *Buchwald et al. 2011*
Design Ground Clearance d_{gc} [mm]	630	Figure 8-1

Table 8-1 Robotic Lunar Lander – Principle geometry and mass properties as used in this case study

	Force F(s) [kN]	Max. Stroke [mm]	Energy Absorption [kJ]	Remark / Reference
Primary Struts	7.5	280	2.10	Airbus DS, private communication
Secondary Strut, comp.	$-3.5 \cdot e^{-0.6 \cdot s}$	140	0.49	Reasonably assumed, compare LEM, chapter 3.3.2.2
Secondary Strut, tens.	$e^{35.0 \cdot s}+2.5$	50	0.24	

Table 8-2 Robotic Lunar Lander – force-stroke-characteristics and energy absorption capability as used in this case study

The scientific objectives are related to preparatory steps for human exploration and utilization of the moon as scientific base, and further with goals specifically expressed in *Carpenter et al. 2012*: investigating the radiation and plasma environment and its interactions with the lunar dust, studying effects of the radiation environment on biological species, identification and demonstration of insitu resource utilization potential and act as platform for fundamental physics such as radio astronomy.

A key objective for the identification of a suitable landing site for the European Lunar Lander was to find a site with continuous illumination for a period of up to several months (*De Rosa et al. 2012*). This is basically achievable at exposed elevations in the mountainous Polar Regions. An initial illumination analysis was carried out by *Vanoutryve et al. 2010* which identified a set of landing sites for such favorable lighting conditions. These sites, however, are still subject to a surface analysis regarding landing hazards. These sites and their geographical coordinates are tabulated in Table 8-3 and refer to the analysis of *Vanoutryve et al. 2010*.

Region	Identifier	Location Lat/Lon [°]
Shackleton Rim 1	SR1	-89.7757 / -155.4047
Shackleton Rim 2	SR2	-89.6874 / -162.5043
Connecting Ridge	CR	-89.4440 / -137.2911
Malapert Peak 1	MP1	-85.9623 / -2.4258
Malapert Peak 2	MP2	-86.0093 / +2.8040
Leibnitz β-Plateau	LP1	-85.4110 / +31.7554

Table 8-3 ESA Lunar Lander primary landing site candidates; DTMs are available for the sites SR1, SR2, CR and MP; the »Connecting Ridge« (CR) is used as landing site in this case study

Refined illumination analysis reported by *Diedrich et al. 2011* confirmed the site "Connecting Ridge" (CR) as the most suitable place with regard to illumination. Therefore this site has been chosen in this thesis as an example to demonstrate the assessment of the landing hazards. Figure 8-2 (a) locates this site in the Lunar South Pole vicinity. A region of $5 \times 5\text{km}^2$ around this site is available as a high-resolution digital terrain model, produced by *Scholten et al. 2012* to support the required landing site surface characterization beyond the study Phase B1. The CR region is shown in an ortho-image mosaic in Figure 8-2 (b). The landing zone is marked by a rectangle of $1 \times 1\text{km}^2$ in Figure 8-2 (b) and extends +/-500m around the nominal landing site. The landing zone is shown enlarged and additionally its local horizon as overlay. The ridge, after which this region is named, stretches in north-southerly direction.

Although the lighting conditions do not affect the performance of the touchdown system, they are critical for the power subsystem. Therefore the flight system's Hazard Detection and Avoidance (HDA) sub-system will have to avoid these unfavorable conditions as well. In addition to the potential hazards already provided by *slope* and *roughness* also the potential hazard posed by the *local shadowing* in the landing zone has to be taken into account. In order to emulate a certain lighting condition for the HDA-driven landing dispersion, a NAC ortho-image (DLR-CR1-NACORT03, *Scholten et al. 2012*, based on LRO image M139817894L) is taken. The landing zone section of this image, shown by Figure 8-2 (d), represents an illumination condition with a sun azimuth of 143.3° and an elevation of 1.12° at the CR nominal coordinates.

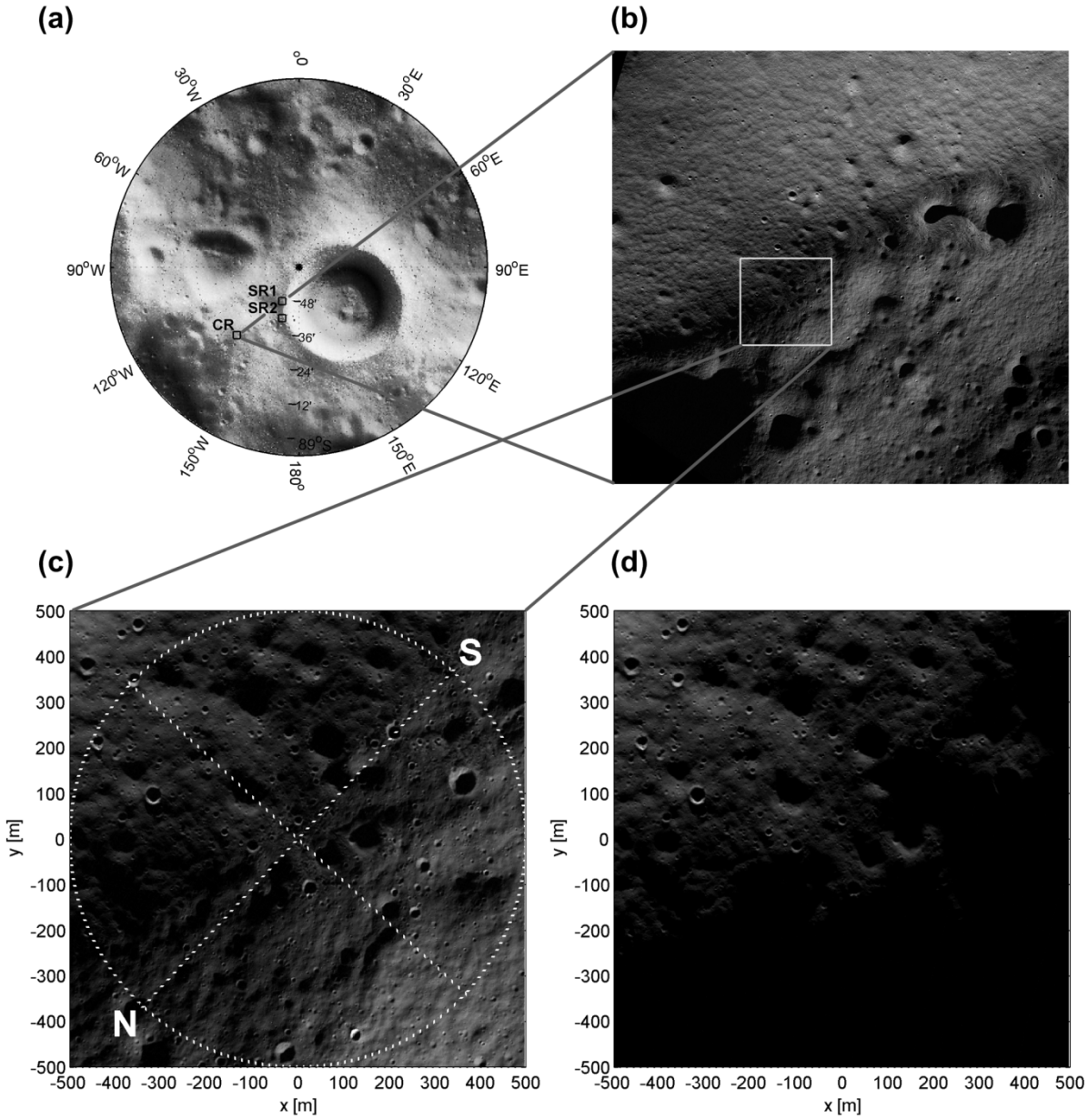

Figure 8-2 Landing site »Connecting Ridge«: (a) located in the Lunar South Pole vicinity, (b) Connecting Ridge region (5×5km² image mosaic), (c) landing zone 1×1km² , and (d) landing zone with an example for illumination conditions.

The landing site characterization with regard to potential hazards for the touchdown system is an integral part for the landing safety assessment which must consider specific properties of the landing platform. In chapter 7 the processing of the high-resolution DTM of the CR region into relevant terrain property information has been described in detail and slope and roughness maps have also been derived. The respective map details for the landing zone are shown in Figure 8-3. Generally, the landing zone is characterized by shallow slopes except for its easterly and westerly corners. It exhibits only a few areas of pronounced terrain roughness. Parts of these areas are, however, adjacent to areas with no or interpolated elevation data. This questions whether identified roughness is true or caused by artifacts. Therefore, the DTM data product is accompanied by ancillary information on the confidence of the elevation data. It differentiates between “based on image matching results” (best data available, marked as white areas in Figure 8-4), “inter- or extrapolated data” (marked gray in Figure 8-4) and

"shadowed" (black areas, although image data was available, the permanent shadowing of this area made a derivation of elevation data impossible).

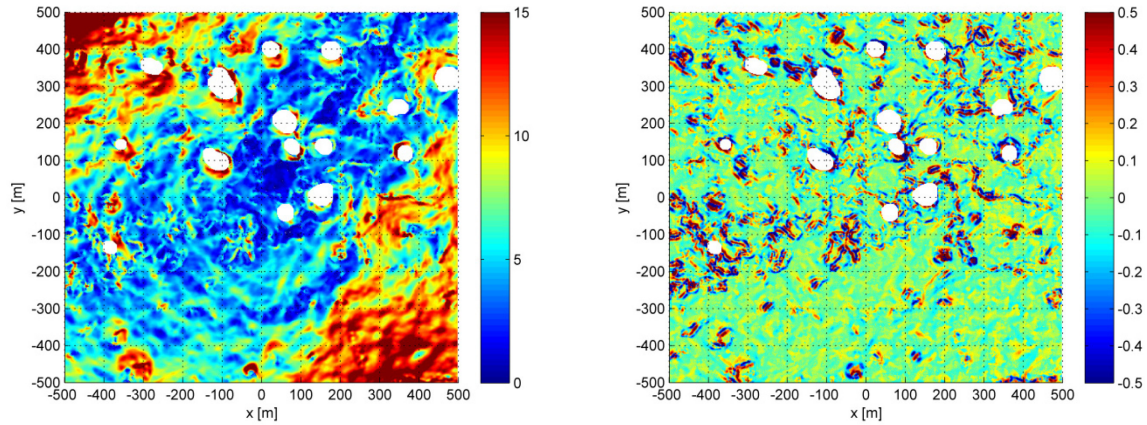

Figure 8-3 Landing zone slope map (left, slope in [°]) and roughness map (right, roughness in [m]): the data has been derived from the CR DTM in chapter 7

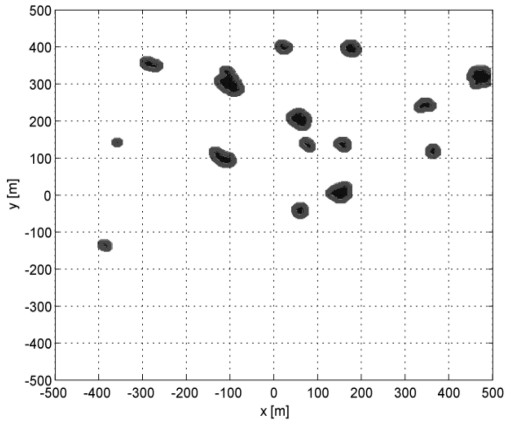

Figure 8-4 Landing zone confidence map (white: best data, gray: interpolated data, black: no elevation data available)

8.2 The Terrain-related Failure Assessment

In this section the probabilities for a terrain-related failure for the Robotic Lunar Landing system are derived. The necessary preparations have been developed and described in the previous chapters, which are the simulation and analysis steps (chapter 6). A four-legged, Cantilever-type landing platform, the LEM-4C, was modelled in chapter 3. As the LEM-4C has the same topology as this Robotic Lunar Lander, the numerical model is just updated to the size and mass properties and energy absorption capabilities of the larger Lunar Lander. The principal values are given in Table 8-1 and Table 8-2. The associated break-down into the individual body elements is provided in the annex A2 – Masses and Geometries of Landing System Models.

While on the basis of the LEM-4C numerical model a systematic "what happens if" assessment on its behavior with respect to several terrain types and features were made, this case study now exploits the intermediate conclusions made upon this assessment in chapter 6. With regard to stability and strut strokes the chapter 6.4.1 concluded that the presence of crater-caused roughness is most adversely

affecting the vehicle's functionality. Therefore, it is a means of safe-guarding against terrain features not resolved by the remote sensing data to allow crater or parts of it to be within the footprint of the landing gear. The question arises then what crater size to be considered in the analysis cases. It is suggested here to handle the terrain sampling issue as a general data sampling problem attempting to resolve a signal's frequency. According to the Nyquist sampling criterion the smallest resolvable signal period is twice the sampling period. Consequently the smallest crater size which can be resolved by the used DTM (refer to chapter 7) with 2m/px is 4m. Craters of smaller diameter remain unresolved or are at least not fully resolved. Accordingly, a terrain file representing a 4m diameter crater is produced with the methods described in chapter 7.3 and read into the numerical touchdown simulator for the stability and strut stroke failure assessment. It thus accounts for and includes the effects due to unresolved, yet uncertain terrain roughness.

8.2.1 Instability

Sampling of the touchdown conditions domain and processing it into the probabilities for an instable landing is again done identical as defined in chapter 6.2. In addition to that crater feature this analysis considers a rigid surface and slope values varying from 15° to 35° in steps of 5° (analysis cases RLL-Sxx-C40-R-L, xx = 15/20/25/30/35° of slope). From the resultant data set the parameter $\hat{\mu}_L$ and $\hat{\sigma}$ for a Log-Normal distribution is identified using the mathematical methods developed in chapter 6.3. The result is provided here in Table 8-4 and is also shown in Figure 8-5 where the data points are denoted as "observed" and the LogNormal distribution fitted into this data set.

LogNormal	$\hat{\mu}_L$	$\hat{\sigma}$	$\hat{\mu}$
Instability	3.3158	0.2081	27.5

Table 8-4 Identified parameter for the LogNormal distribution of probability of instability based on 95% confidence data

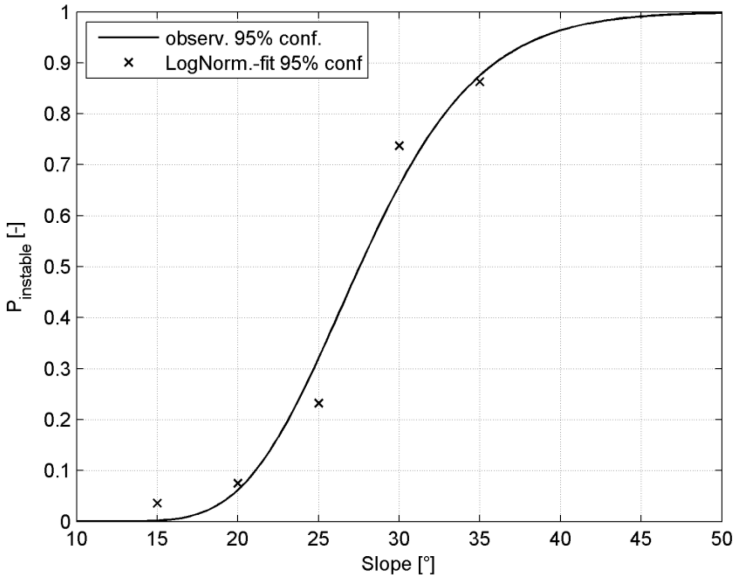

Figure 8-5 LogNormal distributed probability of instability for the Robotic Lunar Lander

The probability for an instable touchdown is described by a Log-Normal distribution through equation 8.1 with the estimated parameters. The letter Φ in this equation denotes here again the standard normal distribution.

$$P_{instable,i} = \Phi\left(\frac{\ln\left(\hat{S}_{ub,i}\right) - \mu_{L,instab.}}{\sigma_{instab.}}\right) \qquad 8.1$$

The new aspect in this equation is the integration of the terrain slope estimate for the landing zone. Therefore, the confidence interval for the slope estimate is computed. Each pixel with index i of the slope map (Figure 8-3) describes the estimated mean slope $\hat{S}_i$ at the associated pixel coordinate. Similarly the slope's standard deviation $\hat{\sigma}_{S,i}$ at this particular position is taken from the respective map product. The upper bound $\hat{S}_{ub,i}$ of the 95% confidence interval of the slope mean value is expressed by equation 8.2 incorporating these two estimators. The parameter η is the number of degrees of freedom of the slope estimate and referred to in chapter 7.2.

$$\hat{S}_{ub,i} = \hat{S}_i + \frac{\hat{\sigma}_{S,i}}{\sqrt{\eta_i}} \cdot t_{\frac{\alpha}{2};\,\eta_i - 1} \qquad 8.2$$

With these equations the mathematical rule to characterize the landing zone with regard to landing stability on a "per map pixel" basis is obtained: Equation 8.1 is evaluated at $\hat{S}_{ub,i}$ to get $P_{instable,i}$. The result after application on the entire slope map is a raster file containing the probabilities for an instable landing which is essentially a map indicating areas in the landing zone with a particular failure probability. The following section 8.2.4 resumes this aspect.

Example: Let $\hat{S}_i = 11.3°$ and $\hat{\sigma}_{S,i} = 1.2°$. With $\eta_i = 20$ and a confidence level of 95% the percentile of Student's t-distribution is t = 1.72. According to equation 8.2 the upper bound of the slope estimate is $\hat{S}_{ub,i} = 11.76°$. With this slope value and the distribution parameter $\hat{\mu}_L$ and $\hat{\sigma}$ from Table 8-4 the probability of instability when touching down at the position associated to pixel i is determined through equation 8.1. In this example this probability is $P_{instable,i} = 2.1 \cdot 10^{-5}$, in this case a considerably low failure probability.

8.2.2 Energy Absorption

A similar assessment is made for the probabilities to exceed the leg's energy absorption capabilities. Chapter 6.4.3 concluded that the strut stroke limit exceedance probabilities do not follow a particular probability distribution with regard to the terrain slope but exhibit at least a certainly identifiable trend which is described by equation 8.3. With the numerical touchdown simulation the probabilities to exceed a certain compression or tension limit was done with the methods developed in chapter 6.3, yielding a data set denoted as "observations". The parameters of the trend function (equation 8.3) are estimated for the primary strut stroke as well as the secondary strut stroke in the compression and tension direction (Table 8-5). The Figure 8-6 shows the data points and the trend curves.

$$P_{\text{Stroke exceedance},i} = \hat{a} \cdot e^{\hat{b} \cdot \hat{S}_{ub,i}} \qquad 8.3$$

This equation is evaluated at every pixel i of the slope map with $\hat{S}_{ub,i}$ for the primary strut as well as for the secondary strut's compression direction and with the confidence interval's lower bound $\hat{s}_{lb,i}$.for secondary strut's tension direction. The result is again a raster for stroke limit containing the respective exceedance probabilities.

Trend	$\hat{a}$	$\hat{b}$
Primary strut stroke limit	$5.4 \cdot 10^{-5}$	0.2369
Secondary strut stroke limit, compression	$1.5 \cdot 10^{-3}$	0.1618
Secondary strut stroke limit, tension	$7.4 \cdot 10^{-3}$	-0.1414

Table 8-5 Identified trend parameter for the probability of stroke limit exceedance

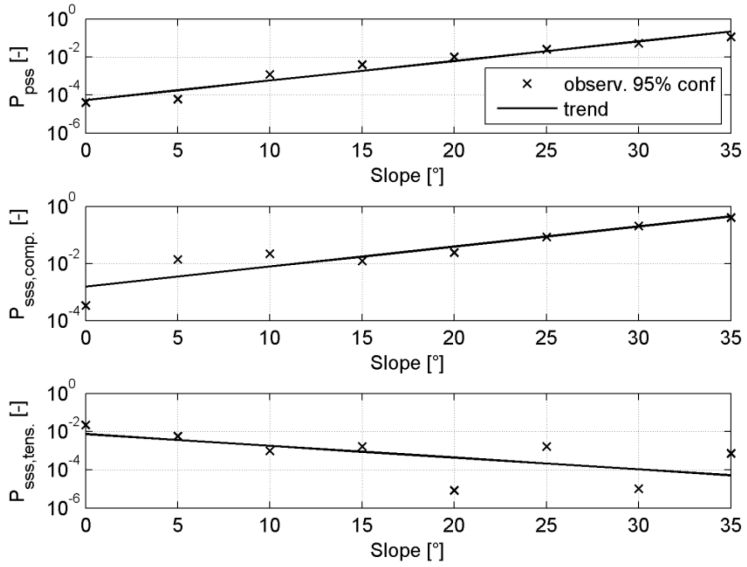

Figure 8-6 Probabilities of stroke limit exceedance for the Robotic Lunar Lander based on 95% confidence data: LOF exceedance probability for the primary strut stroke (top), the secondary strut stroke in compression direction (middle) and the secondary strut stroke in tension direction (bottom)

Example: Let again $\hat{S}_i = 11.3°$, $\hat{\sigma}_{S,i} = 1.2°$ and $n_i = 20$. With a confidence level of 95% the upper bound of the slope estimate is $\hat{S}_{ub,i} = 11.76°$ (see example of previous section). With this slope value and the distribution parameter $\hat{a}$ and $\hat{b}$ from Table 8-5 the probability of exceeding the leg's stroke limit upon touchdown is determined through equation 8.3. In this example this probability is $P_{\text{Stroke exceedance,i}} = 0.010$.

8.2.3 Ground Clearance

Regarding the ground clearance, chapter 6.4.2 elaborated that the clearance between the lander's belly and a flat terrain surface is described by a Normal distribution (eq. 8.4) whose mean value is smaller on soft, granular terrain than the mean value on a rigid surface. Accordingly, the Robotic Lunar Lander's ground clearance distribution is derived from a series of simulated touchdowns on such a flat, non-sloped surface and the granular soil model (analysis case S00-F-S-L) assuming Lunar Regolith with parameters given in annex A3 – Soil Mechanical Data. The Figure 8-7 (top) shows both the empirically obtained CDF and the identified Normal distribution. The following Table 8-6 contains the associated identified parameters. For comparison, this table provides also the distribution parameter for identical touchdown conditions but assuming a rigid surface (analysis case S00-F-R-L). The third column in the table gives the expected loss of ground clearance which is the difference between the mean clearance after touchdown and the design clearance (Table 8-1). The values indicate that ~20% of the mean loss is attributable to the granular soil. Figure 8-7 (bottom) depicts also the PDF of the identified normal distribution for the RLL-S00-F-S-L case.

$$x_{gc,flat} \sim N\left(\mu_{gc,flat}, \sigma^2_{gc,flat}\right) \qquad 8.4$$

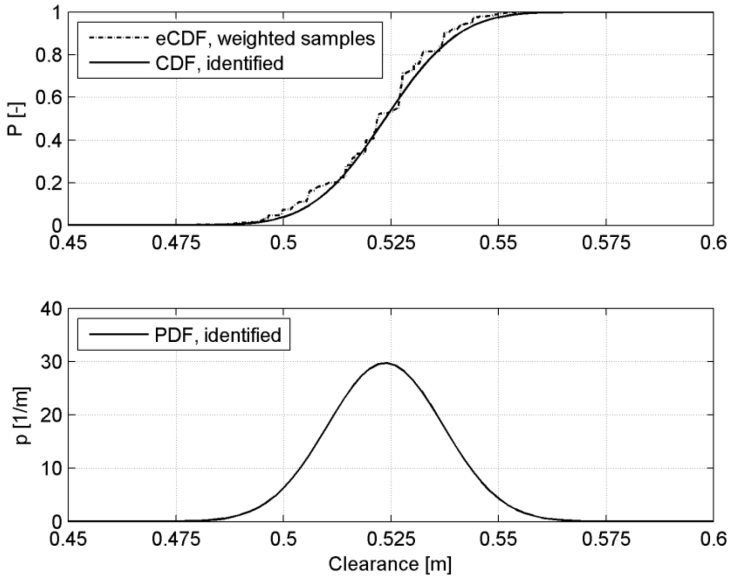

Figure 8-7 Cumulative distribution and probability density of the ground clearance with regard to a granular soil surface (analysis case RLL-S00-F-S-L)

Normal	$\hat{\mu}$ [m]	$\hat{\sigma}$ [m]	Mean loss of clearance (μ-d_{GC}) [m]
Clearance compared to a granular soil surface	0.523	0.0134	0.107
Clearance compared to a rigid surface	0.548	0.0148	0.082

Table 8-6 Identified parameter of the Normal distribution of the RLL's ground clearance

Chapter 6.4.2 concluded furthermore that the terrain undulation by boulder or crater features just adds or subtract to the clearance with regard to the flat reference plane. This relation can be exploited to combine the ground clearance distribution data with the terrain roughness descriptors obtained from the landing site characterization. The processing of the DTM in chapter 7.2 provides in addition to the roughness estimator again an estimate of its standard deviation. This makes the actual roughness value likewise a Normal-distributed random number (eq 8.5) which is measured against the mean plane of the respective terrain section.

$$R_i \sim N\left(\hat{R}_i, \hat{\sigma}^2_{R,i}\right) \qquad 8.5$$

The sum of two normal distribute and independent random numbers is again a normal distribute number.

$$x_{gc,flat} - R_i = x_{gc,i} \sim N\left(\underbrace{\mu_{gc,flat} - \hat{R}_i}_{:=\mu_{gc,i}}, \underbrace{\sigma^2_{gc,flat} + \hat{\sigma}^2_{R,i}}_{:=\sigma^2_{gc,i}}\right) \qquad 8.6$$

Inadvertent contact between the lander body and a terrain feature occurs if the residual ground clearance is less than zero.

$$P_{contact} = P(X_{gc} \leq 0) = \Phi\left(-\frac{\mu_{gc}}{\sigma_{gc}}\right) \qquad 8.7$$

Example: Let a roughness value be determined by $\hat{R}_i = 0.45$ m and $\hat{\sigma}_{R,i} = 0.05$ m at a particular position at pixel i of the respective roughness map. The lander body clearance is determined by its distribution parameter $\hat{\mu}_{gc,flat}$ and $\hat{\sigma}_{gc,flat}$ from Table 8-6. The actual ground clearance is again a Normal-distributed random number according to equation 8.6. Its parameter are then $\hat{\mu}_{gc} = 0.073$ m and $\hat{\sigma}_{gc}$ 0.0517 m. With equation 8.7 the probability for an inadvertent ground contact is determined as $P_{contact} = 0.078$. Figure 8-8 sketches the determined lander ground clearance and the assumed roughness value as well as the resulting actual ground clearance as PDF (top) and CDF (bottom).

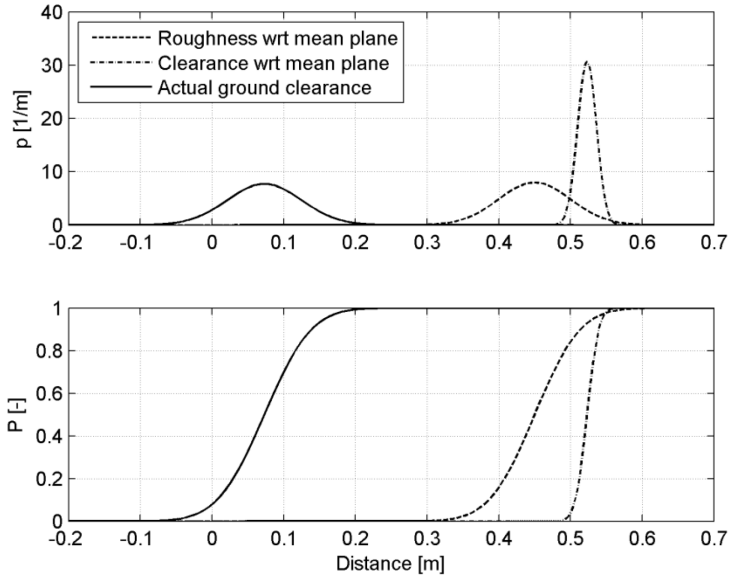

Figure 8-8 Example calculation of the probability of inadvertent ground contact: the Normal distributed actual ground clearance of the lander is derived from the subtraction of the numerically determined Normal distributed ground clearance with regard to the flat surface and the Normal distributed roughness value at the respective map position. Inadvertent contact occurs when the actual clearance falls below zero

8.2.4 Failure Maps for the Robotic Landing at the »Connecting Ridge« site

The previous sections 8.2.1, 8.2.2, and 8.2.3 have shown the results of the probability of failure assessment for a Robotic Lunar Lander and have introduced the mathematical way to combine this information with the terrain property information obtained from the landing site characterization. The evaluation of the landing zone pixel by pixel yielded consequently a map where each pixel describes the particular failure probability conditional to a touchdown at the associated position. These maps a visualized in Figure 8-9 as colored zones according a certain failure probability and are shown as overlay on the landing zone's ortho-image mosaic.

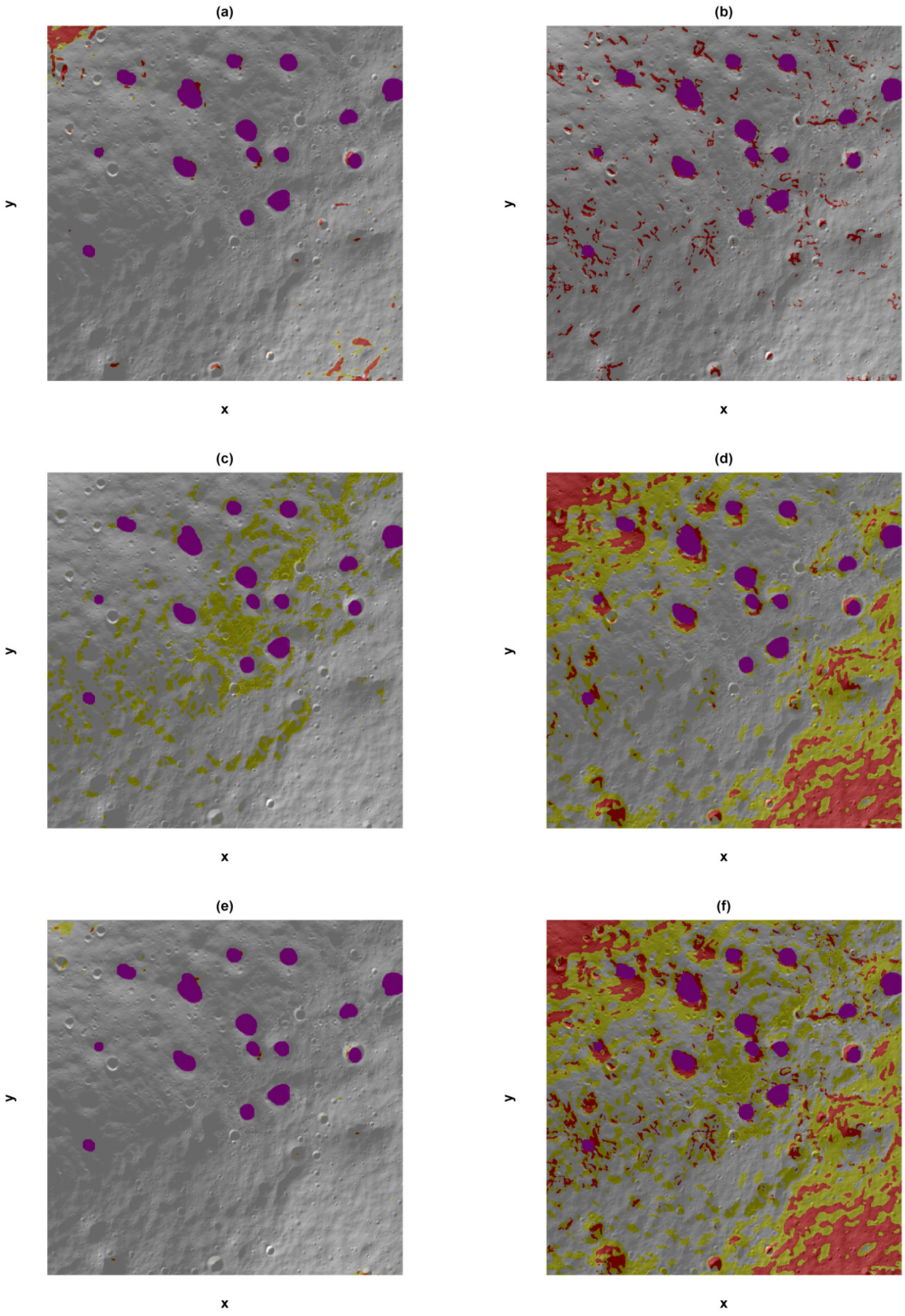

Figure 8-9 Zones of a certain failure probability – (a) instability, (b) inadvertent ground contact, (c) secondary strut stroke tension limit exceedance, (d) secondary strut stroke compression limit exceedance, (e) primary strut stroke limit, (f) composite view. Color code: no color: $P_{Fail} \leq 0.005$, yellow: $P_{Fail} \leq 0.010$, red: $P_{Fail} > 0.010$, magenta: no elevation data.

8.3 Landing Dispersion Pattern

The central theme of this thesis is the derivation of the probabilities of terrain-related failures at the touchdown event. As shown during its derivation, these probabilities are conditional to the exposure of the landing system to unfavorable terrain properties in the landing zone. The determination of such exposure probabilities is part of the landing dispersion analysis. The scatter of the touchdown positions around the targeted site stems thereby from the guidance, navigation and control uncertainties taking effect during the descent and approach phase. The state-of-art of open-loop flight systems has been repeatedly demonstrated by successful Mars landings. Thereby the position scatter is modeled e.g. by *Bonfiglio et al. 2011* as bi-variate Gaussian distribution. The superposition of the landing dispersion ellipse obtained from this model on terrain maps yields probability estimates of an encounter with certain terrain features. To complete the case study, a landing dispersion analysis is added in this section. An exemplary dispersion analysis for a landing system with closed-loop and active hazard detection and avoidance (HDA) system has been published already by the author of this thesis in *Witte 2013* and *Witte 2014*. This section provides a summary out of this work unless referenced otherwise.

The landing dispersion of a robotic landing system is determined by the navigation and hazard detection and avoidance capabilities. The resulting trajectory of such an avoidance maneuver is schematically shown in Figure 8-10. The flight system's performance figures are reasonably assumed on the basis of the Lunar landing related publications by *Neveu et al. 2010*, *Moebius et al. 2008* and *Melloni et al. 2010* and are summarized in Table 8-7. In this landing scenario the spacecraft shall land in the Lunar South Pole site "Connecting Ridge" at nominal landing site coordinates as stated in Table 8-3.

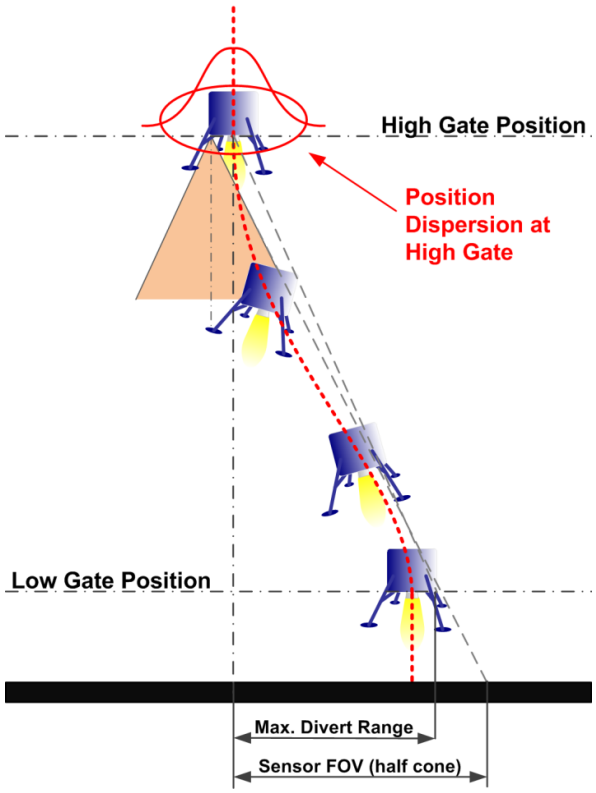

Figure 8-10 Schematic HDA maneuver, showing parameters used in the dispersion calculation

The powered descend is initiated from a polar orbit with a ground track azimuth from North to South (Table 8-7, item 1). The actual landing positions are registered in a Cartesian coordinate system which

is centered in the nominal landing site coordinates (item 2). Navigation uncertainties accumulated during the descend phase result in a position dispersion at the high gate position above the landing zone prior to an HDA-maneuver. They are described by a bi-variate Gaussian distribution with 3σ-errors along and cross track (items 3 and 4 in Table 8-7). From the so called High Gate position the hazard detection sensors acquire the terrain properties underneath the landing system. At an assumed height of 1000m above the surface, the scanning LIDAR with a field of view (item 5) observes an area with 176m radius, yielding 0.5m/px resolution. While the onboard processing of the LIDAR data delivers slope and roughness information to the onboard decision-making entity it is assumed that these figures are affected by errors as given by items 6 and 7. Information on local shadows is complemented by the navigation camera. Its field of view is stated in item 8 and the shadow discrimination error in item 9. Based on the onboard hazard assessment, one divert maneuver can be executed. The flight system shall have therefore a divert capability of 170m (10) to attain an alternate landing spot.

	Parameter	Value
1	Ground Track Azimuth [°]	180
2	Mean of Initial Dispersion at HG (X_0, Y_0) [m]	(0, 0)
3	Along Track Error (3σ) at High Gate [m]	360
4	Cross Track Error (3σ) at High Gate [m]	240
5	LIDAR Field of View [°], resolution [px]	20, 700 × 700
6	Slope Determination Error [°]	2.5
7	Roughness Determination Error [m]	0.35
8	Nav. Camera Field of View [°], resolution [px]	60°, 1024 × 1024
9	Shadow Determination Error [DN]	5
10	Divert Distance Capability, omnidirectional [m]	170

Table 8-7 Navigation and hazard detection and avoidance performance figures used in the case study

The dispersion analysis starts with the calculation of the probability of the landing system to be above a certain position of the landing zone. Therefore the landing zone is partitioned into an n×n grid. The discrete probability p_{ij} to be in a particular grid cell indexed as row i, column j is given by the double integral of the bi-variate Gaussian distribution (equation 8.8) over that particular grid cell (*Witte 2013*). The probability density is parameterized by the nominal landing site $\mathbf{x} = \{x_0, y_0\}$ coordinates and the covariance matrix **C** containing the along track and cross track errors around that nominal site.

$$p_{ij} = \frac{1}{2\pi\sqrt{\det \mathbf{C}}} \cdot \iint_{\text{Grid Cell ij}} e^{-\frac{1}{2}(\mathbf{x}-\mathbf{x_0})^T \mathbf{C}^{-1}(\mathbf{x}-\mathbf{x_0})} \, dxdy \qquad 8.8$$

The resultant matrix $\mathbf{P}_0 = (p_{ij}) \in \mathbb{R}^{n \times n}$ describes the initial dispersion at the high gate position. In the case the flight system has no HDA capability (e.g. it is an open loop system) the landing dispersion analysis ends at this point already. In case HDA functionality exists, as assumed in this study, an appropriate analysis step follows upon this initial calculation. Therefore each grid cell is considered as a state of a stochastic process meaning that the flight system arrives with the probability p_{ij} at the associated position above the surface prior to the HDA maneuver. The initial position probability matrix $\mathbf{P_0}$ is re-written as vector $\mathbf{p}_0 \in \mathbb{R}^{n^2}$. The propagation (equation 8.9) of this initial state vector $\mathbf{p}_0$

requires a $n^2 \times n^2$ transition matrix **T** such that the probability vector $\mathbf{p_1}$ reflect the post-HDA dispersion pattern. The decision dependent transition matrix **T** shall reflects the HDA strategy in this application.

$$\mathbf{p_1} = \mathbf{T} \cdot \mathbf{p_0} \qquad 8.9$$

This means the HDA maneuver is modeled hereby as a stochastic decision process based on Markov chains to map the initial dispersion at an arrival gate according to equation 8.8 to a new dispersion pattern affected by the divert decision-making and system constraints.

The transition matrix **T** captures the flight system technical properties whose macroscopic dispersion pattern is determined by the site selection of the onboard decision-making entity. HDA subsystem key functionalities (Figure 8-11) include: (i) the terrain mapping, determined by the sensors FOV and sensor errors, (ii) the trajectory generation, constrained by the maximum divert range, and hazard assessment & decision-making through cost or score function according equation 8.10. Not considered are the inner loops of the control cascade. Thus the "fine dispersion" around the commanded trajectory is neglected.

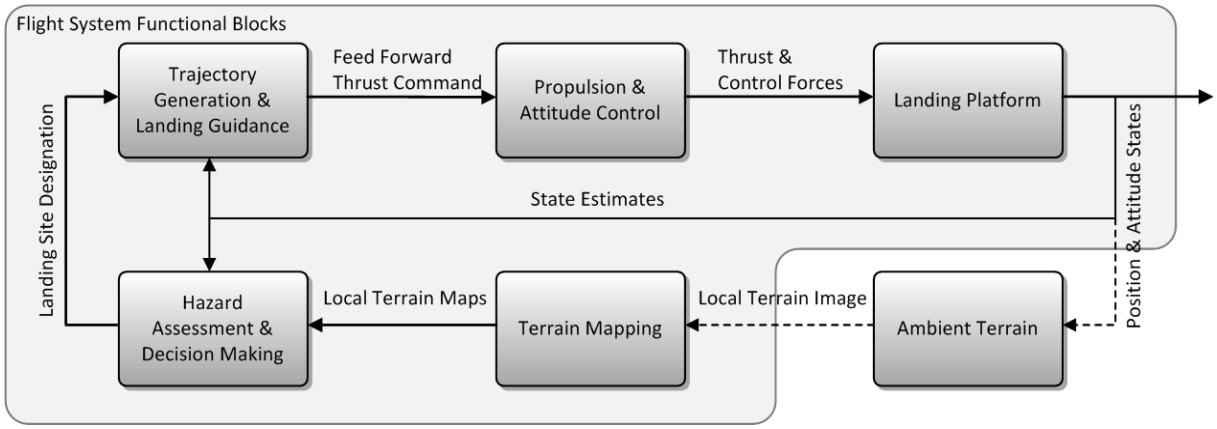

Figure 8-11 Block diagram of the HDA functional loop

The safety ranking of the terrain underneath based on in-situ measured slope, roughness and shadow maps is assumed to be done by the onboard system according to the following score function with w_s, w_r and w_I being weighting coefficients for the measured slope, roughness and illumination intensity, respectively.

$$\text{score}_{ij} = 1 - \left(w_s \cdot s_{ij} + w_r \cdot r_{ij} + w_I \cdot (255 - I_{ij})\right) / (w_s \cdot s_{max} + w_r \cdot r_{max} + w_I \cdot (255 - I_{max})),$$
$$\text{with } w_s = 0.25,\ w_r = 0.5,\ w_i = 0.25. \qquad 8.10$$

A score value of zero marks a safest possible site whereas a one indicates a least safe site. Instead of having in-situ produced maps, this process is mimicked by using the slope, roughness and shadow information from the remote sensing data products as shown in Figure 8-3 (slope, roughness), and Figure 8-2 ((d), shadow). The map sections visible within the field of view determine the hazard situation as seen from each position (node). The full mathematical framework and its numerical implementation to derive then the transition matrix **T** based on such data is provided in annex A5 – Stochastic Modeling of a Hazard Detection and Avoidance Maneuver which is an excerpt from *Witte 2013*. The associated landing dispersion results for the "Connecting Ridge" scenario have been presented separately in *Witte 2014* and are reprinted in the following part of this section.

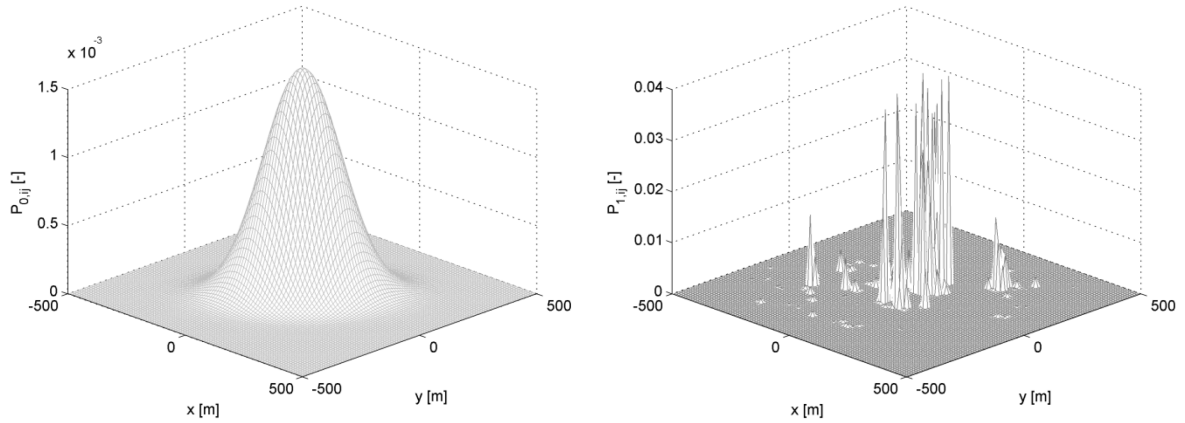

Figure 8-12 Probability to land in a grid cell – initially, pre-HDA (left), post-HDA (right)

Figure 8-12 (left) shows the initial position dispersion $\mathbf{P_0}$ considering the parameters as per Table 8-7. The same figure (right) shows the dispersion after passing the HDA-gate. The probability vector $\mathbf{p_1}$ of the size $n^2 \times 1$ is therefore re-written as $n \times n$ matrix $\mathbf{P_1}$. Both dispersion patterns are also shown in Figure 8-13 as contour line superimposed onto the landing site image given by Figure 8-2 (d). As it can be clearly seen the initial contiguous ellipse disintegrates into several smaller clusters as the flight system favors shallower, less rough and stronger illuminated landing spots.

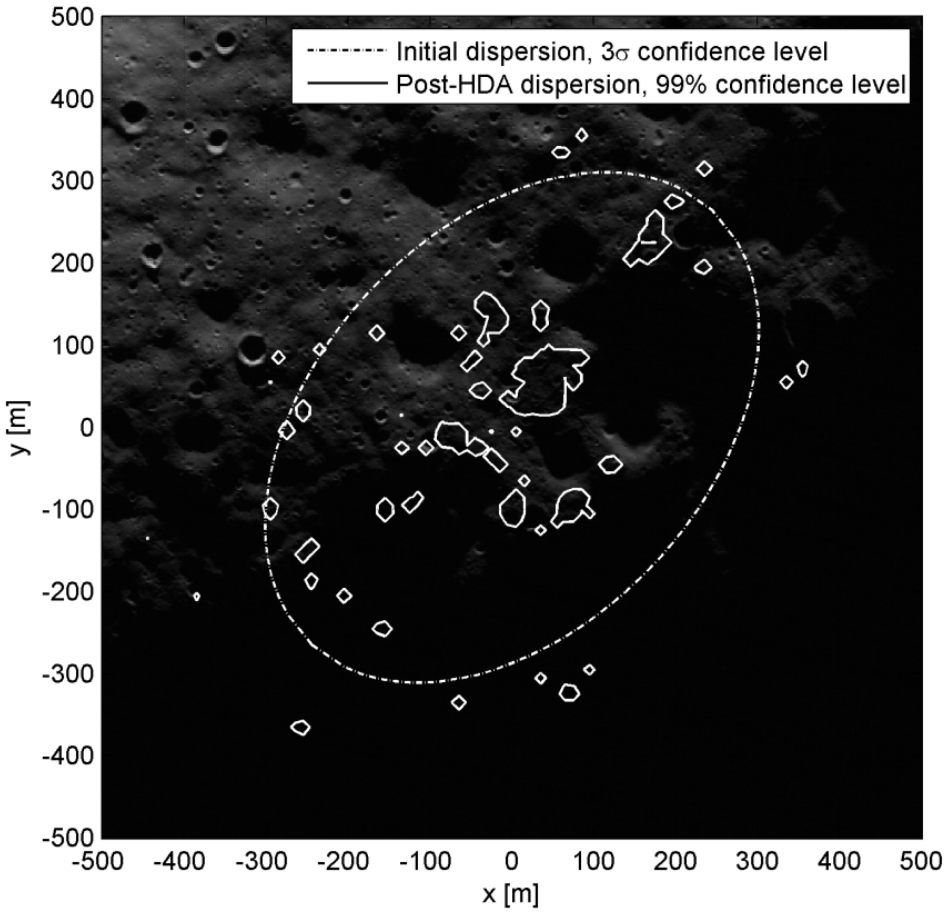

Figure 8-13 Landing dispersion pattern, pre- and post-HDA, superimposed to the landing site image

The landing safety gain by placing the landing dispersion ellipse without HDA capability compared to the HDA-equipped case can be measured by the probability to encounter a potential hazardous terrain property. Figure 8-14 shows the empirical, cumulative distributions of these encounter probabilities. For example, the probability to land on 5° or steeper sloped terrain reduces from 25.1% (without HDA) to less than 0.2% (with HDA). Similarly, the probability to achieve a touchdown on less than 0.5m rough terrain reduces from 22.6% to less than 0.1%. Unlike slope and roughness hazards where larger magnitudes are to be avoided, the stronger illuminated areas – measured in an 8 bit gray scale – are favored. Accordingly, the probability to land in an area better illuminated than 5 in the gray scale increases from 55.1% to 91.9%.

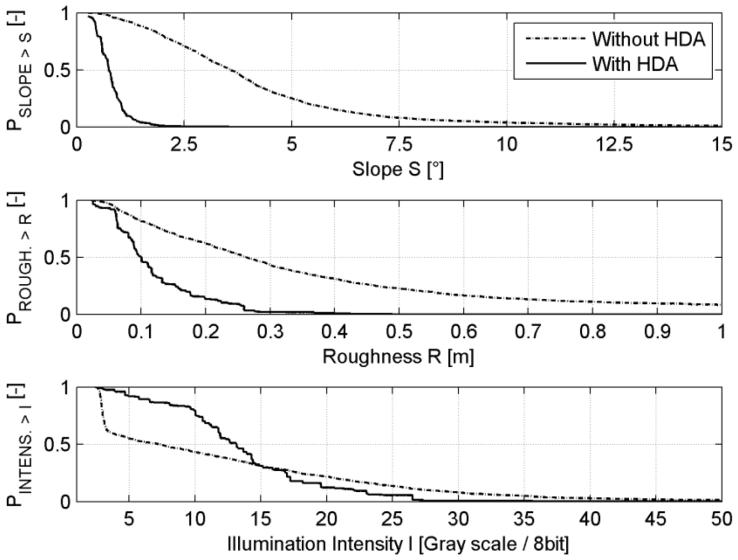

Figure 8-14 Probability to encounter certain slope, roughness and shadow magnitudes for the CR landing scenario: the probabilities to encounter steep slopes and highly rough terrain reduced significantly with an active HDA system. The probability to land in an illuminated part of the landing site increases as intended

8.4 The Landing Safety Assessment

For the final landing safety assessment, this section recalls an important objective made in chapter 1.2 which is to demonstrate the applicability and usefulness of the proposed approach to derive touchdown failure probabilities in the landing site safety assessment context. In chapter 2.2, safety is defined as the complementary state to the failure state: $P_{Safe} = 1 - P_{Fail}$. In the previous section 8.2 the conditional probability of a terrain related failure $P_{Fail \mid Land\ in\ Pixel\ i}$ in terms landing instability, inadvertent ground contact and energy absorption capability have been derived for a robotic lunar landing system. As these probabilities are conditional to a certain landing position and the terrain properties prevailing at this place, the overall terrain-related probability of failure is obtained when the probabilities $P_{Land\ in\ Pixel\ i}$ to actually land at a certain position is considered which is derived in the previous section 8.3. These results are actually the probability terms as required by equation 1.3 which is also well introduced in chapter 1.2. This equation is re-stated below:

$$P_{Safe} = 1 - P_{Fail} = 1 - \sum_i P_{Land\ in\ Pixel\ i} \cdot P_{Fail \mid Land\ in\ Pixel\ i} \qquad \text{(1.3, repeated)}$$

In this equation both probability terms are multiplicatively combined and mean: with a probability of $P_{Land\ in\ Pixel\ i}$ the landing occurs at the associated position of the landing zone and under the terrain conditions at this position the failure probability is $P_{Fail\ |\ Land\ in\ Pixel\ i}$. The summation over all pixels of the landing zone yields the total failure probability and the probability of a failure-free or safe touchdown, respectively. The results of this landing safety assessment for this case study are tabulated in Table 8-8.

Probability of safety with regard to …		P_{Safe} [%], without HDA	P_{Safe} [%], with HDA
Instability		99.85	99.99
Inadvertent ground contact		95.96	99.99
Energy absorption capability exceedance	Exceedance of Primary Strut Stroke Limit	99.97	99.99
	Exceedance of Secondary Strut Stroke Limit (Compression)	99.61	99.82
	Exceedance of Secondary Strut Stroke Limit (Tension)	99.55	99.34

Table 8-8 Probabilities of a safe landing in the case study

Low failure probabilities or high landing safety probabilities are achieved by the ability to either withstand or avoid unfavorable terrain. The first is realized through a design of the landing platform and leg subsystem giving it certain resilience to the terrain slope and roughness. The failure probability curves shown in section 8.2 clearly and not unexpectedly show that a terrain-related failure becomes more likely with an increasing slope or roughness magnitude. The avoidance part is realized through the site selection and navigation with HDA capabilities. The probability to land on a position characterized by a certain slope or roughness value decreases with an increasing magnitude of this value as can be seen in Figure 8-14. Thus the probability to fail and the probability to encounter are complementary to each other and explain the high safety probabilities in Table 8-8. This is the case even without HDA-capability as the "Connecting Ridge" site is only gently sloped and the flat ridge already well inside the landing ellipse. Some values in the table are however striking: The probability for an inadvertent ground contact is ~96% (without HDA) due to several rough spots in the landing zone. These zones coincide well with the areas of interpolated data (Figure 8-4). It is not entirely clear which of the rough spots are real or caused by artifacts in the source DTM. Assuming them as real, the HDA subsystem would clearly reduce an encounter with these spots and, in turn, the inherent uncertainty on the true terrain condition. But the HDA-capability does not improve the probabilities of safety in every case as can be seen from the exceedance probability of the secondary strut (tension) which slightly decreases compared to the non-HDA case. Although shallower places are generally favorable, they increase the burden on the secondary strut's tension direction as indicated by Figure 8-6 (bottom).

From a purely mathematical point of view the assessments outcome is just the result of applying the axioms of stochastic calculus on the given problem. The meaning of probabilistic results is however ambiguous when put into the application context. Two large schools of thought exist in this regard: (i)

Laplace's model considers probabilities a relative frequency of an event, and (ii) the Bayesian interpretation considers the probability as degree of belief or confidence.

This thesis contains indeed elements describing a relative frequency which are mainly the results from sampling the domain of initial touchdown conditions. Out of these samples a certain number exceeded a functional limit thus failed. Likewise, the landing dispersion pattern can be regarded as a position scatter of several landings. Although no actual touchdowns were accounted, but simulations of it using a credible numerical representation, the resultant probabilities could indeed be regarded as relative frequencies. On the other hand the touchdown simulations assume a certain terrain hazard situation beyond the resolution of the used data product to account for the lack of knowledge about the true situation. Confidence levels are computed and used for the subsequent assessments. A landing site terrain context is provided by a set of maps which are derived from remote sensing data products. The slope and roughness situation is represented by an expected value and its variance. The variance hereby reflects the uncertainty about the true value at this position. A higher variance leads into a higher stated probability of failure which consequently carries a lack of confidence in a safe terrain condition. When probability is then regarded as level of confidence it provides a means as decision aid under uncertainty. The author of this thesis follows the latter interpretation here and suggests the following meaning of the results:

In this case study, the available information regarding the landing system, landing site and date, expressed by its respective probability distribution function and relevant parameter, predicts a landing within safe functional limits with about 99% confidence.

9 Summary and Conclusions

Primary objective of this thesis was to evaluate if probabilistic methods are suitable to describe terrain-related failure phenomena. Therefore an analysis process has been developed – the second objective of thesis – in which a numerical representation of the landing system is used to assess whether particular initial touchdown conditions lead to a platform response being within or outside of a functional limit. As these initial conditions are random numbers the platform response is likewise of a random nature. The exceedance of a functional limit is consequently associated with a probability statement. The repetition of these analysis steps for varying terrain properties reveals the dependency of the failure probabilities to these terrain conditions. The results are treated with methods known from the reliability engineering domain to identify certain distribution functions or trends. It can be clearly concluded that terrain-related failure phenomena can be expressed in that way. Furthermore, the analysis process has been used to address the third thesis objective, whether the platform dynamics is robust or sensitive to perturbations by terrain features. Therefore combinations of terrain factors have been combined and the respective results have been compared. This clearly revealed to which terrain feature the platform is robust or not. The specific results for a legged landing platform which was used as study object are summarized below in section 9.1.

With that information, the analysis case was further restricted to the critical feature combinations when applied within an exemplary landing safety assessment, the fourth objective of this thesis. This assessment process involves additional analysis steps to consider the terrain properties from a landing site characterization as well as the dispersions of the actual landing positions. The outcome of this process is a statement to which degree of confidence a landing in a particular site is within safe functional limits of the landing system. This result can support decision-makers during the landing site certification process. A detailed summary of the landing site safety assessment process established with thesis and the associated methods is given in section 9.2 below.

Along these various stations of the analysis process to derive the probabilities of terrain-related failure several questions have been raised as well which could not be addressed within the scope of this study. The most important of them are collected below in section 9.3 to await their further assessment.

9.1 Specific Results for Legged Landing Systems

Specifically for a legged landing system the following primary results and observation were made:

Instability: The probability of an instable touchdown could be modeled as a Log-Normal distribution with respect to terrain slope. Not surprisingly, the likelihood of a lander tip-over increases with steeper slopes, however, this probability varies when further terrain properties are taken into account. The addition of terrain roughness increases the variance in the distribution which in turn further increases the probability of touchdown instability especially in the range of small slopes. The influence of boulder is small compared to the effects of crater-induced roughness. Granular, Regolith-like soil improves the probability of attaining a stable landing compared to a hard, rigid surface. This effect is due to the soil's contribution the touchdown energy absorption.

Exceedance of the energy absorption capability: this capability is measured through the primary and secondary strut's stroke limit. For none of these struts a probability distribution with regard to a terrain property could be identified but exponential trends for the associated failure probabilities were observed with identifiable parameters. Regarding the primary strut, the exceedance probabilities are highest in the presence of crater or boulder caused roughness which is attributable to the added potential of blocking a sliding footpad. The exceedance probability increases with stepper slopes.

Regarding the secondary strut stroke, it is again evident that a small dependency to the terrain slope exists for both stroke directions. The most notably difference is that the probability to exceed the tension stroke direction increases towards shallower slopes but oppositely for the compression stroke direction it increases by a similar order of magnitude towards steeper slopes. This leads to the conclusion that the joint minimum of the secondary strut's stroke limit exceedance probability is not achieved on a non-sloped surface but on a shallow sloped surface.

Inadvertent ground contact: The touchdown analysis cases with regard to ground clearance showed that the reduction in clearance underneath the landing platform is most severe if the touchdown occurs on a non-sloped surface. This observation correlates to the higher exceedance probability for secondary strut's tension stroke limit on non-sloped surfaces due to kinematic relation between leg assembly motion and belly clearance. The clearance distribution could be modeled by a Normal-distribution. The loss of ground clearance becomes larger on granular soil compared to a touchdown on hard, rigid surface. In the robotic lunar landing example the mean loss of clearance with regard to a flat surface plane approximately 20% is attributable to the footpad's penetration into the soil while the majority is caused by the stroking struts. The terrain roughness contribution from boulder or crater to the net clearance below the landing platform is additive the ground clearance distribution and allows the calculation of the probability of an inadvertent ground contact.

9.2 The Landing Safety Assessment Process

With all these probabilities being conditional to a terrain property descriptor, the actual failure probabilities become a matter of choice for a certain landing site. The derivation of suitable terrain property maps is thereby part of the landing site characterization. Each pixel of the derived slope map (roughness map respectively) represents this terrain property for the associated landing site coordinate. An assessment of this position using the probability distribution function of the failure mode of interest yields the probability for a failure upon touchdown at that particular position. The application to all pixels of the map yields a raster map displaying zones of a certain failure probability. As "safety" is defined as the complementary set to "failure" the map outlines zones of high prospects for a safe landing. A further element to derive the final landing safety probability is the consideration of the landing position dispersion. This stems basically from the variances in the guidance and control subsystem. Although the analysis of that subsystem is not part of this thesis, its effect is of high relevance for the further results computation. Therefore the data interface for the dispersion of flight systems with and without hazard detection and avoidance capability is provided as part of the case study.

The three elements landing platform touchdown dynamics, navigation and landing guidance and the resultant position dispersion and the landing site terrain context provide the ingredients for landing safety assessment. In that regard such landing safety assessment is a truly multi-disciplinary task within the systems and mission engineering process. The propagation of the landing system and site information into a coherent safety assessment is facilitated by expressing it as random numbers and using stochastic calculus. The inherent strength of this approach is that the uncertainties and variances in such an analysis are as well considered in the assessment. The work flow developed in this thesis is graphically depicted in Figure 9-1.

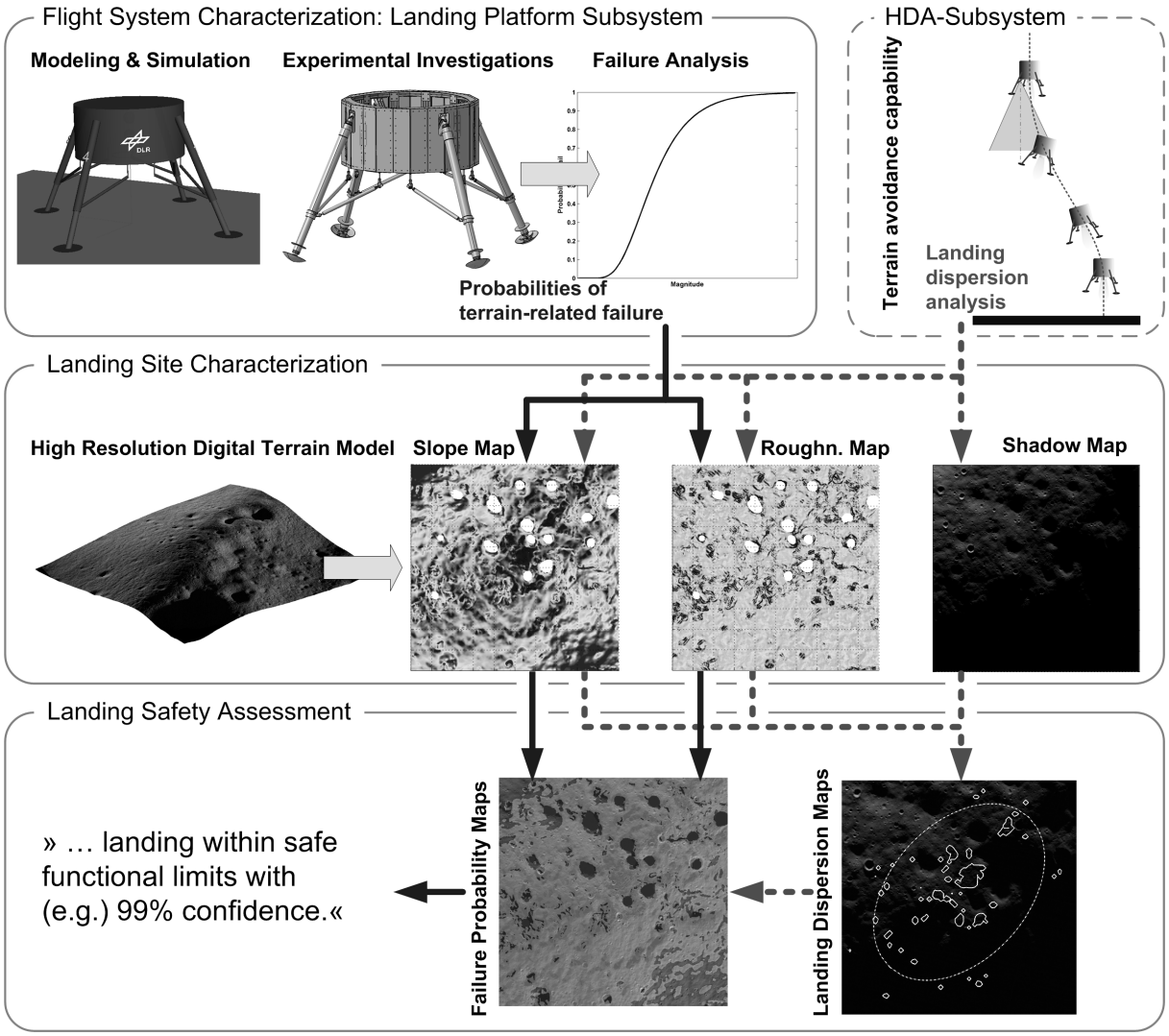

Figure 9-1 Landing site safety assessment flow: this flow chart provides an overview about the different analysis steps developed in this thesis and their interaction towards a safety statement on a given landing site

The process to address the studies objectives and to arrive at the above stated primary results includes various modeling, simulation and analysis steps which contain themselves noteworthy results. The analysis process starts with the set-up of a numerical touchdown simulation. The purpose of a computer simulation of the touchdown event stems from the necessity to have a kinematic and dynamical representation of the vehicle to get full insight into the relation of the various effects deciding upon a successful touchdown. The multi-body formalism was chosen to account for the rigid-body dynamic character of the touchdown. This numerical model is described in chapter 3 and implemented into a commercial multi body simulation software tool. Its model topology describes thereby a four leg Cantilever-type landing system. The model elements are parametrized and allow a scaling of the represented landing system as long as the topology coded in the numerical model remains unchanged. The vehicle-soil-interaction is one form of a terrain-related behavior and is considered in this chapter by formulating a dedicated foot-pad-to-soil contact force law. For this particular aspect dedicated investigations were made on component level which led into a force law implementable into this multibody simulation.

Complementary experimental investigations on the touchdown dynamics play a crucial role for the analysis objectives of this work. In the frame of a test campaign with a physical model of a landing platform, dubbed the Lander Engineering Model LEM, described in chapter 4, drop tests have been conducted. Two of the four test cases aimed at obtaining an experimental fix of the stability boundary of that platform. The other two test cases of this campaign aimed at the evaluation of critical load cases such as maximum compression load onto the primary and secondary struts as well as tension loads on the secondary struts.

The modeling part of the thesis closes with the validation (chapter 5) of the simulation with just that experimental data. Therefore the experimentally executed test cases were implemented and re-done using the numerical simulation. The numerical and experimental test results were correlated and the numerical model step-wise refined until an apriori defined quality criterion was met. Such a quality criteria set – qualitative and quantitative – has been composed for this purpose. In the concrete case of the LEM, a prediction goodness is achieved with is in an acceptable range for similar analyses. The achieved goodness ranges from "good" for the secondary struts simulation model output to "very good" for the primary struts and "excellent" for the platform's attitude angles and their rates. The resultant credibility of the numerical results is a prerequisite for all subsequent analyses based on the touchdown simulation. The validation aspect generates however continuing questions which are addressed further below.

In the key chapter 6 the validated numerical model is then taken as a base to develop the touchdown failure analysis upon. Since the initial touchdown conditions are represented by random numbers due to the dispersions within the guidance and control processes, it becomes immediately clear that the vehicle's response will likewise be of a stochastic nature. Starting with the theory on the transformation of random numbers the mathematical methods needed to process the simulation results are deduced. The numerical multibody simulation is a deterministic simulation which has to consider however the randomness of the initial conditions. Assuming that the landing platform under investigation is well designed, the analysis should expect very small limit of function exceedance probabilities. To take this into consideration and to achieve a faster convergence than classical "crude" Monte-Carlo methods an importance sampling method is used in this thesis instead. Hereby the multibody simulation is nested in a sampling shell and the initial condition parameter space is sampled uniformly rather than preempting a certain probability distribution of the initial conditions. A post processing step factors in then these distributions. This decoupling of the computationally intensive probing of the initial condition space by the numerical simulation and the factoring of the initial conditions actual distributions into the platform's response has a significant advantage besides an improved convergence. If the initial conditions distributions change during the landing system design process their effect can easily factored in again by just re-running the post-processing with updated values. The probability to exceed a functional limit is subsequently determined through an empirical, non-parametric cumulative distribution function. This step is completed by an identification if the empirical distribution suffices probability function (either a normal, log-normal or Weibull-distribution), whose parameter are then estimated. This first set of post-processing steps yields probabilities associated to a given and fixed terrain property descriptor. A second processing step assesses if the probabilities to exceed a respective limit of function out of the first step are functionally related to a varying terrain property. Again parameter identification determines if these data points suffice a probability distribution or at least an identifiable trend. This analysis, applied exemplary on the LEM, yields exactly the conclusions regarding the terrain-related probabilities of failure which are summarized at the beginning of this Conclusions chapter.

As already stated, the probabilities of failure are conditional to the terrain properties prevailing at a landing site of interest. Consequently, the actual of slope and roughness situation at that place must be taken into account. Thus the landing site characterization is a mandatory supplemental analysis task. A high-resolution (pixel size smaller than the landing gear footprint) digital terrain model provides the necessary base for such a landing site characterization. With the landing gear footprint being the characteristic base-length for these terrain properties, their derivation is not independent from the landing system under study anymore. A robust estimation algorithm allows the extraction and separation of the terrain slope and roughness. The implementation and verification of such an algorithm is described in chapter 7. It is applied to an example DTM featuring the Lunar South Pole "Connecting Ridge" region.

9.3 Open Points for further Studies

Applicability to other landing system types: The analysis scheme in this thesis is developed specifically for legged landing systems. The scheme and the conclusions drawn for this class of systems cannot be directly transferred to other classes. Besides a different numerical model representing that system a change to the presented mathematical methodology might be necessary in case computationally more demanding FEM methods for airbags or crushables are used instead of MBS methods for legged variants. However, beyond the point where a specific numerical model of that landing system is used to derive the failure distribution models, the proposed mathematical methods do not refer anymore specifically to a particular systems hence it suggests itself to be applied generally. This assumption is also supported by the fact that touchdown system functions such energy absorption or stability are recurring functions regardless of its technical realization. A further study should investigate the communalities and differences in such an analysis scheme to broaden its applicability to other than legged landing systems.

Numerical model validation: The validation of the numerical model of the legged landing system in this thesis arrived at a point where the difference experimental and numerical results for the LEM's touchdown dynamics fell within an acceptable tolerance. While this result reassures that the used model fidelity is sufficient to analyze landing failure problems, it remains unclear how this predictive capability changes when the numerical model is re-parameterized to represent a landing platform of a different size. Supplementary studies on scaling effects and the propagation of epistemic uncertainty could address this point.

Numerical model verification: In addition to the model validation also the verification is an important element in the modeling and simulation part. As a commercial multibody software tool was used, verification aspects on numerical solvers were out of scope in this work which relied instead on general quality assurance measures of the software vendor. It is suggested to define also verification criteria specifically for related multibody problems to assess or benchmark the software tool's performance in terms of numerical accuracy, convergence and stability.

Remote sensing data products: The terrain context is provided by a high-resolution digital terrain model which itself is the product out of an algorithmic and computerized treatment of remote sensing data. This produces to some extent artifacts especially in the transition between different raw data products or area of no data (some permanently shadow areas here). Although sometimes clearly identifiable by a visual inspection it is difficult to treat and remove them. They cause unrealistically high values for slope and roughness and thus artificially bias the analysis result to a locally higher probability of failure. In the case of this thesis this effect has been excepted as it reflects somehow again a deficit in knowledge which in turn lowers the confidence in a safe landing. Nevertheless the

question remains if and how the data products used for this analysis can be further improved. In that area belongs also the question how to meaningful fill or interpolate gaps in the data products.

Landing site illumination conditions: local shadows at the landing site are not directly affecting the touchdown performance of the landing platform but might be a to-be-avoided hazard for an HDA-capable flight system. In case of this study this was indeed required as with the Lunar South Pole »Connecting Ridge« a high latitude site with pronounced shadowing was assumed. A shadow map was however "mimicked" by just taking a high-resolution image of the site taken at a representative sun position. A real landing site analysis shall replace this reliance by simulating the illumination conditions for user defined date and based on the same high-resolution DTM as used for the slope and roughness determination.

Landing dispersion prediction: The landing dispersion analysis is a large domain on its own and has already a significant heritage for actual flight missions. However the consideration of flight systems with active hazard detection and avoidance capability is also new in this area and an approach to a stochastic modeling has been suggested by the author of this thesis in separate publications. This method is of relevance here as it provides an interface to the respective subsystem domain. Nevertheless this branch in the landing safety analysis flow (Figure 9-1) should to be elaborated further with the same rigorousness as the touchdown system in this work.

With the developed touchdown failure analysis scheme and its associated methods a contribution to the landing safety assessment is made. It may help system and mission engineers to quantify and communicate the necessary confidence in design or site selections when designing for rewarding, but challenging landing mission. The questions raised may trigger follow-on work to further broaden the engineering knowledge for such missions.

References

Adler, M., et al.: Entry, Descent And Landing Roadmap, Technology Area 09. NASA, April (2012)

Albertz, J.: Einführung in die Fernerkundung, Grundlage der Interpretation von Luft- und Satellitenbildern. 3. Auflage, WBG Darmstadt (2007)

Austin Barry, B.: Errors in Practical Measurement in Science, Engineering and Technology. John Wiley & Sons (1978)

Ball, A., et al.: Planetary Landers and Entry Probes. Cambridge University Press (2007)

Ball, R.: The Fundamentals of Aircraft Combat Survivability Analysis and Design. 2nd edition, AIAA Education Series (2003)

Beirlant, J., et al.: Statistics of Extremes – Theory and Applications. Wiley Series in Probability And Statistics, John Wiley & Sons (2004)

Bendix Corporation, Final Report Lunar Module (LM) Soil Mechanics Study. NASA CR 92208 (1968)

Bernard, D., Golombek, M.: Crater and Rock Hazard Modeling for Mars Landing. AIAA Space 2001 Conference and Exhibition, AIAA 2001-4697, USA (2001)

Birolini, A.: Quality and Reliability of Technical Systems – Theory, Practice, Management. 2nd Edition, Springer (1997)

Blanchard, U.: Evaluation of a Full-Scale Lunar Gravity Simulator by Comparison of Landing-Impact Tests of Full-Scale and a 1/6-Scale Model. NASA TN D-4474 (1968)

Bonfiglio, E., et al.: Landing Site Dispersion Analysis and Statistical Assessment for the Mars Phoenix Lander. Journal of Spacecraft And Rockets, Vol. 48, No. 5, September – October (2011). doi: 10.2514/1.48813

Bornemann, F., et al.: Vom Lösen numerischer Probleme, Ein Streifzug entlang der "SIAM 10x10 Digit Challenge". Springer Verlag (2006)

Bronstein, I., et al.: Taschenbuch der Mathematik. 3. Auflage der Neubearbeitung, Verlag Harri Deutsch, Frankfurt am Main, Thun (1997)

Buchwald, R., et al.: First Steps in Experimental Investigation of Legged Lunar Lander Touchdown Dynamics. Proceedings of the 59th International Astronautical Congress, IAC-08.A3.2.B9, Glasgow / United Kingdom (2008)

Buchwald, R., et al.: Stepwise Development Testing and Technology Demonstration of a Landing System with Landing Legs. Proceedings of the Deutscher Luft- und Raumfahrt Kongress 2012, Bremen (2012)

Buchwald, R., et al.: Verification of Landing System Touchdown Dynamics – A Status Report of a German Joint Cooperative Team on Landing Technology. Proceedings of the 62nd International Astronautical Congress, IAC-11.A3.1.3, Cape Town / South Africa (2011)

Cappellari, J.: Where on the Moon? An Apollo Systems Engineering Problem. The Bell System Technical Journal, Vol. 51 No. 5, May-June (1972)

Carpenter, J., et al.: Scientific preparations for lunar exploration. Planetary and Space Science 74 (2012). doi:10.1016/j.pss.2012.08.002

Carrier, W., et al.: Physical Properties of the Lunar Surface. LunarSourcebook – A User's Guide to the Moon. G. H. Heiken, D. T. Vaniman and B. M. French (Eds.), Cambridge University Press, pp. 475 – 594 (1991)

Caspary, W.: Fehlertolerante Auswertung von Messdaten, Daten- und Modellanalyse, robuste Schätzung. Oldenbourg Verlag, München (2013)

Cheatham, D., Bennett, F.: Apollo Lunar Module Landing Strategy, Apollo Lunar Landing Mission Symposium. NASA Manned Spacecraft Center, Houston / Texas, June 25-27 (1966)

Cizelj, L., et al.: Application of first and second order reliability methods in the safety assessment of cracked steam generator tubing. Nuclear Engineering and Design 147 (1994)

Craig, R.F.: Craig's Soil Mechanics. 7th edition, Spon Press (2004)

Crowder, M.: Statistical Analysis of Reliability Data. Chapman & Hall, London (1991)

De Rosa, D., et al.: Characterisation of potential landing sites for the European Space Agency's Lunar Lander project. Planetary and Space Science 74 (2012). doi:10.1016/j.pss.2012.08.002

Diedrich, T., et al.: Lunar Lander Phase B1 – Status, Mission and System Concept. Proceedings of the 62nd International Astronautical Congress, IAC-11.A3.2B.3, Cape Town, South Africa (2011)

Dietrich, C.F.: Uncertainty, Calibration and Probability – The Statistics of Scientific and Industrial Measurement. Published by Adam Hilger, London (1973)

ECSS European Cooperation for Space Standardization. ECSS P-001B Glossary of terms. ESA-ESTEC, Nordwijk / Netherlands (2004)

ECSS European Cooperation for Space Standardization. ECSS-Q-ST-40C Space Product Assurance – Safety. ESA-ESTEC, Nordwijk / Netherlands (2009)

ECSS European Cooperation for Space Standardization, Space Engineering – Structural Finite Element Models. ECSS-E-ST-32-03C. ESA-ESTEC, Nordwijk / Netherlands (2008a)

ECSS European Cooperation for Space Standardization, Space Engineering – Modal Survey Assessment. ECSS-E-ST-32-11C. ESA-ESTEC, Nordwijk / Netherlands (2008b)

ESA Landing System Development, Statement of Work. TEC-MCS/2008/1737/In/BL issue 1, revision 0 (2008)

Girlich, H.-J.: Diskrete Stochastische Entscheidungsprozesse. Teubner Verlagsgesellschaft, Leipzig (1973)

Golombek, M., et al.: Selection of the Mars Exploration Rover landing sites. Journal of Geophysical Research, Vol. 108, No. E12, 8072, doi:10.1029/2003JE002074 (2003)

Golombek, M.: Selection of Mars Landing Sites. Presentation at the Landing Sites for Exploration Missions Workshop, Leiden / The Netherlands (2011)

Gowen, R.: Potential Applications of Micro-Penetrators within the Solar System. International Planetary Probes Workshop IPPW7, Barcelona / Spain (2010)

Grote, K.-H., Feldhusen, J. (eds.): Dubbel – Taschenbuch für den Maschinenbau. 21st Edition, Springer (2004)

Haueis, M., et al.: Herausforderung Toleranzkettendesign für robuste mechatronische Fahrzeugfunktionen. 23. Tagung Technische Zuverlässigkeit, VDI-Berichte Nr. 1984, (2007)

Holmberg, N., et al.: Viking ’75 Spacecraft Design and Test Summary, Volume I – Lander Design. NASA Reference Publication 1027 (1980)

Houdou, B., et al.: The European Lunar Lander: A Human Exploration Precursor Mission. 9th International Planetary Probe Workshop, Toulouse / France (2012)

Howlett, J.: An Analytical Procedure For Predicting The Two-Dimensional Impact Dynamics Of Spacecraft Landing Gear. NASA TN D-4434, Langley Station (1967)

JMP Statistical Discovery. version 11.1.1 (32 bit), www.jmp.com (2014)

Johnson, A.E., et.al.: Lidar-Based Hazard Avoidance for Safe Landing on Mars, Journal of Guidance, Control, and Dynamics. Vol. 25, No.6, November – December (2002)

Kinnersley, M., Bischof, B.: A Lunar Logistics Lander For Europe. AIAA Space Conference & Exposition, AIAA 2009-6742, Pasadena / California (2009)

Knocke, P., et al.: Mars Exploration Rover Landing Dispersion Analysis. AIAA/AAS Astrodynamics Conference, AIAA 2004-5093, Rhode Island (2004)

Kramer, U., Neculau, M.: Simulationstechnik. Fachbuchverlag Leipzig (1998)

Kroese, D., et al.: Handbook of Monte Carlo Methods. Wiley Series in Probability And Statistics, John Wiley & Sons (2011)

Lee, S.H., Chen, W.: A comparative study of uncertainty propagation methods for black-box-type problems. Structural and Multidisciplinary Optimization 37, 239–253 (2009). doi: 10.1007/s00158-008-0234-7

Liebernickel, T.: DLR Footpad-to-Soil Contact Force Law and Touchdown Assessment – SIMPACK User Routine and Scripts for DLR Bremen. Report No 2012-05-13_DLR_Bremen, SIMPACK AG (2012). Internal Report

Limpert, E., et al.: Log-normal Distributions across the Sciences: Keys and Clues. BioScience Vol. 51, No. 5, May (2001)

Lindsey, J.K.: Statistical Analysis of Stochastic Processes in Time. Cambridge University Press (2004)

LN 9300 Blatt 1, Luftfahrt Norm 9300, Beuth Verlag (1970)

Loomes, G., Sugden, R.: Incorporating a stochastic element into decision theories. European Economic Review 39, 641-648, (1995)

Masursky, H., Crabill, N.: Viking Site Selection and Certification. NASA SP-429, Washington DC (1981)

MATLAB, version R2011b (64 bit), The MathWorks, Inc (2011)

McEwen, A.S., et al.: Mars Reconnaissance Orbiter’s High Resolution Imaging Science Experiment (HiRISE). Journal of Geophysical Research, 112, E05S02 (2007). doi:10.1029/2005JE002605

Melloni, S., et al.: GNC Solution for Lunar Pin-Point and Soft Landing. Proceedings of the Global Lunar Conference, GLUC-2010.1.5.B.1, Beijing (2010)

Moebius, B., et al.: Miniaturized 3D-LIDAR for Lunar Landing. 26th International Symposium on Space Technology and Science, Japan (2008)

Montgomery, D.: Design and Analysis of Experiments. 7th Edition, John Wiley & Sons (2009)

MSC Software, http://www.mscsoftware.com/product/adams. Accessed August 2013

MSL Mars Science Laboratory Landing. Press Kit (2012)

Müller, T., Müller, H.: Modelling in Natural Sciences – Design, Validation and Case Studies. Springer-Verlag (2003)

Muraca, R., et al.: A Monte Carlo Analysis of the Viking Lander Dynamics at Touchdown. NASA TN D-7959, Langley Research Center (1975)

NASA Technical Standard, Standard for Models and Simulations. NASA-STD-7009, Washington DC (2008)

Neveu, D., et.al.: Next Lunar Lander: Descent & Landing GNC Analysis, Design and Simulation. AAS Guidance, Navigation & Control Conference, AAS 10-065, Breckenridge / Colorado (2010)

Oberkampf, W., et al.: Verification, validation and predictive capability in computational engineering and physics. Applied Mechanics Review, Vol 57, No 5, September (2004). doi: 10.1115/1.1767847

Oberst, J., et al.: Apollo 17 Landing Site Topography from LROC NAC Stereo Data – First Analysis And Results. 41st Lunar and Planetary Science Conference, No. 2051 (2010)

Pike, R.: Size-dependance in the shape of fresh impact craters on the moon. in: D.J. Roddy et.al (eds.), Impact and Explosion Cratering, Pergamon Press, pp.489-509, New York / USA (1977)

Pillinger, C., et al.: The guide to Beagle 2. Faber and Faber (2003)

Portigliotti, S., et al.: EXOMARS-2016 GNC Approach for Entry Descent and Landing Demonstrator. International Planetary Probes Workshop IPPW8, Portsmouth / USA (2011)

Pradier, A., et al.: The First European Lunar Lander And The ESA-DLR Approach To Its Development. Proceedings of the International Astronautical Congress, IAC-10.A3.2B.8, Prague (2010)

Richards, M.: Multi-Attribute Tradespace Exploration For Survivability. PhD thesis, Massachusetts Institute of Technology, June (2009)

Robinson, M.S., et al.: Lunar Reconnaissance Orbiter Camera (LROC) Instrument Overview, Space Science Reviews. Vol.150, Issue 1-4, pp 81–124, (2010). doi: 10.1007/s11214-010-9634-2

Rogers, W.: Apollo Experience Report – Lunar Module Landing Gear Subsystem. NASA TN D-6850, Houston (1972)

Ross, S.: Statistik für Ingenieure und Naturwissenschaftler. 3. Auflage, Spektrum Akademischer Verlag (2006)

Schiehlen, W., Eberhard, P.: Technische Dynamik – Rechnergestützte Modellierung mechanischer Systeme im Maschinen- und Fahrzeugbau. 3. Auflage, Vieweg+Teubner Verlag (2012)

Schmid, F., Trede, M.: Stochastische Dominanz. SpringerLink, Springer (2006). doi:10.1007/3-540-29795-2_8

Scholten, F., et al.: Mars Express HRSC Data Processing – Methods and Operational Aspects. Photogrammetric Engineering & Remote Sensing Vol. 71, No. 10, pp. 1143–1152, October (2005)

Scholten, F., et al.: NAC_DTM_ESALL_CR1, Connecting Ridge Potential Landing Site for ESA Lunar Lander. http://wms.lroc.asu.edu/lroc/view_rdr/NAC_DTM_ESALL_CR1 (2012)

Schröder, S., et al.: Footpad-Terrain Interaction Tests with the Robotic Landing and Mobility Test Facility LAMA. Proceedings of the 62nd International Astronautical Congress, IAC-11.A5.1.9, Cape Town / South Africa (2011)

Schwarzlander, H.: Probability Concepts and Theory for Engineers. First Edition, John Wiley & Sons (2011)

Schwerin, R.v.: Multibody System Simulation, Numerical Methods, Algorithms and Software. Springer (1999)

Schwertassek, R., Wallrapp, O.: Dynamik flexibler Mehrkörpersysteme. Vieweg (1999)

Schwientek, C.: Quality Assurance in the Software Development at INTEC. SIMPACK User Meeting '04, http:\\www.simpack.com (2004). Accessed July 2013

SIMPACK Documentation. Version 9.1.1, SIMPACK AG (2012)

SIMPACK, http://www.simpack.com, Gilching / Germany (2013). Accessed August 2013

Spencer, D., et al: Phoenix Landing Site Hazard Assessment and Selection. Journal of Spacecraft and Rockets, Vol.46, No. 6, November – December (2009). doi: 10.2514/1.43932

Stamatelatos, M., et al.: Probabilistic Risk Assessment Procedures Guide for NASA Managers and Practitioners. Version 1.1, Washington DC (2002)

Thrun, S., et al.: Probabilistic Robotics. The MIT Press, Cambridge, Massachusetts (2006)

Vanoutryve, B., et al.: An Analysis of Illumination and Communication Conditions near Lunar South Pole Based on Kaguya Data. 7th International Planetary Probe Workshop, Barcelona/Spain (2010)

Walton, W., Durling, B.: A Procedure for Computing the Motion of a Lunar Landing Vehicle During the Landing Impact. NASA TN D-4216 (1967)

Whitmore, G.A., Findlay, M.C. (Eds.): Stochastic Dominance, An Approach to Decision-Making Under Risk. Lexington Books (1978)

Wilun, Z., Starzewski, K.: Soil Mechanics in Foundation Engineering. Vol. 2, Intertext Books, London / UK (1972)

Witte, L., et al.: A Vehicle Dynamics Test Facility For Planetary Surface Mobility. Proceedings of the 11th European Conference on Spacecraft Structures, Materials & Mechanical Testing (ECSSMMT), Toulouse/France (2009)

Witte, L., et al.: Touchdown-Down Dynamics And Terrain Interaction Of Planetary Landing Systems. Proceedings of the Global Lunar Conference, GLUC-2010.15.C13, Beijing / China (2010)

Witte, L.: Landing & Mobility Test Facility – Technical Description. LAMA-DLR-RY-0001_i1_r0, Bremen / Germany (2011). Internal Report.

Witte, L.: Stochastic Modeling of a Hazard Detection and Avoidance Maneuver – The Planetary Landing Case. Reliability Engineering and System Safety 119, 259-269, (2013). doi: 10.1016/j.ress.2013.06.033

Witte, L.: Landing Dispersion Analysis for Hazard Avoidance Capable Flight Systems. Poster Presentation, Science and Challenges of Lunar Sample Return Workshop, ESA/ESTEC, 18th – 19th of February (2014)

Yin, G., Zhang, Q.: Discrete-Time Markov Chains, Two-Time-Scale Methods and Applications. Springer Science + Business Media (2005)

Zhakarov, A.: Phobos Grunt, Presentation at the ESA Workshop on GNC for Small Body Missions. ESTEC, Nordwijk / Netherlands (2009)

Zhou, Q., Liu, X.: Assessing Uncertainties in Derived Slope and Aspect from a Grid DEM. in Q. Zhou, B. Lees, G. Tang (eds.), Advances in Digital Terrain Analysis. Lecture Notes in Geoinformation and Cartography, Springer (2008)

Zupp, G.A., Doiron, H.H.: A Mathematical Procedure For Predicting The Touchdown Dynamics Of A Soft-Landing Vehicle. NASA TN D-7045, Houston (1971)

A1 – Touchdown System Reference Data

The following table provides the data underlying the touchdown v-m-diagram (Figure 2-1) as well as further background and references.

Mission	Short	Dest-ination	Type	T/D-System	T/D-Velocity [m/s]	T/D-Mass [kg]	Nation-ality	Ref.
Mars Pathfinder	MPF	Mars	Robotic	Airbag	14.0	410	USA	*Ball et al. 2007*
Mars Exploration Rover	MER	Mars	Robotic	Airbag	14.0	540	USA	*Ball et al. 2007*
Beagle2	BGL	Mars	Robotic	Airbag	16.7	48	UK	*Pillinger et al. 2003*
Mars Science Laboratory	MSL	Mars	Robotic	Skycrane	0.75	900	USA	*MSL2012*
Exomars 2016 EDL Demo	EXM	Mars	Robotic	Platform	3.7	280	ESA	*Portigliotti et al. 2011*
Venera 14	V14	Venus	Robotic	Platform	7.50	760	USSR	*Ball et al. 2007*
Moonlite	MLI	Moon	Robotic	Penetrator	300	13	UK	*Gowen 2010*
Mars 96	M96	Mars	Robotic	Penetrator	80	63	USSR	*Ball et al. 2007*
Deep Space 2	DS2	Mars	Robotic	Penetrator	200	4	USA	*Ball et al. 2007*
Lunar A	LNA	Moon	Robotic	Penetrator	285	14	JPN	*Ball et al. 2007*
Apollo	APL	Moon	Human	Legged	0.9	8300	USA	*Ball et al. 2007*
ESA Lunar Cargo Lander	LCL	Moon	Robotic	Legged	<3.0	3500	ESA	*Kinnersley 2009*
ESA Lunar Lander	ELL	Moon	Robotic	Legged	2.0	800	ESA	*ESA 2008*
LK Lander	LKL	Moon	Human	Legged	<2.0	<5700	USSR	*Ball et al. 2007*
Philae	PHI	Small Body	Robotic	Legged	<1.2	98	GER	*Ball et al. 2007*
Phobos Grunt	PHG	Small Body	Robotic	Legged	<1.0	1400	RUS	*Zhakarov 2009*
Luna 16	L16	Moon	Robotic	Legged	4.8	1880	USSR	*Ball et al. 2007*
Luna 17	L17	Moon	Robotic	Legged	2.0	1900	USSR	*Ball et al. 2007*
Phoenix	PHX	Mars	Robotic	Legged	1.6	328	USA	*Ball et al. 2007*
Surveyor	SRV	Moon	Robotic	Legged	4.2	300	USA	*Ball et al. 2007*
Viking 1+2	VIK	Mars	Robotic	Legged	2.4	612	USA	*Ball et al. 2007*

A2 – Masses and Geometries of Landing System Models

This annex contains the principal dimensions and the mass breakdown of the body elements of the numerical touchdown simulation model described in chapter 3.

Lander Engineering Model (LEM-4C)

	Leg	Primary Strut	Secondary Strut	Footpad	Platform	Center Mass	Trim Mass	Gripper Flange
R_a [mm]	40	34	17	150	600	93	n/a	n/a
R_i [mm]	35	25	13	n/a	550	68	n/a	n/a
L [mm]	840	830	619	40	580	320	40	50
W [mm]	n/a	n/a	n/a	n/a	n/a	n/a	175	100
H [mm]	n/a	n/a	n/a	n/a	n/a	n/a	175	215
m [kg]	10.77	9.67	1.50	2.70	141.00	20.80	9.20	7.69
ρ_{eff} [kg/m³]	10883	6984	6289	954	1345	5172	7510	7153
I_{xx} [kgm²]	0.0152	0.0086	0.0003	0.0304	46.7063	0.1364	0.0470	0.0360
I_{yy} [kgm²]	0.6409	0.5594	0.0481	0.0155	27.3058	0.2457	0.0247	0.0312
I_{zz} [kgm²]	0.6409	0.5594	0.0481	0.0155	27.3058	0.2457	0.0247	0.0080

Robotic Lunar Lander (RLL)

	Leg	Primary Strut	Secondary Strut	Footpad	Platform	Trim Mass
R_a [mm]	43	35	25	175	1280	250
R_i [mm]	35	25	20	n/a	0	0
L [mm]	2030	1070	1240	40	1658	500
m [kg]	4.60	4.10	0.65	1.50	604	100
ρ_{eff} [kg/m³]	1240	2032	741	390	71	1018
I_{xx} [kgm²]	0.0070	0.0038	0.0003	0.0230	494	3.12
I_{yy} [kgm²]	1.5832	0.3931	0.0835	0.0117	385	3.64
I_{zz} [kgm²]	1.5832	0.3931	0.0835	0.0117	385	3.64

A3 – Soil Mechanical Data

This annex provides ancilliary material on the computation of the soil mechanical coefficients as well as the associated descriptors of the reference soils. These descriptors are the internal friction angle Φ, the cohesion C, the bulk density ρ, and relative density D_r . The coefficients of the dynamic soil mechanical model are derived according the results documented in *Bendix 1968* as:

$$C_{ms} = 29 \cdot (3 + 9.25 \cdot D_r) \cdot \tan\Phi^{1+2.5 \cdot D_r}$$

$$C_D = 0.8 + (4 + 80 \cdot D_r) \cdot n_g \cdot \tan\Phi \quad \text{if Dr} < 0.5,$$

$$C_D = 0.8 + 4 \cdot n_g \cdot \tan\Phi \cdot e^{4.83 \cdot D_r} \quad \text{if Dr} \geq 0.5,$$

and with $n_g = g/9.81$.

The coefficients of the static, ultimate bearing capacity are derived from the theory for shallow foundations which is described in *Craig 2004* and *Wilun 1972*:

$$C_{Nc} = s_c \cdot C^* \cdot N_c$$

$$C_{Nq} = s_q \cdot \rho \cdot g \cdot N_q$$

$$C_{N\gamma} = s_\gamma \cdot \rho \cdot g \cdot D_{Pad} \cdot N_\gamma / 2$$

The factors N_q, N_c, and N_γ are defined as following:

$$N_q = \exp(\pi \cdot \tan\Phi^*) \cdot \tan^2(45° + \Phi^*/2)$$

$$N_c = (N_q - 1)/\tan\Phi^*$$

$$N_\gamma = 2 \cdot (N_q - 1) \cdot \tan\Phi^*$$

C^* and Φ^* are corrections to the cohesion and internal friction which are applicable to loosely consolidated soils *Wilun 1972*:

$C^* = 2/3 \cdot C$, $\Phi^* = \arctan(2/3 \cdot \tan\Phi)$

Shape factors consider the shape of the footing which is here the circular disk of the footpad:

$s_c = 1.25$, $s_q = 1.20$, $s_\gamma = 0.60$

The table below contains the parameter of the quartz sand (Wf34) which was used in the footpad-to-soil force law validation tests as well as parameter representing Lunar regolith assumed in the touchdown simulations for the Lander Engineering Model (LEM) and the Robotic Lunar Lander (RLL) in the case study.

Parameter		**Quarz Sand (Wf34)** Ref.: *Schröder et al. 2011*	**Lunar Regolith** Ref.: *Carrier et al. 1991*
Internal friction angle	Φ [°]	32	42
Cohesion	C [kPa]	0.06	0.5
Bulk density	ρ [kg/m³]	1400	1500
Relative density	Dr [-]	0.22 (at the surface) 0.7 (in 0.4m depth)	0.3 (at the surface) 0.75 (in 0.25m depth)

A4 – Ancillary Validation Data of the Numerical Model

Chapter 5 has introduced a validation scheme to assess the credibility of the numerical touchdown simulation. In order to do so, the simulated platform response is correlated with data obtained from the experimental test campaign. While chapter 5 shows time series data and the associated validation figures (the correlation coefficient, eq. 5.1, and the absolute error, eq. 5.2) for selected and illustrative measurement channels, this annex provides the complete lists of these figures as a reference.

The following tables differentiate between each of the four test cases (refer chapter 4.3) and a combined value over all cases. The mean and the median of the validation figures are calculated. The discussion and the implications of these results are provided in chapter 5.2.6.

Corr.Coeff.	Test Case 1	Test Case 2	Test Case 3	Test Case 4	All Cases
r	0.961	0.893	0.967	0.808	
q	0.979	0.925	-	-	
Mean	0.97	0.91	0.97	0.81	0.92
Median	0.97	0.91	0.97	0.81	0.94
Ψ	0.997	0.999	0.989	0.950	
Θ	0.993	0.998	-	-	
Mean	0.99	1.00	0.99	0.95	0.99
Median	0.99	1.00	0.99	0.95	0.99

Correlation between simulated and experimental data: Platform attitude and attitude rate

Corr.Coeff.	Test Case 1	Test Case 2	Test Case 3	Test Case 4	All Cases
$\mathbf{F_{p1}}$	0.715	0.824	0.810	0.832	
$\mathbf{F_{p2}}$	0.727	0.721	0.832	0.878	
$\mathbf{F_{p3}}$	0.793	0.886	0.701	0.888	
$\mathbf{F_{p4}}$	0.794	0.854	0.848	0.877	
Mean	0.76	0.82	0.80	0.87	0.81
Median	0.76	0.84	0.82	0.88	0.83
$\mathbf{s_{p1}}$	0.999	0.987	0.997	0.885	
$\mathbf{s_{p2}}$	0.993	0.987	0.988	0.989	
$\mathbf{s_{p3}}$	0.958	0.970	0.825	0.989	
$\mathbf{s_{p4}}$	0.970	0.974	0.994	0.988	
Mean	0.98	0.98	0.95	0.96	0.97
Median	0.98	0.98	0.99	0.99	0.99

Correlation between simulated and experimental data: Primary strut force and stroke measurements

Corr.Coeff.	Test Case 1	Test Case 2	Test Case 3	Test Case 4	All Cases
F_{s11}	(0.72)	(0.61)	(0.68)	0.842	
F_{s12}	0.70	0.65	(0.81)	0.847	
F_{s21}	0.80	0.77	0.93	0.805	
F_{s22}	(0.74)	(0.59)	(0.45)	0.857	
F_{s31}	(0.59)	0.56	0.49	0.840	
F_{s32}	0.87	0.92	0.51	0.824	
F_{s41}	0.83	0.90	(0.42)	0.818	
F_{s42}	0.64	0.61	0.89	0.839	
Mean	0.74	0.70	0.65	0.83	0.73
Median	0.73	0.63	0.60	0.84	0.79
s_{s11}	(0.93)	(0.99)	(0.98)	0.579	
s_{s12}	0.40	0.43	(0.97)	0.793	
s_{s21}	0.55	0.82	0.91	0.217	
s_{s22}	(0.93)	(0.99)	(0.27)	0.768	
s_{s31}	(0.35)	0.23	0.28	0.295	
s_{s32}	0.71	0.80	0.43	0.207	
s_{s41}	0.73	0.83	(0.28)	0.765	
s_{s42}	0.45	0.01	0.10	0.749	
Mean	0.63	0.64	0.53	0.55	0.59
Median	0.63	0.81	0.36	0.66	0.65

Correlation between simulated and experimental data: Secondary strut force and stroke measurements. The data in brackets "(…)" indicate a compression of the strut, other are deflected in the tension direction.

Secondary Strut		Force F	Stroke s
(compression)	**Mean**	0.62	0.74
	Median	0.61	0.93
tension	**Mean**	0.77	0.52
	Median	0.82	0.55

Correlation between simulated and experimental data: Secondary strut force and stroke measurements, differentiation between compression and tension direction

Abs. Error	Test Case 1	Test Case 2	Test Case 3	Test Case 4	All Cases
r	16.80	12.44	10.71	9.40	
q	10.57	10.27	-	-	
Mean	13.68	11.36	10.71	9.40	11.70
Median	13.68	11.36	10.71	9.40	10.64
Ψ	0.52	1.50	0.83	1.44	
Θ	0.72	2.04	-	-	
Mean	0.62	1.77	0.83	1.44	1.18
Median	0.62	1.77	0.83	1.44	1.13

Absolute error between simulated and experimental data: Platform attitude and attitude rate

Abs. Error	Test Case 1	Test Case 2	Test Case 3	Test Case 4	All Cases
$\mathbf{F_{p1}}$	0.73	0.81	1.43	0.78	
$\mathbf{F_{p2}}$	0.87	1.08	0.68	0.82	
$\mathbf{F_{p3}}$	0.76	0.92	1.51	0.46	
$\mathbf{F_{p4}}$	0.94	1.13	0.68	0.84	
Mean	0.82	0.99	1.07	0.73	0.90
Median	0.82	1.00	1.05	0.80	0.83
$\mathbf{s_{p1}}$	1.44	6.34	4.88	8.80	
$\mathbf{s_{p2}}$	14.54	15.36	15.40	15.36	
$\mathbf{s_{p3}}$	1.55	6.49	24.62	1.97	
$\mathbf{s_{p4}}$	10.03	6.65	6.36	16.81	
Mean	6.89	8.71	12.81	10.74	9.79
Median	5.79	6.57	10.88	12.08	7.73

Absolute error between simulated and experimental data: Primary strut force and stroke measurements

Abs. Error	Test Case 1	Test Case 2	Test Case 3	Test Case 4	All Cases
F_{s11}	(0.57)	(0.43)	(0.54)	0.30	
F_{s12}	0.54	0.70	(0.52)	0.28	
F_{s21}	0.60	0.54	0.55	0.66	
F_{s22}	(0.53)	(0.43)	(0.86)	0.42	
F_{s31}	(0.57)	0.63	0.58	0.34	
F_{s32}	0.56	0.53	0.61	0.28	
F_{s41}	0.48	0.45	(0.67)	0.44	
F_{s42}	0.53	1.02	0.77	0.56	
Mean	0.55	0.59	0.64	0.41	0.55
Median	0.55	0.54	0.60	0.38	0.54
s_{s11}	(5.79)	(6.20)	(37.61)	2.68	
s_{s12}	12.06	8.04	(7.07)	1.08	
s_{s21}	6.49	2.33	10.79	8.87	
s_{s22}	(16.96)	(22.16)	(4.05)	1.81	
s_{s31}	(3.36)	5.64	2.08	7.54	
s_{s32}	2.97	4.21	2.01	8.65	
s_{s41}	1.62	1.94	(3.05)	1.78	
s_{s42}	2.70	8.74	15.08	5.64	
Mean	6.49	7.41	10.22	4.76	7.22
Median	4.57	5.92	5.56	4.16	5.64

Absolute error between simulated and experimental data: Secondary strut force and stroke measurements. The data in brackets "(…)" indicate a compression of the strut, other are deflected in the tension direction.

Secondary Strut		Force F	Stroke s
(compression)	**Mean**	0.57	11.80
	Median	0.54	6.20
tension	**Mean**	0.54	5.42
	Median	0.54	4.21

Absolute error between simulated and experimental data: Secondary strut force and stroke measurements, differentiation between compression and tension direction

A5 – Stochastic Modeling of a Hazard Detection and Avoidance Maneuver

The content of this annex is an excerpt from the publication *Witte 2013*, the author of this thesis, and shall complement the chapter 8.3 Landing Dispersion Pattern by providing the in-depth description to derive the transition matrix **T**:

"The propagation (equation 6) of this initial state vector $\mathbf{p}_0$ requires a $n^2 \times n^2$ transition matrix **T**. The decision dependent transition matrix in this application shall reflect the HDA strategy. The planning horizon of current implementations of such systems aims at an immediate optimization of the score value at the current state, referred to as "the greedy case" (*Thrun et al. 2006*). The next state vector shall only be dependent on the current state but not from the history of the process. Thus the Hazard Detection and Avoidance process can be regarded as a Markov process (*Yin 2005*, *Lindsey 2004*, *Girlich 1973*). A sequence of observation and decision gates is considered at which the process's state vector is determined. Between these gates it shall be possible to alter the course of action. The transition matrix $\mathbf{T} = (t^a_{ij}) \in \mathbb{R}^{n^2 \times n^2}$ containing these relations shall satisfy the Chapman-Kolmogorov equation.

The model of such a periodically controlled system can then be interpreted in that way, that if the flight system is in state j at the event k and if decision d_k is taken, the course of action $a \in A$ is chosen in a way that at event k+1 it can be found in state i with the conditional probability t^a_{ij} being associated to each alternative a. The theory of these stochastic decision processes can be found in *Girlich 1973*. A sequence $d = (d_k)$ of decisions is hereby called a control policy.

$$\mathbf{p}_{k+1} = \mathbf{T} \cdot \mathbf{p}_k \qquad (6)$$

The conditional probabilities t_{ij} must be equal or larger than 0 while the column sum of all conditional probabilities must be equal to 1 ($\Sigma_i \, t^a_{ij} = 1$ with $t^a_{ij} \geq 0$). With the transition matrix $\mathbf{T}(d_k)$ the propagation of the controlled system from event 0 to event k is described by equation 7.

$$\mathbf{T}_{k+1}(d) = \mathbf{T}(d_k) \cdot \ldots \cdot \mathbf{T}(d_1) \cdot \mathbf{T}(d_0) \qquad (7)$$

Adjacency

To set up such transition matrix it is necessary to identify the sets of feasible alternatives. In the frame of the HDA model this is done by identifying the set of nodes within the footprint capability of the landing system. Each element of the state space can in that regard also be interpreted as a node which lumps together the actual positions of the vehicle inside its associated grid cell. The nodes are connected via edges if they are within reach of each other. The mathematical structure which is given by a set of connected nodes is a graph. It thus considers the visibility of a particular node through the imaging sensors and its accessibility by a divert maneuver, if the Euclidian distance is less than R ($||\Delta \mathbf{x}||_2 \leq R$; R_{VIS} and R_{DIVERT} respectively if required). The nodes and edges information is stored in an adjacency matrix. A graph with n^2 nodes leads to a $n^2 \times n^2$ adjacency matrix **G**. The element g_{ij} is set to 1 if node i is visible and accessible from node j which is the necessary condition that a divert maneuver from j to i is possible. Otherwise g_{ij} is set to 0 as landing sites outside the divert footprint capability are declared non-adjacent. Figure 3 sketches this process. The visibility matrix $\mathbf{G}_{VIS}$ captures the field of view while the range matrix $\mathbf{G}_{DIVERT}$ captures the divert distance. If it is part of the divert strategy to account also for the range to an alternative site and favor shorter distances, then this weighing factors can be carried as well. The elements of a matrix $\mathbf{G}_{RANGE}$ are then allowed to have values $0 \leq g_{ij} \leq 1$ and are considered by an appropriate means in the score scheme.

The adjacency matrix thus captures the flight systems functional and performance limits with regard to its sensor field of view and divert range as function of the height above the surface being valid for a certain decision gate. The adjacency matrix is typically a sparse matrix. The case study analysis […] considers the simple case of a circular FOV pattern and omnidirectional divert capability […]. Nevertheless, the method is not restricted to this simplification.

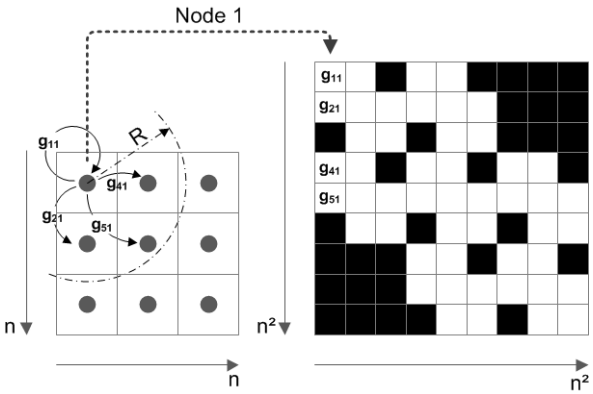

Fig 3 Adjacency matrix (white = adjacent, black = non-adjacent)

Hazard mapping and the Global Score Matrix

The score map captures the combined hazard assessment and divert-preferences after application of score scheme to the local maps acquired by the sensor suite, dependent from the actual position of the flight system. To consider this, the n × n matrices of the terrain property maps of the landing region is re-written as n² × 1 vector, duplicated n²-times and concatenated as matrix $\mathbf{M}_{TP} = (m_{TPij}) \in \mathbb{R}^{n^2 \times n^2}$ each.

Each matrix $\mathbf{M}_{TP}$ is multiplied element wise with the adjacency matrix **G** such as it is masked by it.

$$m'_{TP\,ij} = m_{TP\,ij} \cdot g_{ij} = \begin{cases} m_{TP\,ij} \\ \text{NaN, if } g_{ij} = 0 \end{cases} \qquad (8)$$

Consequently, each column of the resulting matrices represents a local map of the respective terrain property as would be acquired by the flight system from the associated node. Non-adjacent elements are out of view and/or out of reach accordingly. The application of the score scheme […] leads likewise to a n² × n² matrix, in which each column represents the local score map the flight system would have obtained at this site at node j. This matrix $\mathbf{S} = (S_{ij}) \in \mathbb{R}^{n^2 \times n^2}$ is denoted the Global Score Matrix (GSM) as it captures all local score maps for the landing region under investigation. The process described is sketched schematically in Figure 4.

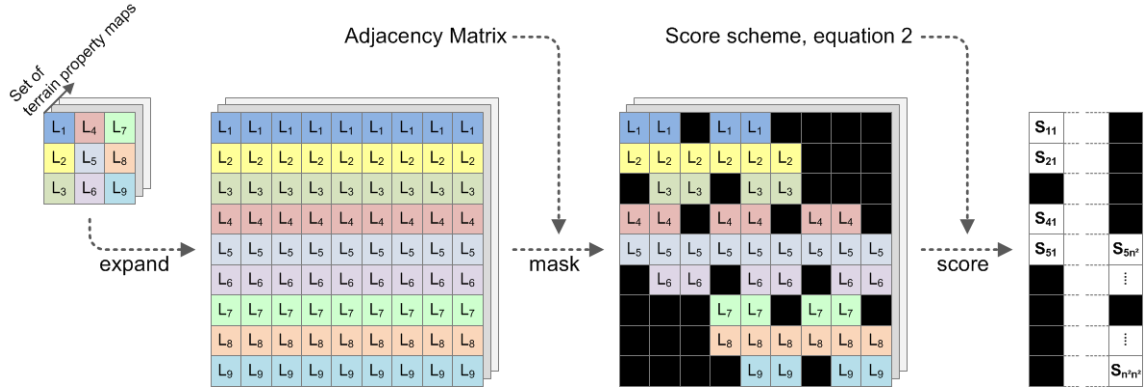

Fig 4 Process steps to compute the Global Score Matrix

Decision Making and Probability Assignment

To make a decision means per definition the selection of one alternative out of several courses of action. It thus requires a judgment or ranking criteria. Such criterion to select the best alternative is provided in this case by the data fusion and scoring process introduced in section 2. As the score values are real numbers, describing the utility of each alternative, the complete ordering axiom (*Whitmore 1978*) applies. This means that all alternative courses of action $a_1, a_2, a_3 \in A$ can be put into an order according their utility.

It is now assumed for a moment that the onboard decision making entity has access to absolutely precise and error-free observations of the landing zone by its sensors. As well the flight systems attitude and motion states are known error-free. The hazard map derived from these ideal data consequently shows the true hazard distribution. From the current position of the flight system the landing site within the field of view then can be selected with certainty according to the underlying score scheme. In such an idealized scenario the flight system always diverts to the safest landing site within view and range, or, if it is already at this site, it stays there.

A transition matrix for the decision d_k, fulfilling the requirements […] is in this case derived by a simple rule from the GSM matrix.

$$t_{i^*j} := 1, \qquad i^* = \mathrm{argmax}_i\{S_{ij}\}, j = 1 \,..n^2 \tag{9}$$

The highest score S_i per column j of the GSM marks the coordinates of the safest available landing site from the current position j. The corresponding element of the transition matrix **T** is set to 1 and represents in this ideal scenario the certain transition from the current node to the safe alternative. Thus at the decision gate the current state is mapped to the best alternative out of the set of feasible alternatives. The inferior alternatives (in terms of their score value) as well as the impossible (non-adjacent sites) are of zero probability as a consequence.

In the real world realization of a hazard detection and avoidance system, the decision making process would be affected by the uncertainties stemming from limited sensor resolutions, process noise and deficiencies of the flight system and terrain representation. The measurements of the imaging sensors thus can be regarded as a random experiment realizing numbers from a probability distribution representing the sensor behavior and the terrain model. Thus the data fusion, scoring and decision making becomes a stochastic process on its own. In that regard *Loomes 1995* suggests to include some kind of processing error as a stochastical element into the model of the decision making process. This idea, originally intended to analyze economic decisions, is here pursued further and adopted for its technical application.

For example, let a_1 and a_2 be realizations of a stochastic experiment of their underlying probability distributions, with $a_1 \sim F$, $a_2 \sim G$, $x \in \mathbb{R}$ and $F(x) \leq G(x)$. The probability $P(a_1)$ that a_1 takes a higher value than x is at least as high as the probability $P(a_2)$ that a_2 takes a higher value than x.

$$P(a_1>x) = 1\text{-}F(x) \geq 1\text{-}G(x) = P(a_2>x) \tag{10}$$

Thus the realization of a_1 is stochastically dominant (*Whitmore 1978*) to a_2 because the expectations are $E(a_1) \geq E(a_2)$. This inequality represents a first order stochastic dominance relation. In practical applications the empirical determination of the distribution functions from observations is limited (*Schmid 2006*). The measurement error can more than offset the difference between the true values of a_1 and a_2. A limited set of observations or in an extreme case only one observation can lead to a result

that a truly best alternative is chosen with a probability of less than 1 and otherwise non-zero probabilities are also assigned to alternative courses of action having not the highest utility.

A prerequisite to exploit this concept in the HDA context is to describe the score value as a random number. Therefore a first step to consider the uncertainties stemming from the terrain property determination is to select a suitable means to propagate the associated error figures through the score function. A comparative study on the relative strength and weaknesses of some widely applied uncertainty propagation techniques, including Monte-Carlo simulations, local expansion based methods or Most Probable Point methods, is done by *Lee 2009*. Further guidance on method selection is provided with regard to methods susceptibility to the performance function's (in this case score function) non-linearity, number and nature of the input parameters and computational considerations.

A key property of the score functions used in the HDA case is that they must be continuous and strictly monotonous. This characteristic mitigates a general weakness of local expansion based methods such as the Taylor approximation of exhibiting large approximation errors in case of highly non-linear functions. For the HDA application Taylor approximation is regarded as suitable as it furthermore computationally efficient.

In a second step assumptions are made on the probability distribution of the score values. A complicacy is the fact that slope, roughness and other terrain properties determined in-situ by the flight system are not direct measurements but themselves the result of a data processing and algorithmic treatment of several input parameters and measurements. Hereby these parameters are affected by multiple errors sources of both random and systematic nature. Although frequency distributions of these derived terrain properties remain typically unknown, it is implied that it is at least possible to constrain the bounds of their error distribution. Related discussion on this aspect, error types and their propagation in computing is given in *Austin Barry 1978*, *Dietrich 1973*.

Thus in the absence of information on the (arbitrarily shaped) probability distribution function of the derived terrain properties but availability of estimations or assumptions on their absolute errors, the error bounds of the score value can be computed using a Taylor approximation of the score scheme (eq. 11). In that regard this paper follows the conclusions of *Dietrich 1973*, that it is at least reasonable to assume then that any uncertainty between the computed upper and lower bounds is equi-probable yielding here a first-order approach to integrate estimates on the measurement and sensor errors into the decision scheme of this paper. The following derivation of the probability assignment to courses of action is based on that approach.

Thus a set of alternatives is assumed which are uniformly distributed $a_i \sim U(a_{i,0}, \varepsilon)$ and defined by their mean value $a_{i,0}$ and the semi-range ε. In the HDA application the set mean values $\{a_{i,0}\}$ is defined as $\{a_{i,0}\} = \{S_i\}'$ with $\{S_i\}'$ being the vector $\{S_i\}$ i=1..n², j sorted into descending order to introduce the principal ranking of the associated sites. The associated semi-range is the error bound derived from the sensor error propagation through the score scheme (equation 2) with ΔL being the systems slope measurement error and ΔR being the roughness measurement error.

$$\varepsilon = \Delta S = \sqrt{\Delta L^2 + \Delta R^2} \,/\, (L_{max} + R_{max}) \qquad (11)$$

Alternatives whose upper bound is smaller than the lower bound of the maximum nominal score alternative have a probability of zeros as they remain inferior despite taking measurement errors into account. Thus not the complete set a_i, i=1..n² needs to be processed but only a subset of length λ, containing all alternatives with a prospect of a non-zero probability.

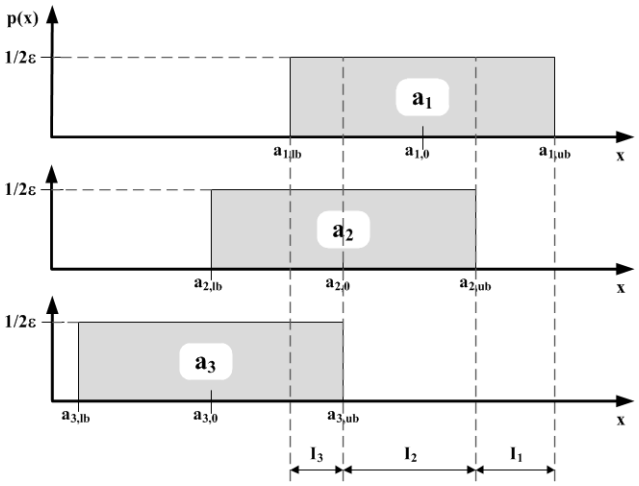

Fig 5 Probability densities of three (λ=3) uniformly distributed alternatives

Figure 5 shows the probability densities for three alternatives in a descending order. For the further processing the range between upper and lower bound of a_1 is subdivided into λ intervals I with its λ+1 boundaries $\alpha = [a_{1,ub}, a_{2,ub}, \ldots, a_{\lambda,ub}, a_{1,lb}]$ and its λ lower bound values $\omega = [a_{1,lb}, a_{2,lb}, \ldots, a_{\lambda,lb}]$ (ub..upper bound, lb..lower bound). The discrete probability that a_i is drawn from I_j is then

$$P(a_i \in I_j) = (\alpha_j - \alpha_{j+1})/(2\varepsilon),\ i=1..\ \lambda,\ j=i..\lambda, \qquad (12)$$

The probability that a_i is not drawn from I_j but from any I_m, m>j is

$$P(a_i \notin I_j) = (\alpha_{j+1} - \omega_i)/(2\varepsilon),\ i=1..\ \lambda,\ j=i..\lambda, \qquad (13)$$

It is noted that $P(a_i \notin I_j) \neq 1 - P(a_i \in I_j)$ except for i=1, j=1.

For example out of a set of two alternatives, the alternative a_1 is dominant when drawn from I_1 ($P(a_1 \in I_1)$) or from I_2 ($P(a_1 \in I_2)$) and a_2 is drawn from I_3 ($P(a_2 \in I_3)$) or both a_1 and a_2 are drawn I_2 and a_1 is larger than a_2 with $P(a_1 > a_2)=1/2$. The latter term is the conditional probability P = 1/i that one alternative exceeds the other(s) in the case that i alternatives are drawn from a particular interval.

$$P(a_1) = P(a_1 \in I_1) + P(a_1 \in I_2) \cdot P(a_2 \notin I_2) + P(a_1 \in I_2) \cdot P(a_2 \in I_2) \cdot P(a_1 > a_2) \qquad (14)$$

The probabilities $P(a_i)$ express here the uncertainty in action selection and can be interpreted in that way that $P(a_1)$ is the likelihood of the true positive decision to divert to the safest site, while $P(a_i)$, i>1 are the likelihoods of the false positive decisions to divert to one of the less safe sites.

Associated to the three alternatives as defined by Figure 5, the Figure 6 shows a 3x3 matrix $\mathbf{Q} = (q_{ij}) \in \mathbb{R}^{\lambda \times \lambda}$. **Q** is an upper triangular matrix, with row i referring to the list of feasible alternatives and column j referring to the interval subdivision of the range of a_1. Each element of this matrix is the partial probability that a respective alternative is drawn from interval j and is dominant to other alternatives.

The probability for a diversion to alternative a_i is the row sum of the elements of **Q**. This scheme presents the exact numerical solution to the problem.

$$P_{exact}(a_i) = \sum_{j=1}^{\lambda} q_{ij} \qquad (15)$$

	I_1	I_2	I_3
a_1	$P(a_1 \in I_1)$	$P(a_1 \in I_2) \cdot P(a_2 \notin I_2)$ $+ P(a_1 \in I_2) \cdot P(a_2 \in I_2) \cdot P(a_1 > a_2)$	$P(a_1 \in I_3) \cdot P(a_2 \notin I_3) \cdot P(a_3 \notin I_3)$ $+ P(a_1 \in I_3) \cdot P(a_2 \in I_3) \cdot P(a_3 \notin I_3) \cdot P(a_1 > a_2)$ $+ P(a_1 \in I_3) \cdot P(a_2 \notin I_3) \cdot P(a_3 \in I_3) \cdot P(a_1 > a_3)$ $+ P(a_1 \in I_3) \cdot P(a_2 \in I_3) \cdot P(a_3 \in I_3) \cdot P(a_1 > a_2 \cap a_1 > a_3)$
a_2	0	$P(a_1 \notin I_2) \cdot P(a_2 \in I_2)$ $+ P(a_1 \in I_2) \cdot P(a_2 \in I_2) \cdot P(a_2 > a_1)$	$P(a_1 \notin I_3) \cdot P(a_2 \in I_3) \cdot P(a_3 \notin I_3)$ $+ P(a_1 \in I_3) \cdot P(a_2 \in I_3) \cdot P(a_3 \notin I_3) \cdot P(a_2 > a_1)$ $+ P(a_1 \notin I_3) \cdot P(a_2 \in I_3) \cdot P(a_3 \in I_3) \cdot P(a_2 > a_3)$ $+ P(a_1 \in I_3) \cdot P(a_2 \in I_3) \cdot P(a_3 \in I_3) \cdot P(a_2 > a_1 \cap a_2 > a_3)$
a_3	0	0	$P(a_1 \notin I_3) \cdot P(a_2 \notin I_3) \cdot P(a_3 \in I_3)$ $+ P(a_1 \in I_3) \cdot P(a_2 \notin I_3) \cdot P(a_3 \in I_3) \cdot P(a_3 > a_1)$ $+ P(a_1 \notin I_3) \cdot P(a_2 \in I_3) \cdot P(a_3 \in I_3) \cdot P(a_3 > a_2)$ $+ P(a_1 \in I_3) \cdot P(a_2 \in I_3) \cdot P(a_3 \in I_3) \cdot P(a_3 > a_1 \cap a_3 > a_2)$

Fig 6 3×3-Matrix Q for an example of three alternatives ($\lambda = 3$)

Implementation and Numerical Challenges

The implementation and generation of **Q** and its elements q_{ij} can be automatized by making use of the combinatory nature of the equations and structure of **Q**. However, the number of combinations of the alternatives being in a certain interval j or not is of the order of 2^{j-1}. And, as the probabilities $P(a \notin I) \neq 1 - P(a \in I)$ the equations of these partial probabilities q_{ij} have to be written and calculated explicitly. Thus the algorithmic effort for the execution of λ alternatives is likewise of $O(2^{\lambda-1})$ which might be prohibitively large for large numbers of λ due to the resulting excessive computation demand.

For large numbers of λ an approximate solution can be obtained as all $P(a_i \in I_j)$ for $i=1..\lambda$ within an interval j are equal and if the probabilities $P(a_i \notin I_j)$ are substituted by a mean value $\tilde{P}$. Hereby $\tilde{P}$ is the geometric mean of the set $\{ P(a \notin I_j)\}$, $j = i..\lambda$. The terms for q_{ij} can then be expressed as a binomial expression (equation 16) to reduce the algorithmic complexity. As it is not the exact solution of q_{ij} but an approximation of their order of magnitude a matrix $\mathbf{M} = (m_{ij}) \in \mathbb{R}^{\lambda \times \lambda}$ is used instead. The resultant complexity of the approximation is of $O(\lambda^3)$.

$$m_{ij} = \frac{1}{j} \cdot \sum_{v=1}^{j} \binom{j}{v} \cdot P^v(a_i \in I_j) \cdot \tilde{P}^{j-v} \qquad (16)$$

Example: the term q_{13} from the matrix **Q** in Figure 6 is approximated by the term m_{13}:

$q_{13} =$ $P(a_i \in I_3) \cdot P(a_2 \notin I_j) \cdot P(a_3 \notin I_j) + 1/2 \cdot P^2(a_i \in I_3) \cdot P(a_3 \notin I_j) + 1/2 \cdot P^2(a_i \in I_3) \cdot P(a_2 \notin I_j) + 1/3 \cdot P^3(a_i \in I_3) \approx 1/3 \cdot (3 \cdot P(ai \in I_3) \cdot \tilde{P}^2 + 3 \cdot P^2(a \in I_3) \cdot \tilde{P} + P^3(a \in I_3)) \cdot = m_{13}$

The approximation $P_{approx}(a_i)$ is finally given by equation 17, where $\|\cdot\|$ denotes the sum of elements of a respective matrix.

$$P_{approx}(a_i) = \left(\sum_{j=1}^{\lambda} m_{ij}\right) / \|\mathbf{M}\| \qquad (17)$$

Still the magnitude of the binomial coefficient requires some extra care as double precision numbers only have about 15 digits which are easily exceeded by the factorial terms from large lists of alternatives. The size of these factorial terms can be balanced by the powers of P and $\tilde{P}$ and equation 16 is rewritten as given by the equations 18 and 19 (*Bornemann et al. 2006*). The coefficient b is calculated recursively. The complexity of the algorithm is further reduced to $O(\lambda^2)$.

$$m_{ij} = \frac{1}{j} \cdot \tilde{P}^j \cdot \sum_{v=1}^{j} b_v \qquad (18)$$

$$\text{with } b_v = \frac{j-v+1}{v} \cdot \frac{P(a_i \in I_j)}{\tilde{P}} \cdot b_{v-1} \qquad \text{and } b_0 = 1 \qquad (19)$$

The order of magnitude for $P(a_i)$ is decreasing exponentially thus reaching rapidly a practically relevant precision or even computing machine precision. Figure 7 shows this for a set of 10 alternatives (evenly spaced with $\Delta a_{i,0} = 0.4$ and e=2.0) computed explicitly as exact solution.

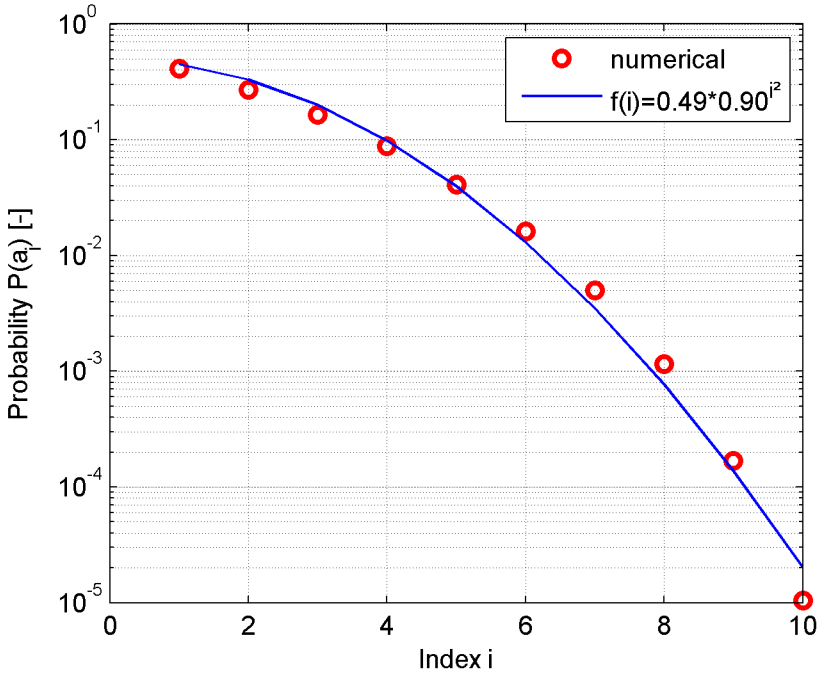

Fig 7 Probability $P(a_i)$ for 10 evenly spaced alternatives

A crude estimate of the level i at which a certain magnitude is reached is given by the following equation 20 with μ denoting the power of the desired magnitude. This estimate is applicable to sets with scores which can be sorted into a descending order. Example: it shall be estimated for which alternatives a probability of less than 10^{-4} is reached. With $\mu = -4$ the index i_{mag} is determined as $i_{mag} = 10$. Thus the probability of the 10^{th} element in the list can be expected to be less than 10^{-4}.

$$i_{mag} \approx \left\lceil \sqrt{\mu / \log_{10}(1 - 1/\lambda)} \right\rceil \qquad (20)$$

The error between the exact solution and the approximate solution can be estimated in a similar way. Figure 8 shows this error $err = |P_{exact}(a_1) - P_{approx}(a_1)|$ for the most significant first alternative a_1 computed for a set of 10 alternatives. The abscissa indicates the list element at which the switch-over from the exact solution to the approximation for the remaining less significant digits occurred. Thus i = 1 means a full approximation and the other a partial approximation.

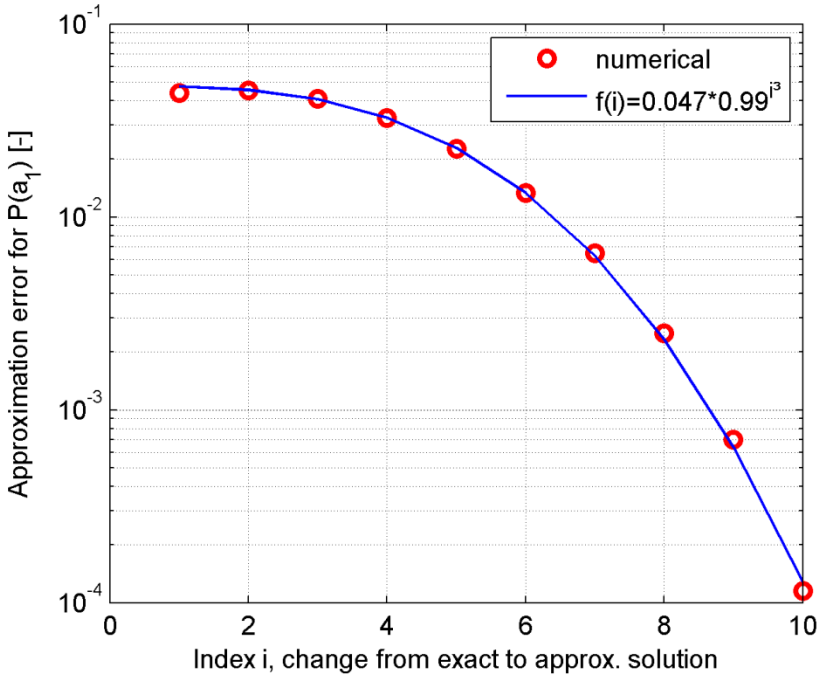

Fig 8 Approximation error for $P(a_1)$

Likewise, a crude estimate of the level i at which a certain accuracy is reached is given by equation 21with μ denoting the power of the desired accuracy. Example: the result shall be accurate to 10^{-3}. With $\mu = -3$ the index i_{err} is determined as $i_{err} = 9$. Thus at least the first 9 alternatives have to be calculated explicitly as exact solution to meet the desired accuracy.

$$i_{err} \approx \left\lceil \sqrt[3]{\mu / \log_{10}(1 - 1/\lambda^2)} \right\rceil \qquad (21)$$

Any termination of the exact calculation of **Q** at $\lambda_{break} < \lambda$ resulting in $\mathbf{Q}_{partial}$, size $\lambda_{break} \times \lambda_{break}$ makes use of the requirement that the sum of $P(a_i)$, i=1..λ must be equal to 1. The residual term R_{break} is allotted according the order of magnitude estimate **M'**.

$$R_{break} = 1 - \|\mathbf{Q}_{partial}\| \qquad (22)$$

$$\mathbf{Q} \approx \mathbf{Q}_{approx} = \mathbf{Q'} + R_{break} \cdot \mathbf{M'} / \|\mathbf{M'}\| \qquad (23)$$

$\mathbf{Q}' = \begin{bmatrix} \mathbf{Q}_{partial} & \mathbf{0} \\ \mathbf{0} & \mathbf{0} \end{bmatrix}$ and $\mathbf{M}' = \begin{bmatrix} \mathbf{0} & \mathbf{M}_{12} \\ \mathbf{M}_{21} & \mathbf{M}_{22} \end{bmatrix}$ are block matrices of size λ×λ and $\mathbf{M}_{12}$, $\mathbf{M}_{21}$, $\mathbf{M}_{22}$ being sub-matrices filling the elements m_{ij}, $i = \lambda_{break}..\lambda$, $j = \lambda_{break}..\lambda$ of **M'** with order of magnitude estimates according equation 16.

The developed solutions for the exact and approximate form give the option to a user to trade the desired or needed accuracy versus the computational effort and accordingly a switch from one to the other method or early termination can occur.

As a final step, the probabilities that the alternatives a_i i = 1…λ is chosen is assigned to the transition matrix element corresponding to its associated original element index in the GSM."